UNIVERSIDAD DE VALENCIA

DEPARTAMENTO DE FÍSICA ATÓMICA, MOLECULAR Y NUCLEAR

INSTITUTO DE FÍSICA CORPUSCULAR

UNIVERSITAT DE VALÈNCIA

Estudio de la Resonancia Gamow-Teller en la Región del ^{146}Gd mediante Espectroscopía Gamma de Absorción Total

DANIEL CANO OTT

TESIS DOCTORAL

FEBRERO DEL 2000

UNIVERSITAT DE VALÈNCIA

INSTITUT DE FÍSICA CORPUSCULAR

DEPARTAMENT DE FÍSICA ATÒMICA,
MOLECULAR I NUCLEAR

Estudio de la Resonancia Gamow-Teller en la Región del ^{146}Gd mediante Espectroscopía Gamma de Absorción Total

DANIEL CANO OTT
TESIS DOCTORAL
FEBRERO DEL 2000

José Luis Taín Enriquez, Científico Titular del Consejo Superior de Investigaciones Científicas (CSIC)

CERTIFICA: Que la presente memoria **"Estudio de la Resonancia Gamow-Teller en la Región del ^{146}Gd mediante Espectroscopía Gamma de Absorción Total"** ha sido realizada bajo su dirección en el Instituto de Física Corpuscular (Centro Mixto Universidad de Valencia - CSIC) por **Daniel Cano Ott** y constituye su Tesis para optar al grado de Doctor en Ciencias Físicas.

Y para que así conste, en cumplimiento con la legislación vigente, presenta ante el la Facultad de Física de la Universidad de Valencia la referida Tesis, firmando el presente certificado en Burjassot (Valencia) a 24 de Noviembre de 1999.

There is a theory which states that if ever anyone discovers exactly what the Universe is for and why it is here, it will instantly disappear and be replaced by something even more bizarre and inexplicable.

There is another theory which states that this has already happened.

Douglas Adams
“The Restaurant at the End of the Universe”

A mis padres y a mi familia

Contents

1 The Physics **1**

1.1 Introduction 1
1.2 The beta decay 2
1.3 The β-strength function 10
1.4 The problem of the missing Strength 12
1.5 The β-strength determination from beta decay measurements 14

2 The Experiment **17**

2.1 The nuclei around ^{146}Gd 17
2.2 The facility 20
2.3 The experimental setup 22
2.4 The Total Absorption Spectrometer 25
2.5 The electronics 29
2.6 The measurements 33

3 The TAGS Inverse Problem **35**

3.1 Introduction 35
3.2 The construction of the response matrix **R** 36
3.3 Algorithms for the solution of ill-posed linear inverse problems 44
  3.3.1 Linear Regularisation (LR) Method 45
  3.3.2 Maximum Entropy (ME) Method 47
  3.3.3 Expectation-Maximisation (EM) Method 48

4 The Data Analysis and Results **51**

4.1 Introduction 51
4.2 The procedure to extract the data 51
4.3 The ^{150}Ho $2^- \rightarrow {}^{150}$Dy data 53
  4.3.1 EC spectra 53
  4.3.2 β^+ spectra 56
4.4 The ^{150}Ho $9^+ \rightarrow^{150}$ Dy data 57
  4.4.1 EC spectra 58
  4.4.2 β^+ spectra 62
4.5 Strength and $\log ft$ calculation 64
4.6 The ^{150}Ho $2^- \rightarrow {}^{150}$Dy results 66

4.6.1 Finding a solution which reproduces the experimental data . . 68
4.6.2 The independent EC and β^+ analysis 73
4.6.3 The dependence of the results on the assumed part of the level scheme 77
4.6.4 The dependence of the results on the analysis method 81
4.6.5 The Q_{EC} determination 83
4.6.6 Concluding remarks 85
4.7 The ^{150}Ho 9^+ → ^{150}Dy results 86
4.7.1 Finding a solution which reproduces the experimental data . . 86
4.7.2 The independent EC and β^+ analysis 91
4.7.3 The dependence of the results on the assumed part of the level scheme 93
4.7.4 The dependence of the results on the analysis method 95
4.7.5 Concluding remarks 97

5 The Interpretation of the Results **99**
5.1 Discussion of the results 99

6 Summary and Conclusions **109**
6.1 Introduction 109
6.2 The analysis 110
6.3 The results for ^{150}Ho 2^- and ^{150}Ho 9^+ 112
6.4 Concluding remarks 114

7 Resumen del trabajo **115**
7.1 Introducción 115
7.2 Las técnicas de análisis 118
7.3 Resultados para los isótopos ^{150}Ho 2^- y ^{150}Ho 9^+ 119
7.4 Conclusiones finales 121

A Calculation of the Strength and $\log ft$ **123**

B De-excitation schemes used in the construction of the response matrices **131**
B.1 Introduction 131
B.2 Statistical model for the electromagnetic de-excitation of the nucleus 132
B.3 Branching ratio matrices 133

C Tabulated β-strenghts **139**
C.1 Tabulated ^{150}Ho2^- β-strength 139
C.2 Tabulated ^{150}Ho 9^+ β-strength 142

List of Figures

1.1 Three different decay processes. In β^- decay, a neutron (udd) is transformed into a proton (uud) by exchange of a virtual W^- boson and emission of an electron e^- and an electron anti-neutrino $\bar{\nu}_e$. In β^+ decay, a proton (uud) is transformed into a neutron (udd) by exchange of a virtual W^+ boson and emission of a positron e^+ and an electron neutrino ν_e. The electron capture process has the same effect as β^+ decay: an electron from the atomic shell has a nonzero probability $|\Psi(r)|^2$ of being inside the nucleus, and thus being captured by a proton which is then transformed into a neutron. The captured electron leaves a vacancy in the atomic shell which is filled by less bound electrons. During this process, characteristic X-rays or Auger electrons are emitted. 3

1.2 Sixteen possible electron-neutrino states in allowed β-decay. 7

2.1 Quasiparticle energies in the ^{146}Gd region. 18

2.2 Region of interest of the nuclide chart. $\mathrm{Q_{EC}}$s, half-lives and ground state spins taken from [BNL99] [AUD97]. 19

2.3 Schematic drawing of the The GSI on-line mass separator 21

2.4 Scheme of the beam time distribution between the TAS and the monitoring setup during the experiment. 22

2.5 The coupling of the TAS to the GSI on-line mass separator 23

2.6 Picture of the TAS setup. Left: the implantation chamber above the last quadrupole of the beamline. Centre: outer part of the TAS shielding. Right: (large) experimenter and the station used for the tape transport behind him. 24

2.7 The TAS at the GSI on-line mass separator 25

2.8 Total and photopeak efficiencies of the TAS for different γ-ray energies obtained by Monte Carlo simulation. Solid lines correspond to the efficiencies of the spectrometer including the polyethylene absorber described in the text, while the dashed lines represent the efficiencies of the configuration without absorber described in [KAR97]. 27

2.9 Electronics scheme (I) 30

2.10 Electronics scheme (II) 31

2.11 Production mechanisms of the ^{150}Ho 2^- and ^{150}Ho 9^+ isomers. 33

3.1 Details of the TAS geometrical description in GEANT. a) Longitudinal cut along the spectrometer showing the main crystal and the plug detector. b) Plug detector with ancillary detectors and absorber. c) Upper part: Ge detector cryostat and cold finger; lower part: Ge crystal and capsule. d) Mounting for Si detectors and transport tape rollers together with the polyethylene absorber 39

3.2 Deviations of TAS spectra peaks from a linear energy calibration. Squares: single γ-ray peaks. Triangles: double γ-ray sum peaks. Circle: triple γ-ray sum peak. 40

3.3 NaI(Tl) relative light yield values for fully stopped electrons as a function of their energy. Circles: from Ref. [ROO96]. Triangles: from Ref. [ZER61]. Continuous line: fit (see text). 42

4.1 X-ray spectrum in the Ge detector recorded during the ^{150}Ho 2^- measurement. The well resolved Tb, Dy and Ho $K_{\alpha1}$ $K_{\alpha2}$ doublets were used to accumulate three TAS-spectra in coincidence. The regions in the Ge spectrum used to require the coincidence are limited by vertical dashed lines. The gates on the Tb and Ho X-rays were set more narrowly in order to have the cleanest possible spectra. 54

4.2 Different contaminations in the Dy X-ray gated spectrum (solid line) during the ^{150}Ho 2^- measurement. In order to get the clean EC-spectrum one has to subtract, the Ho X-ray gated spectrum (dotted) and the Tb X-ray gated spectrum (dashed-dotted) with the normalisations indicated in the figure. 55

4.3 ^{150}Ho2^- EC-decay spectrum free of contamination. The calculated pileup distortion is plotted as a solid line over the experimental points. 56

4.4 Bottom Si detector spectrum recorded during the ^{150}Ho 2^- measurement. The vertical dashed lines define the energy window used for the coincidence with the TAS. The lower value was set to avoid as much as possible the contribution from conversion electrons and Compton scattered γs. Also visible is the peak produced by the 4.2 MeV α-particles emitted in the ^{150}Dy ground state α-decay. 57

4.5 ^{150}Ho 2^- β^+-decay spectrum. The calculated pileup distortion is plotted as a solid line over the experimental points. 58

4.6 X-ray spectrum in the Ge detector recorded during the ^{150}Ho 9^+ measurement. The well resolved Tb, Dy and Ho $K_{\alpha1}$ $K_{\alpha2}$ doublets were used to accumulate three TAS-spectra in coincidence. The regions of the Ge energy spectrum used for the gates lie between vertical dashed lines. The gates on the Tb and Ho X-rays were set for the removal of contamination. 59

4.7 Different contaminations in the Dy X-ray gated spectrum, solid line, during the ^{150}Ho 9^+ measurement. In order to get the clean ^{150}Ho 9^+ decay spectrum one has to subtract, with the normalisations indicated in the figure, the pure Ho 2^- dashed spectrum, the dotted Ho X-ray gated spectrum and the dashed-dotted Tb X-ray gated spectrum. . . 60

4.8 ^{150}Ho 9^+ EC-spectrum. The calculated pileup distortion is plotted as a solid line over the experimental points. 61

4.9 Bottom Si detector spectrum recorded during the ^{150}Ho 9^+ measurement.The vertical dashed lines define the energy window used for the coincidence with the TAS. The lower value was set to avoid as much as possible the contribution from conversion electrons and Compton-scattered γs. Also visible is the peak produced by the 4.2 MeV α-particles emitted in the ^{150}Dy ground state α-decay. 62

4.10 Solid: TAS spectrum registered in coincidence with the bottom Si-detector during the ^{150}Ho 9^+ measurement. Dashed: TAS spectrum in coincidence with the bottom Si-detector used for the ^{150}Ho 2^- contamination of the previous one. 63

4.11 ^{150}Ho 9^+ β^+ spectrum. The calculated pileup distortion is plotted as a solid line over the experimental points. 64

4.12 Results of the ^{150}Ho 2^- decay analysis using the EM method. Both EC and β^+ response matrices were calculated following the electromagnetic de-excitation scheme 1. First row: EC (left) and β^+ (right) experimental spectra used in the analysis. Superimposed are the corresponding simulated spectra (solid lines) reconstructed from the resulting feeding distributions. Second row: relative deviations between the experimental and simulated spectra for both EC (left) and β^+ (right) cases. Third row: resulting EC (left) and β^+ (right) feeding distributions normalised to unity. 69

4.13 χ^2 (in arbitrary scale) between the experimental and Monte Carlo simulated spectra as a function of the number of iterations in the EM method. Top: EC spectra. Bottom: β^+ case. 70

4.14 Results of the ^{150}Ho 2^- β^+ decay EM analysis using three different positron response matrices and electromagnetic de-excitation scheme 1. The circles correspond to the results obtained with the GEANT3 simulated Monte Carlo response, the triangles to a response where the tail above the 1022 annihilation peak was removed and the squares to a response where the tail above the 1022 keV peak was multiplied by a factor of two. Top: the three feeding distributions. Bottom: the corresponding three strength distributions. 72

4.15 Top: strength distributions for the ^{150}Ho 2^- decay calculated from the EC (squares) and β^+ (triangles) feeding distributions. Bottom: relative deviations between the EC and β^+ strength (triangles) 75

4.16 Monte Carlo β^+ detection efficiency of the bottom Si detector as a function of the positron end-point energy. 76

4.17 Results of the ^{150}Ho 2^- decay analysis using the EM method. Both EC and β^+ response matrices were calculated following the electromagnetic de-excitation scheme 2. First row: EC (left) and β^+ (right) experimental spectra used in the analysis. Superimposed are the respective simulated spectra (solid lines) reconstructed from the resulting feeding distributions. Second row: relative deviations between the experimental and simulated spectra for both EC (left) and β^+ (right) cases. Third row: resulting EC (left) and β^+ (right) feeding distributions normalised to unity. 78

4.18 Results of the ^{150}Ho 2^- decay analysis using the EM method. Both EC and β^+ response matrices were calculated following the electromagnetic de-excitation scheme 3. First row: EC (left) and β^+ (right) experimental spectra used in the analysis. Superimposed are the respective simulated spectra (solid lines) reconstructed from the resulting feeding distributions. Second row: relative deviations between the experimental and simulated spectra for both EC (left) and β^+ (right) cases. Third row: resulting EC (left) and β^+ (right) feeding distributions normalised to unity. 79

4.19 Top: strength distributions for the ^{150}Ho 2^- decay calculated from the electromagnetic de-excitation schemes 1, 3 and 3. Bottom: relative differences between the strengths from electromagnetic de-excitation schemes 2 and 1 (squares) and level schemes 3 and 1 (triangles). . . . 80

4.20 Top: strength distributions for the ^{150}Ho 2^- decay calculated by the EM (circles), ME (squares) and 2nd order regularisation. Bottom: relative deviations between the ME and EM strength (squares) and 2nd order regularisation and ME strengths (triangles). 82

4.21 Q_{EC} calculated bin by bin from the EC and β^+ feeding distributions by interpolation of the EC/β^+(Q_{EC}) ratio tabulated in [GOV71]. . . . 84

4.22 Experimental EC (top) and β^+ (bottom) spectra for the ^{150}Ho 9^+ decay. 87

4.23 Results of the ^{150}Ho 9^+ decay analysis using the EM method. Both EC and β^+ response matrices were calculated following the electromagnetic de-excitation scheme 2. First row: EC (left) and β^+ (right) experimental spectra used in the analysis. Superimposed are the respective simulated spectra (solid lines) reconstructed from the resulting feeding distributions. Second row: relative deviations between the experimental and simulated spectra for both EC (left) and β^+ (right) cases. Third row: resulting EC (left) and β^+ (right) feeding distributions normalised to unity. 89

4.24 Top: strength distributions for the ^{150}Ho 9^+ decay calculated with the EM algorithm when the feeding to states below 2403 keV is allowed (circles) or explicitly forbidden (squares). Bottom: relative deviations between the two curves. 90
4.25 Top: strength distributions for the ^{150}Ho 9^+ decay calculated from the EC (squares) and β^+ (triangles) feeding distributions in the case of electromagnetic de-excitation scheme 2. 92
4.26 Top: strength distributions for the ^{150}Ho 9^+ decay EC analysis. The curves correspond to the analysis of three experimental EC spectra from which the ^{150}Ho 2^- contamination was subtracted with the weights: 1.075 (circles), 1.055 (squares) and 1.095 (triangles). Bottom: relative differences between the strengths coming from the central subtraction of 1.075 and those coming from the minimal subtraction of 1.055 (squares) and maximal subtraction of 1.095 (triangles). . 93
4.27 Top: strength distributions for the ^{150}Ho 9^+ decay calculated from the EC spectrum for level-schemes 1 (circles) and 2 (squares). Bottom: relative deviations between the two curves. 95
4.28 Top: strength distributions for the ^{150}Ho 9^+ decay calculated by the EM (circles), ME (squares) and 2^{nd} order regularisation (triangles). Bottom: relative deviations between the ME and EM strength (squares) and 2^{nd} order regularisation and EM strengths (triangles). . 96

5.1 Comparison between the experimental and calculated (in arbitrary units) strength distributions for the ^{150}Ho 2^- decay. 101
5.2 Comparison between the experimental strength distributions for the ^{150}Ho 2^- (solid) and ^{150}Ho 9^+ (dashed) decays. 102
5.3 Comparison of B(GT) as a function of the number of protons in the $h_{11/2}$ orbital: theoretical values including hindrance factors (solid lines) taken from [TOW85], TAS results of this work (squares) and values coming from various high resolution experiments (triangles) [AGR97] [COL97] [KLE85] [MEC92] [MEN94] [MEN91] [NOL82].107

6.1 Comparison between the experimental strength distribution for the ^{150}Ho 2^- (solid) and ^{150}Ho 9^+ (dashed) decays. 112

7.1 Comparación entre las distribuciones de intensidad GT para las desintegraciones del ^{150}Ho 2^- (continuo) y del ^{150}Ho 9^+ (discontinuo). . . . 120

B.1 Branching ratio matrix for the electromagnetic de-excitation scheme 1 for ^{150}Ho 2^-. 134
B.2 Branching ratio matrix for the electromagnetic de-excitation scheme 2 for ^{150}Ho 2^-. 135
B.3 Branching ratio matrix for the electromagnetic de-excitation scheme 3 for ^{150}Ho 2^-. 136

B.4 Branching ratio matrix for the electromagnetic de-excitation scheme 1 for ^{150}Ho 9^{+}. 137
B.5 Branching ratio matrix for the electromagnetic de-excitation scheme 2 for ^{150}Ho 9^{+}. 138

List of Tables

1.1 Selection rules for β-transitions. 8
1.2 Classification of the decay-types with typical total $\log ft$ values from real cases. 10

2.1 Mean energy losses of e^+ in 1 mm of Si and 2.1 cm of polyethylene. Values taken from [PAG72]. 26
2.2 Monte Carlo values of the total and photopeak efficiencies for γ ray energies of the TAS with polyethylene absorber as plotted in Fig. [2.8]. 28
2.3 Time evolution of the centroids of the lines in the energy spectra produced by the light pulser and reference calibration sources. 29
2.4 Notation and key words used in Fig. [2.9] and Fig. [2.10]. The rest of the names are self explanatory. 32
2.5 The information on the production of ^{150}Ho 2^- and ^{150}Ho 9^+ most relevant to the present work. 34

4.1 ^{150}Ho 2^- decay $\log ft$ values integrated up to 7280 keV. The values were obtained for the electromagnetic de-excitation schemes 1, 2 and 3 after a combined analysis of both EC and β^+ feeding distributions. 81
4.2 ^{150}Ho 2^- decay $\log ft$ values integrated up to 7280 keV. The values were obtained from the results of the EM, ME and 2$^{\text{nd}}$ order regularisation combining both EC and β^+ feeding distributions. 83
4.3 Total $\log ft$ and B(GT) values for the ^{150}Ho 2^- decay integrated up to 7280 keV. The uncertainties associated with the strength calculation σ^{par}, the dependence on the de-excitation scheme σ_R^{sys}, the dependence on the analysis algorithm σ_{alg}^{sys} and its squared quadratic sum σ_{tot} are given explicitly. 85
4.4 $\log ft$ values of the strengths in Fig. [4.26] obtained for the three different subtraction factors. 94
4.5 ^{150}Ho 9^+ decay $\log ft$ values integrated up to 7120 keV. The values were obtained for the two electromagnetic de-excitation schemes after the EM-based analysis of the EC spectrum. 94
4.6 ^{150}Ho 9^+ decay $\log ft$ values integrated up to 7120 keV. The values were obtained from the EC results of the EM, ME and 2$^{\text{nd}}$ order regularisation. 97

4.7 Total log ft and B(GT) values for the ^{150}Ho 9^+ decay integrated up to 7120 keV. The uncertainties associated with the strength calculation σ^{par}, the contaminant subtraction σ^{sys}_{sub}, the dependence on the de-excitation scheme σ^{sys}_{R}, the dependence on the analysis algorithm σ^{sys}_{alg} and its squared quadratic sum σ_{tot} are given explicitly. 98

5.1 Two-body matrix elements used in the shell model calculation of J. Blomqvist [BLO98]. 100
5.2 Values of h_{pair} calculated for even masses and for different occupation numbers $n_{h_{11/2}}$. 104
5.3 Values of $h_{c.p.}$ calculated for various finite range forces different and different occupation numbers $n_{h_{11/2}}$. 104
5.4 Hindrance factors h calculated for even masses, for various choices of effective interactions and various occupancies n of the proton $h_{11/2}$ orbital. 105

6.1 Experimental and ESP B(GT) for the isotopes studied. The experimental and calculated hindrance factors are also given together with the decay energies (Q_{EC}) and half-lives ($T_{1/2}$). 113

7.1 Parámetros relevantes de las desintegraciones estudiadas. 121

C.1 ^{150}Ho 2^- β-strength calculated for decay scheme 3. 139
C.2 ^{150}Ho 2^- β-strength calculated for decay scheme 3. 140
C.3 ^{150}Ho 2^- β-strength calculated for decay scheme 3. 141
C.4 ^{150}Ho 2^- β-strength calculated for decay scheme 3. 142
C.5 ^{150}Ho 9^+ β-strength calculated for decay scheme 2. 142
C.6 ^{150}Ho 9^+ β-strength calculated for decay scheme 2. 143
C.7 ^{150}Ho 9^+ β-strength calculated for decay scheme 2. 144
C.8 ^{150}Ho 9^+ β-strength calculated for decay scheme 2. 145

Chapter 1

The Physics

1.1 Introduction

Since the discovery of radioactivity in 1896 by Henri Becquerel, Nuclear Physics has become a field of Science intimately linked to the development of our society. The deep understanding of nuclear matter achieved through both enormous experimental and theoretical efforts has changed our way of looking at Nature. Moreover, the results of such fundamental research affected not only the community of scientists. They had and have a direct impact on the lives of those outside the research community. The advances in nuclear structure, nuclear astrophysics, nuclear energy production, nuclear waste treatment, radiotherapy and so called *nuclear medicine*, detector development, environmental studies, meteorological and geological instrumentation and many others are just a few examples of what Nuclear Physics is able to do for us.

Besides the dissertation on the specific research topic exposed in this work, my aim is to transmit to the reader that Nuclear Physics is far from being exhausted. It is an active field which offers open and unresolved questions: our understanding is quite successful but still far from complete and there is much to be learned from the experiments, the unique way to determine the reality. Much work is needed in order to continue to delve into the secrets of the nucleus, and this has to be done both empirically and theoretically.

This work tries to present answers to questions posed to me several years ago: what happens when a particular nucleus suffers a β-disintegration and decays into another one? How can this be measured? This problem, posed after the discovery of radioactivity, remains without a detailed answer. The most advanced theoretical nuclear models which are available present severe discrepancies when compared with the experimental information. We are not completely able to predict how probable it is that a nuclear system, with a rather well known structure in terms of protons and neutrons, changes to another, particular configuration after a β-disintegration. As which every problem in Science, it is worth spending some time working on it and trying to understand it. In my opinion every such problem is interesting if treated seriously. My hope is that this has been done here. Before addressing the specific topic it is worth reviewing our ideas about β-decay in a simple way.

1.2 The beta decay

Beta decay is the process that governs the transmutation of most of the known nuclear species. Alphabetically labeled in second place after α-decay, it was first observed by H. Becquerel as an ingredient in the discovery of radioactivity. It was Rutherford in 1899 who realized that the radiation from ^{238}U observed by Becquerel had at least two components, one more and one less penetrating. He baptised them as α and β rays, and the names have remained even if nowadays we know that such particles are nothing other than ^{4}He nuclei and electrons. S. Meyer, E. von Schweidler and F. Giesel discovered the charged nature of such particles by studying its deflection with magnetic fields. Not much later, P. Villard added to the list of radiation types a third component: the γ-radiation. In contrast with α and β-rays, he observed that the γ-radiation was even more penetrating and its trajectory remained unchanged by magnetic fields. E. Rutherford and F. Soddy suggested in 1903 that radioactivity was linked to the transmutation of elements. The hypothesis was confirmed by K. Fajans and F. Soddy, and they found that only α and β rays were a consequence of nuclear change. J. Chadwick discovered in 1914 that, in contrast with to α and γ-rays, the electrons forming the β-rays did not present a discrete but a continuous energy spectrum. This constituted a puzzle which even challenged at some point the conservation laws of energy and momentum. It took many years to find the right explanation for this phenomena. In 1931, W. Pauli postulated the existence of an almost non-interacting massless and neutral particle carrying the missing energy-momentum in a three body β-decay. E. Fermi gave it the name which is still in use: the *neutrino* or small neutron.

One of the many particular aspects of β-decay is that it appears in three different ways. The afore-mentioned β-decay is only one mode called β^--decay. Irene and F. Joliot-Curie discovered β^+-decay in 1934, together with the important fact that nuclei can be produced artificially in nuclear reactions. Following the modern understanding, which is very similar to that of the pioneers of radioactivity, a nucleus is transformed in β-decay into another with the same mass number A and a charge $Z \pm 1$ differing by one unit from that of the initial nucleus Z. One major difference with respect to the earlier comprehension is that nowadays we know that protons and neutrons are not elementary and present a structure explained in terms of quarks. This is not needed however to understand the major features of β-decay, and thus, we will not make use of it and consider protons and neutrons as elementary.

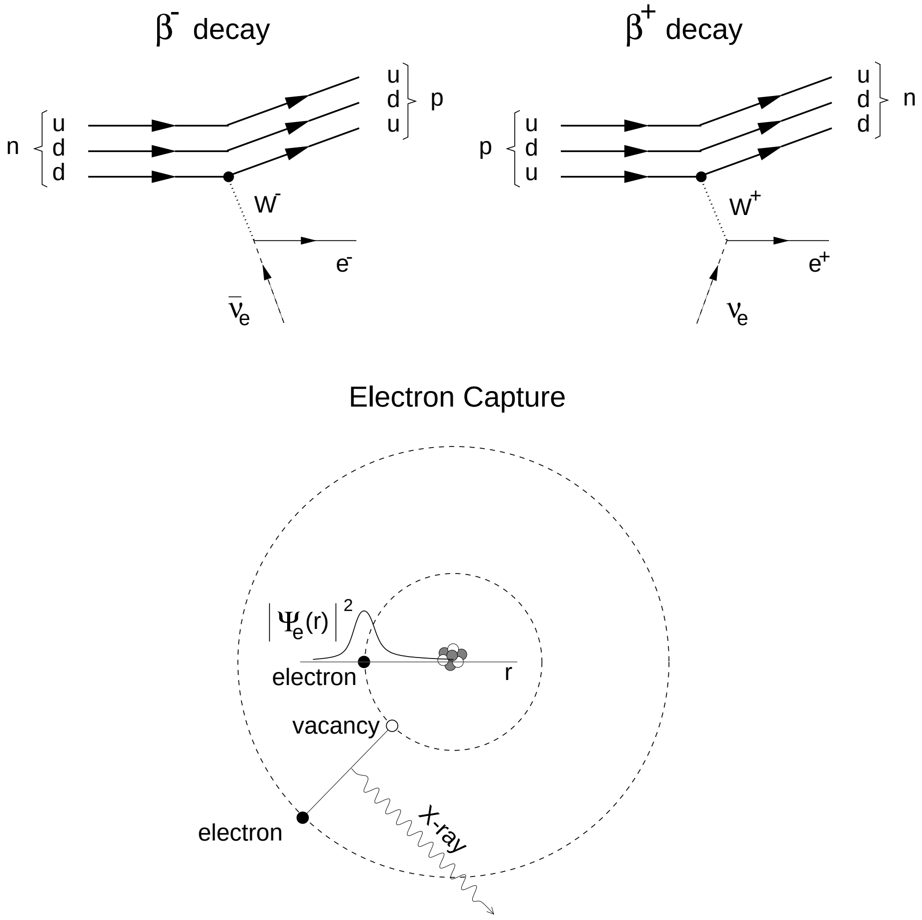

Figure 1.1: Three different decay processes. In β^- decay, a neutron (udd) is transformed into a proton (uud) by exchange of a virtual W^- boson and emission of an electron e^- and an electron anti-neutrino $\bar{\nu}_e$. In β^+ decay, a proton (uud) is transformed into a neutron (udd) by exchange of a virtual W^+ boson and emission of a positron e^+ and an electron neutrino ν_e. The electron capture process has the same effect as β^+ decay: an electron from the atomic shell has a nonzero probability $|\Psi(r)|^2$ of being inside the nucleus, and thus being captured by a proton which is then transformed into a neutron. The captured electron leaves a vacancy in the atomic shell which is filled by less bound electrons. During this process, characteristic X-rays or Auger electrons are emitted.

As shown in Fig. [1.1], three different processes satisfy our definition. In the upper left corner, β^--decay is presented, in which one neutron (udd) changes into a proton (uud) and as a consequence an electron e^- and an electron anti-neutrino $\bar{\nu}_e$ are emitted. The upper right corner and lower part of Fig. [1.1] show the two complementary processes which have the same consequence, namely the β^+-decay and the electron capture EC. In both cases, a proton (uud) is transformed into a neutron (udd). All three processes are summarised through the reactions indicated by Eq. (1.1), Eq. (1.2) and Eq. (1.3):

$$\beta^- : {}^A_Z X_N \rightarrow {}^A_{Z+1} X_{N-1} + e^- + \bar{\nu}_e \tag{1.1}$$

$$\beta^+ : {}^A_Z X_N \rightarrow {}^A_{Z-1} X_{N+1} + e^+ + \nu_e \tag{1.2}$$

$$EC : {}^A_Z X_N + e^- \rightarrow {}^A_{Z-1} X_{N+1} + \nu_e + x_{ray} \tag{1.3}$$

It is important to realise that the processes mentioned occur when they are energetically allowed, that is, when the energy release in the decay is positive. Such energy releases are expressed in terms of the Q-values as defined in Eq. (1.4), Eq. (1.5) and Eq. (1.6):

$$\beta^- : \mathrm{Q}_{\beta^-} = m({}^A_Z X_N) - m({}^A_{Z+1} X_{N-1}) \tag{1.4}$$

$$\beta^+ : \mathrm{Q}_{\beta^+} = m({}^A_Z X_N) - m({}^A_{Z-1} X_{N+1}) - 2m_{e^+} \tag{1.5}$$

$$EC : \mathrm{Q}_{\mathrm{EC}} = m({}^A_Z X_N) - m({}^A_{Z-1} X_{N+1}) - B_n \tag{1.6}$$

where the ms are the atomic masses and B_n in Eq. (1.6) is the binding energy of the captured electron, both in natural units.

While β^--decay happens when the mass difference between the parent and daughter nuclei is positive, the β^+ process requires an additional $2 \times m_e \simeq 1022$ keV to occur. This does not happen for the competing EC process, and the consequence is that in the last 1022 keV of the Q_{EC}-window, only the EC-decay is possible.

So far the kinematics of the processes have been discussed, but it is clear that the structure of the nucleus must also play a role. In fact, it is the structure of the nucleus which establishes the rules of the decay once it is energetically permitted. Hereafter we will refer to the theory of beta decay developed by E. Fermi in 1933, which can be found in any textbook on Nuclear Physics such as [KRA83] [MUS95] [LIP62]. A more complete advanced formulation of the beta decay in terms of the Standard Model for the electroweak interactions can be found in [GRE93]. Such an approach is far beyond the aim of this work and also unnecessary for its understanding.

Fermi's idea was to postulate that the electron and anti-neutrino do not exist inside the nucleus and are created in the process. Additionally, they must be treated relativistically. Since the characteristic time for the weak interaction ($\sim$ 1s) is far larger than the characteristic nuclear times ($\sim 10^{-20}$ s), the decay-causing interaction can be treated by the use of Fermi's Golden Rule. Its application leads to the expression for the transition rate λ indicated by Eq. (1.7).

$$\lambda = \frac{2\pi}{\hbar} |H_{fi}|^2 \rho(E_f) \tag{1.7}$$

The matrix element H_{fi} is the integral of the interaction H between the initial and final state of the system:

$$H_{fi} = \int \Psi_f^{\dagger} H \Psi_i d\overrightarrow{r} \tag{1.8}$$

The factor $\rho(E_f)$ in Eq. (1.7) is the density of final states, which can also be written as dn/dE_f, the number dn of final states in the energy interval dE_f. A transition is more likely to occur if there is a large number of accessible final states.

Fermi did not know the explicit form of H, and thus considered all possible expressions consistent with Special Relativity. Any kind of interaction O can be decomposed in terms of five operators O_x which have well defined properties under Lorentz transformations: vector (x=V), axial vector (x=A), scalar (x=S), pseudo-scalar (x=P) or tensor (x=T). By following this convention, a general interaction matrix element for β^--decay can be constructed as indicated by Eq. (1.9):

$$H_{fi} = \sum_x g_x \int \Psi_f^{\dagger} \phi_e^{\dagger} \phi_{\bar{\nu}}^{\dagger} O_x \Psi_i d\overrightarrow{r} \tag{1.9}$$

where the g_x are the coupling constants corresponding to the different types of interaction (V, A, S, P, T).

In order to evaluate the expression of the leptonic part of the interaction $\phi_e^{\dagger}\phi_{\bar{\nu}}^{\dagger}$, it is fair to assume that the electron and the anti-neutrino behave as free particles whose motion is described by plane waves:

$$\phi_e = \frac{1}{\sqrt{V}} \exp(i\mathbf{p} \cdot \mathbf{r}/\hbar) \tag{1.10}$$

$$\phi_{\bar{\nu}} = \frac{1}{\sqrt{V}} \exp(i\mathbf{q} \cdot \mathbf{r}/\hbar) \tag{1.11}$$

where $\mathbf{p}$ and $\mathbf{q}$ are respectively the momenta of the electron and the anti-neutrino. Their wave functions can be evaluated at the centre of the nucleus where $\phi_e^{\dagger}\phi_{\bar{\nu}}^{\dagger} = \frac{1}{V}$. This is known as the *allowed approximation* and means that in the Taylor expansion of the plane waves, only the first term 1 is taken. Since the wave function of the electron is affected by the nuclear Coulomb field of the Z daughter nucleus, the Fermi Function

$$F(Z,p) = \frac{|\phi_e(0)_{Coulomb}|^2}{|\phi_e(0)_{free}|^2} \tag{1.12}$$

has to be introduced in order to consider the effect, and thus

$$\phi_e^{\dagger}\phi_{\bar{\nu}}^{\dagger} = \frac{F(Z,p)}{V} \tag{1.13}$$

We have still to find the density of states factor in Eq. (1.7). By considering the electron and anti-neutrino as confined to a box of volume V, the number of final electron states dn_e corresponding to momenta in the range p to $p + dp$ is

$$dn_e = \frac{4\pi p^2 dpV}{h^3} \tag{1.14}$$

We can do the same for the anti-neutrino and thus:

$$dn_{\bar{\nu}} = \frac{4\pi q^2 dqV}{h^3} \tag{1.15}$$

Replacing Eq. (1.9), Eq. (1.14) and Eq. (1.15) in Eq. (1.7), we obtain the partial decay rate

$$d\lambda = \frac{2\pi}{\hbar} \sum_x g_x^2 |M_{fi}^x|^2 (4\pi)^2 F(Z,p) \frac{p^2 dp}{h^6} \frac{q^2 dq}{dE_f} \tag{1.16}$$

where the nuclear matrix element M_{fi}^x stands for $\int \Psi_f^\dagger O_x \Psi_i d\overrightarrow{r}$. From the conservation laws of a three body process, the momentum of the anti-neutrino can be expressed in terms of the electron momentum (or its kinetic energy T_e), the energy available in the decay Q and the nuclear recoil energy which is very small. By doing so and neglecting the last one, the total decay rate λ can be obtained from the integration of Eq. (1.16), leading to the expression for allowed decays given in Eq. (1.17).

$$\lambda = \frac{\sum_x g_x^2 |M_{fi}^x|^2}{2\pi^3 \hbar^7 c^3} \int_0^{p_{max}} F(Z,p) p^2 (Q - T_e)^2 dp \tag{1.17}$$

The integral will ultimately depend only on the Z of the daughter nucleus and on the maximum electron total energy E_{max}, and we therefore represent it as

$$f(Z, E_{max}) = \frac{1}{(m_e c)^3 (m_e c^2)^2} \int_0^{p_{max}} F(Z,p) p^2 (E_{max} - E_e)^2 dp \tag{1.18}$$

where the constants have been included to make f dimensionless. The function $f(Z, E_{max})$ is known as the *Fermi integral* and has been tabulated for values of Z and E_{max} [GOV71]. With $\lambda = \ln 2/t_{1/2} \equiv \ln 2/t$ we have

$$ft = 2\ln 2 \frac{\pi^3 \hbar^7}{m_e^5 c^4 \sum_x g_x^2 |M_{fi}^x|^2} \tag{1.19}$$

where t is the reduced half-life which fulfils $\sum 1/t = 1/T_{1/2}$. The quantity on the left hand side of Eq. (1.19) is called the *comparative half-life* or *ft-value.* It provides a way to compare the β-decay probabilities in different nuclei, since variations in the ft values must be due only to differences in the nuclear matrix element and thus to differences in the nuclear wave function. It is worth mentioning that strictly, it only makes sense to refer to the ft-value of a given transition, that is, between one initial and one final level. However, since the decay of a nucleus involves many such transitions, the concept of ft is commonly extended (summed) over all of the transitions involved in the decay, ending up in the integral or total ft. This can be done by adding up the inverse of the ft quantities $\sum 1/ft = 1/fT_{1/2}$ for all the transitions involved in the decay. The range of comparative half-lives in β-decay is enormous. The ft-values may vary from about 10^3 to 10^{20} s. For this reason, what is often quoted is the value of $\log_{10} ft \equiv \log ft$ with t given in seconds.

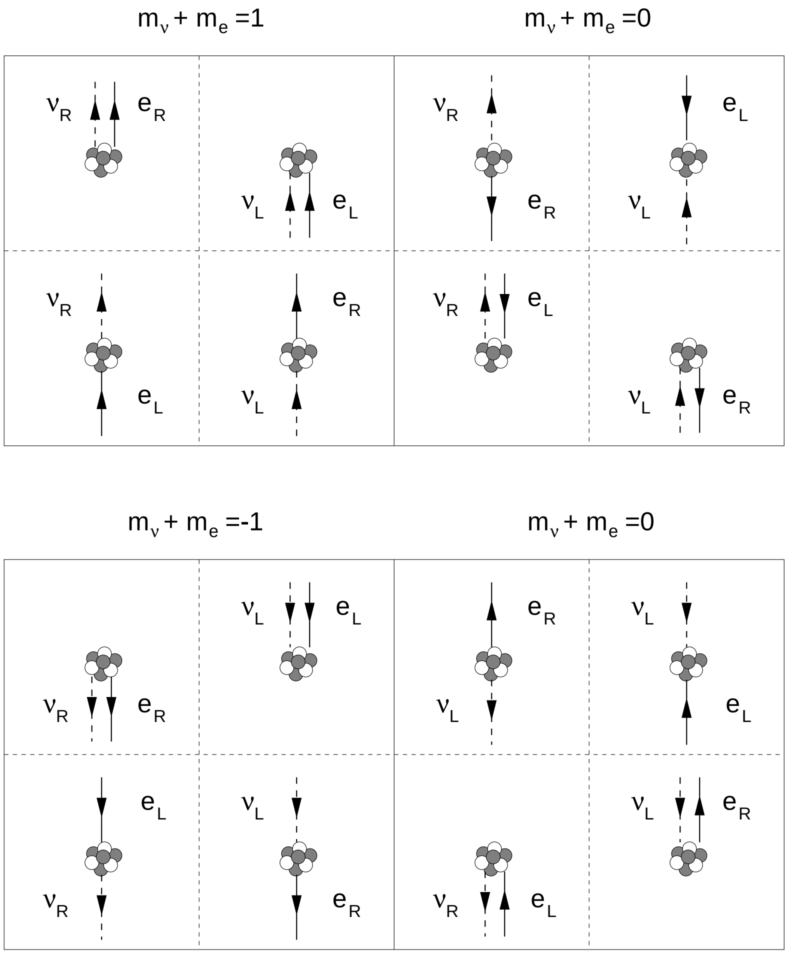

Figure 1.2: Sixteen possible electron-neutrino states in allowed β-decay.

In allowed β-decay transitions, the electron and the anti-neutrino are both emitted in states of total angular momentum $j \equiv s = 1/2$. Since it is known that parity is not conserved in β-decay, it is preferable to label the two states of angular momentum j using its longitudinal polarisation or helicity. We thus have *left-handed* states **L** in which the direction of the spin is parallel to the linear momentum and *right-handed* states **R** in which it is opposite. In allowed decay each lepton has four possible states. It can be either left or right-handed, and its angular momentum can be pointing either *up* ($m_j = +1/2$) or *down* ($m_j = -1/2$) with respect to the axes fixed in the laboratory. There are 4×4 possible states for the combined electron neutrino system. These states are represented graphically in Fig. [1.2]. The lines indicate the paths of the electron and neutrino emitted from the nucleus. The arrows indicate the direction of the spin. Each path is labeled e or ν indicating that the particle is an electron or neutrino. The subscripts **L** and **R** indicate that the particle is left-handed or right-handed. Each diagram in Fig. [1.2] indicates a definite direction of the emission for each lepton with respect to the vertical axis, and therefore with respect to the direction of emission of the other lepton. The law of conservation of angular momentum restricts the possible values of j_t, the magnitude of the total lepton angular momentum, to those between the sum and the difference of the spins J_i and J_f of the initial and final nuclear states.

$$|J_i - J_f| \leq j_t \leq J_i + J_f \tag{1.20}$$

An important example of this restriction is the case where $J_i = J_f = 0$, for which j_t can only be zero. Another restriction is that imposed on the quantum number m_t, the projection of j_t on the fixed axis. If the projections, M_i and M_f of the angular momenta of the initial and final nuclear states are known, then m_t is determined uniquely by

$$m_t = M_i - M_f \tag{1.21}$$

Since $m_t = m_e + m_\nu$, we see that the quantum numbers m_e and m_ν are not independent, and the amplitudes for the lepton channels must vanish for all values of m_e and m_ν which do not satisfy the conservation law of Eq. (1.21). Setting $j_t = 0$ or $j_t = 1$ in Eq. (1.20) we obtain the selection rules for allowed transitions. Two type of transitions can be distinguished: the *Fermi* transitions and the *Gamow–Teller* (GT) transitions. An additional requirement for the Fermi transitions is that they must occur between states belonging to the same isospin (T) multiplet (T_z), that is, the final nucleon must remain in the same orbital where the initial nucleon was. All the selection rules are summarised in Table [1.1].

$\Delta J = J_i - J_f = 0$ $\Delta T = 0$, $\Delta T_z = \pm 1$	in allowed Fermi transitions ($j_t = 0$)
$\Delta J = J_i - J_f = 0, \pm 1$ $J_i = J_f = 0$ excluded	in allowed Gamow–Teller transitions ($j_t = 1$)

Table 1.1: Selection rules for β-transitions.

The question that still remains open is the explicit form of the interaction H in Eq. (1.8). From the selection rules it can be concluded that there must be two contributions: one governing Fermi decays and another governing Gamow–Teller decays. This has the consequence that H_{fi} can be decomposed as expressed by Eq. (1.22):

$$|H_{fi}|^2 = g_F |M_{fi}^F|^2 + g_{GT} |M_{fi}^{GT}|^2 \tag{1.22}$$

The Fermi and Gamow–Teller parts can be decomposed subsequently in terms of matrix elements with well defined properties under Lorentz transformations and at the same time obeying the proper selection rules:

$$g_{GT} |M_{fi}^F|^2 = g_A |M_{fi}^A|^2 + g_T |M_{fi}^T|^2 \tag{1.23}$$

$$g_F |M_{fi}^{GT}|^2 = g_V |M_{fi}^V|^2 + g_S |M_{fi}^S|^2 \tag{1.24}$$

The conclusion of several experiments, mainly about the non-conservation of parity in β-decay, is that Nature seems to have decided that only the axial (A) and vector (V) part contribute to the Gamow–Teller and Fermi transitions. However, small tensor (T) and scalar (S) contribution cannot be excluded within the experimental errors. Thus, it is possible to write that

$$\frac{g_{GT}}{g_F} = \frac{g_A}{g_V} = -1.262 \pm 0.004 \tag{1.25}$$

where the free neutron ratio of vector to axial vector coupling constants was taken from [KLE88] [FRE90]. Hereafter, the expression for the ft-value we will refer to is

$$ft = \frac{D}{|M_{fi}^F|^2 + (\frac{g_A}{g_V})^2 |M_{fi}^{GT}|^2}\ , \tag{1.26}$$

$$\text{where } D = \frac{2 \ln 2 \pi^3 \hbar^7}{m_e^5 c^4 g_V^2} = 6147 \pm 7\text{s}. \tag{1.27}$$

The constant 6147±7s is available from the evaluation of the experimental data on superallowed $0^+ \rightarrow 0^+$ β-decays [HAR90]. The data on the superallowed β-decays have been recently reexamined [WIL93] and a new value of $D = 6127 \pm 10$s has been suggested. There is also a more recent value of the ratio $g_A/g_V = -1.2544 \pm 0.0036$ [ERO91]. However, both of these numbers are outside the $\pm\sigma$ uncertainty interval when compared to earlier evaluations, and they have to be critically reanalysed before being adopted.

A final word has to be said about the classification of *all* the possible decay types. Allowed decays occur with the highest probability, but this does not mean that they are the unique ones. The structure of the nucleus once more plays an important role, and there exist many cases where allowed decays are not possible and β-decay still happens. There is an *empirical* way to classify the decays according to the ft-values, but this procedure should not be considered as rigorous. The different kinds of transition and typical $\log ft$ values extracted from physical cases are shown in Table [1.2].

Type	Selection rules	$\log ft$	Example Nucleus	 $T_{1/2}$
super-allowed allowed	ΔJ=0, ± 1 $\Delta\pi$=no	3.5 ± 0.2 5.7 ± 1.1	^{1}n ^{60}Co	10.37 min 5.26 a
1st-forbidden	ΔJ=0, ± 1 $\Delta\pi$=yes	7.5 ± 1.5	^{198}Au	2.70 d
1st-forbidden unique	ΔJ=± 2 $\Delta\pi$=yes	8.5 ± 0.7	^{91}Y	59 d
2nd-forbidden	ΔJ=± 2 $\Delta\pi$=no	12.1 ± 1.0	^{137}Cs	30 a
2nd-forbidden unique	ΔJ=± 3 $\Delta\pi$=no	11.7 ± 0.9	^{10}Be	$1.6 \cdot 10^{6}$ a
3rd-forbidden	ΔJ=± 3 $\Delta\pi$=yes	18.2 ± 0.6	^{87}Rb	$4.7 \cdot 10^{10}$ a
3rd-forbidden unique	ΔJ=± 4 $\Delta\pi$=yes	15.2	^{40}K	$1.3 \cdot 10^{9}$ a
4th-forbidden	ΔJ=± 4 $\Delta\pi$=no	22.7	^{115}In	$6 \cdot 10^{14}$ a

Table 1.2: Classification of the decay-types with typical total $\log ft$ values from real cases.

1.3 The β-strength function

From the discussion made in the previous section we have seen that the transition rate for a given decay is characterised by its ft-value. This quantity can also be defined [BOH98] as

$$ft = \frac{6147 \pm 7}{\mathrm{B}} \frac{g_V^2}{4\pi} = \frac{6147 \pm 7}{\mathrm{B(F)} + \mathrm{B(GT)}} \frac{g_V^2}{4\pi} \tag{1.28}$$

where B is the total strength and B(F) and B(GT) are respectively the Fermi and Gamow-Teller strengths defined in Eq. (1.29) and Eq. (1.30)

$$\mathrm{B(F)} = \frac{g_V^2}{4\pi} \frac{1}{2J+1} |< J_f \| \sum_k t_\pm^k \| J_i > |^2 \equiv \frac{g_V^2}{4\pi} < \sigma >^2 \tag{1.29}$$

$$\mathrm{B(GT)} = \frac{g_A^2}{4\pi} \frac{1}{2J_i+1} |< J_f \| \sum_k \sigma^k t_\pm^k \| J_i > |^2 \equiv \frac{g_A^2}{4\pi} < \sigma\tau >^2 \tag{1.30}$$

Notice that with these definitions, B, B(F) and B(GT) are not dimensionless: they have the same units as $g_V^2/4\pi$. This is however not the common situation found in the literature. Another possible definition is obtained when B is rewritten like

$$\mathrm{B} = \frac{g_V^2}{4\pi} \left[< \sigma >^2 + \left(\frac{g_A}{g_V} \right)^2 < \sigma\tau >^2 \right] \tag{1.31}$$

Then, for the particular case of pure Gamow-Teller transitions we can define B(GT) as the dimensionless quantity

$$\mathrm{B} = \mathrm{B(GT)} =< \sigma\tau >^2 \tag{1.32}$$

and thus the ft-value becomes

$$ft = \frac{6147 \pm 7}{\left(\frac{g_A}{g_V}\right)^2 \mathrm{B(GT)}} \tag{1.33}$$

where it is implicitly assumed that the B(GT) is given in $g_A^2/4\pi$ units. This ambiguous situation in the definition of B(GT) has to be considered when comparing different references. In this text we will follow the convention established by Eq. (1.32) and Eq. (1.33).

The B(GT) can be procured within the theoretical framework used to describe the decay. However, in order to compare with the experiments, it can be more convenient to express it in terms of a better measurable quantity: the β-strength function $S_\beta(E_x)$. S_β as a function of the excitation energy E_x in the daughter nucleus is related to the β-intensity I_β (or feeding probability) through the relation

$$S_\beta = \frac{I_\beta(E_x)}{f(\mathrm{Q}_\beta - E_x)T_{1/2}} \tag{1.34}$$

Here f represents the statistical rate Fermi integral, which depends on the energy $\mathrm{Q}_\beta - E_x$ available to the decay, and $T_{1/2}$ is the β-decay half-life. All the variables involved in Eq. (1.34) have a clear experimental meaning since they can be measured. It is sometimes preferable to speak in terms of S_β and not B(GT). $S_\beta(E_x)$ is, by definition, an average quantity which stands for the mean value of the B(GT) for all the transitions occurring to levels inside a certain energy bin ΔE_x at central excitation energy of E_x. The quantity is introduced in order to deal with the situation where the level density in the daughter nucleus is too large to distinguish individual levels, either experimentally or theoretically. However, the definition is also applicable where the level density is low. The relation between B(GT) and S_β is given in Eq. (1.35), which permits an unambiguous exchange between both terminologies.

$$S_\beta(E_x) = \frac{1}{6147 \pm 7}\left(\frac{g_A}{g_V}\right)^2 \sum_{E_f \in \Delta E_x} \frac{1}{\Delta E_x}\mathrm{B(GT)}_{i \to f} \tag{1.35}$$

A last word on the S_β is that its integral value is commonly expressed in terms of the total ft-value defined as:

$$\text{total } ft = \frac{1}{\sum_{E_x} S_\beta(E_x)\Delta E_x} \tag{1.36}$$

The motivation of the discussion so far is that determining the probability of occurrence of a basic process mediated by the weak interaction is of fundamental importance. The particular knowledge of the distribution of this probability over the final nuclear states gives information on the complex nuclear wave functions, and subsequently, on the residual nuclear interaction. At the same time, this comprehension gives us the way to understand other phenomena in nuclear physics. One example is the calculations in the Tamm-Dancoff approximation (TDA) by [HAM95]. It indicates that the distribution of GT strength provides information on the nuclear deformation, because it is found to depend sensitively on the nuclear shape for $N = Z$ nuclei. The same feature has been pointed out by [SAR98]. Another example is the calibrations needed for the QRPA calculations related to the double β-decay [ENG88] process.

There are also other fields like particle physics, astrophysics and reactor technology where we find the need for a reliable knowledge of the GT strength. Some of these issues were stressed in the review articles of Klapdor [KLA83] in the mid 80s. The persistence of the validity of such arguments and the continuously renewed interest in related measurements can be shown in two recent examples. The ICARUS liquid argon detector [ICA93] is designed to study the so-called solar neutrino problem [ZUB98] by counting the flux of high energy neutrinos coming from the Sun as well as being sensitive to neutrino oscillations. The calibration of such a detector requires a knowledge of the β-decay probabilities of ^{40}Ti into the excited states of ^{40}Sc, the mirror process to the reaction $^{40}\mathrm{Ar}(\nu_e,\mathrm{e})^{40}\mathrm{K}$, and could only be measured recently with the necessary accuracy (see [LIU98] and references therein). The second example comes from the field of reactor technology. Despite continuous improvements down the years, there remains a sizeable discrepancy between the measurements of the decay heat (energy released by fission products after a reactor shutdown) due to γ-ray emission and the summation calculations based on data libraries combining both theoretical and experimental quantities. In a recent careful analysis [YOS99] it has been pointed out that most of the discrepancy probably comes from inaccurate measurements of the β-decay probability distribution of a few isotopes. A deeper understanding of the discrepancy would certainly have an impact on safety regulations and reactor modelling.

1.4 The problem of the missing Strength

Eq. (1.32) tells us that knowing the initial and final spins and wave-functions of the states involved in a decay, we can determine the transition rate. Moreover, the $\sigma\tau$ operator used to describe the process acts in a very simple way, by changing only the z-projections of isospin (proton into neutron or vice versa) and spin. If this description is correct, and there is no reason why the spin/isospin formalism should fail here, such a simple picture should allow us to confront successfully the theoretical predictions with the experimental data. The common situation is however, that the observed Gamow-Teller strength appears to be systematically smaller than theoretically expected. In particular, very large (up to several orders of magnitude) deviations can be found when comparing with the extreme single particle (ESP) shell model description. The situation improves when a better description of the nucleus is used, but there exists always the need to introduce a re-normalisation or *quenching* factor q for the GT-observables so that the experimental results can be reproduced.

The first kind of data which can be used for comparisons comes from β-decay experiments. A classical work [WIL73] compared the results from shell model calculations made for p-shell and lower sd-shell nuclei (A=17-21) with the experimental information available at that time. In order to reproduce the β-decay data, an overall reduction factor of $q = 0.897 \pm 0.035$ had to be used for the effective GT single particle matrix elements relative to the free-nucleon ones. There are more recent calculations for the p-shell in [CHO93] which end up with $q = 0.82 \pm 0.015$. The result in [WIL73] was expressed in terms of a re-normalisation for the value of g_A/g_V. However, one could also have thought of the re-normalisation as coming from a correction to the nuclear matrix element of $\sigma\tau$. Later on, the study was extended to heavier sd-shell nuclei (A=17-39) in [BRO85]. The conclusion of that work was that again an overall quenching factor, this time of $q = 0.76 \pm 0.03$, has to be used in order to reproduce the experimental GT-strengths. More recently, full $0\hbar\omega$ shell model calculations [PIN96] have been made for pf-shell nuclei (A=41-50). The situation found for such nuclei is very similar to the previous ones: agreement with the experimental results demands the introduction of an overall quenching factor $q = 0.744 \pm 0.015$, which is slightly smaller but compatible with the sd-shell value. Calculations of a very different nature, namely of the RPA-QRPA type, also reveal the same problem [KLE85] [SUH88] [ENG88].

There is also a great deal of experimental information from charge-exchange reactions. Since the time of the pioneering (p,n) [GOO80] [GOO82] [GAA80] and (n,p) [VET82] [VET89] [MAD87a] [MAD87b] experiments, it has been possible to explore the Gamow-Teller strength function of many nuclei in the resonance region and beyond. The main difference with respect to the β-decay experiments is that charge-exchange reactions are not limited by the Q-window and thus a wider excitation energy range can be explored. The most striking result is that a large fraction of the theoretically expected sum rules for $\sigma\tau$ operators, $\sum \mathrm{B(GT)}^+$ for the β^+ case and $\sum \mathrm{B(GT)}^-$ for the β^-, seems to be missing. According to the model independent Ikeda sum rule [IKE63] $\sum \mathrm{B(GT)}^- - \sum \mathrm{B(GT)}^+ = 3(N - Z)$, the strength difference cannot be quenched or suppressed: it is missing, but must be somewhere.

The problem exposed so far can be summarised in one statement: there seems to be a mechanism which makes the observed strength much smaller than expected. The cause might be related to a re-normalisation of the g_A coupling constant originating in sub-nucleonic effects. It could also be that it is the $\sigma\tau$ operator itself that should be re-normalised because of nuclear correlations. Whatever the answer, we should however not forget that part of the problem may be coming from the experimental side. Since we are trying to isolate the nature of the discrepancy between the existing data and the predictions, it is mandatory that the former do not suffer from any pathology which ends up in a systematic strength underestimation. We will see in the next section that this is exactly what happens in some cases, and thus it is possible to propose a way to get rid of them.

1.5 The β-strength determination from beta decay measurements

As in any other instance where the theoretical prediction differs from the results of measurement, the experimental challenge is to assure that the quantity of interest is accurately determined by the technique employed. In the case of the GT strength, essentially all the experimental information available for medium and heavy nuclei is coming from the (p,n) reaction which is equivalent to the β^--process, because the latter one is energetically forbidden. However, it is known that the strength extracted from the (p,n) reaction suffers from uncertainties in the elimination of the background [OST82] and in the calculation of the reaction cross-section [TAD87].

An cleaner alternative is provided by the β-decay experiments, which permit us to determine the strength with the help of Eq. (1.34). Apart from Q_β and $T_{1/2}$ (assumed to be known or measurable) in Eq. (1.34), it remains as the main experimental task to measure the beta intensity. The conventional way of determining I_β in β-decay studies makes use of the γ-ray spectroscopy technique with high resolution Ge detectors. The determination proceeds in two steps. First, the de-excitation scheme in the daughter nucleus is constructed based on the γ-γ coincidence data. Second, the feeding intensity to each level is obtained by γ-ray intensity balance. It has long been recognised [HAR77] that the β-intensity determined in this way tends to be shifted to lower excitation energy levels due to the limited efficiency of Ge detectors, particularly for decays with large Q_β windows. This not only produces a displacement of the intensity but also introduces a large systematic error in the total estimated strength due to the re-normalisation effect of the Fermi integral $f(Q_\beta - E_x)$ in Eq. (1.34). The problem appears because the method is based on the identification of *all* γ-ray cascades. When the decay proceeds to highly excited levels, which are likely to be strongly mixed, the intensity of each cascade becomes weak, both because the feeding probability is distributed over many levels and because for each level many de-excitation patterns are possible. Additionally, the probability that the cascade includes an energetic γ-ray which may easily escape from detection is also increased. We have shown recently [AGR97] that even with a closely packed array of 42 large Ge detectors a substantial fraction of the GT strength in the decay of the ^{150}Ho 2^- isomer ($Q_{EC} = 7.4$ MeV) remains undetected.

A solution to this problem is given by the Total Absorption Gamma-ray Spectroscopy (TAGS) with high efficiency scintillation detectors. The technique was introduced in a pioneering work at ISOLDE [DUK70] as an alternative method to measure the β-decay intensities. An ideal Total Absorption Spectrometer (TAS) would only be sensitive to γ-rays and would have 100 % peak efficiency and an infinitely good resolution. For every γ-ray cascade de-exciting a given level in the daughter nucleus fed in the decay, such a spectrometer would register a count in the spectrum corresponding to that level energy. In this way, the measured spectrum would be proportional to the sought $I_\beta(E_x)$. In contrast, a real TAS has limited efficiency and finite resolution. Actually, the limited efficiency introduces the weak point of the technique, which has prevented the TAGS becoming popular. The analysis of total absorption spectra is a very complex problem, since the β-intensity has to be extracted from the measured spectrum which depends on the spectrometer response. Considering the essentially discrete nature of the information that we deal with, the relation between a measured TAS spectrum $\mathbf{d}$ and the level feeding distribution $\mathbf{f}$ ($\equiv NI_\beta$, $N=$ total number of decays) is best represented by the equation:

$$d_i = \sum_{j=1}^{j_{max}} R_{ij} f_j \ , \qquad i = 1, i_{\max} \qquad \text{or} \qquad \mathbf{d} = \mathbf{R} \cdot \mathbf{f} \tag{1.37}$$

where each column j of the matrix $\mathbf{R}$ represents the average response (or normalised spectrum) of the spectrometer to the decay into the levels in the energy bin represented by the channel j. Eq. (1.37) can equally represent the decay to discrete well-separated levels with j labelling their energy. The response matrix $\mathbf{R}$ depends on the emitted radiation as well as on the apparatus itself. The knowledge of $\mathbf{R}$ is a prerequisite of the analysis of TAS spectra. The way to construct $\mathbf{R}$ can be found in section 3.2 and more details are given in [CAN99a]. The other important issue is finding appropriate methods to solve the *inverse problem* represented by Eq. (1.37), in order to obtain the feeding distribution $\mathbf{f}$. This work is the very first in which there is a rigorous study of such analysis methods applied to the TAGS technique. A full description of the methods developed for this purpose can be found in section 3.2 and also in [TAI99].

The important point to be noted about TAGS is that the higher efficiency of the TAS, the weaker the dependency on $\mathbf{R}$. In fact, the ISOLDE spectrometer described in [DUK70], based on two ⌀15 cm×10 cm NaI(Tl) crystals, had a rather poor peak efficiency (about 28 % for 1 MeV γ-rays and 16 % for 4 MeV γ-rays) which represented a serious limitation. An improved NaI(Tl) TAS with an efficiency about a factor 1.6 larger, described in [BYK80], was used for measurements at PNPI (St. Petersburg). Later a still larger spectrometer [GRE92] (a ⌀25 cm×30 cm NaI(Tl) well crystal) at INEL (Idaho) with an efficiency increase factor of 2.5 was reported.

Recently a TAS using a ⌀35 cm×35 cm NaI(Tl) detector originally constructed by Michael Nitschke at LBL (Berkeley), has been installed at the GSI (Darmstadt) on-line mass separator [KAR97]. This spectrometer has an efficiency up to 3.5 times larger than the ISOLDE spectrometer and has been used for studies of Gamow-Teller β-decay in heavier nuclei. For such nuclei the β-decay information is sparse because of the difficulty of accessing nuclei with allowed decays. This is because the required orbitals for allowed decays lie outside the beta-window in general. There are in principle only two nuclear regions where the $\sigma\tau$ resonance (also called GT giant resonance) is accessible in β-decay. The nuclei we refer to are the nuclei below ^{100}Sn and above ^{146}Gd. However, it is fair to mention that calculations [HAM94] indicate that the GT resonance might also be accessible in very light neutron drip nuclei as well as in $Z \gtrsim 40$ proton drip line nuclei.

For the nuclei in the ^{100}Sn and ^{146}Gd regions, a proton in a high J orbital decays into its spin-orbit partner neutron orbital with J-1, which is in general less bound than the J neutron orbital and therefore empty. The transitions we are refering to are the the $\pi g_{9/2} \rightarrow \nu g_{7/2}$ for the nuclei below ^{100}Sn and the $\pi h_{11/2} \rightarrow \nu h_{9/2}$ for the nuclei above ^{146}Gd. In both cases it should be possible to compare experiments with theoretical calculations and add some new information on the causes of the GT-quenching. The results of the total absorption experiments near ^{100}Sn performed at GSI by the University of Warsaw Group within the Darmstadt-St. Petersburg-Valencia-Warsaw collaboration can be found in [KAR98] and constitute the PhD work of Marek Karny. This work reports on the results obtained by means of three new analysis algorithms from the β-decay studies in the ^{146}Gd region, more particularly on the decays of ^{150}Ho 2^- and ^{150}Ho 9^+. The details of the experiments can be found in the next chapter.

Chapter 2

The Experiment

2.1 The nuclei around ^{146}Gd

As indicated in the previous chapter, we devoted our efforts to the study of the nuclei in the ^{146}Gd region. Even though the number of 64 protons is not magic, the subshell closure with a gap of ~2.4 MeV offers a particularly stable structure which allows ^{146}Gd to have properties analogous to those of the doubly magic nucleus ^{208}Pb. Thus, the nuclei in the ^{146}Gd region can be understood as excitations above the Fermi surface defined by the ^{146}Gd core. However, in contrast to real magic nuclei, one has to refer always to quasi-particle or quasi-hole excitations, since the real particles and holes are always surrounded by a polarisation cloud. This makes the quasi-particle energies vary with the occupancy number of the orbital. Looking at the quasi-particle energies in the semi-magic ^{146}Gd nucleus plot in Fig. [2.1], we can see that nuclei with $Z > 64$ and $N \geq 82$ are susceptible to decay through the fast $h_{11/2} \rightarrow h_{9/2}$ Gamow–Teller transition. The proton $s_{1/2}$, $h_{11/2}$ and $d_{3/2}$ single particle orbitals are all within 260 keV, and the $h_{11/2}$ and $s_{1/2}$ levels are almost degenerate. This opens the uncertainty about where the valence proton (or protons) is placed and which is the configuration of the protons for the ground states of $Z > 64$ nuclei. The case of the neutron side is very different, since the first orbital $f_{7/2}$ above the N=82 neutron shell closure is more clearly separated from the higher lying orbitals.

Our experiment was conceived within an ambitious programme focused on the evolution of the $h_{11/2} \rightarrow h_{9/2}$ GT resonance starting from the $n_{h_{11/2}} = 1$ case. We can find in Fig. [2.2] all the $Z > 64$ nuclei which could be measured, together with the most relevant parameters of their decays. From the physics point of view, the ideal candidates are all the N=82 closed shell nuclei. Many of those have been already studied with high resolution spectroscopy, but the limited sensitivity of this technique (see previous chapter) opens some doubts on the full detection of the Gamow–Teller strength. Unfortunately, the N=82 cases are not good candidates for the TAGS technique. It can be observed in Fig. [2.2] that all (even Z, N=82) nuclei present smaller Q_{EC} values than the daughter decays, which has the consequence that the contamination from the daughter activity would be dangerously extended in the TAS spectra beyond the data corresponding to the main measurement. This does not occur for the (odd Z, N=82) nuclei, but for them we find another problem. All (odd Z, N=82) cases present (at least) two isomers, and there is no experimental way to produce them separately. Any direct fusion-evaporation reaction produces also the parent (Z-1, N=81) nucleus. It can be seen in Fig. [2.2] that this nucleus also have two isomeric states, and its direct production always leads to an admixture of both (Z, N=82) isomers via β-decay or internal transitions. Such experimental handicaps eliminate from the candidate list all N=82 nuclei and force us to consider the N=83 cases. For these nuclei the situation is more favourable, in particular for the odd-odd cases. As is shown in Fig. [2.2], these nuclei present two isomeric states of spins 2^- and 9^+, but the the situation is different from the (odd Z, N=82) cases. Here, due to the Gamow-Teller selection rules, the even-even parent nucleus, which always has $J^\pi = 0^+$, can only decay into the low spin isomer. This particular feature

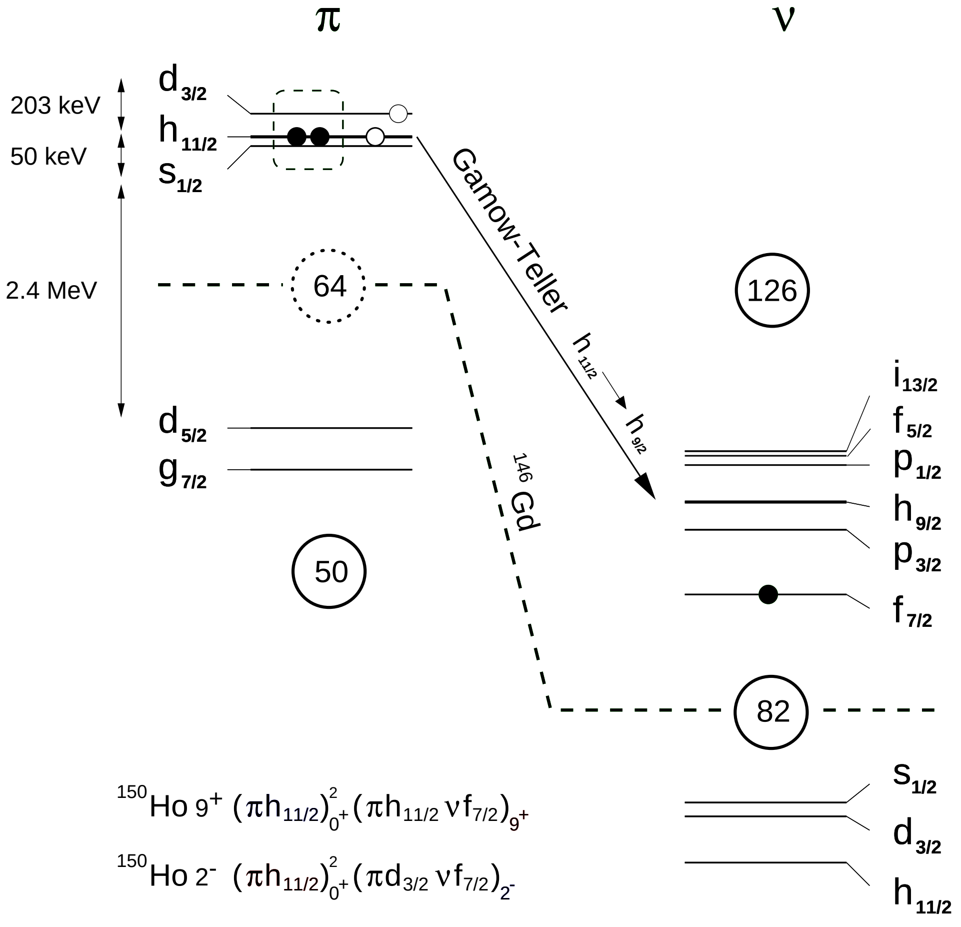

π
ν
203 keV
50 keV
2.4 MeV
$d_{3/2}$
$h_{11/2}$
$s_{1/2}$
64
Gamow-Teller
$h_{11/2} \rightarrow h_{9/2}$
126
$d_{5/2}$
$g_{7/2}$
^{146}Gd
50
$i_{13/2}$
$f_{5/2}$
$p_{1/2}$
$h_{9/2}$
$p_{3/2}$
$f_{7/2}$
82
$s_{1/2}$
$d_{3/2}$
$h_{11/2}$
^{150}Ho 9^+ $(\pi h_{11/2})^2_{0^+}(\pi h_{11/2}\nu f_{7/2})_{9^+}$
^{150}Ho 2^- $(\pi h_{11/2})^2_{0^+}(\pi d_{3/2}\nu f_{7/2})_{2^-}$

Figure 2.1: Quasiparticle energies in the ^{146}Gd region.

allows a selective reaction which produces only the parent of the even-even nucleus through an xp channel and finally reaches the even-even N=83 low spin isomer after β-decay.

<table>
<tr><th></th><th colspan="2">N=81</th><th colspan="2">N=82</th><th colspan="2">N=83</th><th colspan="2">N=84</th></tr>
<tr><td>Z=69</td><td colspan="2">^{150}Tm</td><td colspan="2">^{151}Tm</td><td colspan="2">^{152}Tm</td><td colspan="2">^{153}Tm</td></tr>
<tr><td></td><td>(6-)
2.2(2)s
11100(500)</td><td>(10+)
5.2(3)ms
11100(500)</td><td>(11/2-)
4.17(10)s
7400(300)</td><td>(1/2+)
6.6±1.4s
7400(300)</td><td>(2)-
8(1)s
8600(300)</td><td>(9)+
5.2(6)s
8600(300)</td><td>(11/2-)
1.48(1)s
6459(24)</td><td>(1/2+)
2.5(2)s
6502(24)</td></tr>
<tr><td>Z=68</td><td colspan="2">^{149}Er</td><td colspan="2">^{150}Er</td><td colspan="2">^{151}Er</td><td colspan="2">^{152}Er</td></tr>
<tr><td></td><td>(1/2+)
4(2) s
7800(471)</td><td>(11/2-)
8.9(2) s
8542(470)</td><td colspan="2">0+
18.5(7) s
4108(?)</td><td>(7/2-)
23.5±1.3 s
5400(300)</td><td>(27/2-)
0.58(2) s
7986(300)</td><td colspan="2">0+
10.3(1) s
3109(44)</td></tr>
<tr><td>Z=67</td><td colspan="2">^{148}Ho</td><td colspan="2">^{149}Ho</td><td colspan="2">^{150}Ho</td><td colspan="2">^{151}Ho</td></tr>
<tr><td></td><td>1+
2.2±1.1 s
9400(272)</td><td>6-
9.59(15) s
9400(272)</td><td>(11/2-)
21.1(1) s
6014(24)</td><td>(1/2+)
56(3) s
6063(24)</td><td>2-
72(4) s
7372(27)</td><td>(9)+
23.3(3) s
7390(60)</td><td>(11/2-)
35.2(1) s
5124(13)</td><td>(1/2+)
47(1) s
5165(13)</td></tr>
<tr><td>Z=66</td><td colspan="2">^{147}Dy</td><td colspan="2">^{148}Dy</td><td colspan="2">^{149}Dy</td><td colspan="2">^{150}Dy</td></tr>
<tr><td></td><td>1/2+
40±10 s
6373(53)</td><td>11/2-
55.7(7) s
7123(53)</td><td colspan="2">0+
3.1(1)m
2682(44)</td><td>(7/2-)
4.20(14) m
3812(12)</td><td>(27/2-)
0.490(15) s
6473(12)</td><td colspan="2">0+
7.17(5) m
1794(9)</td></tr>
<tr><td>Z=65</td><td colspan="2">^{146}Tb</td><td colspan="2">^{147}Tb</td><td colspan="2">^{148}Tb</td><td colspan="2">^{149}Tb</td></tr>
<tr><td></td><td>1+
8(4) s
8267(9)</td><td>5-
23(2) s
8267(9)+X</td><td>(1/2+)
1.7(1) m
4659(12)</td><td>(11/2)-
1.83(6) m
4659(12)</td><td>2-
60(1) m
5764(17)</td><td>9+
2.20(5) m
5854(17)</td><td>1/2+
4.118(25) m
3638(6)</td><td>11/2-
4.16(4) m
3673(6)</td></tr>
<tr><td>Z=64</td><td colspan="2">^{A}Z
GS spin/parity
half life
Q$_{EC}$ in keV</td><td colspan="2">^{146}Gd
0+
48.27(10) d</td><td colspan="2">^{147}Gd</td><td colspan="2">^{148}Gd</td></tr>
</table>

Figure 2.2: Region of interest of the nuclide chart. Q$_{EC}$s, half-lives and ground state spins taken from [BNL99] [AUD97].

The high spin isomer can be produced, together with the low spin one, by a direct reaction, and the pure low spin spectrum can be subtracted afterwards from the admixture, thus procuring clean high spin data. In this way, the decays of the two isomers can be measured. Another advantage is that the Q_{EC} of the daughter nucleus is significantly smaller than the Q_{EC}s of the decays we are interested in.

Our total absorption experiment, carried out at GSI in 1996, provided β-decay data for ^{148}Tb 2^-, ^{148}Tb 9^+, ^{150}Ho 2^- and ^{150}Ho 9^+. An accepted and still pending experiment will supplement this information with further measurements on the decays of ^{152}Tm 2^- and ^{152}Tm 9^+. This work reports on the results for the two ^{150}Ho 2^- and ^{150}Ho 9^+ decays. The simple interpretation of these two isomers in terms of the extreme single particle shell model (ESP) allows an immediate qualitative understanding. The low spin isomer, with a $(\pi h_{11/2})^2_{0^+}$ $(\pi d_{3/2}\ \nu f_{7/2})_{2^-}$ valence particle configuration around the ^{146}Gd core, decays only to the 1^-, 2^- and 3^- 4 quasiparticle (qp) states in ^{150}Dy. The high spin isomer, characterised by the $(\pi h_{11/2})^2_{0^+}$ $(\pi h_{11/2}\ \nu f_{7/2})_{9^+}$ configuration, decays to the 8^+ 2qp-states and to the 8^+, 9^+ and 10^+ 4qp-states. In both cases, the Gamow–Teller resonances are expected to lie inside the Q_{EC} window, which means that most of the GT-strength should be observed.

2.2 The facility

After taking the decision about which nucleus (or nuclei) one wants to study, one has to find the right place to do the experiment. This implies to find out which nuclear physics facility provides the right equipment and at the same time offers the proper conditions in terms of yield and purity of the requested nuclei. We decided to do our experiment at the GSI on-line mass separator [BRU81] for two reasons. The first is that a very efficient and advanced version of a Total Absorption Spectrometer (TAS), electronics and related hardware are available there [KAR97]. The second reason is that the yield of the rare earths we were interested in, ^{150}Ho 2^- and ^{150}Ho 9^+, is excellent at the separator.

GSI is a heavy ion research centre located in Darmstadt, Germany. The laboratory performs basic and applied research in physics and related natural science disciplines. GSI operates a heavy ion accelerator facility consisting of the linear accelerator UNILAC (energy 2 - 20 MeV per nucleon), the heavy-ion synchrotron SIS (1 - 2 GeV/u), the storage cooler ring ESR (0.5 - 1 GeV/u) and about 30 experimental set-ups. The UNILAC can accept ions coming from the Penning, Chordis or Mevva ion sources and also from an ECR ion source. The ions are accelerated to a maximum energy of 20 MeV per nucleon and can be used for experiments at the UNILAC experimental area (as in our case) or injected into SIS for re-acceleration up to relativistic energies.

Fig. [2.3] displays a schematic view of the GSI on-line mass separator. In its leftmost part we can see how the UNILAC primary beam, typically with energies of a few MeV per nucleon, is directed onto a thin target to produce fusion-evaporation reactions. Empirical knowledge or results from simulation codes such as HIVAP [REI84] or CASCADE [PUL77] permit us to find the beam energy which maximises the cross section of the desired fusion-evaporation channel. The use of a degrader in front of the target can be a helpful practice since it allows one to modify the beam energy slightly without changing the accelerator settings. Continuing with the description of Fig. [2.3], the fusion-evaporation reaction products diffuse out of the thin target and enter into the ion source. There, they are ionised to a given charge state by a cathode at high voltage. A TIS [KIR81][KIR90] (Thermal surface Ionisation Source) source type was used in our experiments, since it provided the highest integrated production yields. The ion chemistry in the case of the rare earths is very difficult, because all of them have very similar chemical properties and diffusion coefficients. Thus, all the rare earths come out together from the ion source, and the purity has to be achieved by playing with the reaction channel (beam/targets election), the beam energy (cross section balance for the different reaction channels), mass separation and half life discrimination.

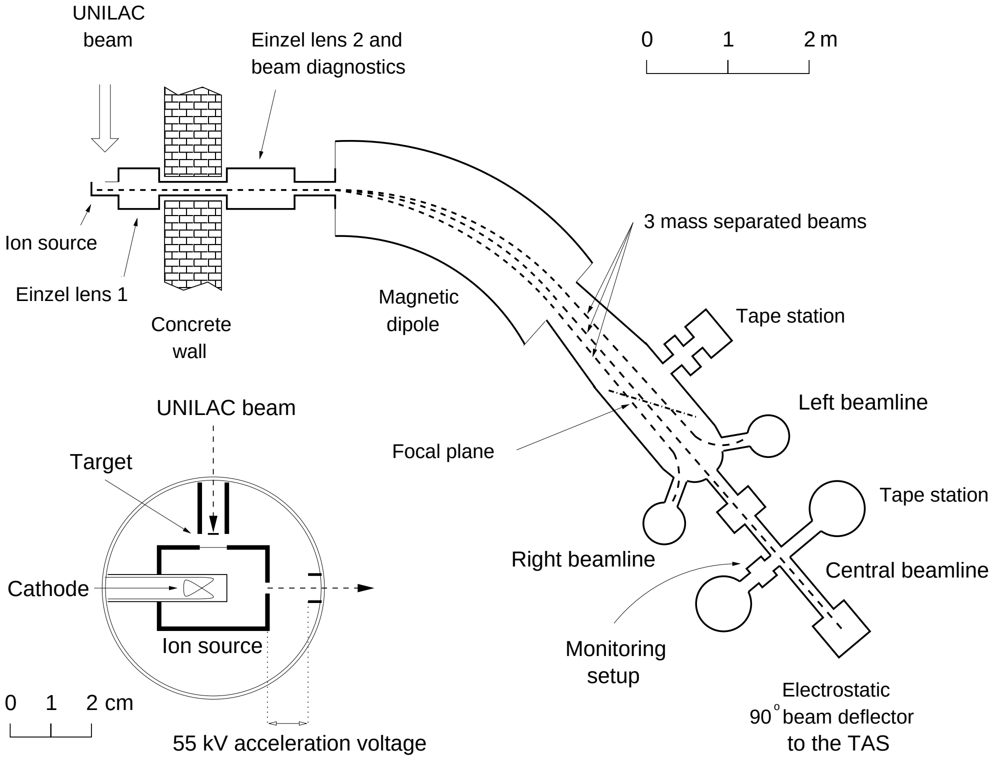
UNILAC beam
Einzel lens 2 and beam diagnostics
0 1 2 m
3 mass separated beams
Ion source
Einzel lens 1
Concrete wall
Magnetic dipole
Tape station
Left beamline
UNILAC beam
Target
Focal plane
Tape station
Right beamline
Central beamline
Cathode
Ion source
Monitoring setup
0 1 2 cm
Electrostatic 90° beam deflector to the TAS
55 kV acceleration voltage

Figure 2.3: Schematic drawing of the The GSI on-line mass separator

The ions are extracted from the source with an electrostatic field and accelerated in a 55 kV potential applied at the entrance of the magnetic dipole. Two Einzel lenses are responsible for the focusing and control of the secondary beam: one close to the ion source, inside a controlled area, and the other in the experimental hall, just after the concrete wall visible in Fig. [2.3]. The separator has a resolving power of $\Delta M/M \approx 1/1500$ with a slit of 0.5 mm. A distribution chamber at the focal plane of the dipole allows one to separate simultaneously into three beam lines (right, central and left in the sense of travel of the ions) masses in a range between -4.5% and +4.5% of the selected central mass. The three separated beams are channeled through three beam pipes, which permits up to three measurements at the same time. During our experiment, only the central beam line was used for both TAS and source composition measurements.

2.3 The experimental setup

Fig. [2.5] shows that the central beam line allows two measurements: the source composition monitoring and the main TAS experiment. As can be observed in Fig. [2.4], during the run one fourth of the total time was dedicated to determining the purity of the radioactive samples measured by the TAS. This was done by periodic implantation of the mass separated beam onto a tape. The radioactive source collected was transported in front of a 30% hyperpure Ge detector, as shown schematically in Fig. [2.5].

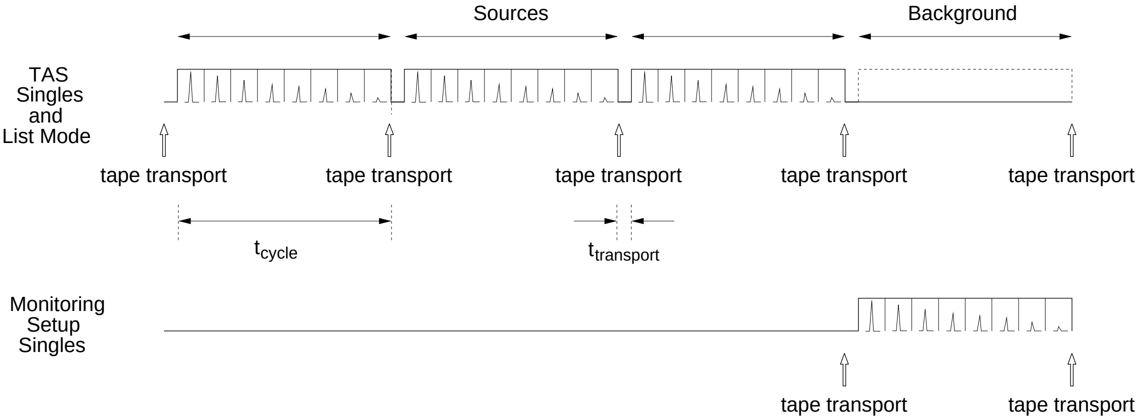

Figure 2.4: Scheme of the beam time distribution between the TAS and the monitoring setup during the experiment.

The time dedicated to the purity control of the source was used for background measurements with the TAS. The rest of the time (three quarters), the beam was assigned to the TAS for the source measurements. The scheme of the time distribution between the TAS and monitoring setup is shown in Fig. [2.4]. The measuring cycle t_{cycle} was set to a value typically 1-2 times the half-life of the isotope to be studied. This interval, which has the same length as the implantation or collection period t_{coll}, was divided in a set of subgroups which provided information on the decay of the source. Measurements and implantations were carried out in parallel, and after the completion of a cycle, a tape transport occurred so that the old source was replaced by a new one.

Fig. [2.5] exhibits how the ions travelling along the central beam line were sent to the TAS, located inside an air-conditioned hut above the floor level. An electrostatic mirror with a transmission of ≈80% deflects them 90° upwards. One Einzel-lens and an electrostatic quadrupole control further focusing, and finally the beam traverses a collimator and is implanted on a tape. The implanted source spot has a size of ≈8 mm. After a given collection time, the sources are transported to the centre of the TAS. Since the implantation is done in vacuum (10^{-5} mbar) and the measurement happens at room pressure, the tape with the implanted sources has to be extracted via a two step differential pumping system. As can be seen in Fig. [2.5], the NaI(Tl) detector is shielded with 5 cm lead and 7.5 cm borax on the bottom and the sides against environmental background radioactivity (γs and neutrons). The mechanical design of the upper part of the spectrometer does not allow screening on the top.

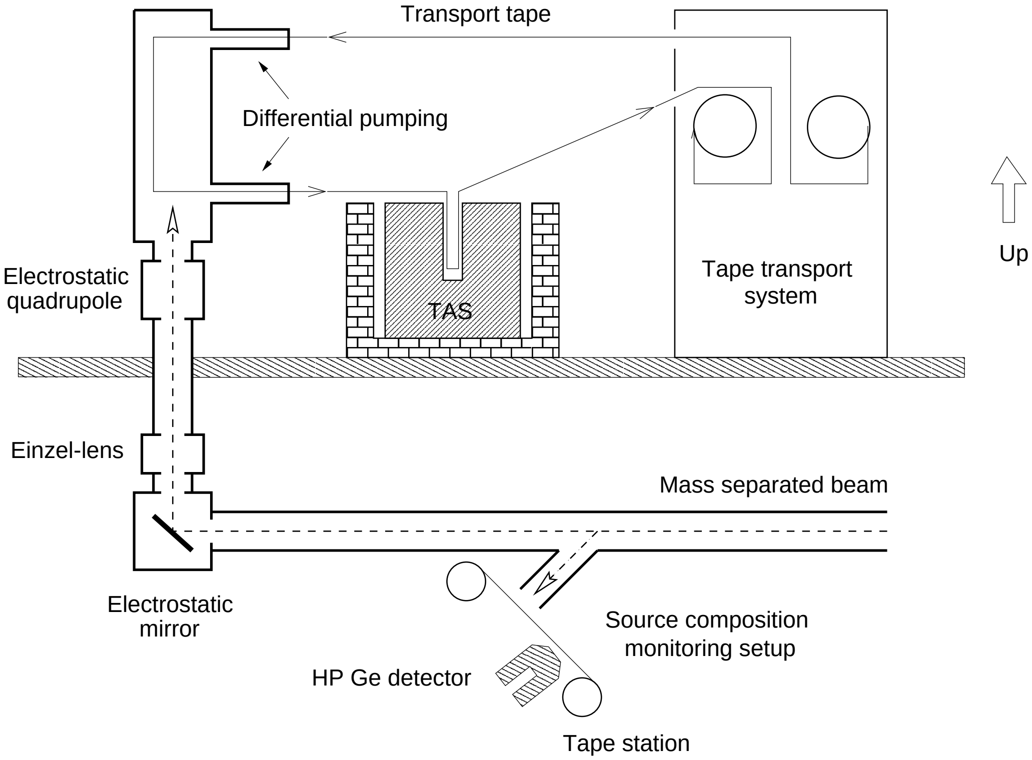
Transport tape
Differential pumping
Electrostatic quadrupole
TAS
Tape transport system
Up
Einzel-lens
Mass separated beam
Electrostatic mirror
Source composition monitoring setup
HP Ge detector
Tape station

Figure 2.5: The coupling of the TAS to the GSI on-line mass separator

Under normal experimental conditions with a ^{58}Ni beam on target, the background rate amounted to 10^3 counts/s. After the beam is turned off, the value decreased slowly after a few hours to 650 counts/s and remained stable at that value.

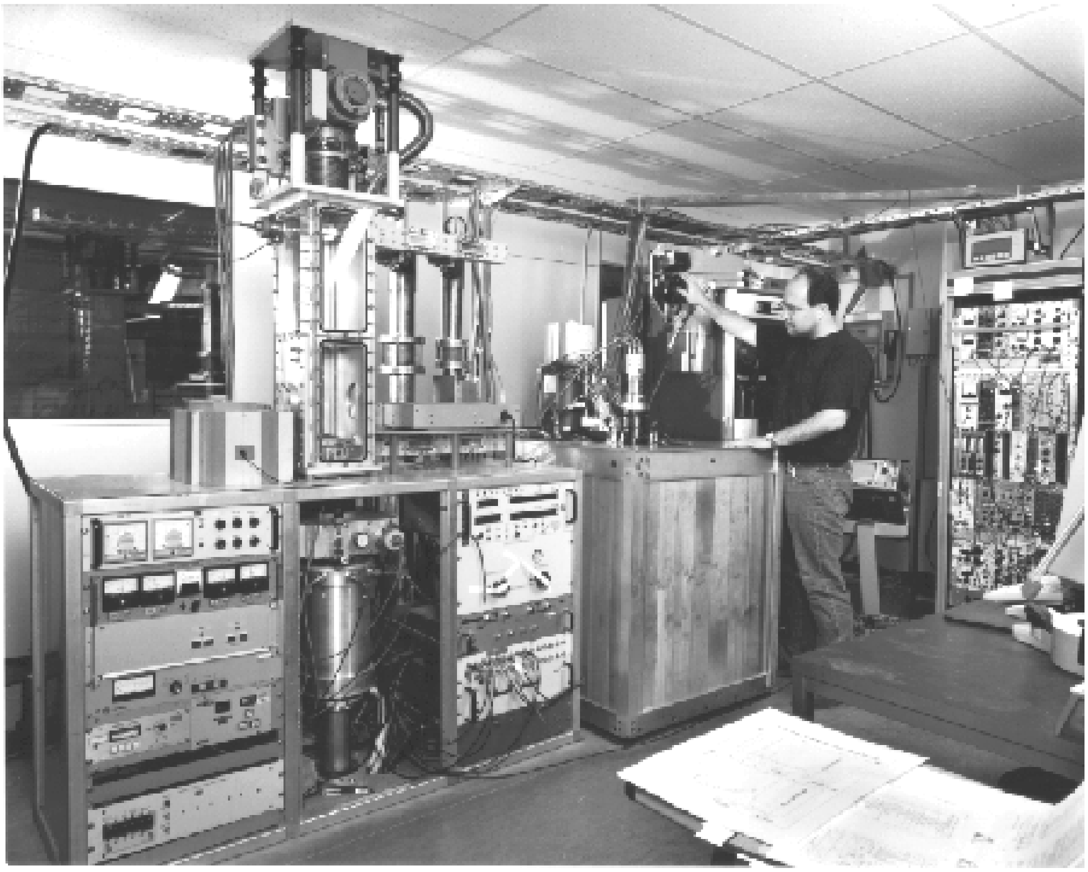

Figure 2.6: Picture of the TAS setup. Left: the implantation chamber above the last quadrupole of the beamline. Centre: outer part of the TAS shielding. Right: (large) experimenter and the station used for the tape transport behind him.

The photograph shown in Fig. [2.6] offers a view of the inside of the hut with the author adjusting the apparatus. On the bottom left, the last quadrupole of the beam line is visible between two racks with the vacuum control electronics. On top of it is the main part of the vacuum chamber where the implantation of the isotopes takes place. Comparing Fig. [2.6] with the scheme in Fig. [2.5], it is possible to recognise the two branches of the differential pumping system: the lower one, used as an exit to room pressure, and the upper one through which the tape returns into vacuum. The outer aluminium box which surrounds the TAS and its shielding is sitting on the floor (platform), next to the implantation chamber. The tape unit which transports the implanted sources is hidden by the experimenter.

2.4 The Total Absorption Spectrometer

Fig. [2.7] is a schematic drawing of the geometry of the TAS as used in the experiment. The spectrometer was conceived and designed for the study of EC/β^+ decays. The detector consists of a large, well type NaI(Tl) crystal (⌀35.6 cm×35.6 cm external dimensions). The 4π geometry is restored by a smaller plug NaI(Tl) crystal (⌀4.7 cm×15.0 cm) inserted in the hole.

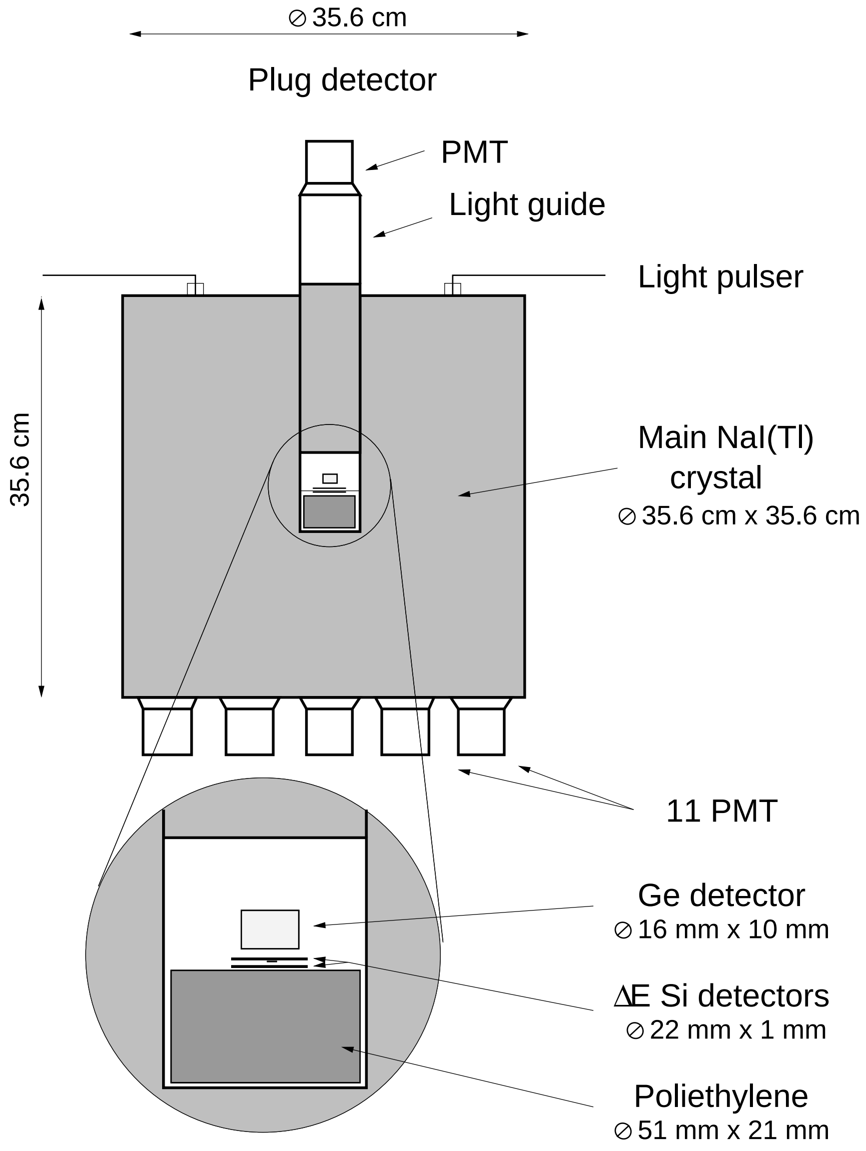
⌀35.6 cm
Plug detector
PMT
Light guide
Light pulser
35.6 cm
Main NaI(Tl) crystal
⌀35.6 cm x 35.6 cm
11 PMT
Ge detector
⌀16 mm x 10 mm
ΔE Si detectors
⌀22 mm x 1 mm
Poliethylene
⌀51 mm x 21 mm

Figure 2.7: The TAS at the GSI on-line mass separator

A holder for two thin Si(Li) detectors (⌀22 mm×1 mm) is attached to the bottom of the plug detector. The holder also supports two rollers which sustain the implantation tape between the two Si(Li) detectors. The distance between the Si(Li) is of 1 mm and the solid angle covered by them amounts to 97.6% of 4π. The Si(Li)s are energy-loss trigger detectors which allow one to register signals in the NaI(Tl) in coincidence with β-particles (positrons in our case). The β^+-component of the decay can be tagged in this way. The thickness of 1 mm of Si means that a threshold can be set which minimises the effect of undesired triggers coming from conversion electrons. The threshold was adjusted to ≈300 keV, significantly above the expected conversion electron energies, but still below the values of positron mean energy losses in 1 mm of Si given in Table [2.1]. However, the threshold introduces some distortion in the NaI(Tl) spectra in coincidence with the Si: due to the continuous energy spectrum of the β-particles, there is always a fraction of positrons which remains undetected, and this fraction becomes larger as its end-point energy approaches the threshold. For the lowest β end-point energies, which correspond to β-transitions to levels close to Q_{EC} - $2m_ec^2$, most or all of the positrons will have an energy below the threshold and thus not fire the system. This effect has been taken into account in the analysis, but as explained in subsection 4.6.2, it has some important consequences.

E_{e^+}	E_{loss} in 1 mm of Si ρ_{Si} =2.33 g/cm^3	E_{loss} in 2.1 cm of polyethylene ρ_{pol} =2.33 g/cm^3
0.5 MeV	380 keV	all
1 MeV	360 keV	all
4 MeV	400 keV	3.8 MeV
6 MeV	430 keV	3.9 MeV
8 MeV	560 keV	4.0 MeV

Table 2.1: Mean energy losses of e^+ in 1 mm of Si and 2.1 cm of polyethylene. Values taken from [PAG72].

A small Ge X-ray detector is also located inside the main NaI(Tl) crystal, fixed to the bottom of the plug and above the top Si detector. A Be cold finger inside an aluminium housing runs parallel to the plug crystal and keeps the X-ray detector at the liquid nitrogen temperature. The Ge crystal (⌀16 mm×10 mm) is located between the upper Si detector and the plug, centred at a distance of 6 mm above the source position. Its main purpose is the detection of the characteristic X-rays emitted in the EC process, which selects the EC component of the decay by requiring a coincidence with an energy signal in the NaI(Tl). The X-ray coincidence technique allows an unambiguous Z identification, which makes the EC spectra extremely clean in comparison to the the β^+ ones. This is an extremely important feature of the spectrometer, which was not present in the previous spectrometers described in [DUK70] [BYK80] [GRE92]. As mentioned in sections 4.6 and 4.7, the purity of the spectra is the most important requisite for the reliability of the results obtained by the TAGS technique. Unfortunately, we pay a large price for the atomic selection facet. The insertion close to the source position of a non-negligible piece of high Z material like Ge, has a strong negative influence on the photopeak efficiency of the TAS. The compromise adopted in the design was to favour the TAS efficiency by placing the X-ray detector at a distance which reduces significantly the solid angle covered and leads to a small X-ray detection efficiency (≈few percent). Thus, in the studies of nuclei with low production rates, only the β^+-component of the decay is measurable in practice.

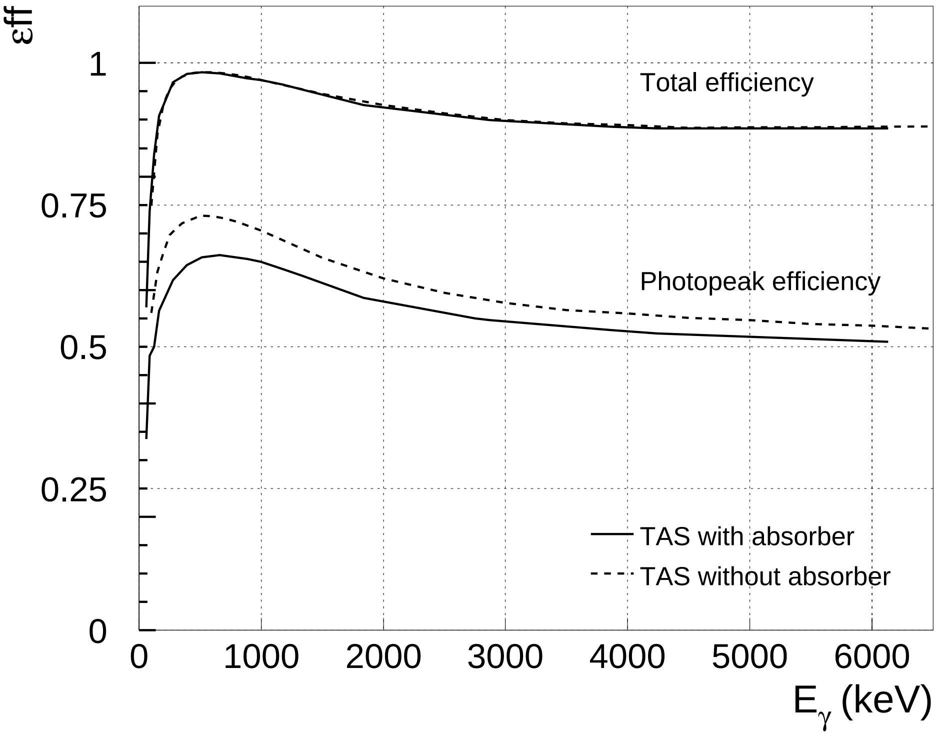

Figure 2.8: Total and photopeak efficiencies of the TAS for different γ-ray energies obtained by Monte Carlo simulation. Solid lines correspond to the efficiencies of the spectrometer including the polyethylene absorber described in the text, while the dashed lines represent the efficiencies of the configuration without absorber described in [KAR97].

Also visible in Fig. [2.7] is the presence of a polyethylene absorber (⌀51 mm×21 mm) at the bottom of the plug assembly, which represents a difference with respect to the original set-up of the TAS described in [KAR97]. The polyethylene was not included in the original design, and thus the assembly had to be lifted from its standard position by 18 mm. The purpose of this absorber is to minimise the penetration of the β-particles in the NaI(Tl) detector (see section 3.2 and section 4.6.2). From the values of Table [2.2] and the curves in Fig. [2.8], it can be observed that the insertion of the absorber lowers significantly the photopeak efficiency of the TAS (lower solid line) with respect to the same configuration in which the absorber is not present (lower dashed line). For this reason, and according to the mean energy loss values of e^+ in polyethylene shown in Table [2.1], we decided to insert an absorber which stops e^+ of $\approx$4 MeV and reduces significantly the penetration of e^+ up to 6.3 MeV), the maximum expected positron energy. Such a compromise avoided spoiling the high photopeak efficiency of the spectrometer unnecessarily.

E_γ (keV)	$\epsilon_{photopeak}$ (%)	ϵ_{total} (%)	E_γ (keV)	$\epsilon_{photopeak}$ (%)	ϵ_{total} (%)
60	33.7	56.9	997	65.0	97.0
88	48.5	73.9	1173	63.7	96.2
122	50.0	83.9	1333	62.6	95.3
166	56.3	90.7	1836	58.6	92.6
279	61.7	96.6	2754	55.0	90.2
392	64.4	98.1	2870	54.7	89.9
514	65.8	98.4	3867	52.9	88.8
662	66.2	98.2	4238	52.4	88.5
889	65.5	97.3	6130	50.8	88.5

Table 2.2: Monte Carlo values of the total and photopeak efficiencies for γ ray energies of the TAS with polyethylene absorber as plotted in Fig. [2.8].

The scintillation light of the NaI(Tl) is collected by 11 photomultiplier tubes (Hamamatsu R1911-01 PMTs) coupled to the bottom of the main crystal and an additional PMT (R1911-01) coupled to the plug detector. The light output drifts and gain matching variations between the individual PMTs were prevented by keeping the spectrometer at a constant temperature. An on-line control of the stability of the system is provided by a reference light pulser of 200 Hz frequency. The light pulser consists of a pulsed LED whose light is sent to the TAS via six randomised-fibre bundles, five to the main crystal and one to the plug. The LED is stabilised by a smaller and independent NaI(Tl) reference detector, manufactured together with the TAS. Two linked digital stabilisers control the temperature of the LED by comparing the signals of the light pulser and the 2506 keV sum pulse of a ^{60}Co source inside the reference detector. During the approximately 80 hours of experiment, the stability of the TAS was controlled periodically by following the centroid of the light pulser and individual peaks from calibration sources. The values of the reference centroids (in channels) as a function of time are listed in Table [2.3]. When compared to its respective mean values μ shown in the last row of Table [2.3], it can be seen that none of the peaks moved more than ± 0.3 % along the whole experiment.

^{137}Cs centroid 662 keV	^{60}Co centroid 1173 keV	^{88}Y centroid 1836 keV	^{60}Co centroid 2506 keV	Light pulser centroid	time (hr)
143.3	252.1	391.8	541.9	2468.4	0.0
142.9	251.5	391.0	540.9	2454.2	17.5
142.8	251.4	390.8	540.7	2449.5	27.5
142.8	251.4	390.7	540.7	2449.4	39.5
142.7	251.3	390.5	540.5	2449.4	54.9
-	-	-	-	2454.8	77.9
$\mu = 142.9$	$\mu = 251.5$	$\mu = 390.9$	$\mu = 540.93$	$\mu = 2454.3$	-

Table 2.3: Time evolution of the centroids of the lines in the energy spectra produced by the light pulser and reference calibration sources.

2.5 The electronics

The complete electronics scheme of the TAS setup is shown in Fig. [2.9] and Fig. [2.10]. The notation and key words used in the scheme can be found in Table [2.4]. Following the lines ended by a black arrow, which represent the different energy signals, we can see that a total of 15 energy signals were taken from the TAS and the ancillary detectors: 2 corresponding to the top and bottom Si detectors, 1 for the Ge X-ray detector, 11 from the PMTs on the main NaI(Tl) crystal readout and another for the Plug detector. The signals of the 12 PMTs were summed by hardware in a mixing module. The 12^{th} PMT, corresponding to the plug detector, was divided before the summing in order to have an independent readout. The output of the Ge detector transistor reset preamplifier was also divided before processing. This allowed us to record pulses at two different gains: a high one for the X-ray tagging and a low one for monitoring and an eventual β-tagging which was not needed.

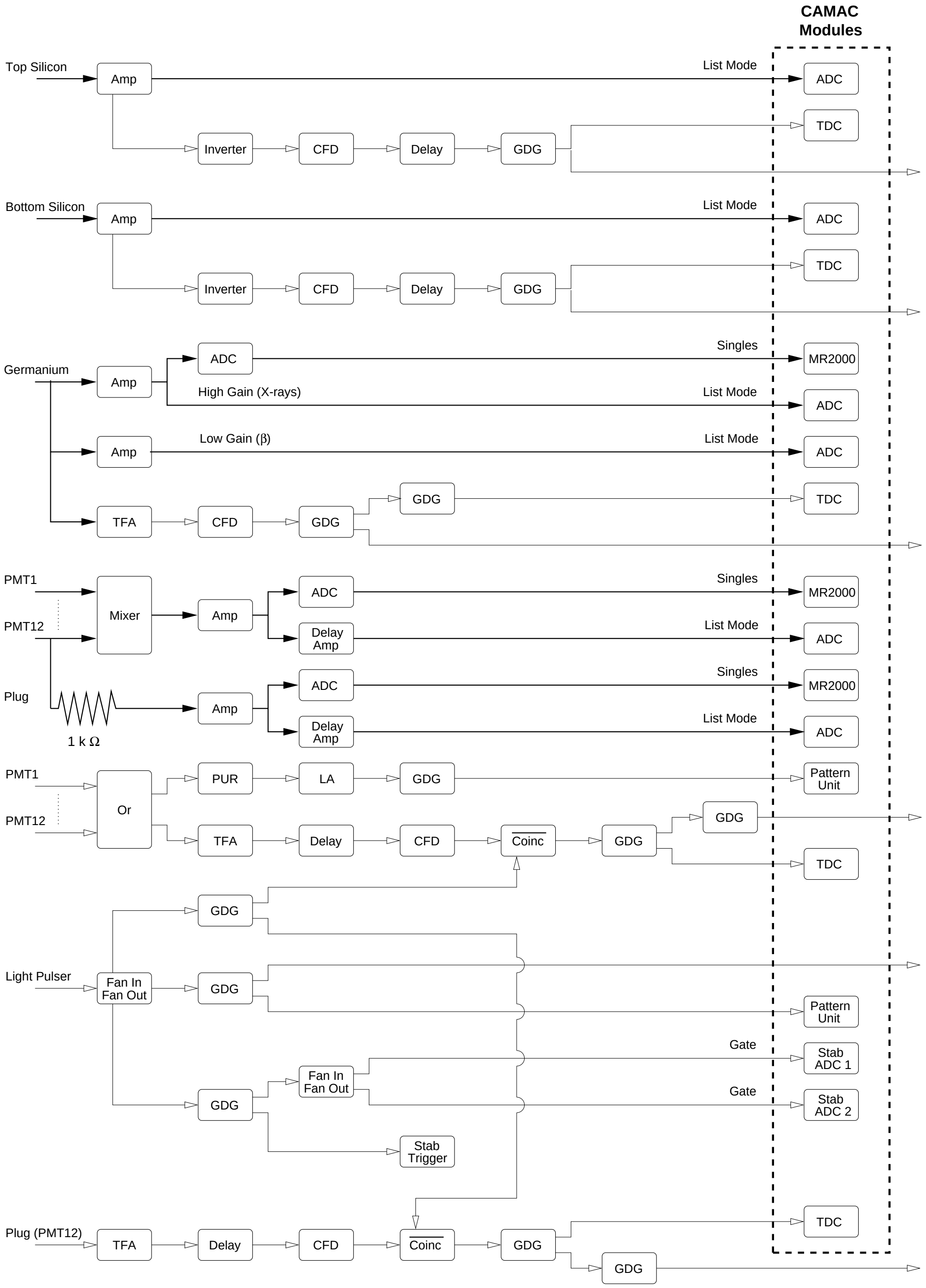
CAMAC
Modules
Top Silicon
Amp
List Mode
ADC
Inverter
CFD
Delay
GDG
TDC
Bottom Silicon
Amp
List Mode
ADC
Inverter
CFD
Delay
GDG
TDC
Germanium
Amp
ADC
Singles
MR2000
High Gain (X-rays)
List Mode
ADC
Amp
Low Gain (β)
List Mode
ADC
TFA
CFD
GDG
GDG
TDC
PMT1
PMT12
Mixer
Amp
ADC
Singles
MR2000
Delay Amp
List Mode
ADC
Plug
1 k Ω
Amp
ADC
Singles
MR2000
Delay Amp
List Mode
ADC
PMT1
PMT12
Or
PUR
LA
GDG
Pattern Unit
TFA
Delay
CFD
Coinc
GDG
GDG
TDC
GDG
Light Pulser
Fan In Fan Out
GDG
Pattern Unit
Gate
Stab ADC 1
Fan In Fan Out
Gate
Stab ADC 2
GDG
Stab Trigger
Plug (PMT12)
TFA
Delay
CFD
Coinc
GDG
TDC
GDG

Figure 2.9: Electronics scheme (I)

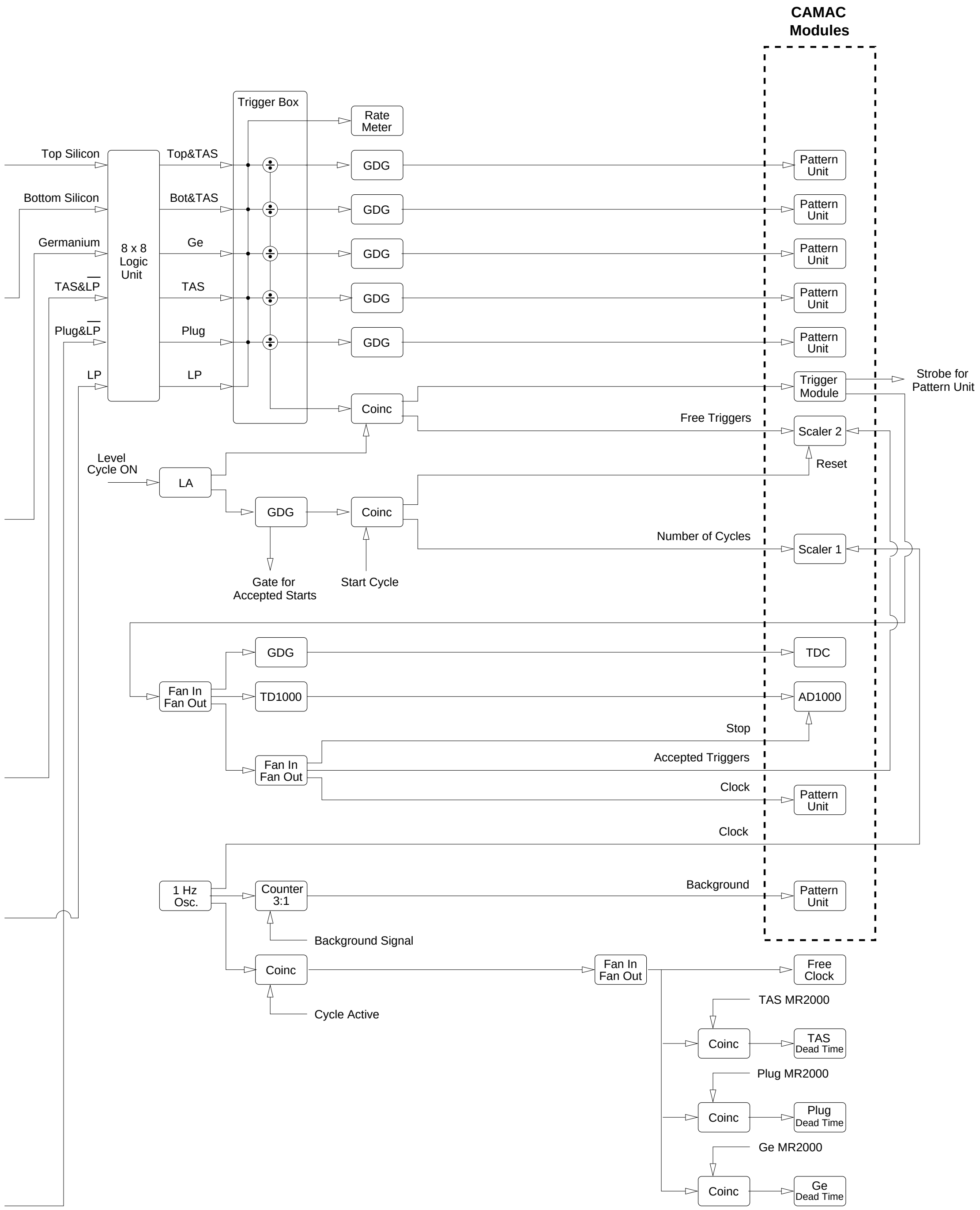
CAMAC Modules
Trigger Box
Rate Meter
Top Silicon
Bottom Silicon
Germanium
TAS&$\overline{\text{LP}}$
Plug&$\overline{\text{LP}}$
LP
8 x 8 Logic Unit
Top&TAS
Bot&TAS
Ge
TAS
Plug
LP
GDG
GDG
GDG
GDG
GDG
Pattern Unit
Pattern Unit
Pattern Unit
Pattern Unit
Pattern Unit
Trigger Module
Strobe for Pattern Unit
Coinc
Free Triggers
Scaler 2
Reset
Level Cycle ON
LA
GDG
Coinc
Number of Cycles
Scaler 1
Gate for Accepted Starts
Start Cycle
GDG
TDC
Fan In Fan Out
TD1000
AD1000
Stop
Fan In Fan Out
Accepted Triggers
Clock
Pattern Unit
Clock
1 Hz Osc.
Counter 3:1
Background
Pattern Unit
Background Signal
Coinc
Fan In Fan Out
Free Clock
Cycle Active
TAS MR2000
Coinc
TAS Dead Time
Plug MR2000
Coinc
Plug Dead Time
Ge MR2000
Coinc
Ge Dead Time

Figure 2.10: Electronics scheme (II)

The two Si energy pulses were directly amplified and registered. The slow response of Ge, in comparison to the rest of the detectors, made necessary the use of delay amplifiers in order to have all logic and energy signals on time.
Two different acquisition systems were employed in the data taking. The first one consisted of three Silena 7423UHS ADCs coupled to three CAMAC MR2000 histogramming memories and had a total intrinsic dead time of 10 μs. This extremely fast system was used for monitoring purposes and recorded only the energy signals coming from the TAS, Plug and Ge detectors. The spectra collected in this way are the so called *singles* data, that is, registered with no further conditions. Since such a rigid way of storing the data does not allow one to make any link between the recorded parameters, the data used in the real analysis have to be recorded in a *list mode* which allows the establishment of multiple conditions in software. As visible in Fig. [2.9] and Fig. [2.10], most of these signals were converted by CAMAC modules. A set of 34 parameters forming one *event*, were written onto a DLT tape whenever an accepted trigger pulse fired the system.

⟶	(slow) energy signals	⇾	(fast) timing signals
⨸	Rate divider	〰	impedance
Amp	Spectroscopy Amplifier	Delay Amp	Linear Delay Amplifier
TFA	Timing Filter Amplifier	Mixer	Hardware Sum
GDG	Gate and Delay Generator	MR2000	Histogramming Memories
ADC	Analog to Digital Converter	TDC	Time to Digital Converter
PUR	Pileup Rejector	LA	NIM/TTL convertor
$\overline{\text{Coinc}}$	Anticoincidence Unit	Coinc	Coincidence Unit
TD1000	Time sequencer	AD1000	TD1000 CAMAC Interface
CFD	Constant Fraction Discriminator	8×8 Logic Unit	Multiple Coincidence Unit

Table 2.4: Notation and key words used in Fig. [2.9] and Fig. [2.10]. The rest of the names are self explanatory.

All the CAMAC modules appearing in Fig. [2.9] and Fig. [2.10] surrounded by dashed boxes were standing in two crates, each one of them accessible by a STRUCK CVC intelligent CAMAC controller. The CVC is a UNIX computer capable of running the complete data taking system with a large total dead time of $\approx$900 μs for a 34 parameter event. Fortunately, the acquisition software available at GSI, the Multi Branch System (MBS), is able to handle a task sharing master/slave configuration when two or more such controllers are present. By using two such controllers we lowered the total dead time to $\approx$200 μs for the same event length of 34 parameters. The master CVC was standing alone in the same crate as the 3 histogramming memories and was responsible for the event building, tape writing through its SCSI bus and for serving a fraction of the data buffers (typically 10%) to the on-line analysis system. The slave CVC, sitting in the other crate with the rest of the CAMAC modules, was generally busy reading the different stations and sending them to the master CVC through an VSB bus.

2.6 The measurements

The ^{150}Ho 2^- and ^{150}Ho 9^+ nuclei were produced in two different reactions, as it is shown in Fig. [2.11] The first reaction, ^{96}Ru(^{58}Ni, $4p$)^{150}Er at 307 MeV bombarding energy, was chosen to produce ^{150}Ho 2^- through its parent decay. Fig. [2.11] illustrates that the use of a ^{58}Ni beam on a ^{96}Ru target produces a ^{154}Hf compound nucleus which can never reach an isotope with $N > 82$, in particular any of the ^{150}Ho isomers. The $4p$ channel populates ^{150}Er, and because of the Gamow–Teller selection rules, ^{150}Er, which has a 0^+ ground state, can only populate ^{150}Ho 2^- and never ^{150}Ho 9^+. Fig. [2.11] illustrates that in this way it is possible to measure the allowed decay of the low spin isomer into the 4qp-states in ^{150}Dy with spins and parities 1^-, 2^- and 3^- . The mass separation of the reaction products guaranteed that only the isotopes in the ... ^{150}Tm $\overset{\tau\sim5s}{\rightarrow}$ ^{150}Er $\overset{\tau=18.5s}{\rightarrow}$ ^{150}Ho 2^- $\overset{\tau=72s}{\rightarrow}$ ^{150}Dy $\overset{\tau=7.2m}{\rightarrow}$ ^{150}Tb ... isobaric decay chain were present in the sources. This fulfilled the condition for obtaining clean EC spectra, since the tagging on Dy X-rays selects only the ^{150}Ho 2^- decay. As we will see in section 4.4, the obtention of a pure ^{150}Ho 2^- EC spectrum is imperative if we are to produce a clean ^{150}Ho 9^+ EC spectrum by subtraction. The very different half-lives of the isobars helped additionally to reduce the

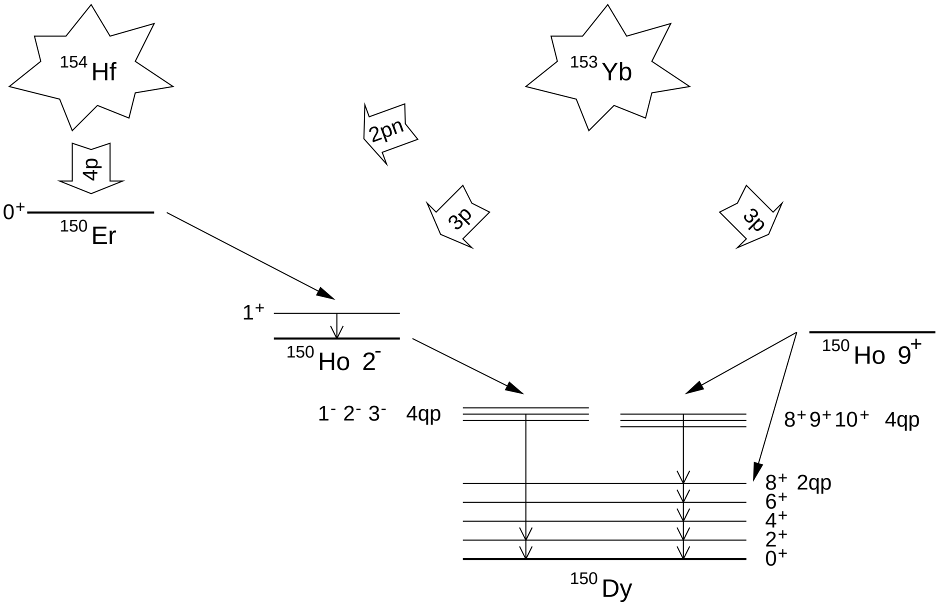

Figure 2.11: Production mechanisms of the ^{150}Ho 2^- and ^{150}Ho 9^+ isomers.

ratio of contaminants. As we will see in section 4.3, this was of great importance in the reduction of the ^{150}Er contamination present in the ^{150}Ho 2^- β^+ spectra. Also important is that ^{150}Er and ^{150}Dy have Q_{EC}s of 4108(11) keV and 1794(9) keV [AUD97] respectively, which are significantly lower than the Q_{EC}=7372(27) of ^{150}Ho 2^- [BEC97]. This guaranteed at least a contaminant-free region above 3.1 MeV in the β^+-spectrum.

Concerning the ^{150}Ho 9^+ isomer, we were interested in measuring its decay into the 4qp and 2qp-states in ^{150}Dy with spins and parities 8^+, 9^+ and 10^+. Unfortunately, there is no way to produce ^{150}Ho 9^+ independently of ^{150}Ho 2^-: any direct reaction also opens the channel for the production of ^{150}Er and the undesired decay product ^{150}Ho 2^-. Under such circumstances, even the clean EC-spectra are an admixture of two decays, and the only possibility is to subtract the clean low spin component from the admixture. As we will see in section 4.4, this was possible for the EC-spectrum and very difficult for the β^+ one. The beam and target combination used opened the channel ^{95}Mo(^{58}Ni, $3p$)^{150}Ho 9^+ at 307 MeV bombarding energy, which is approximately 30% as intense as the ^{95}Mo(^{58}Ni, $2pn$)^{150}Er reaction at the same beam energy. As for the low spin decay, a proper measuring time reduced the proportion of isobaric contaminants. The most relevant parameters and the production mechanisms are summarised in Table [2.5].

Target Degrader	Reaction at 307 MeV bombarding energy	Yield at/s·10·part·nA
^{96}Ru 1.8$\frac{mg}{cm^2}$ (96.52%) ^{93}Nb 0.85$\frac{mg}{cm^2}$	^{96}Ru(^{58}Ni, $4p\beta$)^{150}Ho 2^-	∼2000
^{95}Mo 2.96$\frac{mg}{cm^2}$ (96.47%) ^{93}Nb 2.98$\frac{mg}{cm^2}$	^{95}Mo(^{58}Ni, $3p$)^{150}Ho 9^+ ^{95}Mo(^{58}Ni, $2pn\beta$)^{150}Ho 2^-	∼600

Table 2.5: The information on the production of ^{150}Ho 2^- and ^{150}Ho 9^+ most relevant to the present work.

Chapter 3

The TAGS Inverse Problem

3.1 Introduction

The common problem of experimental science is the determination of the values and associated uncertainties of several magnitudes of interest (parameters) from a set of measured quantities (data). Often the data can be thought of as a direct consequence of the parameters in the sense that there exists a cause-effect relationship. The distribution of the data follows a certain relation with the distribution of the parameters which can be formally expressed as:

$$d = \mathcal{R}\left[p\right] \tag{3.1}$$

where d represents the distribution of the experimental data, p the distribution of the parameters one wants to determine from the data and $\mathcal{R}$ is the so called response, the functional which links both distributions.

There are cases for which the existing relation between d and p is so simple that one can easily invert the expression given by Eq. (3.1) in order to determine the distribution of the true observables and its accuracy. Unfortunately, this is not the usual situation. In practice it is often found that the mathematical inversion of the functional relation is plagued with numerical difficulties, which would render the problem insoluble. Moreover, after more careful considerations one would realize that the mathematical inversion cannot be the proper solution of the problem since it disregards the statistical nature of the measured data: one can only hope to reproduce the data in a statistical sense. The numerical difficulties alluded to before are related to the fact that in certain cases several sets of parameters (including completely unreasonable values) can reproduce closely the same data set. These are the so-called *ill-conditioned* or *ill-posed* problems. The way out of this pathology comes precisely from the inclusion of the *a priori* information on the reasonableness of the solution in the statistical formulation of the problem.

There exists a large collection of methods, successfully applied in many different fields, which allows one to obtain the desired information from a set of experimental data. These methods can be based on different principles (minimisation or maximisation of a functional regularisation of a set of equations, statistical inference...), but all of them have in common that it is always necessary to add some additional information (called *a priori* information) in order to get a result. The correctness of these initial guesses, conditions or constraints will be translated into the reliability of the final output. Which of the methods should be applied in order to get the best results is not a simple question. It is normally given by the nature of the inverse problem one is dealing with and several trials have to be made before arriving at a satisfactory situation.

In the case of the Total Absorption Gamma-ray Spectroscopy (TAGS), the situation is extremely complex. When can define a linear expression analogous to Eq. (3.1)

$$\mathbf{d} = \mathbf{R} \cdot \mathbf{f} \tag{3.2}$$

where **d** represents a total absorption spectrum, **R** is the response function of the Total Absorption Spectrometer used and **f** is the feeding distribution which produced the measured spectrum. This equation, apparently simple, hides all the difficulties involved in determining **f**. Eq. (3.2) can be rewritten more explicitly:

$$d_i = \sum_{j=1}^{j_{max}} R_{ij}\, f_j \qquad (i = 1...i_{max}) \tag{3.3}$$

where d_i represents the content of channel spectrum i, f_j represents the decay feeding to the level labeled j, and the column labeled j of the matrix **R** which will be designated by $\mathbf{R}_j$ represents the response of the spectrometer to the decay into level j. How we obtain the response **R** is presented in section 3.2 as well as in [CAN99a].

3.2 The construction of the response matrix R

A very detailed description of the construction of the response matrix can be found in [CAN99a]. However, it is worth mentioning important points again, since some of them are essential for the understanding of the analysis and the results.

According to the definition of the response matrix **R** given in the previous section, the column of the matrix labeled j will be called level j response distribution. The level response depends both on the feeding decay and the subsequent electromagnetic de-excitation. The feeding decay could be an electron if we deal with β^--decay, a positron for β^+-decay or an X-ray or Auger electron for EC-decay. The electromagnetic de-excitation contribution to the level response involves all γ-ray or conversion electron cascades which originate in that level. That is to say, the level response distribution depends on all quanta emitted in the decay. If the response to a given quantum does not depend on the response to the other quanta, then the response matrix can be constructed from the individual response distributions. In the sense that we are using it, a response is simply a discrete probability distribution. The response $\mathbf{q} = \{q_i\}$ for a single quantum of energy E represents the probability that the spectrometer will register a count in a given channel i (related in our case to the light collected by the photomultiplier tubes). Generally there will be a probability of not registering any count. This is most conveniently handled by introducing a fictitious channel zero for the probability of non-interaction. Including this channel the response will be normalised to unity: $\sum_{i=0}^{i_{\max}} q_i = 1$. The response to two coincident quanta can then be obtained by convolution of the respective responses $\mathbf{p}$ and $\mathbf{q}$: $[\mathbf{p} \otimes \mathbf{q}]_i = \sum_{k=0}^{i} p_{i-k} q_k$. By successive convolution of the adequate single quantum responses the total response can be constructed. We introduce the following notation:

$\{R_{ij}\}_{j\text{fixed}} \equiv \mathbf{R}_j$: level j response
$\mathbf{r}_j$: response to the electromagnetic de-excitation of level j
$\mathbf{g}_{jk}$: response to the γ-ray transition from level j to level k
$\mathbf{e}^{\mathrm{K}}_{jk}, \ldots$: response to the K,... conversion electron transition $j \to k$
$\mathbf{b}^{\pm}_j$: response to the e^+/e^- emission in β-decay to level j
$\mathbf{x}$: response to X-ray emission
b_{jk} : branching ratio for transition $j \to k$
$\alpha^{\mathrm{tot}}_{jk}, \alpha^{\mathrm{K}}_{jk}, \ldots$: conversion electron coefficients for transition $j \to k$

Let us first consider the response to the electromagnetic de-excitation. It is readily seen that $\mathbf{r}_j$ can be obtained in a recursive way starting from the level of lowest excitation energy. The algorithm can be written in a very compact form if we conventionally introduce the ground state level $j = 0$ response $\mathbf{r}_0$: $r_{00} = 1$ and $r_{i0} = 0, \forall i \neq 0$. For a pure γ-ray de-excitation it takes the form:

$$\mathbf{r}_j = \sum_{k=0}^{j-1} b_{jk} \mathbf{g}_{jk} \otimes \mathbf{r}_k \tag{3.4}$$

The conversion electron process can be taken into account with the replacement:

$$\mathbf{g}_{jk} \longrightarrow \left(\frac{1}{1+\alpha^{\mathrm{tot}}_{jk}} \mathbf{g}_{jk} + \frac{\alpha^{\mathrm{K}}_{jk}}{1+\alpha^{\mathrm{tot}}_{jk}} \mathbf{e}^{\mathrm{K}}_{jk} \otimes \mathbf{x} + \ldots \right) \tag{3.5}$$

In general, it is only necessary to consider the response $\mathbf{x}$ to the K X-ray emitted after the conversion electron process. This is so because X-rays filling higher atomic shells or Auger electrons would have too low an energy to be able to reach the sensitive part of the detector after traversing the dead material surrounding the source.

The response $\mathbf{R}_j$ is constructed by convolution of the response $\mathbf{r}_j$, Eq. (3.4), with the corresponding decay emission response depending on the decay process:

$$\mathbf{R}_j^{\beta^-} = \mathbf{b}^- \otimes \mathbf{r}_j \tag{3.6}$$

$$\mathbf{R}_j^{\beta^+} = \mathbf{b}^+ \otimes \mathbf{r}_j \tag{3.7}$$

$$\mathbf{R}_j^{\mathrm{EC}} = \mathbf{x} \otimes \mathbf{r}_j \tag{3.8}$$

For β^-- and β^+-decay the response $\mathbf{b}$ corresponds to the continuum distribution of electron or positron energies, respectively, extending up to $\mathrm{Q}_\beta - E_j$ if E_j is the excitation energy of level j. It should be noted that $\mathbf{b}^-$ and $\mathbf{b}^+$ are distinctly different due to the occurrence of the two annihilation quanta in the case of the β^+-decay. In any case, both $\mathbf{b}^-$ and $\mathbf{b}^+$ will introduce a considerable departure from the behaviour of an ideal TAS. For conversion electrons, as in the case of EC-decay Eq. (3.8), only the effect of K X-rays has to be considered in general. It has to be noticed that the use of tagging introduces modifications in the response of the spectrometer, Eq. (3.6)-(3.8). In general they cannot be taken into account simply by the introduction of a tagging efficiency. For instance, in the case of the EC component, since the selection is done on the K X-rays entering the Ge detector, they will not penetrate into the NaI(Tl) crystal and the effect has to be eliminated from the response. Additionally, there is a small distortion in the EC-response coming from the compound probability of tagging an X-ray when a conversion process happens. We considered this effect at first order by just doubling the weight for the conversion term in the expression of $\mathbf{g}_{jk}$:

$$\mathbf{g}_{jk} \longrightarrow \left(\frac{1}{1+\alpha_{jk}^{\mathrm{tot}}} \mathbf{g}_{jk} + \frac{2\alpha_{jk}^{\mathrm{K}}}{1+\alpha_{jk}^{\mathrm{tot}}} \delta_{jk} \right) \tag{3.9}$$

As we have seen, the problem of constructing the TAS response (assuming knowledge of the de-excitation branching ratios b_{jk} and eventually the conversion electron coefficients α_{jk}) can be reduced to the problem of obtaining all the individual quanta responses $\mathbf{g}_{jk}$, $\mathbf{e}_{jk}$ and $\mathbf{b}_j^{\pm}$ involved in the decay. The only suitable way to accomplish this task for the general case is by means of Monte Carlo simulations. An advantage of the Monte Carlo method is that any conditions, as for example those introduced by tagging, can be readily incorporated in the response. The key question becomes then: how accurately can one predict the response of the spectrometer through simulation? Ultimately, the answer is related to the accuracy with which the interactions of photons, electrons and positrons are modeled by the Monte Carlo code. Usually of equal importance is the ability to reproduce as close to reality as possible the geometry and characteristics of the materials encountered by the particles. Particular care was taken to describe accurately the geometry of the detector, especially the material surrounding the source. The dimensions were taken from direct measurements, whenever it was possible, or from construction drawings.

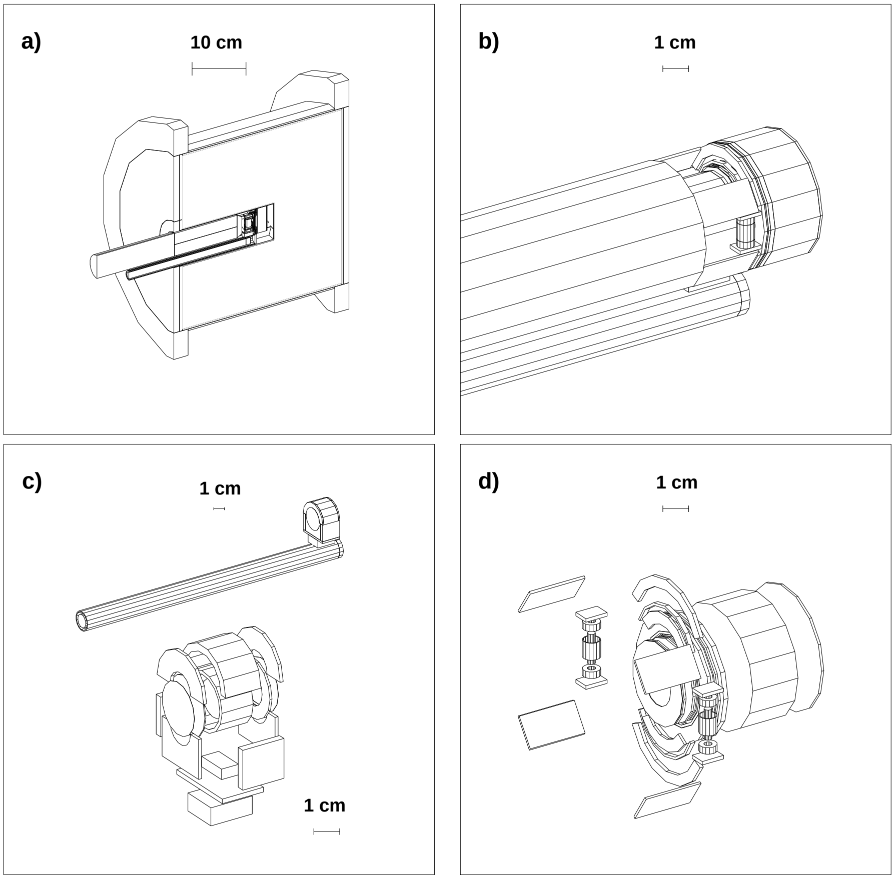

Figure 3.1: Details of the TAS geometrical description in GEANT. a) Longitudinal cut along the spectrometer showing the main crystal and the plug detector. b) Plug detector with ancillary detectors and absorber. c) Upper part: Ge detector cryostat and cold finger; lower part: Ge crystal and capsule. d) Mounting for Si detectors and transport tape rollers together with the polyethylene absorber

Fig. [3.1] shows some details of the geometry as it is included in the simulation program. More schematic drawings can be found in chapter 2 or in [KAR97]. As mentioned earlier, the TAS includes a Ge detector and two Si detectors which are situated very close to the source in order to increase their efficiency. As a consequence, the emitted radiation has to pass through a rather large quantity of material before entering into the sensitive NaI(Tl) crystal. Since we know it is very important to model faithfully this complex geometry, we have chosen to perform the simulations by means of the Monte Carlo code GEANT3 [GEA94], which has a very powerful geometry package.

While the precise emulation of the primary interaction of photons with matter (photoelectric, Compton, pair production) is affordable in terms of computing time, the simulation of the interaction of e^-/e^+ has to be done in an approximate way. GEANT3 (as several other codes [BER88]) uses a condensed history approximation for the interaction of charged particles. The effect of a large number of microscopic interactions is reduced to the computation of an energy loss (via an energy loss fluctuation theory) and a new direction (via a multiple scattering theory). The code also allows one to consider the knock-out of energetic electrons (δ-rays) and the production of bremsstrahlung radiation. Considering this, more problems in the simulation of $\mathbf{b}_j^{\pm}$ responses than for $\mathbf{g}_{jk}$ are expected, because in the latter case the electrons (or positrons) generated by the primary interactions of the γ-rays are produced in the bulk of the detecting material, while in the first case they must traverse a considerable amount of dead material. It has been proven by comparison with several experimental decays in [CAN99a], that the response to the γ-radiation is reproduced in our case with an excellent accuracy. However, it was also found that the Monte Carlo response to β-particles (penetration in the NaI(Tl) and bremsstrahlung) deviated significantly from the experimental one. Thus, we almost eliminated the distortion in the response introduced by the β-particles by placing a low Z absorber backing the β-detector in a convenient geometry, minimising in this way the penetration of the e^-/e^+ or their bremsstrahlung radiation in the NaI(Tl) detector. The influence of the residual effect on the analysis of the β^+ component of the decay is discussed with care in chapter 4.

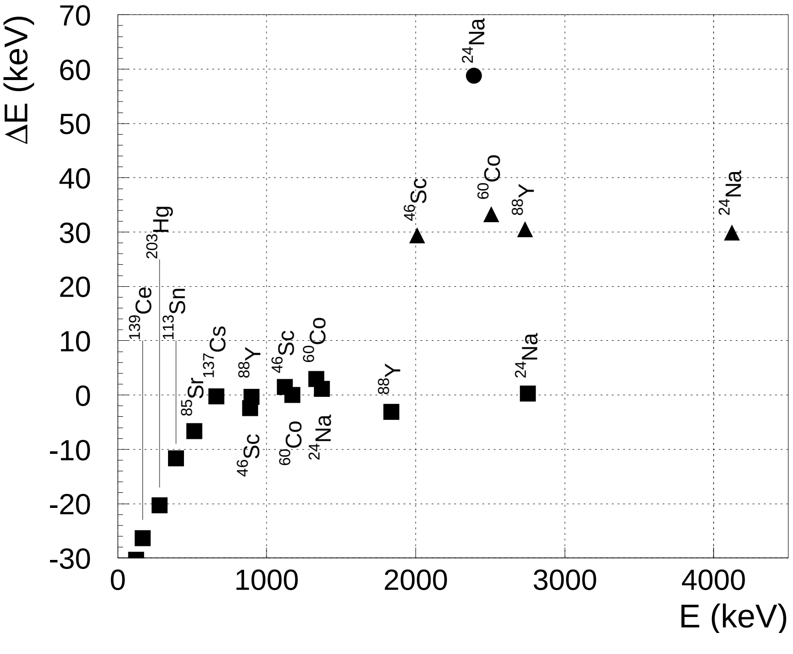

Figure 3.2: Deviations of TAS spectra peaks from a linear energy calibration. Squares: single γ-ray peaks. Triangles: double γ-ray sum peaks. Circle: triple γ-ray sum peak.

The Monte Carlo code allows one to calculate the distribution of energy deposited by a particle, say a γ-ray, in a material medium. In a detector the deposited energy is converted in a more or less complex way into the final information registered in the spectrum. For instance, a scintillation detector converts the energy into light. Part of the light is collected by a photomultiplier tube and transformed into an electric signal. The signal is amplified by the tube and processed by the electronic chain. Usually the effect of all these statistical processes is condensed in an empirical instrumental resolution distribution. This distribution (usually a Gaussian) is convoluted with the zero resolution energy deposition Monte Carlo spectrum. The spectrum obtained in this way is then re-calibrated to the experimental one.

Surprisingly, this procedure cannot be applied to a NaI(Tl) TAS. It was recognised at an early date [ENG56] that the scintillation light produced in NaI(Tl) crystals by γ-rays depositing all their energy is not proportional to the energy. This non-proportionality has the striking consequence that γ-ray sum peaks are displaced in the measured spectrum with respect to single γ-ray peaks. Fig. [3.2] shows the deviations from a linear energy calibration of the peak positions in measured TAS spectra for a set of different radioactive sources: ^{24}Na, ^{46}Sc, ^{57}Co, ^{60}Co, ^{85}Sr, ^{88}Y, ^{109}Cd, ^{113}Sn, ^{137}Cs, ^{139}Ce, ^{203}Hg and ^{241}Am. The linear calibration was obtained using the single γ-ray peaks of energies ranging from $E_\gamma = 0.662$ MeV to $E_\gamma = 2.754$ MeV. Several of the calibration sources produce strong double γ-ray sum peaks in the recorded spectra: ^{24}Na (1368.6+2754.0 keV), ^{46}Sc (889.3+1120.5 keV), ^{60}Co (1173.2 + 1332.5 keV) and ^{88}Y (898.0 + 1836.1 keV). As can be seen from Fig. [3.2], the positions of all these peaks are shifted upwards by 30 keV from the positions that peaks of a single γ-rays of equivalent energies would have. In the spectrum of ^{24}Na is visible a triple γ-ray sum peak ($1368.6 + 2 \times 511.0$ keV), which is displaced by 60 keV. The two annihilation quanta in this case are coming from pair production by the 2.754 MeV γ-ray. The increasing negative deviation observed for single γ-ray peaks of energies below 600 keV is due to the non-linearity of the electronic chain. It is worth noting the constancy of the value of the shift that we found ($\Delta E = 30.5 \pm 1.5$ keV). This effect has very important consequences for total absorption gamma-ray spectroscopy with NaI(Tl) detectors. It is not possible to speak of the energy calibration of the measured spectra in the usual sense since the counts in one channel may come from different deposited energies. It is evident, that in order to analyse TAS spectra properly, this effect has to be included in the simulated response.

The non-proportional light yield for γ-rays is a consequence of the non-proportional light yield for the secondary electrons generated by the interactions of the photon [MUR61]. Fig. [3.3] displays the values of the ratio L/E_e, where L is the light yield in NaI(Tl) produced by an electron whose energy E_e is fully absorbed. The ratio is arbitrarily normalised to unity at $E_e = 3$ MeV. The values are taken from Ref. [ZER61] above 500 keV and from Ref. [ROO96] below 500 keV. The use of L/E_e can be easily implemented in the simulation code. After each tracking step the energy deposited by the particle in the NaI(Tl) medium is converted into light equivalent. For convenience the data shown in Fig. [3.3] were fitted to the curve:

$$\frac{L}{E_e} = \frac{a_1\left(1 - e^{-a_2 E_e}\right) + a_3 E_e + a_4 E_e^2}{a_5 + a_6 E_e + a_7 E_e^2} \qquad (3.10)$$

$$\{a_i\} = \{1.6(2), 0.058(8), 0.580(4), 0.00490(2), 0.25(2), 0.479(4), 0.00494(2)\}$$

which extends above $E_e = 3$ MeV the linear behaviour of L for energies greater than 0.5 MeV. If E was the energy of the particle and ΔE the energy lost in the step then the light ΔL produced is calculated as:

$$\Delta L = L(E) - L(E - \Delta E) \qquad (3.11)$$

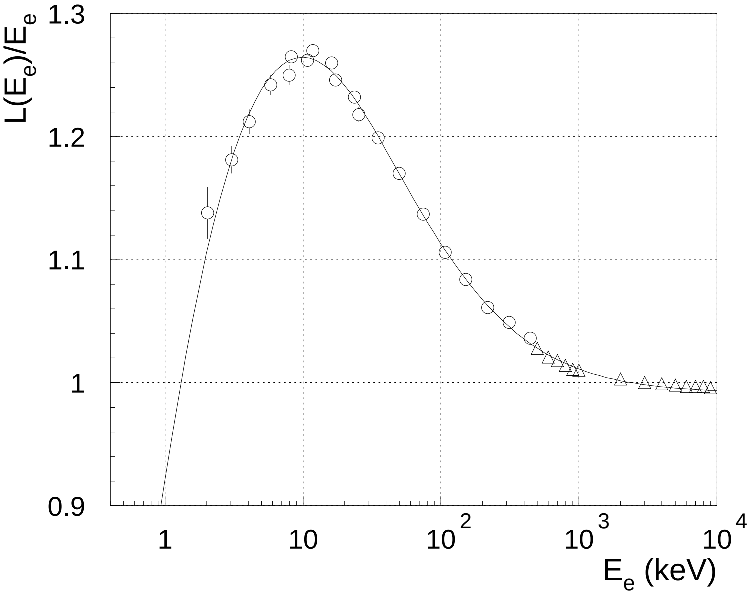

Figure 3.3: NaI(Tl) relative light yield values for fully stopped electrons as a function of their energy. Circles: from Ref. [ROO96]. Triangles: from Ref. [ZER61]. Continuous line: fit (see text).

In this way, the Monte Carlo simulated spectra naturally include the effect of non-proportionality. The full absorption peak in the simulated light spectra of γ is displaced with respect to the position of the peak in the energy deposition spectra. It was found that this displacement amounts to 30.2 keV and stays constant within 1 keV for γ-ray energies in the 0.6-4.0 MeV range. This value is in agreement with the experimental value of the light offset ($\Delta E = 30.5 \pm 1.5$ keV).

The response to the β-continuum is obtained by simulating the light produced in the interactions of electrons of momenta η (in units of $m_e c$) sampled from the distribution [KON65]:

$$\begin{aligned} N(\eta) = \eta^{2\sqrt{1-\alpha^2 Z^2}} \left(\varepsilon_0 - \sqrt{1+\eta^2}\right)^2 e^{\pi \frac{\alpha Z}{\eta} \sqrt{1+\eta^2}} \\ \left| \Gamma \left(\sqrt{1-\alpha^2 Z^2} + \mathrm{i} \frac{\alpha Z}{\eta} \sqrt{1+\eta^2} \right) \right|^2 \end{aligned} \tag{3.12}$$

Here $\alpha = e^2/\hbar c$ is the fine-structure constant, Z the charge of the daughter nucleus, $\varepsilon_0 = 1 + E_{\beta^-}^{\max}/m_e c^2$, and Γ is the complex gamma function. It was demonstrated in [CAN99a] that an excellent agreement with measured responses for several radioactive isotopes, can be obtained when the individual γ-ray responses are generated by Monte Carlo simulation.

For the analysis, more concretely for the construction of the response matrices, we have generated a set of γ response functions from 10 keV up to 8 MeV in steps of 20 keV. Additionally, 18 responses to β^+ particles were generated for end-point energies between 310 keV and 7.0 MeV.

Before finishing the discussion, several comments are pertinent at this point. In the case of β-decay far from the stability line, the number of levels accessible in the decay inside the energetically allowed window ($\simeq$ 10 MeV) can become easily of the order of $10^4 - 10^5$. One cannot hope to handle a problem of such dimension. Even more, it has little sense since the resolution of the spectrometer ($\approx$ 230 keV at 5 MeV for a NaI(Tl) spectrometer) will be in general much larger than the level energy separations.

For densely spaced levels, rather than the decay probability to each level, it would be more appropriate to determine the average probability over a certain energy interval or bin, the so called strength function. In this spirit one can reinterpret Eq. (3.2) assuming that j represents a certain energy bin of mean energy $(j - \frac{1}{2})\Delta E$, f_j the average feeding to levels within that interval and $\mathbf{R}_j$ the average response. Choosing an energy bin size ΔE comparable to the data bin size, the dimension of Eq. (3.2) is greatly reduced.

A new difficulty arises however, namely that the average response $\mathbf{R}_j$ is not calculable using an expression similar to Eq. (3.4). The reason is that the branching ratio matrix $\boldsymbol{b}$ cannot be grouped into bins: the branching out of the levels within a given bin depends on how these levels are reached. Thus, the construction of the average response should be based on individual cascades. However, a simple calculation shows that even for a moderate number of m=250 bins (a range of 10 MeV with ΔE = 40 keV), the number of convolutions necessary to build the response matrix using Eq. (3.4) is $m(m-1)/2 \approx 3 \times 10^4$, while the number of convolutions necessary using individual cascades is $(m-2)2^{m-1}+1 \approx 2 \times 10^{77}$.

The other important consideration is that the branching ratios are usually known for few levels lying at relatively low excitation energy. Strictly speaking, the unknowns in our problem are the feedings and the unknown branching ratios. This does not only increase tremendously the dimension of the problem but also converts it to a highly nonlinear one.

The way out from this apparently hopeless situation comes from the fundamental property of a total absorption spectrometer. For an ideal spectrometer, there is no dependence of the response on the branching ratios, and thus, it is expected for a good spectrometer (i.e. one like ours with large detection efficiency), that there is little dependence on them. Based on this property, we can use Eq. (3.4) to build the response matrix for binned levels. This is the most convenient way to introduce the dependence on cascade multiplicity and energies, the most important features of the de-excitation. Furthermore, the branching ratios for the unknown part of the level scheme will be handled as external parameters introduced by hand. In this way we reduce the problem to a strictly linear one. Then the inverse problem can be solved by some appropriate method, providing us with the quantities relevant to the physical problem: the feeding distribution. If the reproduction of the measured spectrum is poor, this indicates that our guess on the branching ratios is not correct and it has to be modified. The whole procedure is repeated until an adequate reproduction of the measured spectra is attained. The fundamental property of the total absorption spectrometer guarantees that this can be achieved in a reduced number of steps.

3.3 Algorithms for the solution of ill-posed linear inverse problems

We have to solve the linear problem represented by the matrix Eq. (3.2): $\mathbf{d}=\mathbf{R}\cdot\mathbf{f}$, i.e. we have to find $\mathbf{f}$ for the known $\mathbf{d}$ and a given $\mathbf{R}$. By choosing the dimension of $\mathbf{f}$ (m) equal to the dimension of $\mathbf{d}$ (n), the mathematical solution is

$$\mathbf{f}=\mathbf{R}^{-1}\cdot\mathbf{d} \tag{3.13}$$

if the inverse of the matrix $\mathbf{R}$ exists (i.e. $\mathbf{R}$ is non singular). One could argue that we are disregarding the fact that $\mathbf{d}$ is the result of a particular measurement and as such, only represents a sample from the family of statistically distributed possible data. Thus, it would only be meaningful to find the $\mathbf{f}$ distribution which reproduces the data in a statistical sense. We can introduce as an approximate measure of the data the least-squares estimator [EAD71]

$$\chi^2[\mathbf{f}]=(\mathbf{d}-\mathbf{R}\cdot\mathbf{f})^{\mathrm{T}}\cdot\mathbf{V}_d^{-1}\cdot(\mathbf{d}-\mathbf{R}\cdot\mathbf{f}) \tag{3.14}$$

where $\mathbf{V}_d^{-1}$ represents the inverse of the covariance matrix of the data

$$\mathbf{V}_{d_{ij}} = \sigma_{ij}^2 \tag{3.15}$$

and the superscript T means matrix transposition. Then the solution to our problem is given by distribution $\mathbf{f}$ which minimises Eq. (3.14), which adopts the expression

$$\mathbf{f} = (\mathbf{R}^{\mathrm{T}} \cdot \mathbf{V}_d^{-1} \cdot \mathbf{R})^{-1} \cdot \mathbf{R}^{\mathrm{T}} \cdot \mathbf{V}_d^{-1} \cdot \mathbf{d} \tag{3.16}$$

if $\mathbf{R}^{\mathrm{T}} \cdot \mathbf{V}_d^{-1} \cdot \mathbf{R}$ is non singular. If $n = m$, Eq. (3.16) leads to Eq. (3.13). If $n < m$, there is no solution, but for $n > m$ there is a solution which depends on the data uncertainties and correlations.

It happens very often that the matrix $\mathbf{R}$ or $\mathbf{R}^{\mathrm{T}} \cdot \mathbf{V}_d^{-1} \cdot \mathbf{R}$ is nearly singular. This is a consequence of the fact that the responses produced by feeding to contiguous energy bins, particularly in regions at high excitation energies, are very similar. In these regions, there is a high level density and the de-excitation occurs through a large number of γ-ray cascades, which are therefore very similar on average. The nearly-degenerate columns of $\mathbf{R}$ causes very large computer round-off errors or overflows, depending on the severity of the problem, during the calculation of the inverse matrix. In the first case, the inverse matrix tends to amplify the statistical variations of the data and produce solutions that oscillate in an “unphysical” manner. We are confronted with a so called “ill-conditioned” (sometimes also called “ill-posed”) inverse problem. These type of inverse problem occur frequently in science, whenever the measured data are not very sensitive to the search parameters. This tends to be the case if the number of parameters involved is very large, and of course is not restricted to linear problems. It does not mean that one cannot extract useful information from the data, only that the answer is not given simply by Eq. (3.16).

As pointed out in the introduction to this chapter, a wealth of methods have been developed in different fields to attack ill-conditioned inverse problems. There is great disparity in the principles used and also in the actual algorithms. Nevertheless, one can find a unifying underlying idea and it is the use of *a priori* information on the solution. It was not clear which of the existing methods will be more appropriate to our specific problem of analysing TAS spectra. Also, which kind of differences different methods would bring to the solution. In order to investigate these issues, we have implemented three different algorithms: a) linear regularisation algorithm, b) maximum entropy algorithm and c) expectation-maximisation algorithm. Their description can be found in the next three sections.

3.3.1 Linear Regularisation (LR) Method

The idea behind the LR-method is to use the *a priori* knowledge that the distribution $\mathbf{f}$ has to be smooth (since it represents an average quantity), and seek the solution that minimises the least squares estimator subject to certain condition expressed by a functional of the form [PRE92]:

$$min : \chi^2[\mathbf{f}] + \lambda|\mathbf{B} \cdot \mathbf{f}|^2 \tag{3.17}$$

λ is the Lagrange multiplier and the $(m-o) \times m$ matrix $\mathbf{B}$ take different forms for different orders o:

$$\begin{array}{lllllll}
(3.18) & o = 0 & : & B_{ii} = 1, & & & \\
(3.19) & o = 1 & : & B_{ii} = -1, & B_{ii+1} = 1 & & \\
(3.20) & o = 2 & : & B_{ii} = -1, & B_{ii+1} = 2, & B_{ii+2} = -1 & \\
(3.21) & o = 3 & : & B_{ii} = -1, & B_{ii+1} = 3, & B_{ii+2} = -3, & B_{ii+3} = 1 \\
 & \ldots & & & & &
\end{array}$$

the remining matrix elements being null. The minimisation of Eq. (3.17) is equivalent to solving $\nabla_f(\chi^2[\mathbf{f}] + \lambda|\mathbf{B} \cdot \mathbf{f}|^2) = \mathbf{0}$ which leads to a set of linear equations whose solution is given by:

$$\mathbf{f} = (\mathbf{R}^{\mathrm{T}} \cdot \mathbf{V}_d^{-1} \cdot \mathbf{R} + \lambda \mathbf{B}^{\mathrm{T}} \cdot \mathbf{B})^{-1} \mathbf{R}^{\mathrm{T}} \cdot \mathbf{V}_d^{-1} \cdot \mathbf{d} \tag{3.22}$$

The regularising functional of Eq. (3.17) imposes the condition that the solution has minimum norm (zeroth order), or is constant (first order), linear (second order), quadratic (third order), etc. Of course, the actual solution does not need to be of such types, and the Lagrange multiplier λ serves to balance this condition against the requirement that the solution reproduces the data. The key points of the LR-method are that the term $\lambda \mathbf{B}^{\mathrm{T}} \cdot \mathbf{B}$ removes the singularities (regularises) from Eq. (3.22) and that the algorithm is equivalent to solving a set of linear equations by any of the available techniques. We have chosen the *LU* decomposition which can be found in [PRE92].

We are left nevertheless with the need to specify the regularisation parameter λ. Up to now, there is not a clear criterion on how to choose it (see [HAN93] [DES95] for an overview on different criteria). A particularly simple criterion is to choose a λ value such that the least squares estimator χ^2 equals the number of data points n, implicitly assuming that the data are normally distributed. Another criterion seeks the exact equilibrium between the adjustment to the data and regularisation given by the λ value corresponding to the corner of the so called "L" shaped curve (L-curve), which can be obtained by plotting $\log \chi^2[\mathbf{f}]$ versus $\log|\mathbf{B} \cdot \mathbf{f}|^2$ as a function of λ.

Since the solution $\mathbf{f}$ given by Eq. (3.22) depends linearly on the data $\mathbf{d}$, the propagation of errors law provides a way to calculate exactly the covariance matrix $\mathbf{V}_f$ [FRO79], which has the form:

$$\mathbf{V}_f = (\mathbf{R}^{\mathrm{T}} \cdot \mathbf{V}_d^{-1} \cdot \mathbf{R} + \lambda \mathbf{B}^{\mathrm{T}} \cdot \mathbf{B})^{-1} \cdot \mathbf{R}^{\mathrm{T}} \cdot \mathbf{V}_d^{-1} \cdot \mathbf{R} \cdot (\mathbf{R}^{\mathrm{T}} \cdot \mathbf{V}_d^{-1} \cdot \mathbf{R} + \lambda \mathbf{B}^{\mathrm{T}} \cdot \mathbf{B})^{-1} \tag{3.23}$$

As we can observe, the magnitude of uncertainties and correlations of the extracted parameters **f** depends on the value of the regularisation parameter λ. We would like to remark that the result we obtain in Eq. (3.23) does not coincide with the one given in Ref. [DOU95].

One last cautionary word on the regularisation method: the algorithm of Eq. (3.22) does not prevent the components of the solution **f** from having negative values. In cases such as the present one, where the solution cannot be negative, it may lead then to unphysical results. Of course, this new *a priori* knowledge could be added to Eq. (3.17), but then the solution does not take the simple form Eq. (3.22). We have preferred to keep the simple form and investigate the actual effects on the solution.

3.3.2 Maximum Entropy (ME) Method

The ME-method is based on the Maximum Entropy Principle of statistical inference [JAY57]. It states that the optimal solution for an inverse problem, optimal in the sense of less biased by our ignorance, corresponds to the one which maximises the information theoretic entropy $S[\mathbf{f}]$ of Shannon [SHA48] and is consistent with other constraints. In particular, if the constraint is to reproduce the data in the least squares sense, the principle can be formulated:

$$max : S[\mathbf{f}] - \mu\chi^2[\mathbf{f}] \tag{3.24}$$

where μ is a Lagrange multiplier. The entropy $S[\mathbf{f}]$ represents our *a priori* knowledge of the solution. The fundamental character of the method is often stressed and it has been shown [SHO80] [TIK84] that it can be derived from simple consistency conditions. Alternatively [TIT85], the method can be viewed as another type of regularisation method, by recognising that Eq. (3.24) can be rewritten as

$$min : \chi^2[\mathbf{f}] - \lambda S[\mathbf{f}] \tag{3.25}$$

with the entropy acting as regularisation functional. Several forms of the entropy $S[\mathbf{f}]$ have been proposed and used. We have chosen the form

$$S[\mathbf{f}] = -\sum_{i=1}^{n}(f_i \ln\frac{f_i}{h_i} - f_i + h_i) \tag{3.26}$$

where **h** represents an initial reference. The minimisation of (3.25) is equivalent to: $\nabla_f(\chi^2[\mathbf{f}] - \lambda S[\mathbf{f}]) = \mathbf{0}$, but now, in contrast to the LR-method, the non linear character of the entropy functional forces us to perform the minimisation numerically. Efficient algorithms have been developed for this specific case [SKI84]. In this work we have preferred to use as a simple iterative algorithm the one used in Ref. [COL82]. The minimisation leads to the set of equations (for uncorrelated data):

$$\sum_{i=1}^{n}\frac{2}{\sigma_i^2}R_{ij}(d_i - \sum_{k=1}^{m}R_{ik}f_k) = \lambda\ln\frac{f_j}{h_j}, \quad j = 1,\ldots,m \tag{3.27}$$

whose form suggests an iterative solution where at each step $s+1$, h_j is taken as the previous result and the right hand side is also evaluated at the previous step:

$$f_j^{(s+1)} = f_j^{(s)} \exp\left(\frac{2}{\lambda}\sum_{i=1}^{n} R_{ij}(d_i - \sum_{k=1}^{m} R_{ik} f_k^{(s)})/\sigma_i^2\right), \quad j = 1, \ldots, m \tag{3.28}$$

The form of the algorithm Eq. (3.28) shows two of the most important properties of the ME-method: the results will be positive or zero if this is our initial expectation. As for the LR-method, there is no clear prescription as to what the correct parameter λ should be. Besides, as in any iterative method of solution, one would have to worry about the influence on the final solution of the initial guess $\mathbf{h}$ and the number of iterations (stopping criteria).

Once the algorithm has converged to a certain solution, the uncertainties can be evaluated from Eq. (3.28) by applying the law of propagation of errors. The expression for the covariance matrix is:

$$\sigma_{f_i f_j} = \frac{4}{\lambda^2} f_i f_j \sum_{l=1}^{n} \frac{R_{li} R_{lj}}{\sigma_{d_i}^2} \tag{3.29}$$

Notice that due to the non-linearity of Eq. (3.28), the covariance matrix in Eq. (3.29) is only a first order approximation.

3.3.3 Expectation-Maximisation (EM) Method

The EM-algorithm is a general method for maximum likelihood estimation of parameters from incomplete data [DEM77]. The method is in essence iterative and receives the name from the two steps required for its application: 1) compute the conditional *expectation* of the log-likelihood, 2) perform the *maximisation* of the expectation. The method was applied to the problem of image reconstruction in emission and transmission tomography, by explicitly assuming that the data follow the Poisson statistics [SHE82][LAN84]. The algorithm obtained in this way could also be applied to our particular TAGS inverse problem. Interestingly, the same algorithm is obtained in Ref. [DAG95] by using Bayes theorem. The Bayes theorem relates the causes (parameters $\mathbf{f}$) with its effects (data $\mathbf{d}$) and can be summarised, using a notation close to our problem, in the formula:

$$P(f_j|d_i) = \frac{P(d_i|f_j)P(f_j)}{\sum_{j=1}^{m} P(d_i|f_j)P(f_j)} \tag{3.30}$$

Here $P(f_j)$ ($\equiv f_j/\sum_{j=1}^{m} f_j$) represents the *a priori* probability on the feedings f_j. $P(d_i|f_j)$ represents the conditional probability that the datum d_i is produced by the cause f_j, which is by definition equivalent to R_{ij}. Finally, $P(f_j|d_i)$ is the *a posteriori* conditional probability that the parameter f_j was cause of the datum d_i. The denominator on the right hand side of Eq. (3.30) ensures the proper normalisation and presumes that the causes (feedings) are independent. The Bayes formula gives a way to improve our initial estimation of the parameters based on the measurements, which can be exploited by recognising that the expected value of the feeding f_j can be related to the expected values of the data $\hat{\mathbf{d}}$ through

$$f_j = \frac{1}{\sum_{i=1}^{n} R_{ij}} \sum_{i=1}^{n} P(f_j|d_i)\hat{d}_i, \quad j = 1, \dots, m \tag{3.31}$$

where $\sum_{i=1}^{n} R_{ij}$ represents the efficiency for detecting a decay to level j. Taking for the expected value $\hat{\mathbf{d}}$ the measured value $\mathbf{d}$ and inserting Eq. (3.30) into Eq. (3.31), we arrive at the iterative algorithm:

$$f_j^{(s+1)} = \frac{1}{\sum_{i=1}^{n} R_{ij}} \sum_{i=1}^{n} \frac{R_{ij} f_j^{(s)} d_i}{\sum_{k=1}^{m} R_{ik} f_k^{(s)}}, \quad j = 1, \dots, m \tag{3.32}$$

The EM algorithm shares with the ME algorithm the property of positiveness of the solution, and has the advantage of not involving any regularisation parameter. Since the relation of the feedings with the data represented by Eq. (3.32) is linear, $\mathbf{f}^{(s+1)} = \mathbf{M}^{(s)} \cdot \mathbf{d}$, it is possible to estimate the uncertainties and correlations of the parameters by applying the law of propagation of errors at the point where convergence is obtained:

$$\mathbf{V}_f = \mathbf{M} \cdot \mathbf{V}_d \cdot \mathbf{M}^{\mathrm{T}} \tag{3.33}$$

As can be observed, no explicit assumption about the statistics applicable to the data has been invoked in obtaining the algorithm.

Chapter 4

The Data Analysis and Results

4.1 Introduction

In this chapter, the data and results obtained, are presented. As mentioned in section 3.2, every event recorded on tape consists of a set of 34 parameters. A sorting program, written in PL1 language, was used to histogram the pulse-height data from the events on tape. In this way, the two components of the EC/β^+-decay were extracted by requiring coincidences between a small Ge X-ray detector or a ΔE Si detector and the NaI(Tl) (TAS). However, as explained in sections 4.3 and 4.4, such raw spectra had to be processed in order to get the right spectra for analysis. The feeding distributions and β-strengths of the decays studied are presented in sections 4.6 and 4.7 together with a careful discussion.

4.2 The procedure to extract the data

All the list-mode energy signals were sampled by 4K ADCs. However, it was rapidly found that the CPU time required by the analysis programs when energy spectra of such a bin size were employed, exceeded by far the computing power of the fully dedicated ALPHA Au workstation with 128MB RAM and a 433 MHz DEC-ALPHA processor. Thus, the size of the TAS-spectra had to be compressed by a factor of ≈8 in order to make the analysis feasible. As an example, it is worth mentioning that the construction of the response matrix when spectra of 400 channels are used, requires ≈ 40 min, while only ≈ 3.5 min are needed when the size is only 200 channels.

Both simulated and experimental responses need to have the same calibrations for the analysis. The spectra, with an energy calibration given by Eq. (4.1)

$$E_{exp}(c) = \begin{cases} -97.508 + 5.111\,c + 1.522 \cdot 10^{-3}\,c^2\,(keV) & c < 160.885 \\ -147.893 + 5.670\,c\,(keV) & c > 160.88 \end{cases} \tag{4.1}$$

were re-calibrated to the simulated responses used in the analysis with a calibration given by Eq. (4.2)

$$E_{sim}(c) = \begin{cases} -14.315 + 36.731\,c + 3.441 \cdot 10^{-2}\,c^2\,(keV) & c < 23.902 \\ -33.627 + 38.345\,c + 7.345 \cdot 10^{-4}\,c^2\,(keV) & c > 23.902 \end{cases} \tag{4.2}$$

At this point, one must discuss the statistical distribution used to estimate the uncertainties of the TAS-spectra. The distribution applied in most of the situations in spectroscopy, and in other fields, is the Poisson one. This happens even for several doubtful cases where the conditions for the applicability of the Poisson distribution are no longer fulfilled. For the situation presented here, the requirement that the decay probability αdt for an infinitesimal time interval remains constant, where α is the counting rate, is no longer true. The measuring time of the different sources studied in this work extended to several half lives, which means that a major part of the possible decays were registered. Since the detector used has a detection efficiency of ≈ 1, the total number of counts N of a condition-free TAS spectrum can be considered as the total number of decays, and the uncertainty associated with it smaller than the one expected from a Poisson distribution. This argument is however not valid for the TAS coincidence spectra, since the limited efficiency of the ancillary detectors used to require the coincidence introduces additional statistical fluctuations. Thus, the criterion adopted in this work is to consider that the contents of the TAS spectra (coincident or not) follow the Poisson distribution. However, the influence of considering a multinomial behaviour of the experimental spectra was also checked for comparison. The conclusion after doing so was that slightly smaller (in few percent) uncertainties are obtained for the final results. It is worth mentioning that the multinomial behaviour introduces correlations between the data. The expressions for the calculation of the uncertainties in the strength given in appendix A, explicitly consider this feature. In the case of Poisson statistics, all off-diagonal elements of the covariance matrices corresponding to the data are null. Nevertheless, the notation we decided to follow in the text is the most general one and refers explicitly to covariance matrices and not only to its diagonal elements.

The raw EC and β^+-spectra needed to be corrected for contamination. The procedure is presented in Eq. (4.3). The spectrum free of contaminants S is obtained from the raw list-mode spectrum A by subtracting the pure contaminants B and C with the proper normalisations λ_B and λ_C. The covariance matrix $\sigma_{S_iS_j}$ of S is calculated in terms of the other covariances as given by Eq. (4.4), which is a direct result from the Gauss error propagation formula. The spectra and normalisations used for the different cases are described in detail in sections 4.3.1, 4.3.2, 4.4.1 and 4.4.2.

$$S_k = A_k - \lambda_B B_k - \lambda_C C_k \quad k = 1...n \tag{4.3}$$

$$\sigma_{S_iS_j} = \sigma_{A_iA_j} + \lambda_B^2 \sigma_{B_iB_j} + \lambda_C^2 \sigma_{C_iC_j} + B_iB_j\sigma_{\lambda_B} + B_iB_j\sigma_{\lambda_B} \tag{4.4}$$

The distortion of the spectra induced by the electronic pulse pileup must also be removed from the spectra. Otherwise, as explained in [CAN99b], the unphysical contribution of the pulse pileup to the deduced β-strength is dramatically enhanced. A very precise method based on the true pulse shape was especially developed for this application. Following the procedure described in [CAN99b], the distortion P introduced by electronic pulse pileup was calculated for each spectrum. Then, as expressed by Eq. (4.5), the distortion was subtracted from the contaminant free spectrum S. The normalisation λ_P of the distortion used in the subtraction was determined by a least squares fit within the region of the spectrum where only the pileup contribution is present, that is, above the Q_{EC}.

$$SP_k = S_k - \lambda_P P_k \quad k = 1...n \tag{4.5}$$

$$\sigma_{SP_iSP_j} = \sigma_{S_iS_j} + \sigma^2_{\lambda_P} P_i P_j \tag{4.6}$$

The covariances $\sigma_{SP_iSP_j}$ after the subtraction in Eq. (4.6), have been evaluated considering only the error σ_{λ_P} associated to the normalisation factor λ_P, assuming that the calculated distortion P is free of uncertainties. The results for the different cases can be found in sections 4.3.1, 4.3.2, 4.4.1 and 4.4.2.

4.3 The ^{150}Ho 2^- → ^{150}Dy data

The total time dedicated to the ^{150}Ho 2^- → ^{150}Dy measurement was 11.4 hours. During this time, a total number of $5.35 \cdot 10^7$ events were registered by the acquisition system.

4.3.1 EC spectra

The EC-component of the ^{150}Ho 2^- →^{150} Dy decay was measured by requiring a coincidence between the TAS and the characteristic X-rays of Dy. This very selective condition did not avoid a small amount of contamination coming from the ^{150}Er →^{150}Ho and ^{150}Dy→^{150}Tb decays due to the finite energy resolution of the X-ray detector and Compton events. Fig. [4.1] shows the region of interest of the energy spectrum recorded in the Ge X-ray detector during the measurement. The three $K_{\alpha1}$ $K_{\alpha2}$ doublets coming from the ^{150}Dy decay (Tb X-rays) on the left side, ^{150}Ho decay (Dy X-rays) in the centre, and ^{150}Er decay (Ho X-rays) on the right side, are clearly visible. In order to remove the contaminations, three different TAS-spectra were accumulated by requiring a coincidence with the Tb, Dy and Ho X-rays. The three pairs of vertical dashed lines in Fig. [4.1] limit the energy regions used to establish the coincidence. The number of counts registered in the Tb, Dy and Ho regions was, respectively, $2.10 \cdot 10^5$, $5.58 \cdot 10^5$ and $1.24 \cdot 10^5$, while the number of counts in the corresponding coincidence TAS-spectra was $2.02 \cdot 10^5$, $5.47 \cdot 10^5$ and $1.14 \cdot 10^5$.

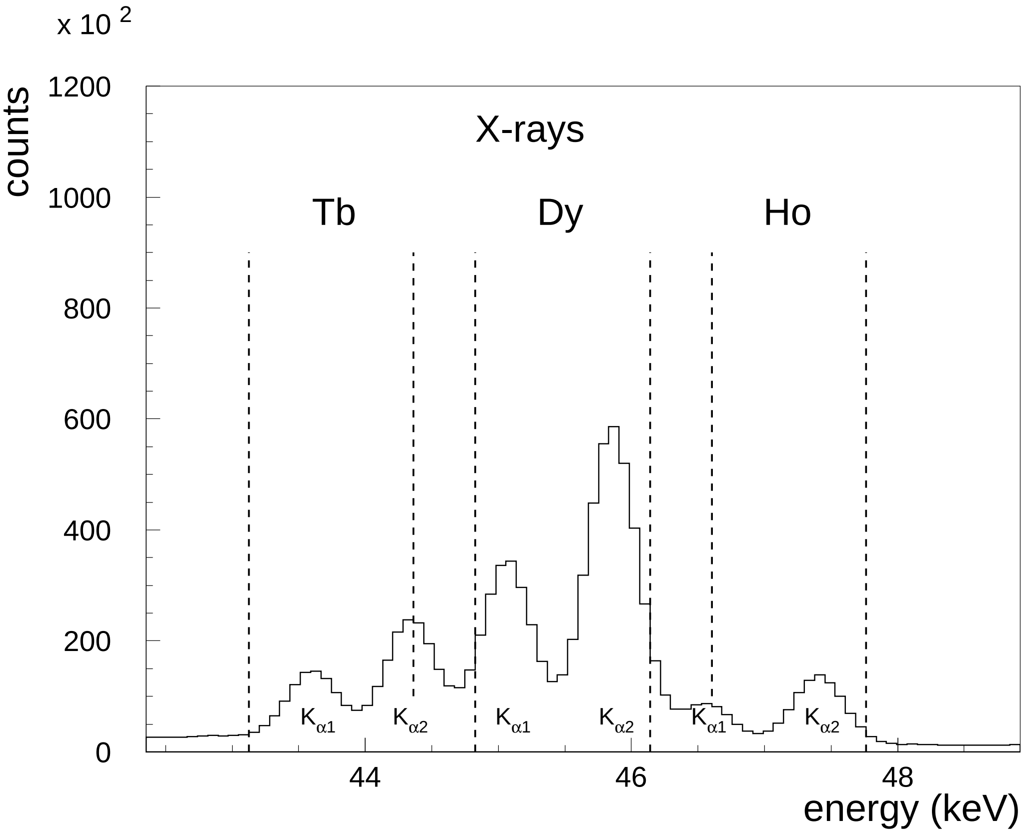

Figure 4.1: X-ray spectrum in the Ge detector recorded during the ^{150}Ho 2^- measurement. The well resolved Tb, Dy and Ho $K_{\alpha 1}$ $K_{\alpha 2}$ doublets were used to accumulate three TAS-spectra in coincidence. The regions in the Ge spectrum used to require the coincidence are limited by vertical dashed lines. The gates on the Tb and Ho X-rays were set more narrowly in order to have the cleanest possible spectra.

Fig. [4.2] shows the corresponding coincidence TAS-spectra. The raw ^{150}Ho 2^- EC-decay spectrum is plotted as a solid line. The dotted spectrum is the gate on the Ho X-rays, that is, a ^{150}Er EC-decay spectrum. Finally, the dashed-dotted spectrum is the gate on the Tb X-rays, which comes from the EC-decay of ^{150}Dy. The last two spectra are scaled by the factors indicated in the figure, which correspond to the magnitude of the contamination present in the main ^{150}Ho 2^- EC-decay spectrum. It can be seen in Fig. [4.2], that the contributions to the peak at 476 keV in the ^{150}Er EC-spectrum and the peak at 397 keV in the ^{150}Dy EC-spectrum are also present in the first 500 keV region of the raw ^{150}Ho 2^- EC decay spectrum. Also visible in Fig. [4.2] is that the contaminations are harmless above 500 keV, because the overall contribution is $\lesssim 1\%$. Both contaminations were subtracted from the ^{150}Ho 2^- EC decay spectrum as expressed by Eq. (4.7). The weights λ were determined from the ratio of areas between the 476 keV and 397 keV lines in the individual ^{150}Er and

^{150}Dy EC-decay spectra and in the ^{150}Ho 2^- EC-decay spectrum respectively. For this purpose the 4K spectra were used, since the peaks there were better resolved. They are given in Eq. (4.8) and Eq. (4.9).

$$EC = EC_{^{150}\mathrm{Ho}\,2^-} - \lambda_{^{150}\mathrm{Er}} EC_{^{150}\mathrm{Er}} - \lambda_{^{150}\mathrm{Dy}} EC_{^{150}\mathrm{Dy}} \tag{4.7}$$

$$\lambda_{^{150}\mathrm{Er}} = 0.067 \pm 0.003 \tag{4.8}$$

$$\lambda_{^{150}\mathrm{Dy}} = 0.025 \pm 0.001 \tag{4.9}$$

A further correction was needed in order to remove the distortion introduced by the electronic pulse pileup. Even if the counting rates were kept at a low value $\lesssim 5 \cdot 10^3$ counts/s, it can be seen in Fig. [4.3] that the distortion is still present in the contaminant-free spectrum, in particular above channel ≃192, which corresponds to the physical end of the spectrum imposed by the Q_{EC}. Fig. [4.3] shows also the pileup distortion, calculated by the procedure described in [CAN99b], overlapped to the experimental spectrum. The excellent agreement above channel ≃192 reflects the quality of the correction.

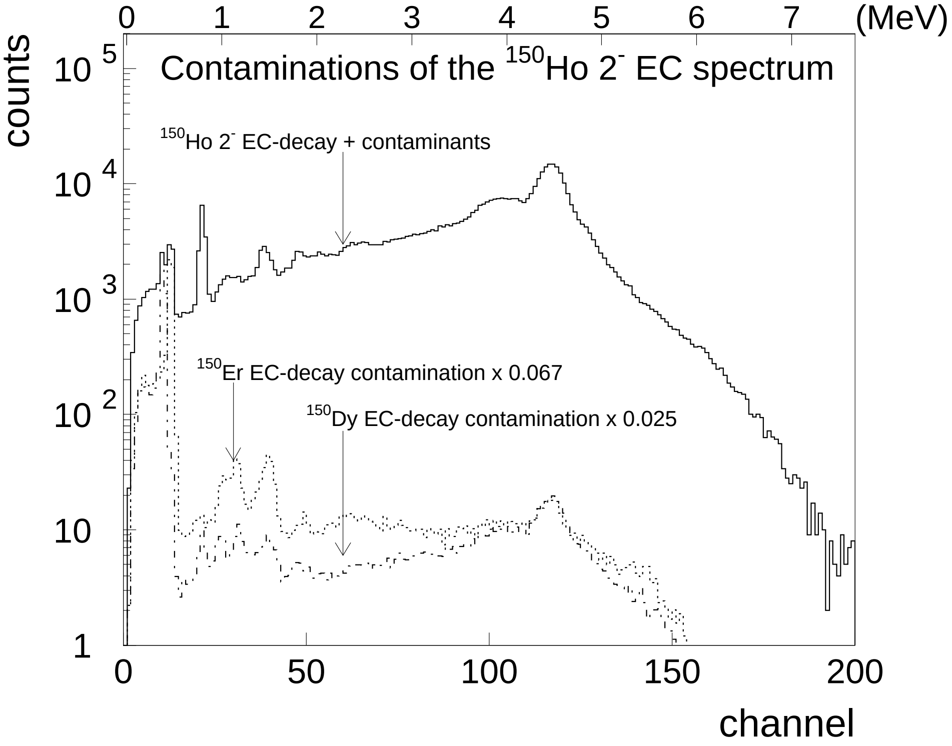

Figure 4.2: Different contaminations in the Dy X-ray gated spectrum (solid line) during the ^{150}Ho 2^- measurement. In order to get the clean EC-spectrum one has to subtract, the Ho X-ray gated spectrum (dotted) and the Tb X-ray gated spectrum (dashed-dotted) with the normalisations indicated in the figure.

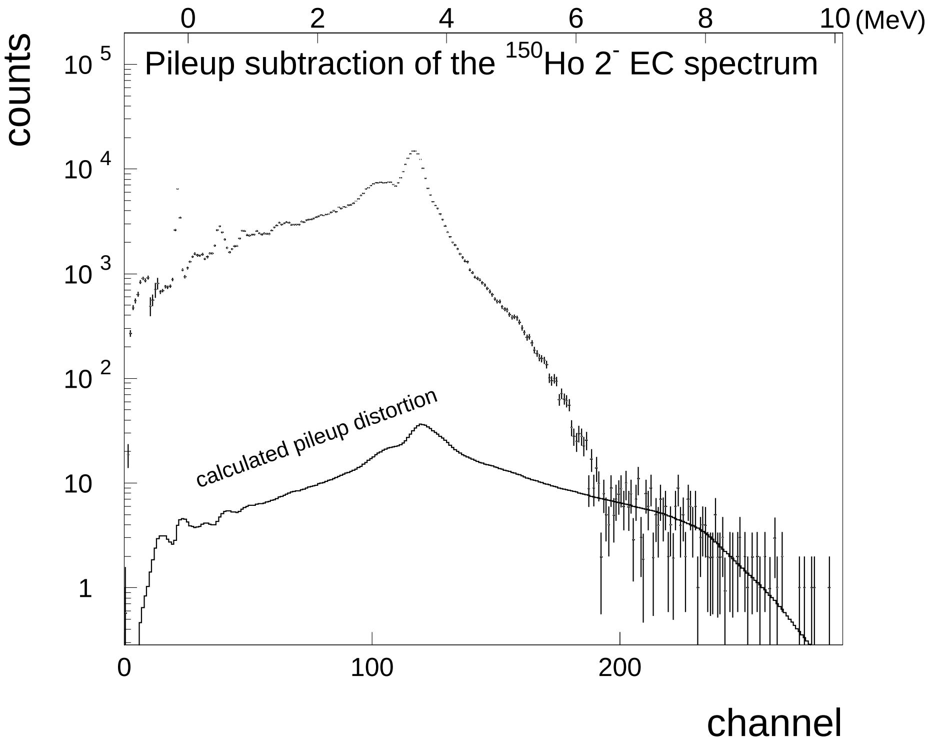

Figure 4.3: ^{150}Ho2$^-$ EC-decay spectrum free of contamination. The calculated pileup distortion is plotted as a solid line over the experimental points.

4.3.2 β^+ spectra

In comparison with the clean X-ray coincidence technique, the β-particle tagging is a much less selective procedure. Due to its continuous energy spectrum, the β-particles can not be used for an isobaric identification. Moreover, if their energy loss is too small, they even lie below the ancillary detector threshold and do not fire the acquisition system.

Fig. [4.4] shows the energy spectrum which was accumulated during the ^{150}Ho 2$^-$ measurement in the bottom Si detector. The main component of the spectrum visible as a continuum are the signals produced by the energy loss of positrons in the detector. The bump at $\simeq$380 keV corresponds to the mean energy loss of positrons in 1 mm of Si, which is a rather constant value for the different energies. Marked by vertical dashed lines are the lower and upper thresholds set by software during the off-line processing of the data. The lowest value was set as high as possible in order to avoid false triggers coming from conversion electrons and γs. A Monte Carlo simulation of the whole decay revealed that this contribution is smaller than 0.5%. The upper threshold corresponds to the last ADC channel. The spectrum in Fig. [4.4] also presents a peak at $\simeq$4.2 MeV corresponding to the ground state α-decay of ^{150}Dy.

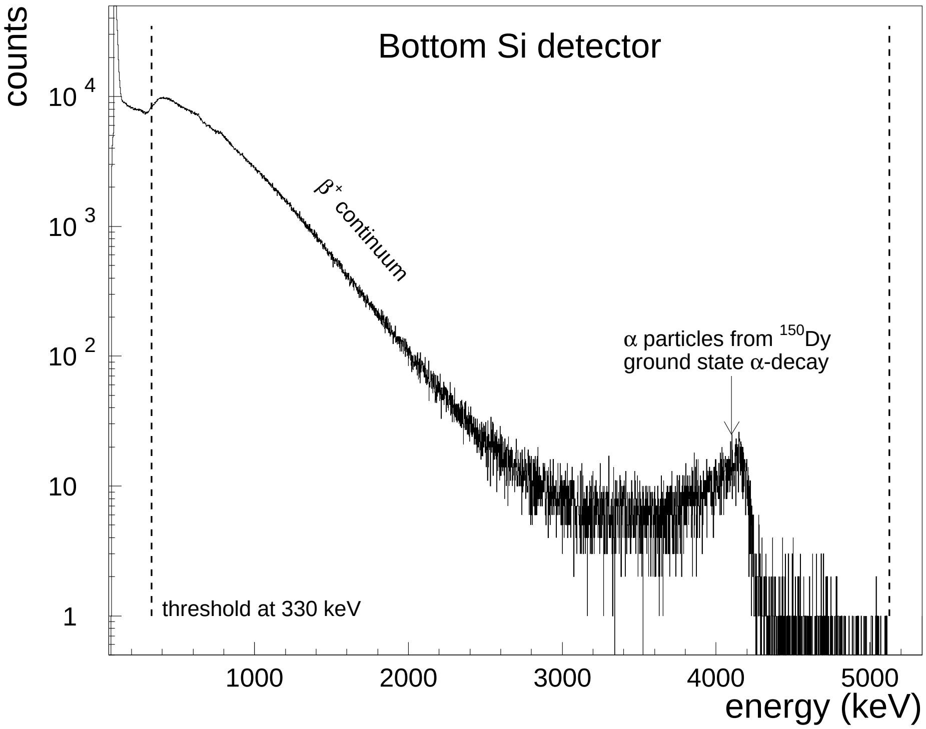

Figure 4.4: Bottom Si detector spectrum recorded during the ^{150}Ho 2^- measurement. The vertical dashed lines define the energy window used for the coincidence with the TAS. The lower value was set to avoid as much as possible the contribution from conversion electrons and Compton scattered γs. Also visible is the peak produced by the 4.2 MeV α-particles emitted in the ^{150}Dy ground state α-decay.

The original spectrum presented a small ^{150}Tm ($\langle Q_{EC}\rangle_{\text{isomers}}$=11.4 MeV [AUD97]) and a strong ^{150}Er (Q_{EC}=4.108(11) keV [AUD97]) contamination. Fortunately ^{150}Tm, with $T_{1/2} \approx 5$ s, and ^{150}Er, with $T_{1/2}$=18.5 s, have significantly smaller half lives than ^{150}Ho 2^-, with $T_{1/2}$=72(4) s. This allowed its suppression by using only the statistics acquired during the last 30 s of a total measurement interval per source of 120 s. The spectrum stored during this reduced time registered $5.49 \cdot 10^4$ counts and can be seen in Fig. [4.5], together with the calculated pileup distortion used for the pileup correction. The corresponding corrected spectrum is the one that was used for the β^+ component analysis.

4.4 The ^{150}Ho $9^+ \rightarrow^{150}$ Dy data

The total time dedicated to the ^{150}Ho $9^+ \rightarrow^{150}$ Dy measurement was 15.1 hours. During this time, a total number of $5.85 \cdot 10^7$ events was registered by the acquisition system.

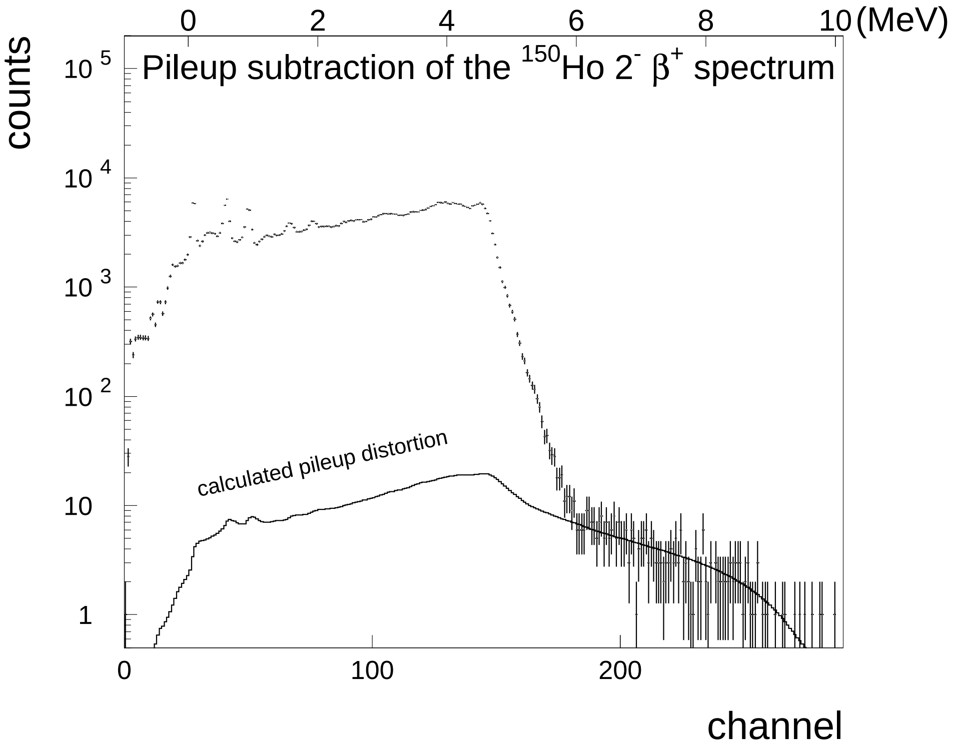

Figure 4.5: ^{150}Ho 2^- β^+-decay spectrum. The calculated pileup distortion is plotted as a solid line over the experimental points.

4.4.1 EC spectra

As in the case of the low spin isomer, three different TAS-spectra were recorded in coincidence with X-rays. Fig. [4.6] shows the region of interest of the energy spectrum recorded in the Ge X-ray detector during the ^{150}Ho $9^+ \rightarrow ^{150}$Dy measurement. The three $K_{\alpha 1}$ $K_{\alpha 2}$ doublets of Tb, left side, Dy, centre, and Ho, right side, are visible. The three pairs of vertical dashed lines in Fig. [4.6] limit the energy regions used to establish the coincidence. The number of counts registered in the Tb, Dy and Ho regions was, respectively, $1.84 \cdot 10^5$, $8.66 \cdot 10^5$ and $4.89 \cdot 10^5$, while the number of counts in the corresponding coincidence TAS-spectra was $1.78 \cdot 10^5$, $8.54 \cdot 10^5$ and $4.48 \cdot 10^5$. The main difference with respect to the low spin isomer is that ^{150}Ho 9^+ could not be produced in a clean way. The reaction did also populate ^{150}Er, which as we have seen previously, decays into ^{150}Ho 2^-. Thus, the high and low spin isomer decays were both present at the same time in a fraction as expressed by Eq. (4.10).

$$\frac{N_{^{150}\text{Ho}\,9^+}}{N_{^{150}\text{Ho}\,2^-}} \simeq \frac{1}{2} \tag{4.10}$$

A subtraction of the low spin isomer contribution is demanded in order to get a pure ^{150}Ho 9^+ EC-decay spectrum. This could be done because a pure ^{150}Ho 2^- EC-

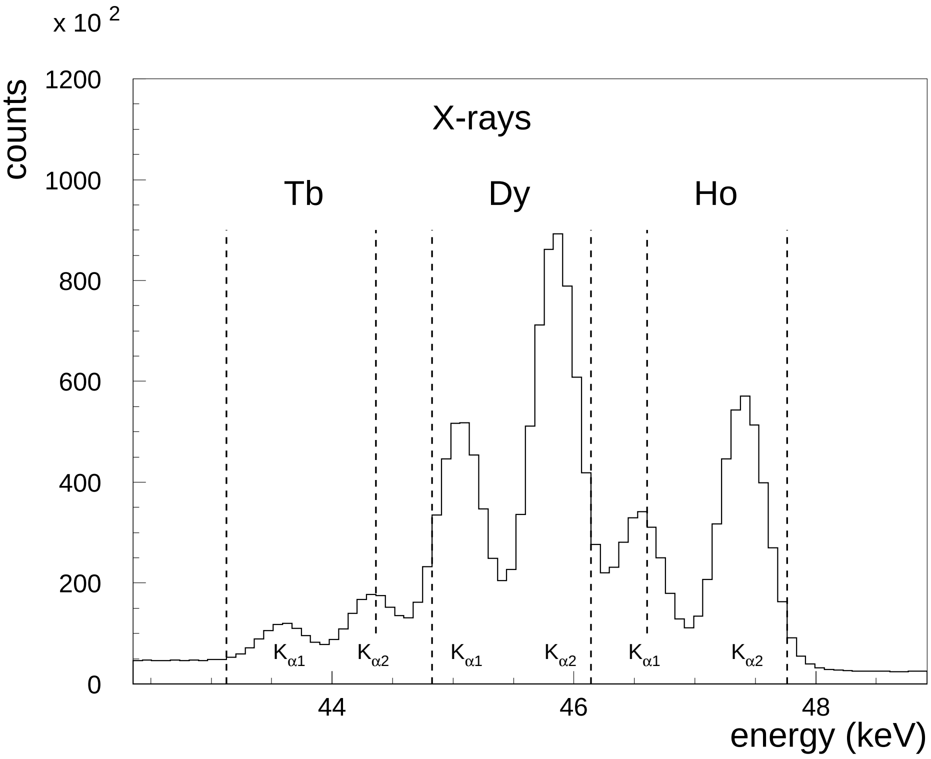

Figure 4.6: X-ray spectrum in the Ge detector recorded during the ^{150}Ho 9^+ measurement. The well resolved Tb, Dy and Ho K$_{\alpha1}$ K$_{\alpha2}$ doublets were used to accumulate three TAS-spectra in coincidence. The regions of the Ge energy spectrum used for the gates lie between vertical dashed lines. The gates on the Tb and Ho X-rays were set for the removal of contamination.

decay spectrum was obtained during the independent low spin measurement. The problem was to determine which amount of it is present in the composite spectrum. In a general case this could not have been done very precisely, but fortunately, due to the particular decay scheme, it was possible here. The normalisation method resides in the spin difference of both isomers. The low spin isomer populates 1^-, 2^- and 3^- states in ^{150}Dy. The 1^-, 2^- de-excite to the 0^+ ground state directly or through very few or one intermediate levels. The 3^- de-excitation path states must at least include one level. In any case, the multiplicity of the cascades is expected to be between 1 and 2, which is a low value. On the other hand, the high spin isomer populates 8^+, 9^+ and 10^+ states in ^{150}Dy. The de-excitation path to the ground state must include a larger number of γ-transitions, which amount to an average multiplicity between 4 and 5. In both high and low spin decays, most of the fragmented intensity is collected into the strong first $2^+ \to 0^+$ transition, which connects the first excited state at 803 keV with the ground state. Moreover, the 2^+ is poorly fed due to selection rules, especially in the high spin decay. Thus, the γ-cascades ending at the 2^+ state have a small multiplicity (1-2) in the low spin

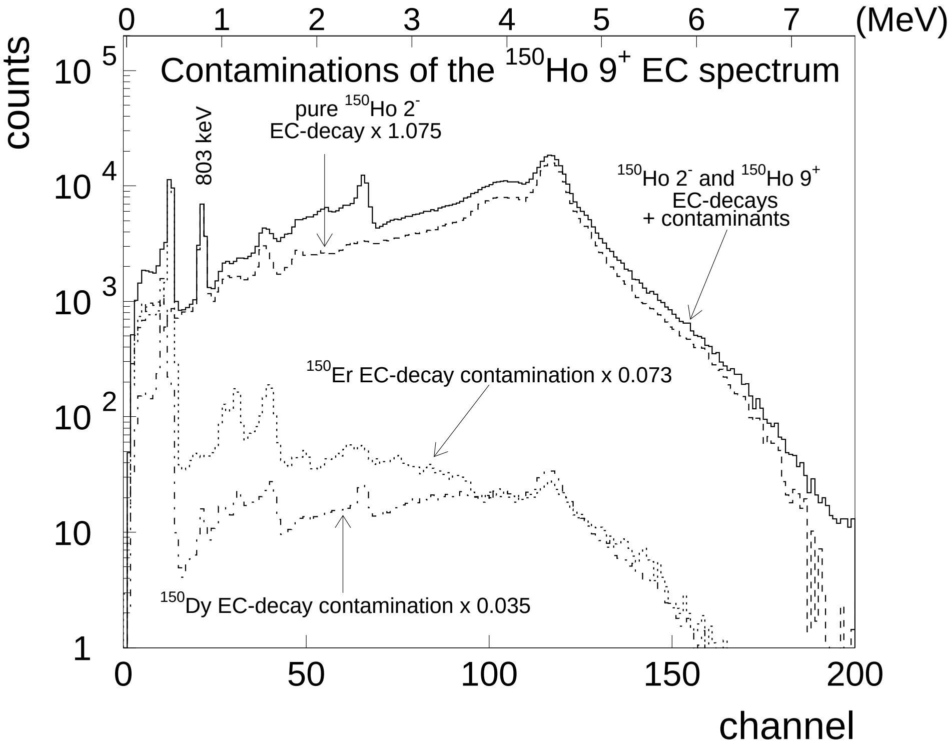

Figure 4.7: Different contaminations in the Dy X-ray gated spectrum, solid line, during the ^{150}Ho 9^+ measurement. In order to get the clean ^{150}Ho 9^+ decay spectrum one has to subtract, with the normalisations indicated in the figure, the pure Ho 2^- dashed spectrum, the dotted Ho X-ray gated spectrum and the dashed-dotted Tb X-ray gated spectrum.

decay and a large multiplicity in the high spin decay (4-5), which brings us to the point that the peak observed at 803 keV in the TAS-spectrum must belong only to the low spin component. In fact, the probability of observing this escape peak is negligible small in the high spin decay due to the large efficiency of the spectrometer. An observation of the 803 keV line in the high spin isomer decay spectrum would mean that three-four γs completely escaped and the 803 keV γ was detected. As an example, Eq. (4.11) shows the probability P of this to happen for the dominant $8^+(2401) \rightarrow 6^+(1801) \rightarrow 4^+(1457) \rightarrow 2^+(803) \rightarrow 0^+$ cascade.

$$P = \epsilon_{ph}(803)[1 - \epsilon_{tot}(551)][1 - \epsilon_{tot}(393)][1 - \epsilon_{tot}(653)] \simeq 5.4 \cdot 10^{-6} \tag{4.11}$$

where $\epsilon_{ph}(E_\gamma)$ and $\epsilon_{tot}(E_\gamma)$ are respectively the photopeak and total efficiencies for a given γ energy and $[1 - \epsilon_{tot}(E_\gamma)]$ the escape probability.

This permits us to establish a normalisation using the areas of the 803 keV line present in both ^{150}Ho 9^+ $+^{150}$ Ho 2^- and pure ^{150}Ho 2^- spectra. The other contaminants from the ^{150}Er and ^{150}Dy decays were subtracted using the normalisations given by the ratios of areas of the 476 keV and 397 keV lines, respectively. The subtraction and weights of all the terms are given by Eq. (4.12), Eq. (4.13), Eq. (4.14) and Eq. (4.15).

$$EC = EC_{^{150}\mathrm{Ho}\,2^-,9^+} - \lambda_{^{150}\mathrm{Er}} EC_{^{150}\mathrm{Er}} - \lambda_{^{150}\mathrm{Dy}} EC_{^{150}\mathrm{Dy}} - \lambda_{^{150}\mathrm{Ho}\,2^-} EC_{^{150}\mathrm{Ho}\,2^-} \quad (4.12)$$

$$\lambda_{^{150}\mathrm{Er}} = 0.073 \pm 0.002 \quad (4.13)$$

$$\lambda_{^{150}\mathrm{Dy}} = 0.035 \pm 0.003 \quad (4.14)$$

$$\lambda_{^{150}\mathrm{Ho}\,2^-} = 1.075 \pm 0.02 \quad (4.15)$$

The different X-ray gated experimental spectra measured can be seen in Fig. [4.7]. The solid line in the plot is the combined ^{150}Ho $9^+ +^{150}$ Ho 2^- EC decay spectrum (Dy X-ray gate). Just below, we see the pure ^{150}Ho 2^- with the proper normalisation (dashed). The dotted spectrum corresponds to the normalised ^{150}Er EC-decay spectrum (Ho X-ray gate) and the dashed-dotted is the normalised ^{150}Dy EC-decay spectrum (Tb X-ray gate).

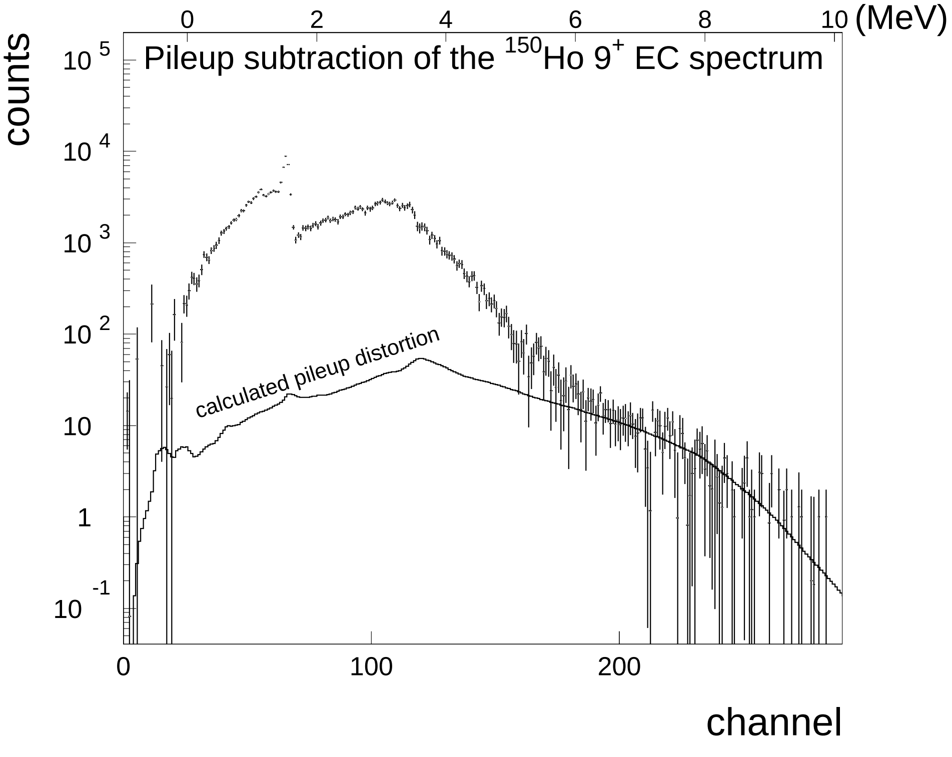

Figure 4.8: ^{150}Ho 9^+ EC-spectrum. The calculated pileup distortion is plotted as a solid line over the experimental points.

The correction for the pileup distortion was done in the same way as for the low spin isomer. Fig. [4.8] shows the contaminant free EC-spectrum and the calculated pileup distortion (solid).

4.4.2 β^+ spectra

The number of counts in the TAS-spectrum in coincidence with the bottom Si detector was $1.03{\cdot}10^7$. However, considering only the last 20 s of a cycle of 40 s/source, this number is reduced to $4.36{\cdot}10^6$.

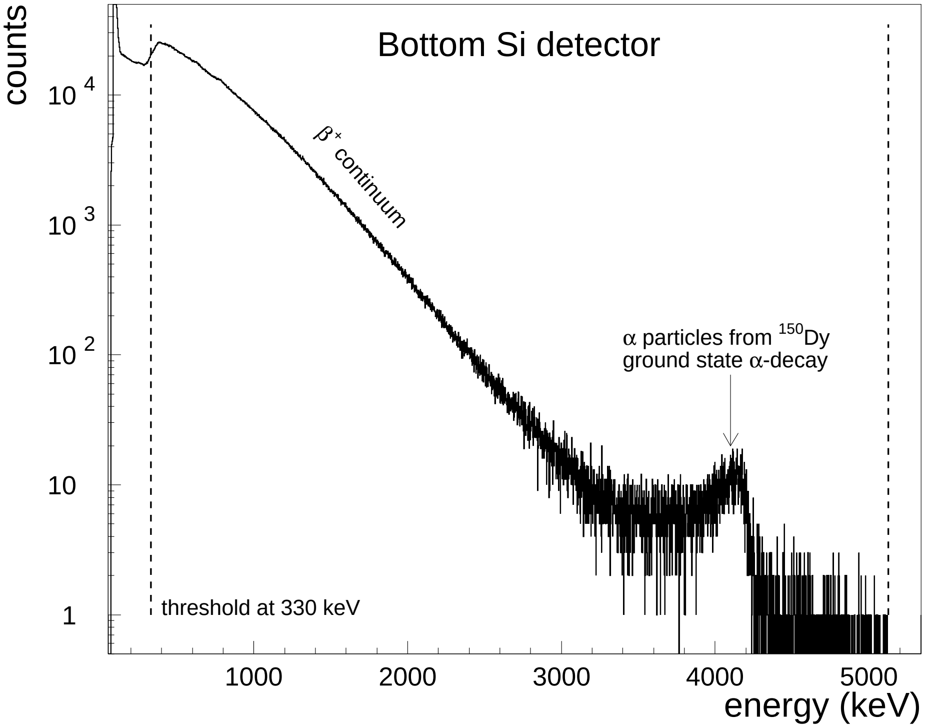

Figure 4.9: Bottom Si detector spectrum recorded during the ^{150}Ho 9^+ measurement.The vertical dashed lines define the energy window used for the coincidence with the TAS. The lower value was set to avoid as much as possible the contribution from conversion electrons and Compton-scattered γs. Also visible is the peak produced by the 4.2 MeV α-particles emitted in the ^{150}Dy ground state α-decay.

The problem of contamination becomes even more acute in the case of the ^{150}Ho 9^+ β^+-spectra. As already mentioned, the β-particle tagging technique does not provide clean spectra, and this is of crucial importance when a subtraction procedure is demanded. Fig. [4.9] shows the energy spectrum registered in the bottom Si detector during the ^{150}Ho 9^+ β^+ measurement. As for the one in Fig. [4.4], it presents a continuum produced by the energy loss of the positrons in 1 mm of silicon. The energy window used for the coincidence with TAS is marked by the dashed vertical lines, with a lower threshold of 330 keV. Also visible is the peak produced by the 4.2 MeV α-particles coming from the ^{150}Dy ground state α-decay. The TAS-spectrum in coincidence with the bottom Si detector is plotted as a solid line in Fig. [4.10]. Besides the ^{150}Ho 2^- produced at the same time, the β^+ spectra had strong ^{150}Tm

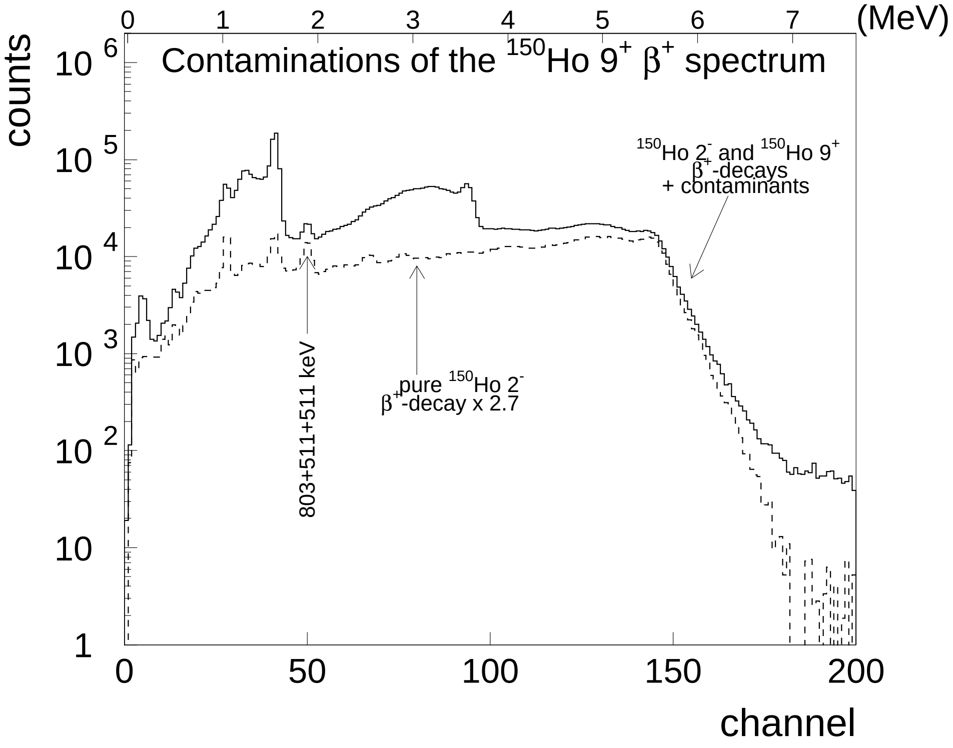

Figure 4.10: Solid: TAS spectrum registered in coincidence with the bottom Si-detector during the ^{150}Ho 9^+ measurement. Dashed: TAS spectrum in coincidence with the bottom Si-detector used for the ^{150}Ho 2^- contamination of the previous one.

and ^{150}Er contaminations. ^{150}Tm, with $T_{1/2} \approx 5$ s, was easily removed by half-life discrimination rejecting the first 20 s of the 40 s measurement interval per source. Unfortunately, this did not reduce significantly the contamination of ^{150}Er, since its half life $T_{1/2}$=18.5 s is very similar to the $T_{1/2}$=24 s of ^{150}Ho 9^+. The ^{150}Ho 2^- contamination was removed by subtracting the β^+ spectrum obtained during the independent low spin isomer measurement. The procedure is expressed by Eq. (4.16).

$$\beta^+_{^{150}\mathrm{Ho}\;9^+} = \beta^+_{^{150}\mathrm{Ho}\;2^-,9^+} - \zeta_{^{150}\mathrm{Ho}\;2^-}\beta^+_{^{150}\mathrm{Ho}\;2^-} \tag{4.16}$$

$$\zeta_{^{150}\mathrm{Ho}\;2^-} = 2.7 \pm 0.2 \tag{4.17}$$

The normalisation factor given in Eq. (4.17) was determined by the ratio of areas of the 803 + 511 + 511 keV peak present in both spectra. This turned out to be less precise than for the EC case due to the difficulty in fitting properly the very small peak. It can be seen in Fig. [4.10] that the peak sits in a kind of valley. This introduces a large systematic error in Eq. (4.17). Additionally, the ^{150}Ho 2^- β^+-spectrum used for the subtraction was not pure but contaminated, since as mentioned before, the ^{150}Er could not be reduced by half-life discrimination. All these problems add up and bring us to the point that the analysis of the β^+ component of the ^{150}Ho 9^+ decay has to be questioned.

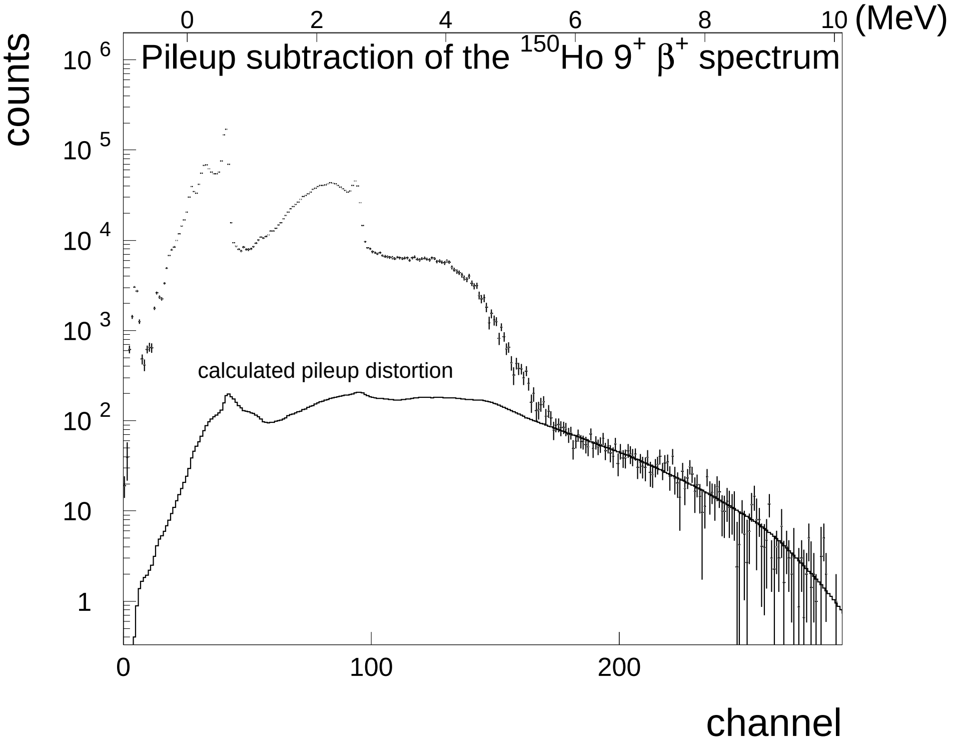

Figure 4.11: ^{150}Ho 9^+ β^+ spectrum. The calculated pileup distortion is plotted as a solid line over the experimental points.

To conclude, the proper pileup correction was done as for the rest of the previously presented spectra. Fig. [4.11] shows the final ^{150}Ho 9^+ β^+ spectrum, and on top of it, the calculated pileup distortion (solid).

4.5 Strength and $\log ft$ calculation

The analysis methods provide the EC and β^+-feeding distributions and their uncertainties. They can be used independently or together in order to obtain the β-strength. Considering the discrete nature of the data, the β-strength distribution for a given energy bin i can be obtained from Eq. (4.18)

$$S_{\beta_i} = \frac{1}{\Delta E} \frac{I_{\beta_i}}{f(\mathrm{Q_{EC}} - E_i)\, T_{1/2}} \tag{4.18}$$

where ΔE is the energy bin width (40 keV in this work) f represents the Fermi integral, E_i the energy of the i-th bin, $T_{1/2}$ stands for the half life of the decay and

I_{β_i} is obtained using Eq. (4.19) from the EC and β^+ feeding distributions EC_i and β_i^+ and its respective weights a and b:

$$I_{\beta_i} = \frac{aEC_i + b\beta_i^+}{\sum_{bins} aEC_i + b\beta_i^+} \tag{4.19}$$

The use of the Gauss error propagation formula provides the uncertainty of the strength as shown in Eq. (4.20), in terms of the uncertainties of the variables involved in Eq. (4.18):

$$\sigma_{S_{\beta_i}}^2 = \left(\frac{\partial S_{\beta_i}}{\partial I_{\beta_i}}\right)^2 \sigma_{I_{\beta_i}}^2 + \left(\frac{\partial S_{\beta_i}}{\partial T_{1/2}}\right)^2 \sigma_{T_{1/2}}^2 + \left(\frac{\partial S_{\beta_i}}{\partial f_i}\right)^2 \sigma_{f_i}^2 \tag{4.20}$$

The explicit form of the coefficients in Eq. (4.20) can be found in appendix A. The integral value of the strength can be expressed in terms of the total $\log ft$

$$\log ft = \log_{10}\left(\frac{1}{\sum_i S_{\beta_i}\Delta E}\right) = \log_{10}\left(\frac{1}{\sum_i \frac{I_{\beta_i}}{f_i T_{1/2}}}\right) \tag{4.21}$$

Further details on the $\log ft$ uncertainty calculation can be found in appendix A.

It is also possible to get the β-strength from only one of both EC or β^+ feeding distributions by using the $r = \mathrm{EC}/\beta^+$ relation tabulated in [GOV71]. The total intensity I_β can be expressed in terms of the EC intensity I_{EC} or the β^+ intensity $I_{\beta+}$ as indicated by Eq. (4.22) and Eq. (4.23), respectively.

$$I_{\beta_i} = \begin{cases} \left(1+\frac{1}{r_i}\right) I_{EC\,i} = \left(1+\frac{1}{r_i}\right)\frac{EC_i}{\sum_k^{\mathrm{Q_{EC}}} EC_k} & i\Delta E < \mathrm{Q_{EC}} - 1022 \\ I_{EC\,i} = \frac{EC_i}{\sum_k^{\mathrm{Q_{EC}}} EC_k} & i\Delta E > \mathrm{Q_{EC}} - 1022 \end{cases} \tag{4.22}$$

$$I_{\beta_i} = \begin{cases} (1+r_i) I_{\beta+} = (1+r_i)\frac{\beta_i^+}{\sum_k^{\mathrm{Q_{EC}}-1022} \beta_k^+} & i\Delta E < \mathrm{Q_{EC}} - 1022 \\ 0 & i\Delta E > \mathrm{Q_{EC}} - 1022 \end{cases} \tag{4.23}$$

r_i represents the interpolated value of the average EC/β^+ ratio for the i-th bin calculated in Eq. (4.24)

$$r_i = 10^{\widetilde{m}_i(\mathrm{Q_{EC}} - E) + \widetilde{b}_i} \tag{4.24}$$

where $\widetilde{m}_i$ and $\widetilde{b}_i$ are the coefficients from the linear regression for a given energy E. It is worth recalling that the EC feeding distribution is extended over the whole $\mathrm{Q_{EC}}$-window, while the β^+ feeding distribution ends at an energy of $\mathrm{Q_{EC}} - 2m_ec^2$. This means that no information on the β-strength in the last 1022 keV of the $\mathrm{Q_{EC}}$-window can be extracted if only the β^+ feeding distribution is available. The discrete

β-strength can be calculated in the two cases with the help of the Eq. (4.25) and Eq. (4.26)

$$S_{\beta_i} = \begin{cases} \frac{1}{\Delta E}\left(1+\frac{1}{r_i}\right)\frac{I_{EC\,i}}{f_i T_{1/2}} & i\Delta E < \mathrm{Q_{EC}} - 1022 \\ \frac{1}{\Delta E}\frac{I_{EC\,i}}{f_i T_{1/2}} & i\Delta E > \mathrm{Q_{EC}} - 1022 \end{cases} \tag{4.25}$$

$$S_{\beta_i} = \begin{cases} \frac{1}{\Delta E}(1+r_i)\frac{I_{\beta^+\,i}}{f_i T_{1/2}} & i\Delta E < \mathrm{Q_{EC}} - 1022 \\ 0 & i\Delta E > \mathrm{Q_{EC}} - 1022 \end{cases} \tag{4.26}$$

The application of the Gauss error formula arrives to the expression of Eq. (4.27), which is analogous to Eq. (4.20) but with one additional term coming from the interpolation of the tabulated EC/β^+ values.

$$\sigma^2_{S_{\beta_i}} = \left(\frac{\partial S_{\beta_i}}{\partial I_{\beta_i}}\right)^2 \sigma^2_{I_{\beta_i}} + \left(\frac{\partial S_{\beta_i}}{\partial T_{1/2}}\right)^2 \sigma^2_{T_{1/2}} + \left(\frac{\partial S_{\beta_i}}{\partial f_i}\right)^2 \sigma^2_{f_i} + \left(\frac{\partial S_{\beta_i}}{\partial r_i}\right)^2 \sigma^2_{r_i} \tag{4.27}$$

The integrated $\log ft$ can be procured analogously to the case were both feeding distributions are available. The complete details on this calculation as well as the uncertainty evaluation are described in appendix A.

4.6 The ^{150}Ho 2^- $\rightarrow$ ^{150}Dy results

Since this is the very first time that the analysis methods presented in section 3.3 have been applied to the TAGS inverse problem, we will not be concerned with the results obtained for the ^{150}Ho 2^- decay alone. We will also describe the proper usage of the analysis methods, illustrate their main features, including advantages and disadvantages, and demonstrate the consistency of the technique through a clear set of examples.

The starting point of the analysis is the spectra corresponding to the EC and β^+-components of the ^{150}Ho 2^- decay, free of contaminants and corrected from pileup distortions as described in subsection (4.3.1) and (4.3.2). Each one of the three analysis algorithms described in section 3.3 has been translated into a FORTRAN program. The objective of any of the three codes is the same: to calculate independently both EC and β^+-feeding distributions, starting from the corresponding spectra and the proper response matrices. As explained in section 3.2, one needs to input the decay scheme for the construction of the response matrices. This means that the part of the electromagnetic de-excitation scheme which is unknown has to be guessed by some method, which introduces an unknown element into the results. However, their correctness can be assessed if they are very similar (or equivalent) for different initial guesses. Moreover, the differences permit us to determine the systematic uncertainties coming from the dependency on the response. We should not forget that we are dealing with a tremendously complex problem which has many more unknowns than data. The quality checks which have been applied are summarised as follows:

1. The calculated feeding distribution must reproduce the data, that is, the Monte Carlo spectra generated for a decay calculated with the EC and β^+-feeding distributions must reproduce the respective experimental EC and β^+-spectra. This is the primary goal of the analysis algorithms, since all of them include this feature as a prerequisite.

2. The independent analysis of the EC and β^+-spectra must provide the same strength. This feature is not automatically fulfilled, since the responses used in both analysis are completely different. In the calculation of the EC response, only γ-radiation has to be considered, while for the β^+ one, the energy loss of positrons has to be included (including the two 511 keV quanta produced after the annihilation process). The large difference is clearly illustrated by the different shapes of the experimental spectra. Thus, the argument we follow is that if different spectra, different responses and different feeding distributions produce the same strength, the latter has to be close to the truth.

3. The degree of dependence of the calculated EC and β^+-feeding distributions on the assumptions made on the unknown part of the level scheme must be determined. Small overall deviations are a further proof of the correctness of the result.

4. The nature of the three methods used to solve the inverse problem is completely different. Thus, equivalent final results provide two consistency checks. The first is that the methods are working, which should not be considered as automatically fulfilled. The second is that their convergence provides a strong evidence of the correctness of the analysis.

5. As indicated in [GAD94], the EC and β^+ feeding distributions, with the proper normalisations, can be used to determine the Q_{EC} along the whole energy range by interpolation of the EC/β^+ ratio tabulated in [GOV71]. The consistency of the result along the energy range is another proof of the correctness of the results.

We start from the view that the TAGS technique leads to the proper shape of the strength distribution and accurate and reliable integrated values. However, due to the limitations introduced by the low resolution of the detector, it does not resolve closely placed individual levels. In fact, the strength distributions have to be interpreted as average distributions, since there is a correlation (or migration) between contiguous energy bins. As we will see, this particularly affects the accuracy of the Q_{EC} calculation from the EC/β^+ ratio.

4.6.1 Finding a solution which reproduces the experimental data

The discussion on this topic can be started with any of the analysis methods. We have chosen the EM (presented in subsection 3.3.3) because we consider it best adapted to our problem: it is easy to implement, it converges fast to the solution, deals naturally with probabilities and provides positive solutions.

Several electromagnetic de-excitation schemes were used in the construction of the response matrices needed by the analysis methods. All of them have in common the same de-excitation scheme up to 2.7 MeV, which was obtained from a separate high resolution experiment with the Cluster Cube [AGR97] [RUB97]. Thus, the differences between the three schemes used consist only in the decay properties of the levels (bins) in the region between 2.7 MeV and the Q_{EC}. Further details on this aspect of the analysis can be found in appendix B.

- Electromagnetic de-excitation scheme 1: It is an average scheme based on the experimental decay properties of the levels above 2.7 MeV which were observed with the Cluster Cube [RUB97]. All the levels (bins) above 2.7 MeV decay to the lowest lying ones in the same manner and preserving the observed γ-intensity.
- Electromagnetic de-excitation scheme 2: An unphysical scheme which considers that *all* the bins above 2.7 MeV decay in the same manner with *equal* probability to any of the states below 2.7 MeV.
- Electromagnetic de-excitation scheme 3: A scheme based on a statistical model for the electromagnetic de-excitation of the nucleus above 2.7 MeV. A description of the model can be found in appendix B.

Fig. [4.12] shows the result of the analysis of the EC and β^+-spectra for the ^{150}Ho 2^- decay presented in section 4.3. We will initially deal with the results obtained for de-excitation scheme 1 after an EM analysis. The left column of plots corresponds to the EC case, while the right for the β^+. The first row of plots shows the comparison between the experimental spectra (points) and the Monte Carlo responses (solid line) obtained from the calculated feeding distributions (normalised to unity) in the last row. The second row of plots shows the relative deviations between the respective experimental and Monte Carlo reconstructed spectra calculated by Eq. (4.28)

$$\text{rel. dev.} = \frac{N_{exp} - N_{sim}}{\sigma_{exp}} \tag{4.28}$$

where N_{exp} and N_{sim} are the number of counts in the experimental and simulated spectra and σ_{exp} are the experimental uncertainties.

The large discrepancy observed for the β^+ case below channel ~58 is due to a ^{150}Er contamination (see later for more details).

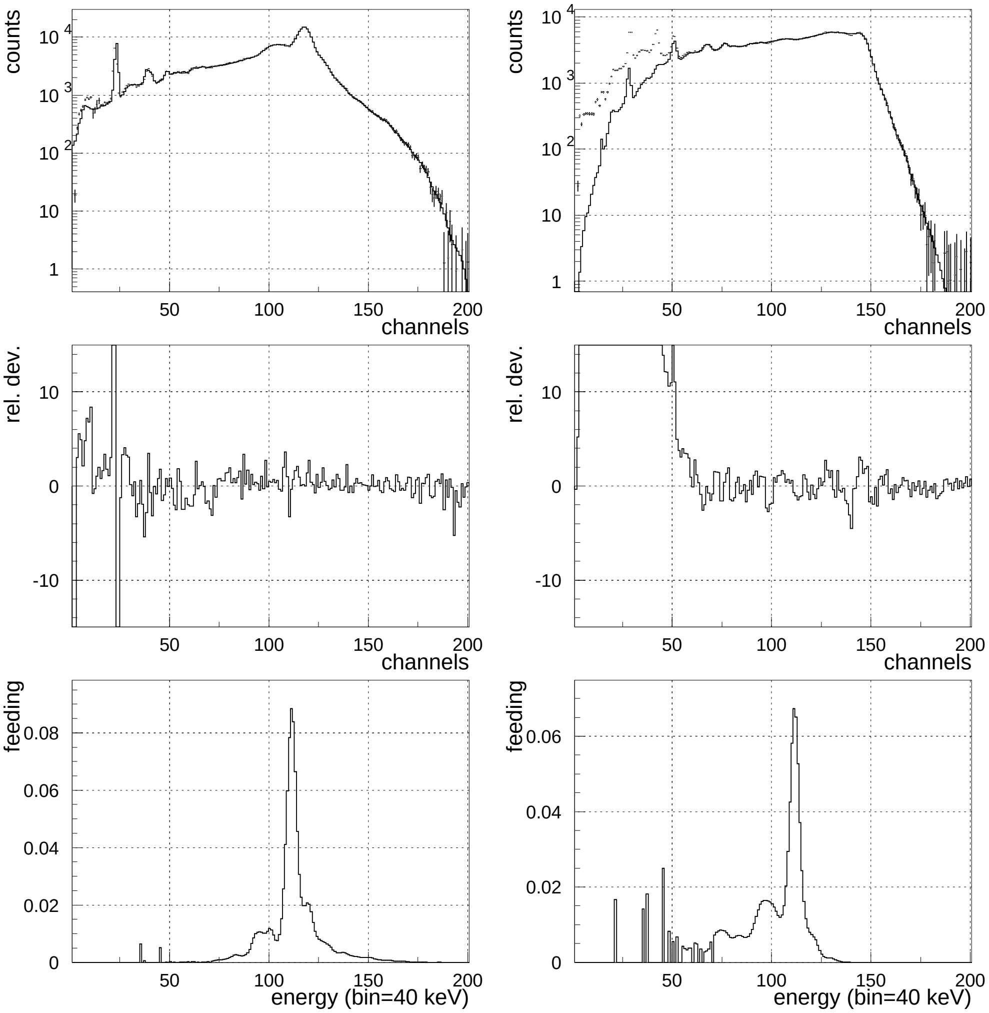

Figure 4.12: Results of the ^{150}Ho 2^- decay analysis using the EM method. Both EC and β^+ response matrices were calculated following the electromagnetic de-excitation scheme 1. First row: EC (left) and β^+ (right) experimental spectra used in the analysis. Superimposed are the corresponding simulated spectra (solid lines) reconstructed from the resulting feeding distributions. Second row: relative deviations between the experimental and simulated spectra for both EC (left) and β^+ (right) cases. Third row: resulting EC (left) and β^+ (right) feeding distributions normalised to unity.

It was mentioned previously that the EM method implies an iterative approach to the solution. As in any other iterative procedure, a convergence criterion has to be established in order to stop the iterations. The criterion we have followed obeys two directives:

1 We want the Monte Carlo reconstructed spectra to be as close as possible to the experimental ones.

2 The feedings obtained from the EM method are average distributions and should not show unrealistic oscillations. If the number of iterations is too large, the EM method tends to reproduce the statistical fluctuations of the experimental spectra, especially in the regions where the number of counts is low.

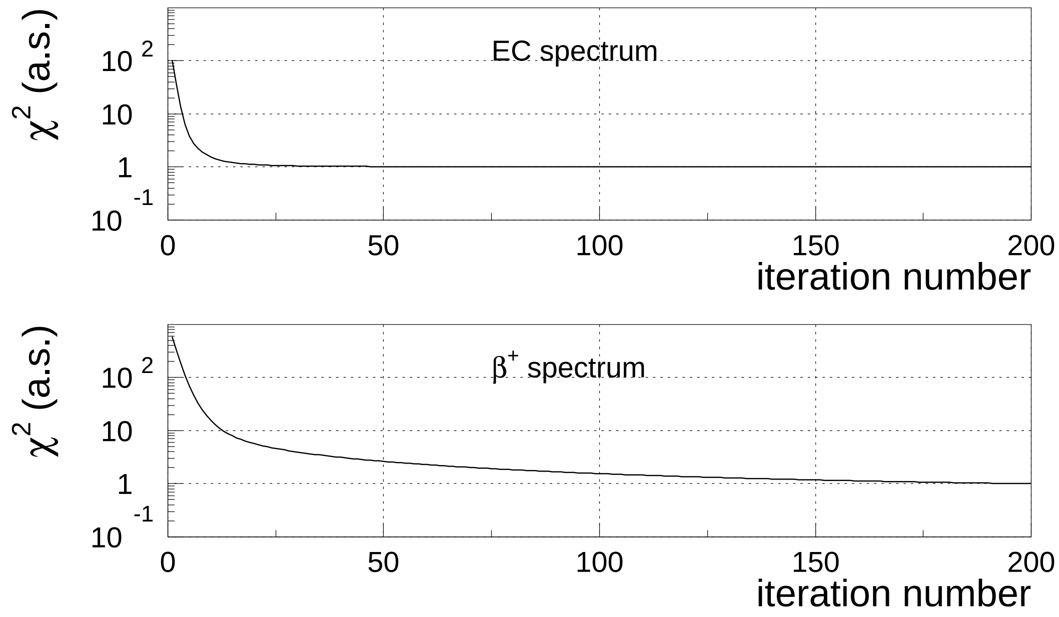

Figure 4.13: χ^2 (in arbitrary scale) between the experimental and Monte Carlo simulated spectra as a function of the number of iterations in the EM method. Top: EC spectra. Bottom: β^+ case.

This forces us to study where the differences, given by the χ^2 between the experimental and Monte Carlo reconstructed spectra, do not improve significantly and at the same time the solutions do not unphysically oscillate in order to reproduce the statistical fluctuations of the data. Fig. [4.13] shows the behaviour of the χ^2, in arbitrary scale, between the experimental and Monte Carlo simulated spectra as a function of the number of iterations in the EM method. For the EC case (upper part) it can be observed that a convergence to a constant value is rather fast, since for 30 iterations one arrives to a stable value of χ^2. For the β^+ case (lower part), the convergence is slower. This is probably related to the different response function and nature of the spectrum. We have decided to stop the iterations at a value of 100, because for this value the solutions have a smooth behaviour and at the same time a good reproduction of the experimental spectra is achieved.

The analysis of the spectra was done by selecting only a part of them. The region for the EC spectrum was chosen to be between channels 12 and 192, excluding only the part at lowest energies. This region is affected by systematic errors coming from the contaminant subtraction, and lies below the first excited state (2^+) at 803 keV. The inclusion or not of the 803 keV peak (at channel 22) has a strong influence on the reduced-χ^2 of the fit made between the experimental and Monte Carlo EC spectra, but none in the calculation of the EC feeding distribution. The source of the problem is that the responses for the γ-quanta were calculated in regular energy intervals (see section 3.2 for details) and not for the right energies (803 keV in this case). In fact, the value of $\chi^2 = 6144/180 \simeq 34.1$ obtained for the complete spectrum is reduced to 2.3 when the 803 keV is not present. This value might be considered as still too large, but we have to recall that the response used in the analysis includes only average features of the de-excitation. This makes it well suited to reproduce the overall structure of the spectrum, but not the detailed structure which would require a better knowledge on the electromagnetic de-excitation scheme. For the β^+ spectrum, the region of analysis was chosen between channels 58 and 158 in order to avoid the ^{150}Er contamination up to channel 58. This has the consequence that the feedings corresponding to that region have to be questioned, since they were calculated indirectly. But fortunately, as will be shown later, such feedings have a very small influence on the total strength. The reduced-χ^2 obtained is 2.4. Once more, the problem of using an average response is present. For both EC and β^+-responses, it can be seen in Fig. [4.2] that the relative deviations between the experimental and simulated spectra oscillate all around zero in the regions of analysis, which means that the average trend is reproduced.

Concerning the β^+-spectrum analysis, it has been mentioned already in section 3.2 that the penetration of positrons is underestimated by the GEANT3 Monte Carlo code [CAN99a]. This is an important point, because if it is not possible to reproduce the response for β-rays, it affects the result of the β^+-component analysis. As said in section 3.2, this forced us to back the β-detector by a piece of polyethylene, in order to minimise the penetration of the e^-/e^+ or their bremsstrahlung radiation in the NaI(Tl) detector. By doing so, even a relatively large discrepancy in the predicted β response has only a very small influence in the total response, since now most of the positrons/bremsstrahlung do not enter in the crystal. In order to better understand the influence of this effect in the analysis, it is worth spending some time describing the nature of the β^+ spectrum.

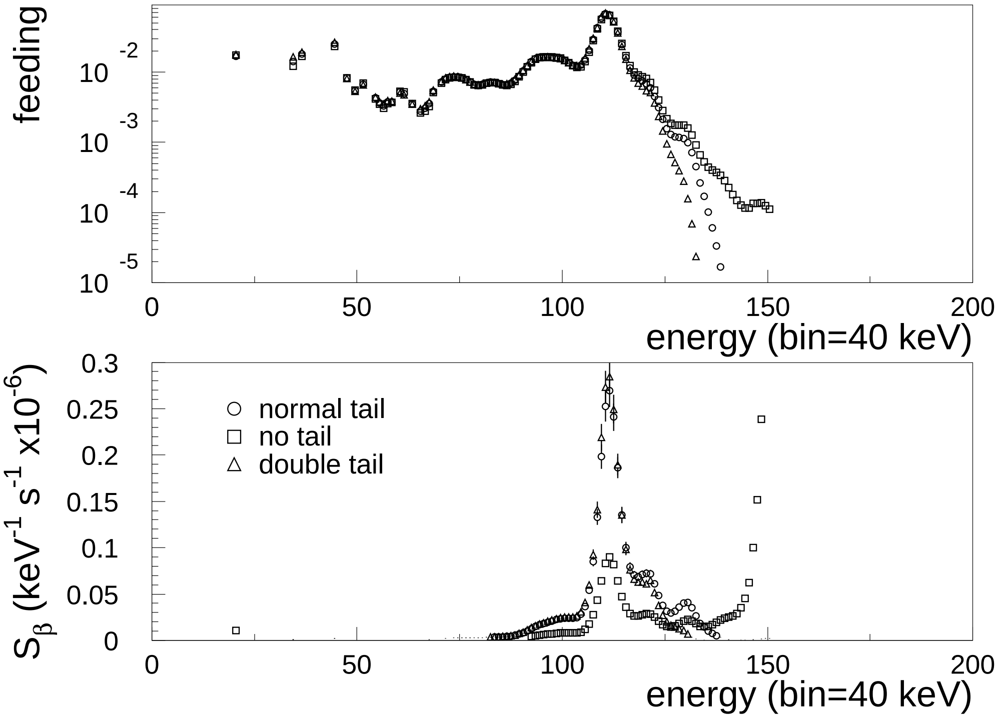

Figure 4.14: Results of the ^{150}Ho 2^- β^+ decay EM analysis using three different positron response matrices and electromagnetic de-excitation scheme 1. The circles correspond to the results obtained with the GEANT3 simulated Monte Carlo response, the triangles to a response where the tail above the 1022 annihilation peak was removed and the squares to a response where the tail above the 1022 keV peak was multiplied by a factor of two. Top: the three feeding distributions. Bottom: the corresponding three strength distributions.

The response to a positron has two components: the response to the energy loss of the positron itself (penetration or bremsstrahlung) and the response to the two subsequently produced 511 keV annihilation γ-quanta. Most of the positrons are stopped in the dead material surrounding the radioactive sample, basically inside the Ge detector or in the polyethylene absorber. Only the two 511 keV γs have a large probability of being detected, producing a peak at 1022 keV and a Compton background. Under these circumstances, we can assess that the Monte Carlo generated response has no pathologies, since the interaction of γ radiation is properly treated. However, few positrons of high energies (or associated bremsstrahlung) have a chance to enter inside the crystal after passing through the absorber. In this case, the energy lost by the positron in the NaI(Tl) is added to the energy deposited by the two 511 keV photons, and as we already know, this is not well evaluated by the Monte Carlo code. The penetration of the positrons/bremsstrahlung produces a tail in the region above the $511 + 511 + \sum E_\gamma$ keV sum peak, and can play an important role when looking at decays to levels lying at low excitation energies (higher positron energies). The influence of this effect on the analysis of the β^+ component has been studied by modifying artificially the response to positrons.

Fig. [4.14] shows the feeding distributions (top) and strengths (bottom) obtained from the analysis with three different positron responses: the response obtained directly from GEANT3 (circles), a response where the positron tail has been suppressed (squares) and a response where the positron tail has been multiplied by a factor of two (triangles). It can be seen in Fig. [4.14] that the feeding distributions are very similar up to the resonance. Significant differences are observed above 5 MeV, especially for the feeding distribution obtained when the positron penetration is neglected. This can be explained as follows. The tail produced by the positrons extends the β^+ response to a larger energy range. Thus, some of the counts at high energies come from events where all the energy deposited by the γs and the two 511 keV quanta has to be added to the energy lost by the positrons. If the Monte Carlo response does not include the effect, the analysis algorithm tries to reproduce the experimental spectrum by placing more feeding at higher energies. That is why the distribution marked by squares lies on top of the one defined by the circles. On the other hand, if the positron penetration is overestimated, then the spectrum at high energies can be reproduced by placing less feeding. This explains why doubling the penetration we obtain less feeding. The real problem arrives when converting the β^+ feeding into strength with help of Eq. (4.26). Then, the extra feeding at high energies is enhanced by the Fermi function and as a consequence the strength is dramatically larger. This can bee seen in the lower part of Fig. [4.14], where the strength obtained by disregarding the positron penetration (squares) explodes at high excitation energies. The remarkable point is that the results after considering a single or double penetration of positrons are not too different. Thus, the message is that even if the penetration of positrons is not included well in the response, it has to be considered: the effect on the strength is not too large and can be treated as a systematic error.

From the point of view of physics, we can see in the third row of plots in Fig. [4.12] that both EC and β^+-feeding distributions reveal a very sharp resonance of ($\sim$230 keV width) at $\sim$4.5 MeV excitation energy. This is particularly spectacular for the β^+ case: the experimental β^+-spectrum does not indicate so evidently as the EC one the presence of the narrow bump at 4.5 MeV, which is the consequence of the completely different responses involved in both processes. The fact that the same shape is recovered in both strength distributions is already an important success.

4.6.2 The independent EC and β^+ analysis

The next topic to be discussed is the comparison of the strengths obtained from the different EC and β^+-feeding distributions. As mentioned in section 4.5, the strength can be calculated from the EC-feeding distribution with the help of Eq. (4.25), from the β^+-feeding distribution as expressed by Eq. (4.26) and from both together as indicated by Eq. (4.18). For the first two cases, a knowledge of the Q_{EC} is demanded, while for the last only the weights of the two components is needed. We know that

$$N_{tot} = N_{\mathrm{EC}} + N_{\beta^+} \tag{4.29}$$

being N_{tot} the total number of decays and N_{EC}, N_{β^+} are respectively the total number of decays of the EC and β^+ components. Since the detection efficiency of the TAS is $\epsilon_{tot} \simeq 1$, the expression of Eq. (4.29) is analogous to

$$n_{tot}(t) = \frac{n_{\mathrm{EC}}(t)}{\epsilon_{\mathrm{EC}}} + \frac{n_{\beta^+}(t)}{\epsilon_{\beta^+}} \tag{4.30}$$

where $n_{tot}(t) \simeq N_{tot}(t)$ is the number of observed counts in a condition and background-free spectrum, and $n_{\mathrm{EC}}(t)$, $n_{\beta^+}(t)$ are respectively the number of counts in the EC and β^+ spectra measured during the same time interval t. The two coefficients are the efficiency for the X-ray detection ϵ_{EC} and the efficiency for the positron detection ϵ_{β^+}. Eq. (4.30) can be rewritten in terms of the total, EC and β^+ spectra, channel by channel, measured in different time intervals t_1, t_2 and t_3

$$\mathrm{TOT}_i(t_1) = a \cdot \mathrm{EC}_i(t_2) + b \cdot \beta_i^+(t_3) \tag{4.31}$$

In this way, we can find the search weights a, b by doing a two component least squares fit of the EC and β^+-spectra to a condition and background-free spectrum. In our case, the values of a and b were found to be

$$a = 5.30 \pm 0.02 \tag{4.32}$$

$$b = 2.27 \pm 0.01 \tag{4.33}$$

An important remark is that $1/a$ and $1/b$ should not be identified with ϵ_{EC} and ϵ_{β^+}, since the analysed EC and β^+-spectra were measured during different times. They can only be used to calculate the total β-intensity I_β as indicated by Eq. (4.19), where the EC and β^+ feeding distributions must have the same normalisation as the respective experimental spectra. The efficiencies for the EC and β^+ detection are $\epsilon_{\mathrm{EC}} = 3.5\%$ and $\epsilon_{\beta^+} = 44.8\%$. They were determined in the same way as a and b but using spectra measured over the same time. Actually, three fits were done for spectra obtained during three time intervals. The ratio of efficiencies kept constant at 12.8 ± 0.2.

The strength distributions calculated from the EC (squares) and β^+-feeding (triangles) distributions are shown in the upper part Fig. [4.15]. The lower part of Fig. [4.15] illustrates the relative deviations between the EC (squares) and β^+ (triangles) deduced strengths. The deviations and associated uncertainties are calculated with the help of Eq. (4.34) and Eq. (4.35):

$$\text{rel.dev.} = \frac{c_i - r_i}{r_i} \tag{4.34}$$

$$\sigma_{\text{rel.dev.}} = \frac{c_i}{r_i}\sqrt{\left(\frac{\sigma_{r_i}}{r_i}\right)^2 + \left(\frac{\sigma_{c_i}}{c_i}\right)^2} \tag{4.35}$$

Here r_i is the content of the i-th bin of the reference curve (EC-strength in our case), c_i is the content of the i-th bin of the curve to be compared and σ_{r_i} and σ_{c_i} are the respective uncertainties.

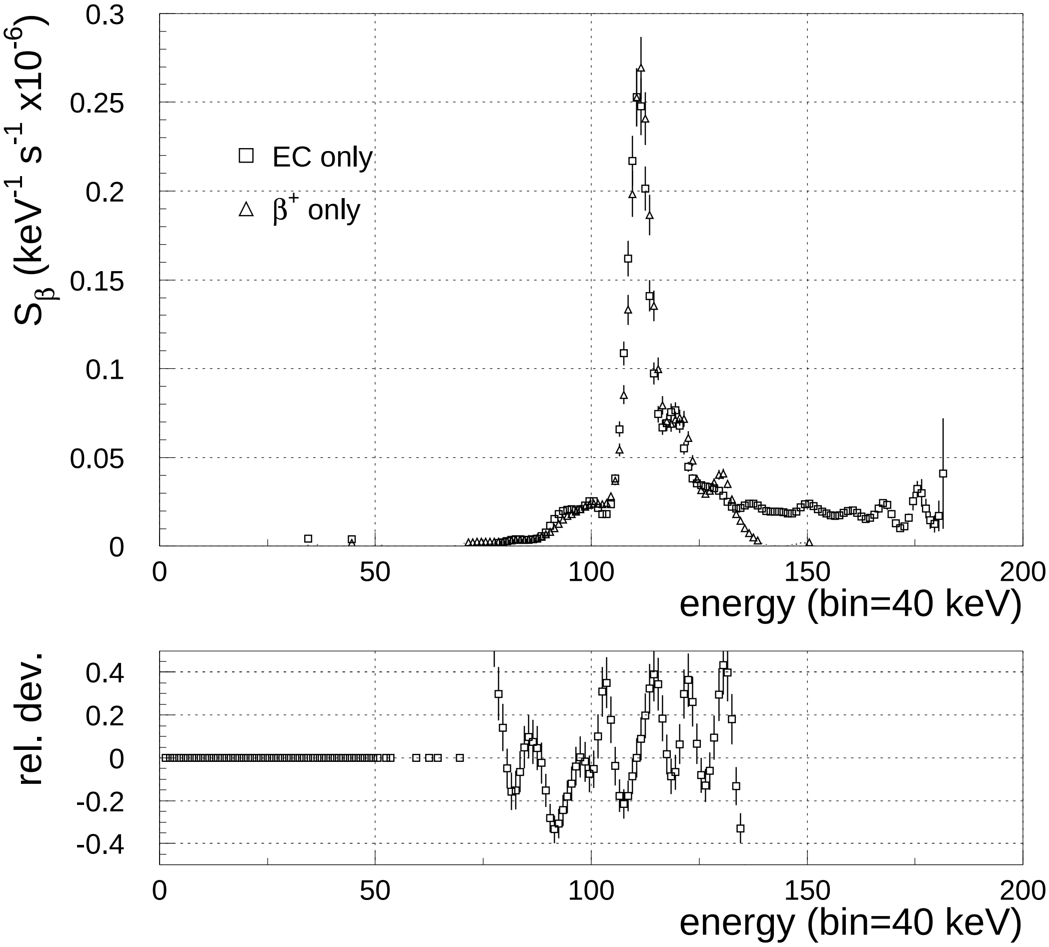

Figure 4.15: Top: strength distributions for the ^{150}Ho 2^- decay calculated from the EC (squares) and β^+ (triangles) feeding distributions. Bottom: relative deviations between the EC and β^+ strength (triangles)

Considering the large difference between the EC and β^+ experimental spectra, the shape of the two strengths looks surprisingly similar on average up to 5 MeV, which is evidence of the correctness of the analysis. However, there exist large differences bin to bin, particularly in the regions where the strength takes its lowest values. These deviations provide an estimate of the systematic uncertainties coming from the independent EC and β^+-analysis. It is important to remark that these uncertainties affect the shape, but the integrated values are more accurately determined because the overall features are preserved by the technique. The strength calculated from the β^+-feeding distribution (triangles) deviates from the EC one (squares) above 5 MeV up to the Q_{β^+}. It should be remembered that $Q_{\beta^+} = Q_{EC} - 2m_e$, and therefore no information on the strength can be obtained from the β^+ spectrum in the last 1022 keV of the Q_{EC} window.

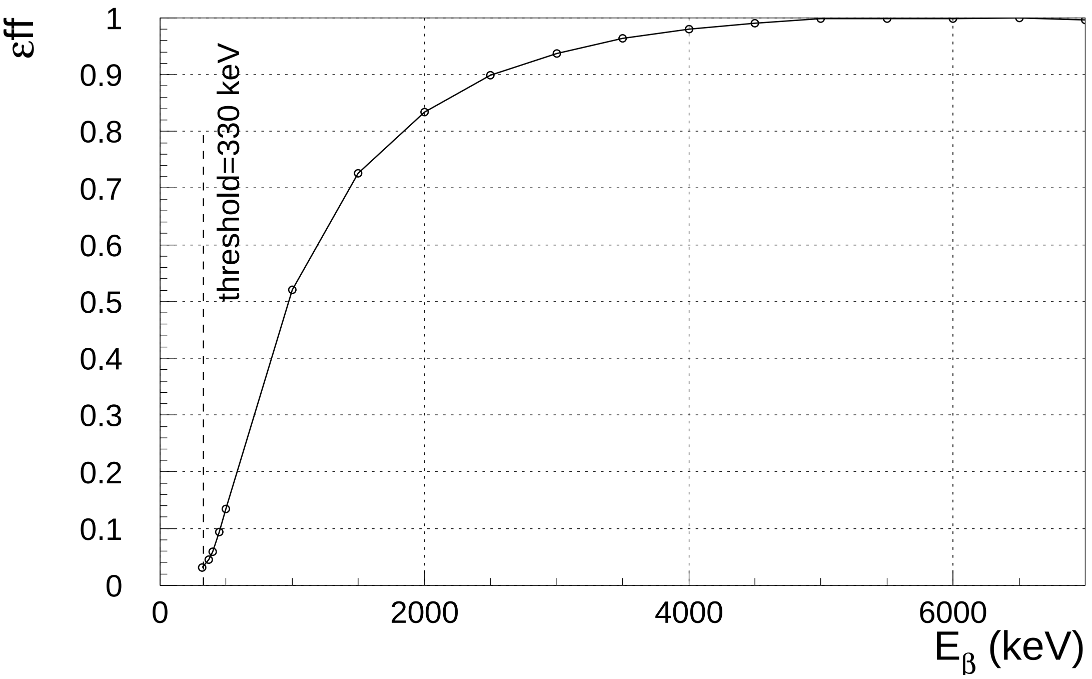

Figure 4.16: Monte Carlo β^+ detection efficiency of the bottom Si detector as a function of the positron end-point energy.

The difference existing between 5 and 6 MeV is a consequence of a distortion present in the β^+-feeding distribution. The distortion is introduced by the dependence of the β^+ detection efficiency $\epsilon_{\beta^+}(E_{\beta^+})$ on the energy of the positrons. Their continuous energy spectrum means that a fraction of them remains undetected because of the threshold set in the Si detector. The effect becomes larger for smaller end-point energies. Fig. [4.16] shows the β^+ detection efficiency calculated by GEANT3, as a function of the positron end-point energy. It can be seen that the highest variations in the slope occur in the first 2 MeV, since for such energies there is a large fraction of positrons below the threshold. This is the most sensitive part of the curve and its computation depends on a proper treatment of border effects in the simulation: the very close geometry of the Si detector introduces a strong dependence of its effective thickness on the crossing angle of the incident particle. The Monte Carlo efficiency we have found seems to be larger than the real one for low energy positrons, which correspond mainly to β^+ transitions to states at high excitation energies. Its overestimated detection means that the same number of counts in the β^+-spectrum produces less feeding than there really is. Once the source of the problem is known, the message is clear: the last MeV of the strength obtained from the β^+ component analysis is not correct, but it is not a failure of the analysis algorithm. Fortunately, the EC spectrum contains the missing information, so that nothing is lost.

4.6.3 The dependence of the results on the assumed part of the level scheme

Continuing with our discussion, we will now evaluate the influence on the strength of the assumptions made in the construction of the response matrices. Certainly, one of the most delicate points of the analysis is the fact that one has to complete the unknown part of the γ de-excitation pattern in order to build the needed response matrices. However, the dependence of the results on the assumptions made can be considered by comparing the outcomes for different initial guesses. Moreover, the variations found can be used to estimate the systematic uncertainties associated with the unknown part of the response. The results shown so far were obtained with the de-excitation scheme 1. Figs. [4.17] and [4.18] are equivalent to Fig. [4.12] and present the results of the EM-based analysis for the de-excitation schemes 2 and 3 after 100 iterations, respectively. The electromagnetic de-excitation scheme 3 is so to say the most realistic assumption one can make, since it includes the experimental information available and completes it with a statistical de-excitation model of the nucleus (see appendix B for further details).

Opposite to it, Fig. [4.17] shows what happens when the unphysical de-excitation scheme 2 is considered. A first inspection reveals that the feeding distributions obtained are poorly able to reconstruct the experimental spectra. However, this situation becomes less dramatic than might be expected if we consider the strength.

In fact, looking at the strength distributions in the upper part of Fig. [4.19], which correspond to the electromagnetic de-excitation schemes 1 (circles), 2 (squares) and 3 (triangles), we can see that the three curves are very similar on average. As indicated by the relative differences and their uncertainties, calculated with the help of Eq. (4.34) and Eq. (4.35), the major discrepancies occur where the strengths take their lowest values. It is remarkable that even the distribution for the unphysical

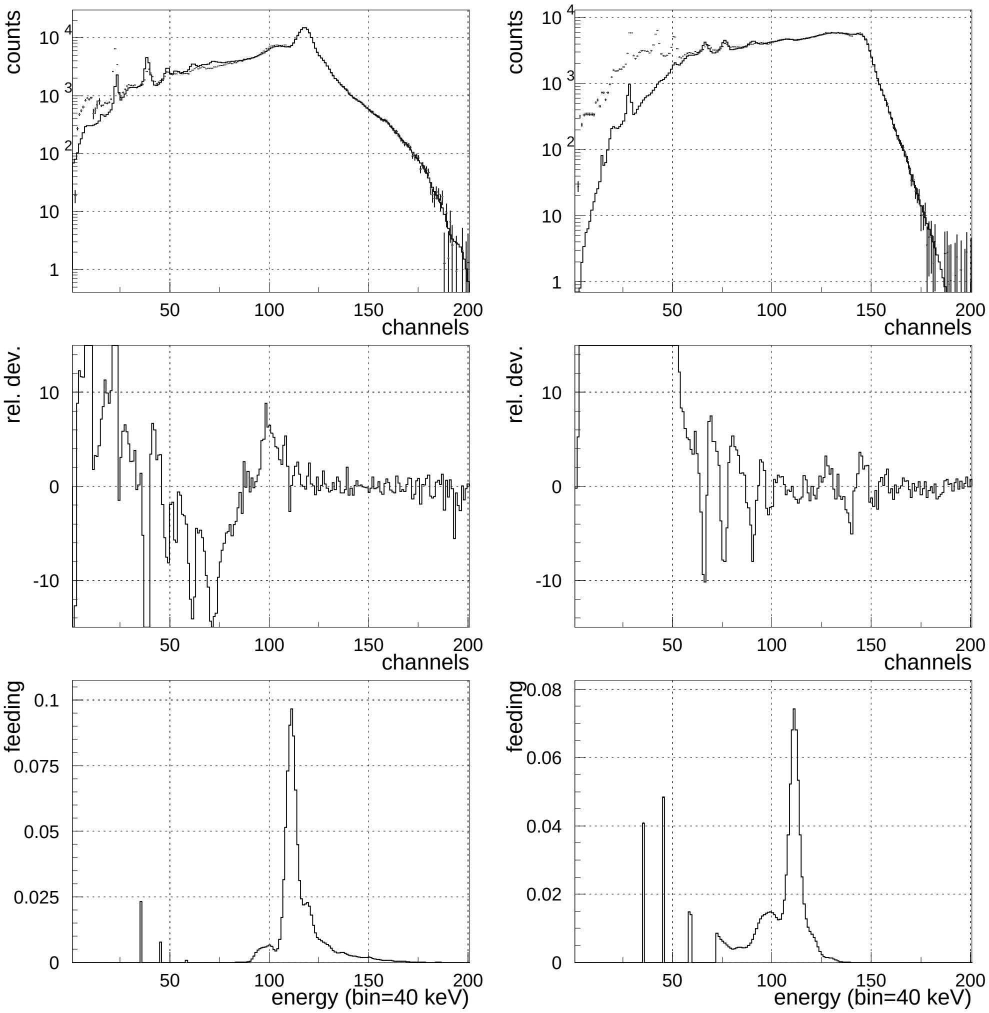

Figure 4.17: Results of the ^{150}Ho 2^- decay analysis using the EM method. Both EC and β^+ response matrices were calculated following the electromagnetic de-excitation scheme 2. First row: EC (left) and β^+ (right) experimental spectra used in the analysis. Superimposed are the respective simulated spectra (solid lines) reconstructed from the resulting feeding distributions. Second row: relative deviations between the experimental and simulated spectra for both EC (left) and β^+ (right) cases. Third row: resulting EC (left) and β^+ (right) feeding distributions normalised to unity.

electromagnetic de-excitation scheme 2 does not differ in shape from the other two, which is very impressive. Furthermore, this weak dependency on the level scheme permits us to guarantee the correctness of the result. The fact that the resulting strengths do not depend too much on the assumptions made on the level-scheme, is a direct consequence of the high efficiency of the spectrometer. The comparison of

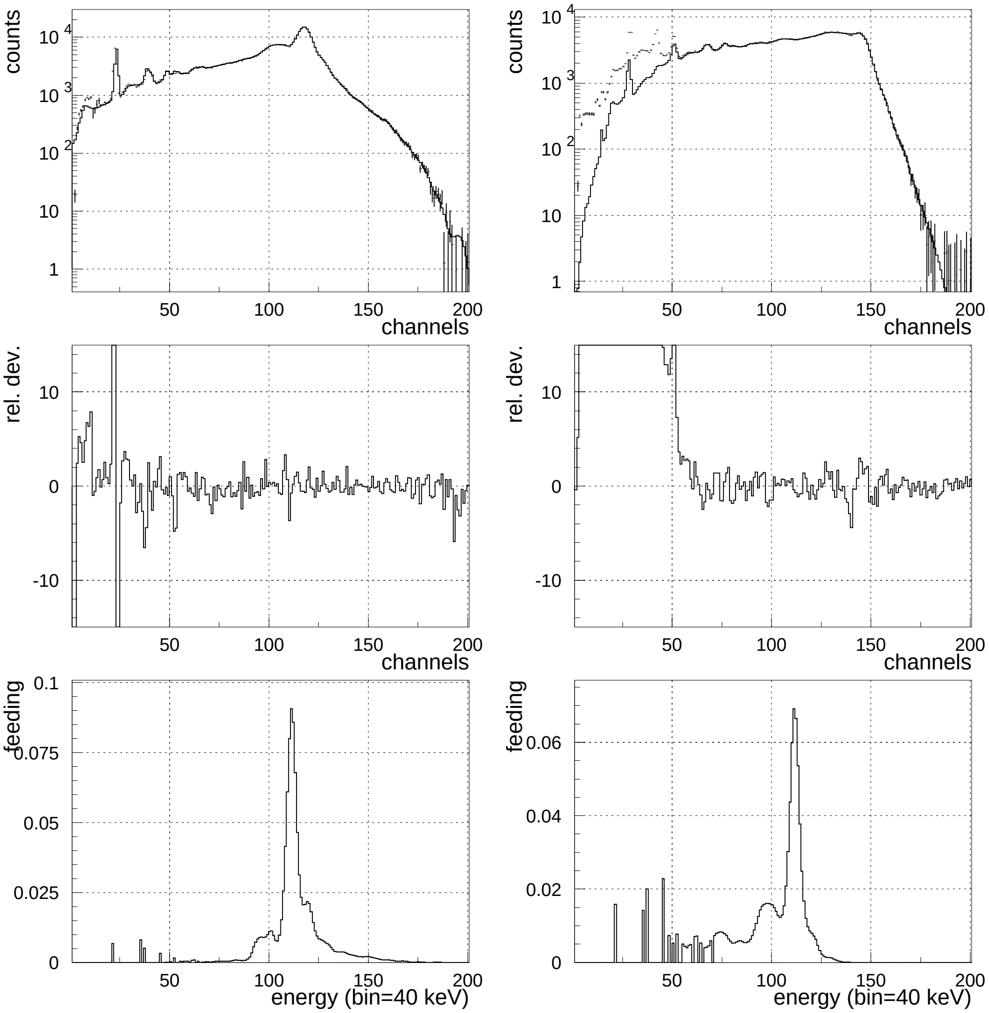

Figure 4.18: Results of the ^{150}Ho 2^- decay analysis using the EM method. Both EC and β^+ response matrices were calculated following the electromagnetic de-excitation scheme 3. First row: EC (left) and β^+ (right) experimental spectra used in the analysis. Superimposed are the respective simulated spectra (solid lines) reconstructed from the resulting feeding distributions. Second row: relative deviations between the experimental and simulated spectra for both EC (left) and β^+ (right) cases. Third row: resulting EC (left) and β^+ (right) feeding distributions normalised to unity.

the three curves in Fig. [4.19] allows one to estimate the systematic errors introduced by the assumptions made in the construction of the response matrix $\mathbf{R}$.

The integrated $\log ft$ values in Table [4.1] for the three level schemes confirm also the equivalence of the results. It can be seen that the $\log ft$ values lie between

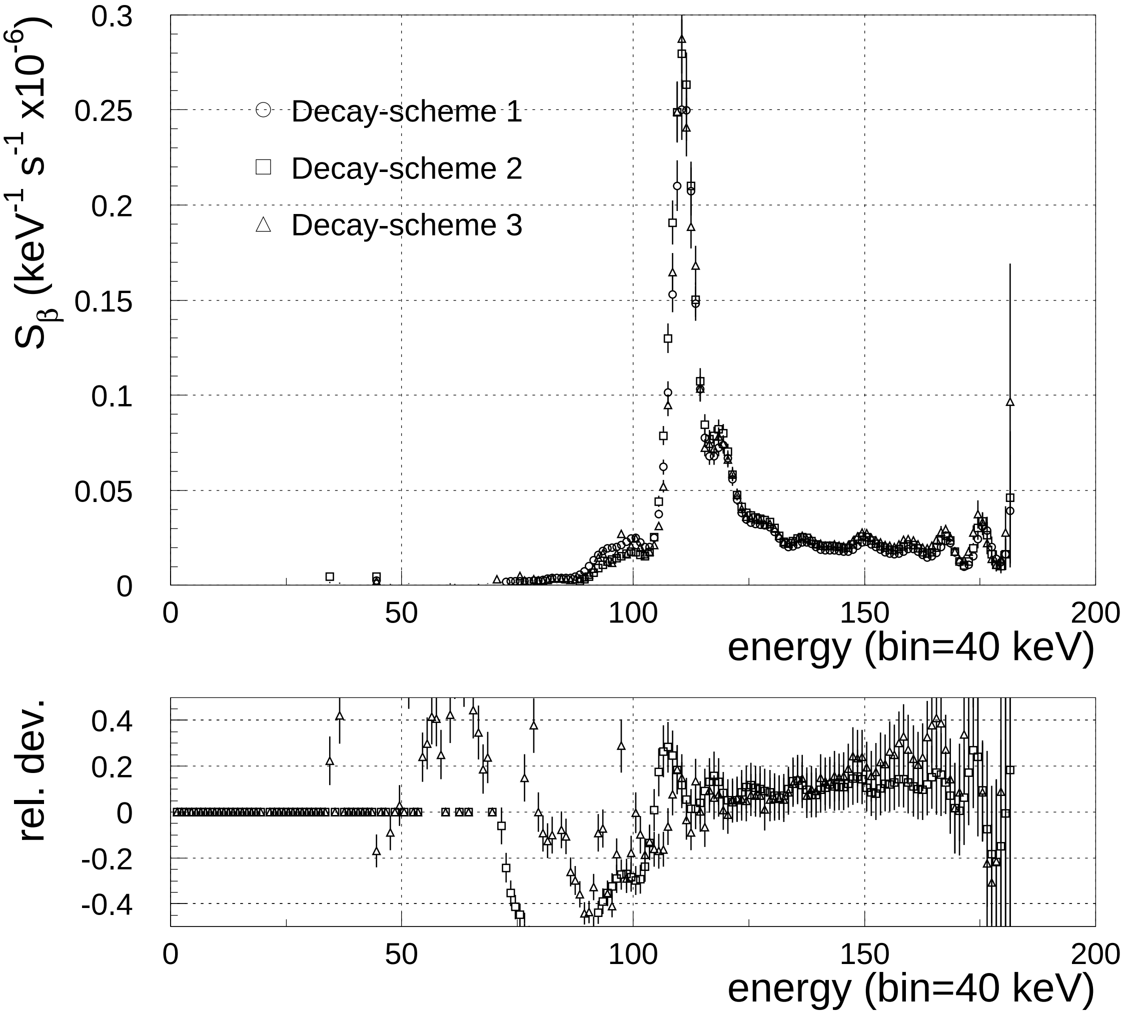

Figure 4.19: Top: strength distributions for the ^{150}Ho 2^- decay calculated from the electromagnetic de-excitation schemes 1, 3 and 3. Bottom: relative differences between the strengths from electromagnetic de-excitation schemes 2 and 1 (squares) and level schemes 3 and 1 (triangles).

3.80 and 3.83 and are consistent with the error coming from the analysis. The three different contributions to the total error, namely the uncertainty in the Q_{EC}, the uncertainty in the half-life $T_{1/2}$ and the uncertainties in the feedings coming from statistics, are explicitly indicated in the corresponding columns. The major contribution is the one coming from the uncertainty in $T_{1/2}$. The other two are much smaller. Thus, a better measurement of the half-life would significantly reduce the overall uncertainty.

Level scheme	$\log ft \pm \sigma_{\log ft}$	$\sigma_{\mathrm{Q_{EC}}}$	$\sigma_{T_{1/2}}$	$\sigma_{\mathrm{feeding}}$
1	3.83 ± 0.03	$0.81 \cdot 10^{-3}$	$0.25 \cdot 10^{-1}$	$0.16 \cdot 10^{-2}$
2	3.81 ± 0.03	$0.84 \cdot 10^{-3}$	$0.25 \cdot 10^{-1}$	$0.15 \cdot 10^{-2}$
3	3.81 ± 0.03	$0.88 \cdot 10^{-3}$	$0.25 \cdot 10^{-1}$	$0.13 \cdot 10^{-2}$

Table 4.1: ^{150}Ho 2^- decay $\log ft$ values integrated up to 7280 keV. The values were obtained for the electromagnetic de-excitation schemes 1, 2 and 3 after a combined analysis of both EC and β^+ feeding distributions.

The systematic uncertainty in the total $\log ft$ coming from the assumptions about the de-excitation pattern can be estimated by the standard deviation of the two $\log ft$ values from its mean value. Thus, we propose the value $\sigma^{sys}_{\log ft} = 0.015$.

4.6.4 The dependence of the results on the analysis method

Another consistency check is provided by the comparison of the results coming from the three different analysis methods described in section 3.3. The resulting three distributions are plotted in the upper part of Fig. [4.20]: the circles correspond to the EM analysis, the squares to ME and the triangles to a 2nd-order regularisation. The same response matrix, calculated from the de-excitation scheme 1, was used for the three cases in order to make the discrepancies depend only on the analysis method. The fast convergence of the EM method made us decide to stop after 100 iterations. Around this value, we arrived at the point where only a small improvement in the reproduction of the experimental data is achieved after one step. As mentioned before, this means that the solution is trying to reproduce the statistical fluctuations of the spectra. The number of iterations in the case of the ME solution was 200, and the regularisation parameters for both EC and β^+ component analysis were chosen to be $\lambda_{\mathrm{EC}} = \lambda_{\beta+} = 1$, on the corner of the L-curve. It was found that λ_{EC} and $\lambda_{\beta+}$ smaller than 1 derived in convergence problems, while values about 1.1 or higher provided solutions which were too smooth in the resonance region. The shape of the 2nd-order regularisation solution suggested also regularisation parameters for EC and β^+ close to the corner of the L-curve. Thus, we used $\lambda_{\mathrm{EC}} = 6.5 \cdot 10^{-6}$ and $\lambda_{\beta+} = 7.5 \cdot 10^{-5}$. For values higher than those, the solutions found were too smooth in the resonance region, while values about one order of magnitude lower (and below) ended up in wildly oscillating feeding distributions. It can be observed in Fig. [4.20] that the shape of the strength for the 2nd-order regularisation case is significantly smoother than the other two. The effect is produced after having tried

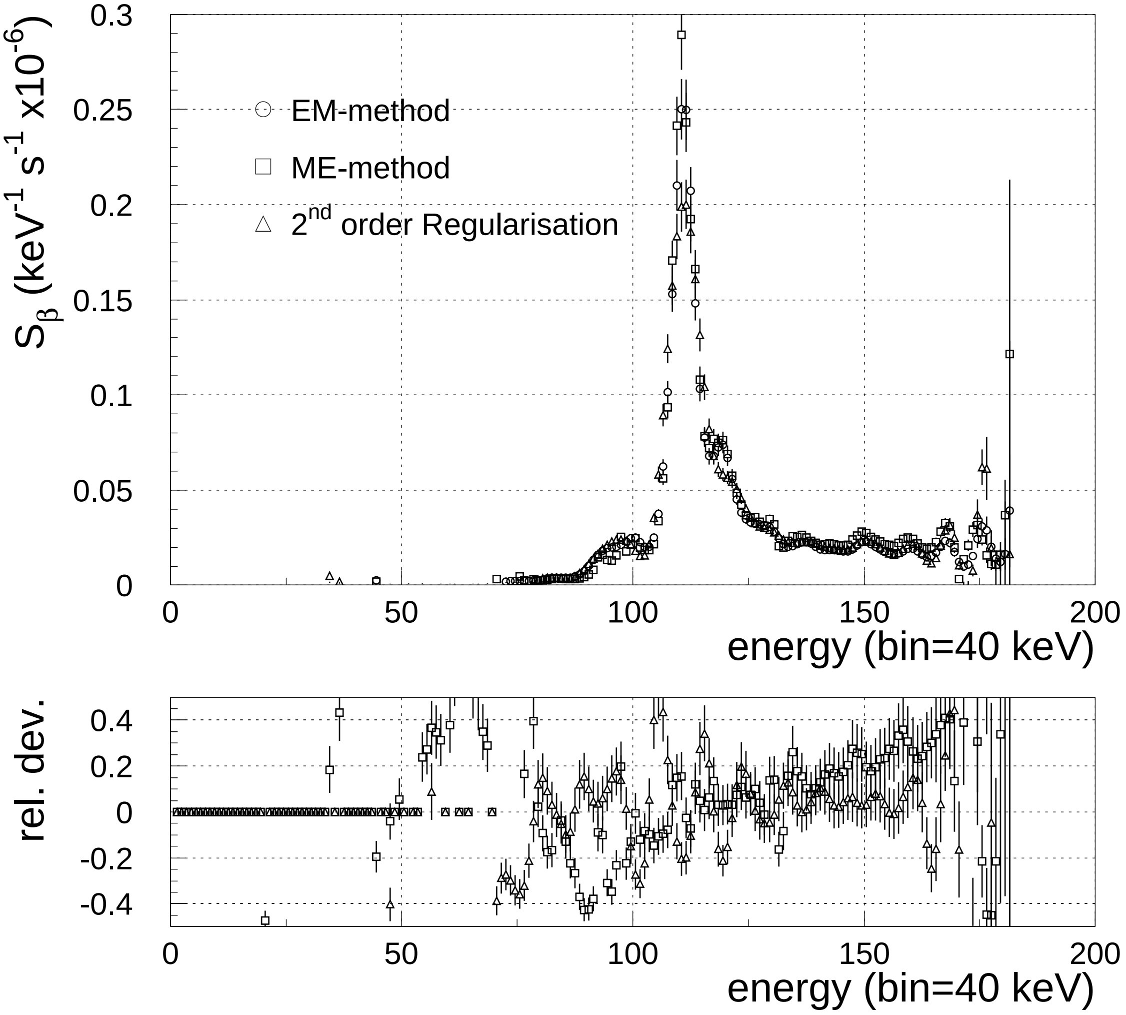

Figure 4.20: Top: strength distributions for the ^{150}Ho 2^- decay calculated by the EM (circles), ME (squares) and 2nd order regularisation. Bottom: relative deviations between the ME and EM strength (squares) and 2nd order regularisation and ME strengths (triangles).

to reduce the oscillations of the curve above 6.8 MeV. Actually, the regularisation method produces there negative feedings (set to zero for the strength calculation) which are compensated by larger neighbouring positive values.

The similar shapes of the three curves on average suggest and underpin the robustness of the analysis techniques and the correctness of the resulting strength. The relative differences and its uncertainties, calculated with help of Eq. (4.34) and

Eq. (4.35), can be used to estimate the systematic uncertainties introduced by the analysis algorithms. Table [4.2] contains the $\log ft$ for the EM, ME and 2$^{\rm nd}$ order regularisation. It can be observed that they are consistent with each other.

Analysis Method	$\log ft \pm \sigma_{\log ft}$	$\sigma_{\rm Q_{EC}}$	$\sigma_{T_{1/2}}$	$\sigma_{\rm feeding}$
EM	3.83 ± 0.03	$0.81{\cdot}10^{-3}$	$0.25{\cdot}10^{-1}$	$0.16{\cdot}10^{-2}$
ME	3.80 ± 0.03	$0.4{\cdot}10^{-3}$	$0.25{\cdot}10^{-1}$	$0.11{\cdot}10^{-2}$
2$^{\rm nd}$ order reg.	3.83 ± 0.03	$0.12{\cdot}10^{-3}$	$0.25{\cdot}10^{-1}$	$0.14{\cdot}10^{-1}$

Table 4.2: ^{150}Ho 2^- decay $\log ft$ values integrated up to 7280 keV. The values were obtained from the results of the EM, ME and 2$^{\rm nd}$ order regularisation combining both EC and β^+ feeding distributions.

The systematic uncertainty in the total $\log ft$ coming from the analysis algorithms can be estimated by the standard deviation of the first two $\log ft$ values from its mean value. The $\log ft$ coming from the 2$^{\rm nd}$ order regularisation solution should not be considered as a safe number because of the problem with the negative feedings mentioned before. Thus, we propose the value $\sigma^{sys}_{\log ft} = 0.015$

4.6.5 The $\mathrm{Q_{EC}}$ determination

The last consistency check we have made is the calculation of the $\rm Q_{EC}$ from the EC/β^+ ratio. This is not only a test, but also a method in itself which allows one to determine the $\rm Q_{EC}$ from the calculated EC and β^+ feeding distributions [GAD94]. The ratio between both distributions leads to the $\rm Q_{EC}$ by interpolation of the EC/β^+($\rm Q_{EC}$) values tabulated in [GOV71]. The $\rm Q_{EC}$ values obtained bin to bin for the region between 3 and 6 MeV are shown in Fig. [4.21]. The 6 MeV upper limit corresponds to the end of the β^+ component $\rm Q_{\beta^+} = Q_{EC} - 1022$ minus 330 keV (threshold of the Si detector). The region which can be used for the $\rm Q_{EC}$ calculation is limited in Fig. [4.21] by vertical dashed lines. The lower limit of 3.2 MeV corresponds to the end of the small ^{150}Er contamination present in the β^+ spectrum. The upper limit of 5.2 MeV was taken in order to avoid the distortion present in the last MeV of the β^+ feeding distribution (see subsection 4.6.2 for further details).

The oscillations found between 3.2 and 5.2 MeV are an effect of the strong dependence of the $\rm Q_{EC}$ on the detailed shape of the feeding distributions. There, the average shape of the feeding distribution is not accurate enough to reproduce the detailed structure. The finite resolution, included in the response function used for the analysis, plays an important role. It introduces correlations between the calculated

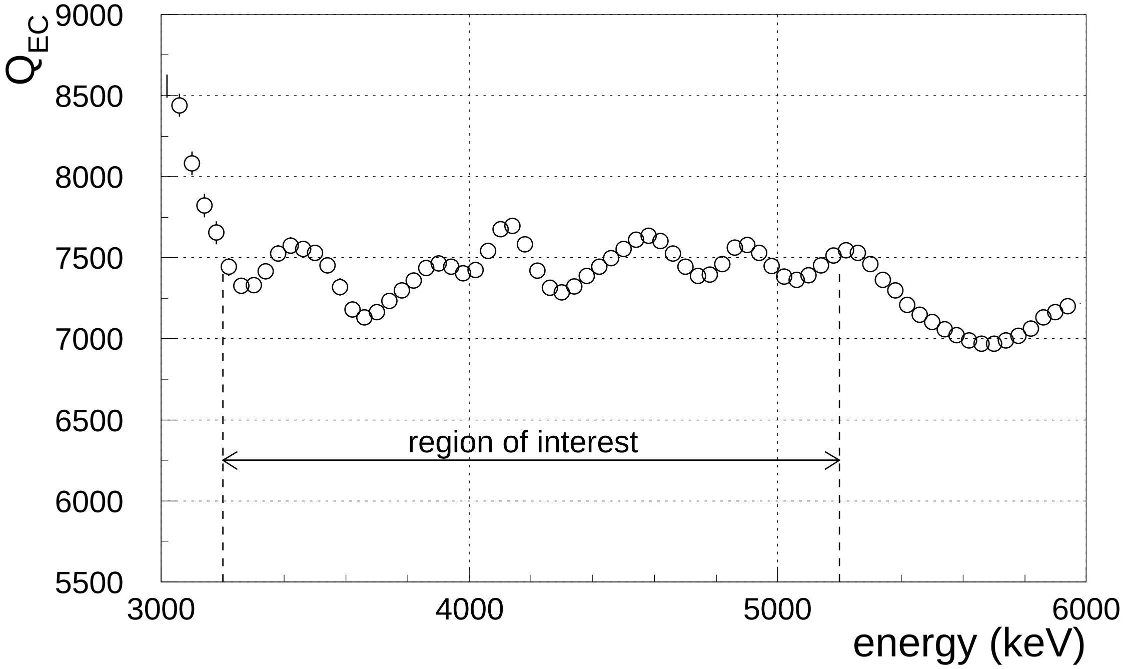

Figure 4.21: Q_{EC} calculated bin by bin from the EC and β^+ feeding distributions by interpolation of the EC/β^+(Q_{EC}) ratio tabulated in [GOV71].

feedings in contiguous cells. The absence of sharp structures in the experimental spectra forces the analysis program to do some kind of averaging, and this is propagated along several bins. A migration of feeding from one bin to the neighbouring ones has negligible influence on the strength and integrated $\log ft$ determination, but affects substantially the value of the experimental EC/β^+ ratio, and this can be translated into the observed oscillations. To conclude our discussion, the anomalous behaviour of the calculated Q_{EC} values between 5.2 and 6 MeV, visible in Fig. [4.21], is a consequence of pathology in the β^+ feeding distribution in the last MeV below the Q_{β^+}. As it was mentioned during the discussion on the strength obtained from the β^+ feeding distribution, the efficiency of the Si detector introduces a distortion there.

The mean value of the Q_{EC} in the region where it has to be calculated amounts to $Q_{EC} = 7444 \pm 126$ keV. Here the uncertainty is the standard deviation of the points with respect to the mean value. This value is in fairly good agreement with the experimental value of Q_{EC}=7372(27) obtained from an ion trap measurement [BEC97].

4.6.6 Concluding remarks

The message to be transmitted after having gone through all the topics introduced so far, is that we have to look at the results with averaging and integrating eyes: TAGS allows one to measure the shape of the β-strength function and its integrated value because no γ-intensity is missed. The analysis algorithms reallocate the counts of the experimental spectra in order to get the original feeding distribution. The poor resolution of the TAS detector does not permit one to obtain a detailed structure, but the results are correct on average. TAGS is a robust and reliable technique which allows us to study the overall properties of the β-decay, complementary to high resolution spectroscopy.

Table [4.3] shows the integral values of the strength for the ^{150}Ho 2^- decay in the form of total $\log ft$ and total B(GT). Also given in the table are the different contributions to the total uncertainty σ_{tot}, which was obtained from its squared quadratic sum. We have taken as a reference the results obtained for de-excitation scheme 1 after the EM analysis. We can see that the major contribution σ^{par} in σ_{tot} comes from the uncertainties in the parameters involved in the strength calculation, mostly from that in the half-life (see Table [4.1] or [4.2]). The systematic uncertainties associated to the assumption on the de-excitation scheme σ_R^{sys} and the analysis algorithms σ_{alg}^{sys} are very similar.

total $\log ft$	σ^{par}	σ_R^{sys}	σ_{alg}^{sys}	σ_{tot}
3.825	0.025	0.015	0.015	0.033

total B(GT)	σ^{par}	σ_R^{sys}	σ_{alg}^{sys}	σ_{tot}
0.577	0.033	0.020	0.020	0.043

Table 4.3: Total $\log ft$ and B(GT) values for the ^{150}Ho 2^- decay integrated up to 7280 keV. The uncertainties associated with the strength calculation σ^{par}, the dependence on the de-excitation scheme σ_R^{sys}, the dependence on the analysis algorithm σ_{alg}^{sys} and its squared quadratic sum σ_{tot} are given explicitly.

4.7 The ^{150}Ho $9^+ \rightarrow$ ^{150}Dy results

After the detailed discussion made in section 4.6 we can proceed faster with the results obtained for the ^{150}Ho 9^+ decay, since the procedure we will follow is the same one. However, there are two major differences with respect to the low spin case. First, the analysed experimental spectra shown in section 4.4 reveal stronger contamination. This is not a big problem in the EC case, since all the contaminations were removed properly, but it demanded a more careful study of the systematic uncertainties coming from the subtraction. However, the β^+-spectrum could not be corrected, which implies that the results coming from it should be interpreted with care. Actually, we will see that the total strength was finally extracted from the analysis of the EC component.

4.7.1 Finding a solution which reproduces the experimental data

The information we are looking for is, so to say, more hidden in the ^{150}Ho 9^+ spectra than it was in the previous ^{150}Ho 2^- case, which is a consequence of the higher γ-multiplicity in the decay. This higher multiplicity washes out the structures in the spectra, since the efficiency to fully absorb a cascade consisting of 4-5 γs is smaller than the total absorption efficiency for 1-2 γs carrying the same energy. Additionally, the decay of ^{150}Ho 9^+ proceeds to the 4qp-states (8^+,9^+ and 10^+) at high excitation energies and the 2qp-states (8^+) at lower excitation energies.

However, some of the overall features of the decay can be easily deduced from the experimental spectra plotted in Fig. [4.22]. The EC spectrum, in the upper part of Fig. [4.22], presents an intense peak at an energy of about 2.4 MeV, which corresponds to the lowest excited 8^+ state in ^{150}Dy. This single 2qp-state carries a significant part of the strength, as is reflected in the spectrum. The rest of the strength is mainly distributed among the 4qp-states at higher excitation energies, also marked in the spectrum. The difference with respect to the EC spectrum of the low spin isomer is that here we do not observe such a clear and intense structure but a wide bump. This is partially an effect of the smoothing introduced by high multiplicity γ-cascades, which can be best observed when looking at the region of the EC spectrum below the 2.4 MeV peak. The increasing continuum is mainly produced by the escapes of the individual γs de-exciting the 8^+ state. On the other hand, the low number of counts in the first 25 channels of the spectrum reveals the high detection efficiency of the TAS: the probability of detecting low energy events is very small due to the large summing.

Looking at the β^+-spectrum plotted in the lower part of Fig. [4.22], we can find similar properties. They are even more pronounced due to the influence of the two additional 511 keV annihilation quanta from the response to positrons. The peak

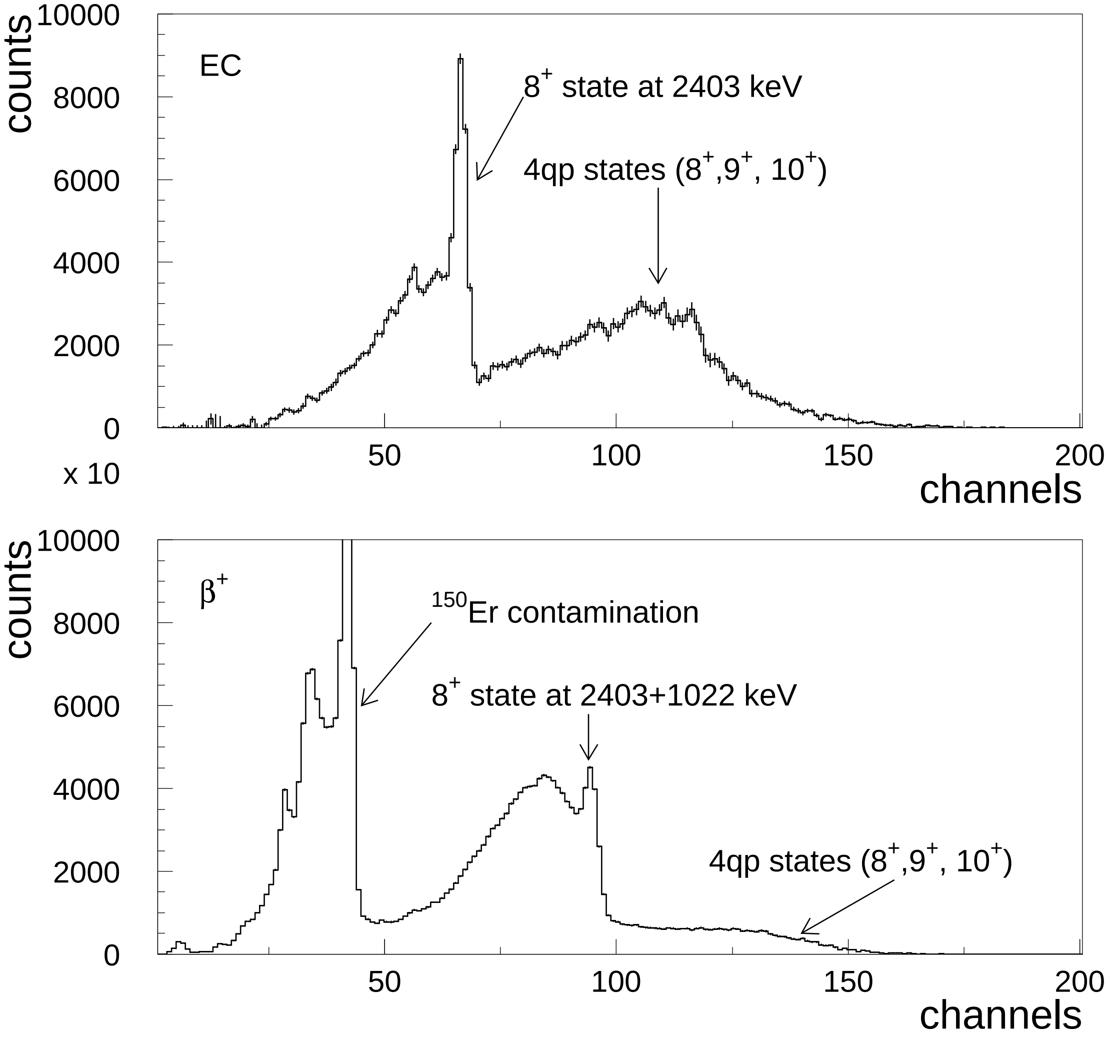

Figure 4.22: Experimental EC (top) and β^+ (bottom) spectra for the ^{150}Ho 9^+ decay.

corresponding to direct feeding to the 8^+ state at 2.4 MeV is also visible in the β^+ spectrum. But now, when compared to the EC case, there appears a bell-shaped continuum on its left side, which is produced by a higher multiplicity of 6-7 (the two additional 511 keV quanta) with respect to the EC response. The differences are more dramatic when looking at the region where the 4qp-states are, but this is mostly the consequence of the high EC/β^+ ratio there.

The previous discussion illustrates how fundamental is the role of the response function in the TAS technique, particularly in the case of a high multiplicity decay.

In order to construct the response matrices for the analysis, nine types of electromagnetic de-excitation schemes were assumed. Most of them lead to very similar outputs, and for this reason we will discuss only the results obtained from the two electromagnetic de-excitation schemes with produced the maximal differences (see appendix B). Both of them have in common the same de-excitation scheme up to 2.4 MeV (the $8^+ \rightarrow 6^+ \rightarrow 4^+ \rightarrow 2^+ \rightarrow 0^+$ cascade), which was obtained from a previous high resolution experiment [GAD94]. Thus, the differences between the two schemes used consist only in the decay properties of the levels (bins) in the region between 2.4 MeV and the Q_{EC} (see appendix B).

- Electromagnetic de-excitation scheme 1: The region between 2.4 MeV and the Q_{EC} was divided into four energy windows. The bins (levels) in the first window, between 2450 and 2800 keV decay all in the same way to the first 2^+, 4^+ and 6^+ excited states. The bins in the second window, between 2800 and 3300 keV, decay in the same manner to all the bins in the first region. The bins in the third region, between 3300 and 3800 keV, decay in the same manner to the bins in the second region. Finally, the bins in the fourth region, between 3800 and the Q_{EC}, decay to the first 6^+ and 8^+ excited states as well as to the other regions. All the branchings were adjusted in order to preserve the γ intensities measured in [GAD94].

- Electromagnetic de-excitation scheme 2: A scheme based on a statistical model for the electromagnetic de-excitation of the nucleus which includes the information from [GAD94]. A description of the model can be found in appendix B.

The electromagnetic de-excitation scheme 1 is one of the simplest assumptions one can make if nothing but the major features of the decay (like multiplicity) are known. On the other hand, the level scheme 2 is a well educated guess based on all the experimental information available. Thus, we expect that the most reliable results will be obtained when scheme 2 is used, and that for scheme 1 illustrates how far we can go if almost no information is put into the analysis.

The results of the EM analysis based on electromagnetic de-excitation scheme 2 are shown in Fig. [4.23]: the EC case in the left column, and β^+ case in the right column. As in the ^{150}Ho 2^- analysis, a number of 100 iterations was enough to converge to a solution. The first row illustrates how the EC (left) and β^+ (right) Monte Carlo spectra (in solid) reproduce the respective experimental TAS spectra (dashed). The whole range of the EC spectrum between channel 1 and 200 was used for the analysis. The contaminations present in the β^+ spectrum forced us to take a reduced analysis range between channels 68 and 180. The plots of the second row in Fig. [4.23] exhibit the differences between the Monte Carlo and corresponding experimental spectra, calculated as expressed by Eq. (4.28). The full EC spectrum is well reproduced, with the exception of the region where the 2403 peak is located.

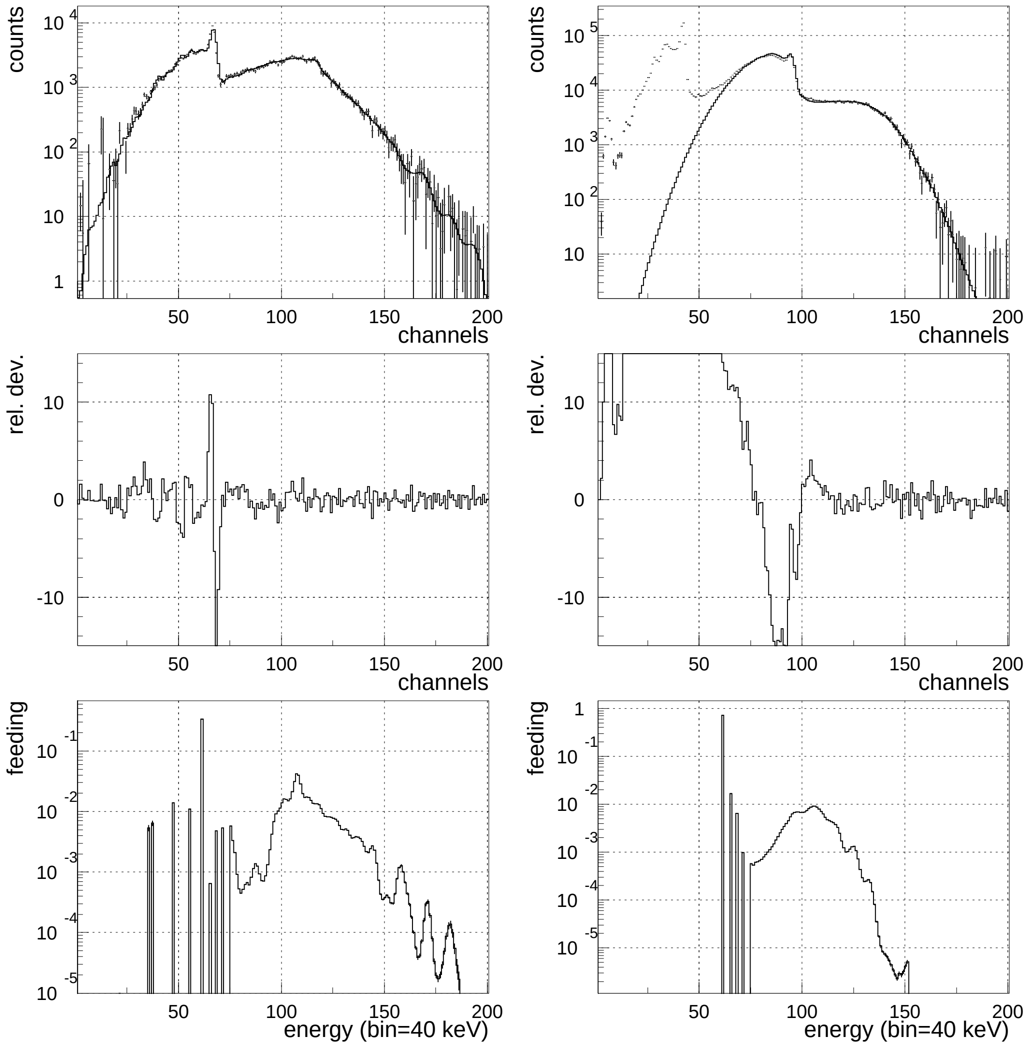

Figure 4.23: Results of the ^{150}Ho 9^+ decay analysis using the EM method. Both EC and β^+ response matrices were calculated following the electromagnetic de-excitation scheme 2. First row: EC (left) and β^+ (right) experimental spectra used in the analysis. Superimposed are the respective simulated spectra (solid lines) reconstructed from the resulting feeding distributions. Second row: relative deviations between the experimental and simulated spectra for both EC (left) and β^+ (right) cases. Third row: resulting EC (left) and β^+ (right) feeding distributions normalised to unity.

Looking carefully, we observe that the differences manifest an oscillation at the position of the peak, indicating that the problem is a consequence of the binning. In the case of the β^+ spectrum, the reproduction is not good below the the 2403 keV peak. The analysis algorithm is doing its best, but the contaminations clearly spoil the results. The calculated EC (left)and β^+ (right) feeding distributions are displayed

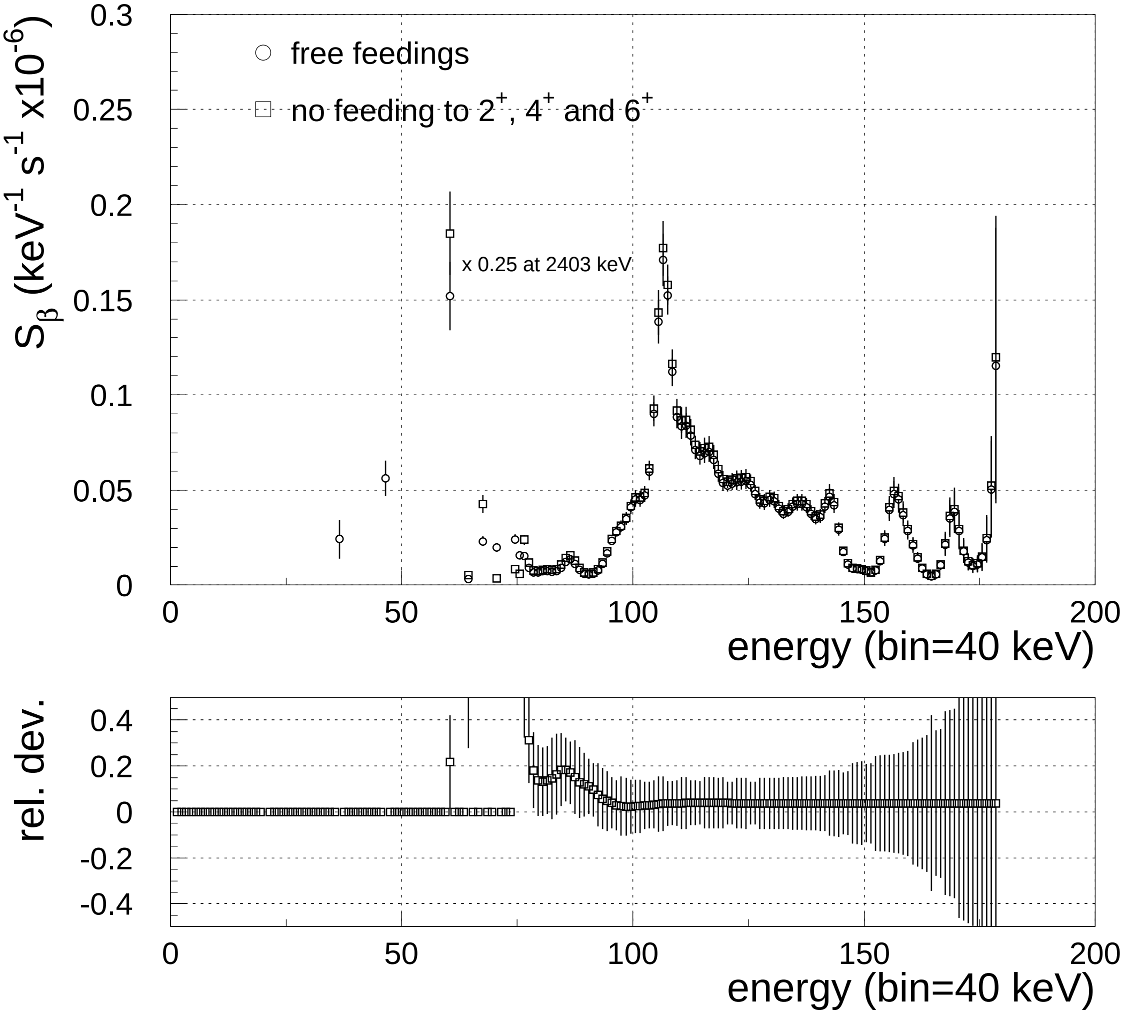

Figure 4.24: Top: strength distributions for the ^{150}Ho 9^+ decay calculated with the EM algorithm when the feeding to states below 2403 keV is allowed (circles) or explicitly forbidden (squares). Bottom: relative deviations between the two curves.

in the third row of Fig. [4.23]. While looking at the EC feeding distribution, we want to focus the attention on two points.

The first is the small fraction of "not allowed" feeding (~4%) assigned to low spin (4^+ and 6^+) states below the 8^+ level at 2403 keV. The tail at the left side of the 8^+ peak is best reproduced when the responses of the lower excited states are included, and that produces the assignment to these levels. We do not consider that there is a problem in the response to the $8^+ \to 6^+ \to 4^+ \to 2^+ \to 0^+$ cascade because of the excellent agreement obtained for the simulations of known decays [CAN99a]. We also do not think there is a problem of contamination in the EC spectrum, since all contaminants were properly removed. We rather tend to think instead that this is an effect of low energy γ transitions which were not considered in our electromagnetic de-excitation schemes. We have verified the influence on the total strength of the effect by forbidding explicitly feeding to these low lying states and the differences found are smaller than 5%. In particular, we get a $\log ft$ =3.73(1) when no condition is applied and a $\log ft$ =3.71(1) when the decay is forbidden to the states below the 8^+. The comparisons between the shapes of the strengths resulting when the feedings are freely set by the program or explicitly forbidden at energies below the 8^+ state are shown in Fig. [4.24]. We can see that the major differences occur for the strength assigned to the 8^+ level, which is higher when no feeding is allowed below it. The region between the 8^+ state and the resonance also presents some minor variations. For the rest, the shapes are completely analogous and only a small bias is present.

The second point is about the oscillations of the EC feeding distribution between 6 and 7.4 MeV. They correspond to fluctuations in the high energy part of the EC-spectrum, most probably introduced by the contaminant and pileup subtraction in a region of low statistics. The analysis algorithm tries to reproduce them with changes in the shape of the feeding distribution. Thus, we have to be careful before interpreting these fluctuations as real structures.

4.7.2 The independent EC and β^+ analysis

As mentioned in subsection 4.6.2, the strength can be calculated from both EC and β^+-feeding distributions. However, in the particular case of ^{150}Ho 9^+, the β^+ analysis leads to a wrong result. Besides the distortion introduced in the last MeV of the strength distribution by the efficiency in the silicon detector (see subsection 4.6.2 for details), the major problem here are the contaminations present in the β^+-spectrum. Fig. [4.25] illustrates how different are the strengths obtained from the EC (squares) and β^+ (triangles) analysis. This example reveals how important it is to have clean spectra in order to arrive at the right result. It also illustrates the importance of the X-ray tagging technique, since it allows an isobaric discrimination. The conclusion is that no information can be extracted from the β^+-spectra and have to rely only on the EC analysis.

The situation of having only one spectrum for the analysis made us study with even more care the influence of the contaminant subtraction in the EC case. As mentioned in section 4.4, the ^{150}Ho 9^+ EC spectrum was obtained by subtracting the pure ^{150}Ho 2^- EC spectrum from an admixture of both decays. The normalisation of the ^{150}Ho 2^- EC spectrum was determined to be λ_{EC} =1.075. The value comes from the ratio of areas of the 803 keV peak in the admixture and in the

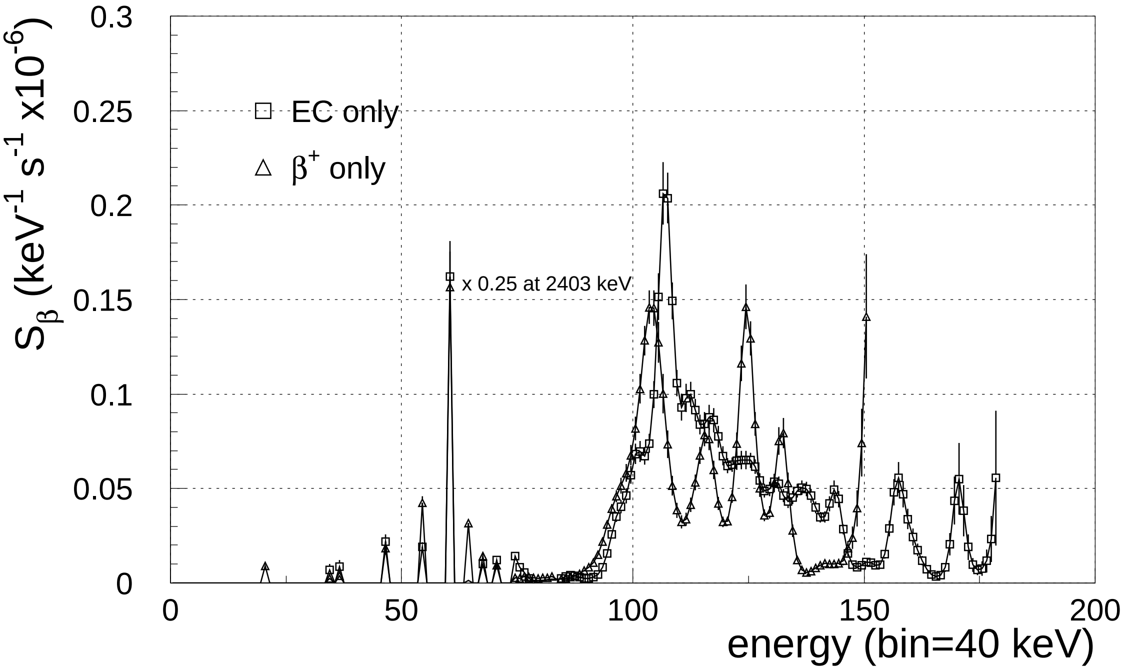

Figure 4.25: Top: strength distributions for the ^{150}Ho 9^+ decay calculated from the EC (squares) and β^+ (triangles) feeding distributions in the case of electromagnetic de-excitation scheme 2.

pure low spin spectrum. However, small variations of this parameter of ±2% are still compatible within the errors. Thus, we decided to perform the analysis with three different ^{150}Ho 9^+ EC spectra, corresponding to the low spin subtraction parameters λ_{EC} = 1.055, 1.075 1.095. The resulting strength distributions can be seen in Fig. [4.26]. The strength calculated for λ_{EC}=1.075 is plotted with circles, the strength for λ_{EC}=1.055 is plotted with squares and the one for λ_{EC}=1.095 is plotted with triangles. The relative deviations, as defined by Eq. (4.34), between the strengths for the maximal (triangles) and minimal (squares) subtraction factors with respect to the central one, reveal a fully symmetric picture. This is a direct consequence of the linear propagation of the perturbation introduced by a small variation in the subtraction factor. The deviations, always smaller than 20%, can be used to determine the size of the systematic uncertainties associated with the subtraction. The $\log ft$ values for the three cases given in Table [4.4], indicate that the systematic error in the total strength is smaller than 3%. The systematic uncertainty in the total $\log ft$ associated with subtraction has been estimated by the standard deviation of the three results from its mean value. Thus, we propose a value of $\sigma^{sys}_{\log ft} = 0.010$.

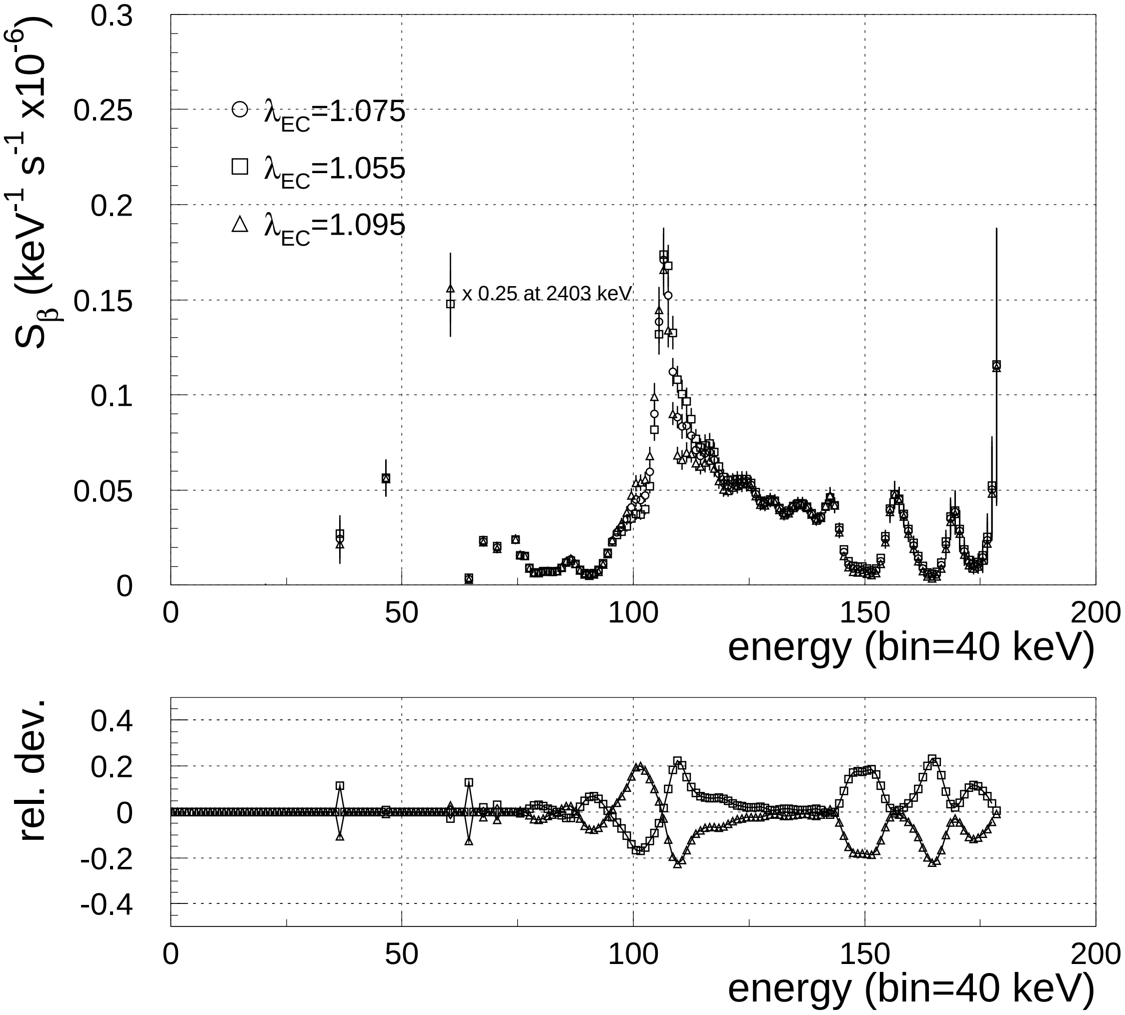

Figure 4.26: Top: strength distributions for the ^{150}Ho 9^{+} decay EC analysis. The curves correspond to the analysis of three experimental EC spectra from which the ^{150}Ho 2^{-} contamination was subtracted with the weights: 1.075 (circles), 1.055 (squares) and 1.095 (triangles). Bottom: relative differences between the strengths coming from the central subtraction of 1.075 and those coming from the minimal subtraction of 1.055 (squares) and maximal subtraction of 1.095 (triangles).

4.7.3 The dependence of the results on the assumed part of the level scheme

Fig. [4.27] shows the strength distributions resulting from the analysis when electromagnetic de-excitation schemes 1 (circles) and 2 (squares) were used for the con-

Subtraction factor	1.055	1.075	1.095
$\log ft$	3.72(1)	3.73(1)	3.74(1)

Table 4.4: $\log ft$ values of the strengths in Fig. [4.26] obtained for the three different subtraction factors.

struction of **R**. We observe considerably larger discrepancies than for the ^{150}Ho 2^- results shown in Fig. [4.19]. However, it is important to stress that we are comparing the strengths for two extreme cases. The electromagnetic de-excitation scheme 1 includes the minimum amount of information from the experimental decay scheme [GAD94], namely the dominant $8^+ \rightarrow 6^+ \rightarrow 4^+ \rightarrow 2^+ \rightarrow 0^+$ cascade. The de-excitation pattern on top of it was completely invented but preserving the major features of the decay like the average multiplicity and the experimental γ-intensity from [GAD94]. Thus, it is not surprising that we find the large differences shown in Fig. [4.27] when comparing with the results obtained for a statistical decay model. As mentioned at the beginning of this section, this statistical decay was generated with all the experimental information available, and thus, might be interpreted as more correct than electromagnetic de-excitation scheme 1. However, our aim is to show the real limits of the technique, and for this reason a conservative comparison was chosen. The relative differences between the two curves (~25% on average), calculated according to Eq. (4.34), provide an estimation of the systematic uncertainties introduced by the dependence on the response matrix.

Level scheme	$\log ft \pm \sigma_{\log ft}$	$\sigma_{\mathrm{Q_{EC}}}$	$\sigma_{T_{1/2}}$	$\sigma_{\mathrm{feeding}}$
1	3.66 ± 0.01	$0.60 \cdot 10^{-3}$	$0.50 \cdot 10^{-2}$	$0.70 \cdot 10^{-2}$
2	3.73 ± 0.01	$0.67 \cdot 10^{-3}$	$0.47 \cdot 10^{-2}$	$0.11 \cdot 10^{-1}$

Table 4.5: ^{150}Ho 9^+ decay $\log ft$ values integrated up to 7120 keV. The values were obtained for the two electromagnetic de-excitation schemes after the EM-based analysis of the EC spectrum.

The integrated $\log ft$ resulting from both analyses and given in Table [4.5] also present larger discrepancies as in the ^{150}Ho 2^- case . However, the two total strengths are still compatible within ~10%. The systematic uncertainty in the total

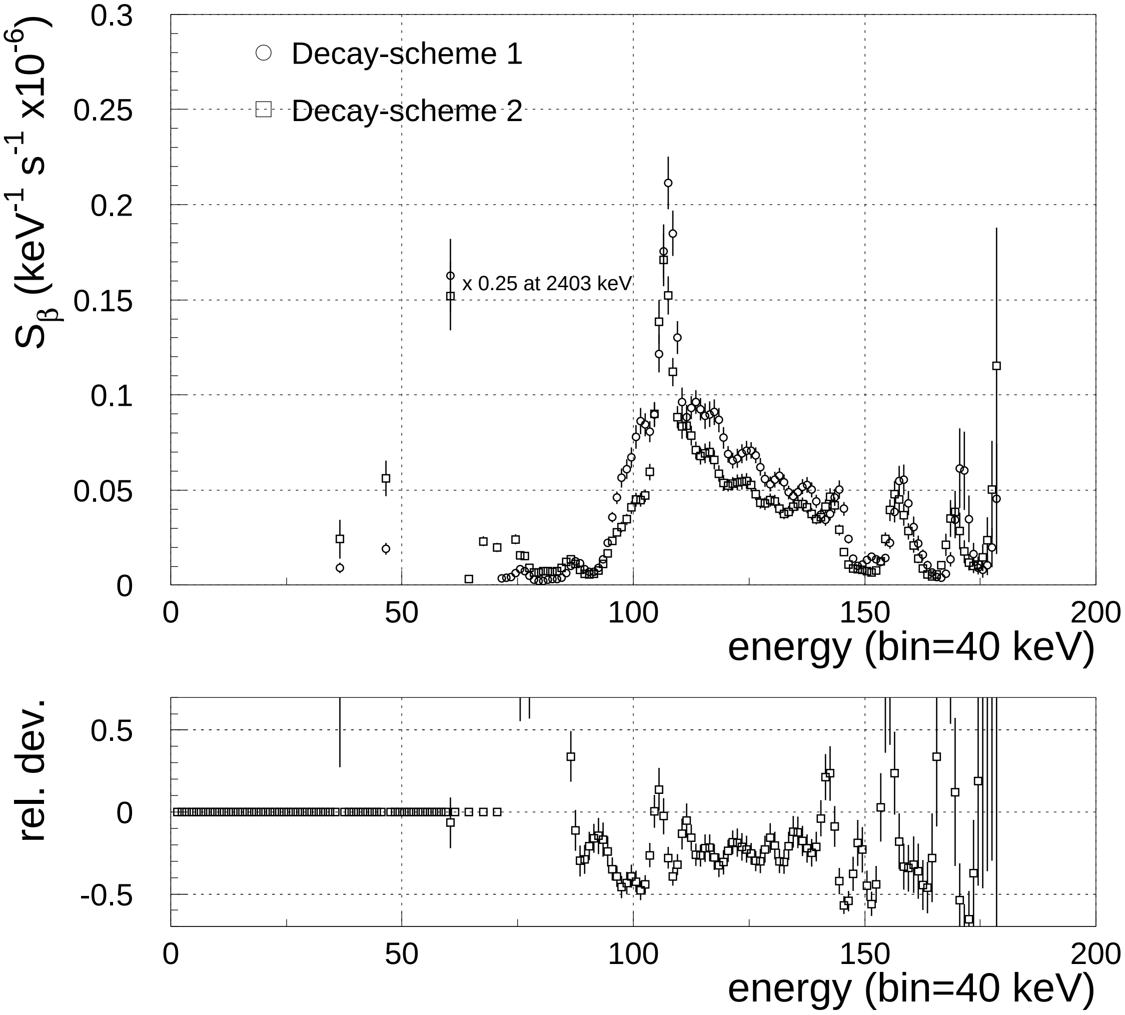

Figure 4.27: Top: strength distributions for the ^{150}Ho 9^+ decay calculated from the EC spectrum for level-schemes 1 (circles) and 2 (squares). Bottom: relative deviations between the two curves.

$\log ft$ associated with the two different de-excitation schemes can be estimated by the standard deviation of the two results from its mean value. Thus, we propose a value of $\sigma^{sys}_{\log ft} = 0.049$.

4.7.4 The dependence of the results on the analysis method

Fig. [4.28] shows the comparison of the strength distributions obtained for electromagnetic de-excitation scheme 2 by application of the 2$^{\text{nd}}$ order regularisation method (triangles), ME method (squares) and EM method (circles). A total of 100 iterations was enough to converge to the EM-solution, while 200 where used in the ME case. An ME parameter of $\lambda = 1.05$ was chosen, which corresponds to the corner of the L-curve.

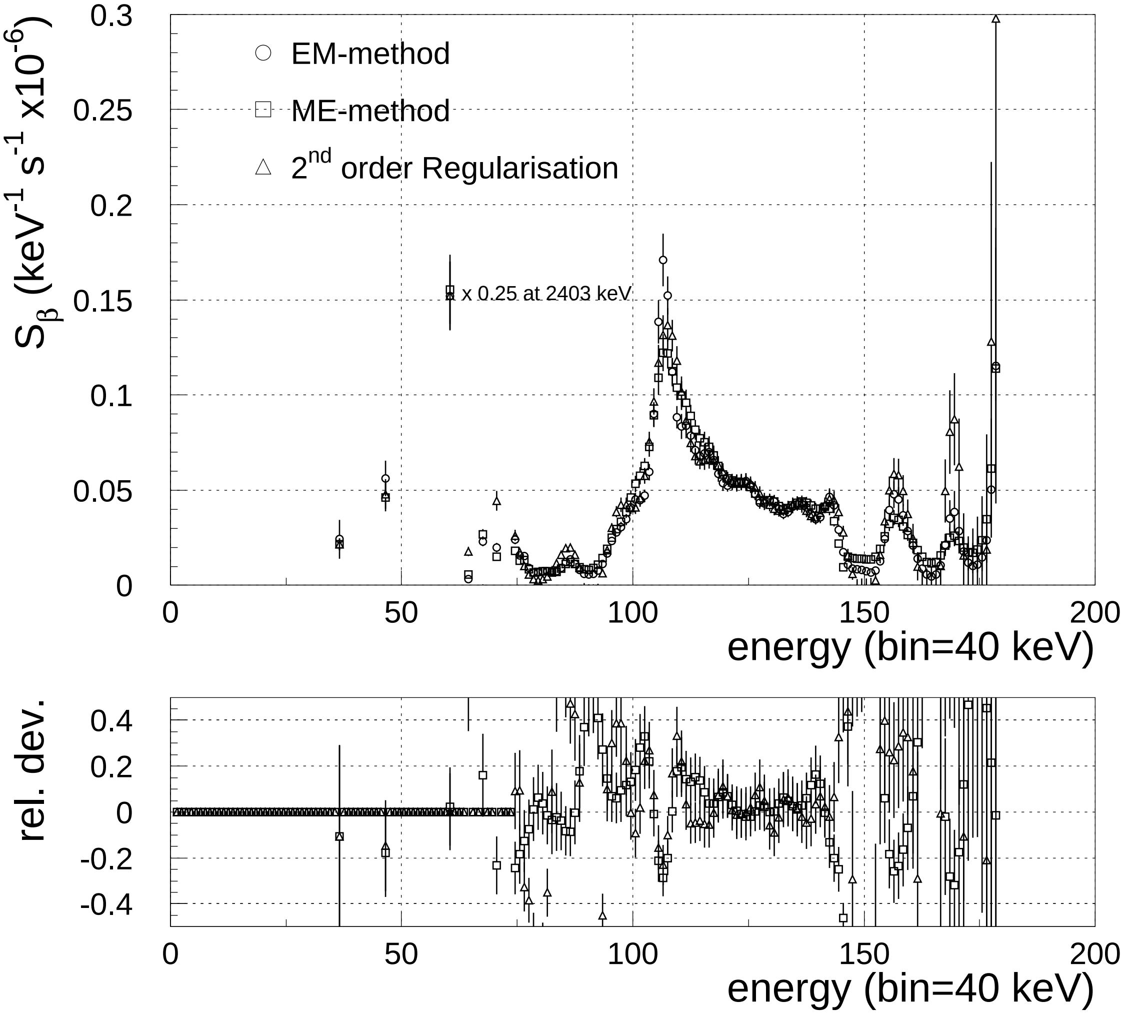

Figure 4.28: Top: strength distributions for the ^{150}Ho 9^+ decay calculated by the EM (circles), ME (squares) and 2$^{\rm nd}$ order regularisation (triangles). Bottom: relative deviations between the ME and EM strength (squares) and 2$^{\rm nd}$ order regularisation and EM strengths (triangles).

The same criterion was adopted for the 2$^{\rm nd}$-order regularisation parameter by taking a value of $\lambda = 1.0 \cdot 10^{-5}$. It can be observed that the three distributions present a very similar average shape. However, the ME and 2$^{\rm nd}$-order regularisation strength distributions are less sharp in the resonance region, since an attempt was made in order to smooth the oscillations present at the higher energy part of the distributions. This was done by the election of regularisation parameters still on the corner of the L-curve but favouring a higher regularisation. It is worth mentioning that the 2$^{\mathrm{nd}}$-order regularisation method produces negative feedings in the energy region above 5.6 MeV, more precisely, in the channels of lower statistics. The algorithm tries to compensate for the problem by producing extra positive feeding in the neighbouring regions, ending up in a pronounced oscillating behaviour. The negative feedings were set to zero in order to calculate the strength. Nevertheless, the extra positive feeding was such, that the total $\log ft$-value obtained finally is still lower than for the other methods. The total $\log ft$ values found are given in Table [4.6]. The systematic uncertainty in the total $\log ft$ associated with the different algorithms has been considered to be the same as in the low spin case. The $\log ft$ value coming from the 2$^{\mathrm{nd}}$ order regularisation solution should be neglected because of the problem with the negative feedings. On the other hand, the EM and ME values are too close to provide a conservative estimate of the systematic uncertainty. Thus, we propose a value of $\sigma^{sys}_{\log ft} = 0.015$.

Analysis Method	$\log ft \pm \sigma_{\log ft}$	$\sigma_{\mathrm{Q_{EC}}}$	$\sigma_{T_{1/2}}$	$\sigma_{\mathrm{feeding}}$
EM	3.73 ± 0.01	$0.67 \cdot 10^{-3}$	$0.47 \cdot 10^{-2}$	$0.11 \cdot 10^{-1}$
ME	3.73 ± 0.01	$0.10 \cdot 10^{-3}$	$0.56 \cdot 10^{-2}$	$0.10 \cdot 10^{-1}$
2$^{\mathrm{nd}}$ order reg.	3.69 ± 0.02	$0.26 \cdot 10^{-3}$	$0.15 \cdot 10^{-2}$	$0.15 \cdot 10^{-1}$

Table 4.6: ^{150}Ho 9^{+} decay $\log ft$ values integrated up to 7120 keV. The values were obtained from the EC results of the EM, ME and 2$^{\mathrm{nd}}$ order regularisation.

4.7.5 Concluding remarks

To conclude this section, we have to say that no information on the $\mathrm{Q_{EC}}$ could be obtained for the ^{150}Ho 9^{+} decay. As has been mentioned repeatedly, the β^{+} feeding distribution could not be extracted reliably. This case constitutes a very illustrative example on the power of the X-ray tagging technique. Even in the particularly unfavourable situation we have found, the isobaric discrimination allowed us to obtain a clean EC spectrum and thus, a reliable strength distribution.

Table [4.7] shows the integral values of the strength for the ^{150}Ho 9^{+} decay in the form of total $\log ft$ and total B(GT). Also given in the table are the different contributions to the total uncertainty σ_{tot}, which was obtained by its squared quadratic sum. We have taken as a reference the results for de-excitation scheme 2 after the EM analysis. We consider them as the closest to reality, because de-excitation scheme 2 best includes the most important physical features of the γ decay. As we can observe, the largest contribution σ_R^{sys} to the total uncertainty comes precisely from the dependence on the response. Thus, the knowledge on the real de-excitation pattern becomes more important when the complexity of the decay increases. The uncertainty σ_{alg}^{sys} associated with the analysis algorithms was taken to be the same as for the ^{150}Ho 2^- case. A difference appears between the two cases when looking at the uncertainty resulting from the strength calculation σ^{par}. Since the uncertainty in the half-life of ^{150}Ho 9^+ is significantly lower than for the low spin isomer, its contribution to σ^{par} is now comparable to the other two coming from the Q_{EC} determination and statistics. To conclude, we had to consider also the systematic uncertainty associated to the contaminant subtraction σ_{sub}^{sys}.

total log ft	σ^{par}	σ_{sub}^{sys}	σ_R^{sys}	σ_{alg}^{sys}	σ_{tot}
3.725	0.012	0.010	0.049	0.015	0.054

total B(GT)	σ^{par}	σ^{sub}	σ_R^{sys}	σ_{alg}^{sys}	σ_{tot}
0.727	0.020	0.017	0.082	0.025	0.090

Table 4.7: Total log ft and B(GT) values for the ^{150}Ho 9^+ decay integrated up to 7120 keV. The uncertainties associated with the strength calculation σ^{par}, the contaminant subtraction σ_{sub}^{sys}, the dependence on the de-excitation scheme σ_R^{sys}, the dependence on the analysis algorithm σ_{alg}^{sys} and its squared quadratic sum σ_{tot} are given explicitly.

Chapter 5

The Interpretation of the Results

5.1 Discussion of the results

From the observation of the strength functions plotted in sections 4.6 and 4.7 we can reach a quantitative understanding of the physics involved in the ^{150}Ho 2^- and ^{150}Ho 9^+ decays respectively. In both cases, a concentration of the strength which can be interpreted as the GT resonance was observed at an excitation energy of $\sim$4.5 MeV. However, further quantitave knowledge requires a comparison with theoretical calculations, which at the present time are unfortunately only available for the ^{150}Ho 2^- decay.

A shell model calculation based on effective two-body interactions was carried out by J. Blomqvist [BLO98] in order to investigate the excitation energies of the 1^-, 2^- and 3^- states corresponding to the dominant $\pi\mathrm{h}_{11/2}\pi\mathrm{d}_{3/2}\nu\mathrm{h}_{9/2}\nu\mathrm{f}_{7/2}$ configuration involved in the GT resonance of the ^{150}Ho 2^- decay. The calculation consists basically in a diagonalisation which provides the excitation energies of the states in a restricted (but dominant) configuration space. The important feature is that all the effective interactions used and given in Table [5.1] correspond to experimental values , with the exception of $\pi\mathrm{d}_{3/2}\nu\mathrm{h}_{9/2}$ [BLO98], taken from [LAC91] [ZHA93] [STY87] [TAI89] and references therein. The six $\pi\pi$ 0^+ matrix elements for $\mathrm{h}^2_{11/2}$, $\mathrm{s}^2_{1/2}$ and $\mathrm{d}^2_{3/2}$ were introduced in order to represent reasonably the proton pairing. The off-diagonal matrix elements were taken proportional to $(2J_1+1)(2J_2+1)$ and the overall strength fixed by putting the ^{148}Dy ground state at zero. Thus, the ground state of ^{150}Ho 2^- was assigned 75.8% to $\pi\mathrm{h}^2_{11/2}\pi\mathrm{d}_{3/2}\nu\mathrm{f}_{7/2}$, 17.04% to $\pi\mathrm{s}^2_{1/2}\pi\mathrm{d}_{3/2}\nu\mathrm{f}_{7/2}$ and 7.16% to $\pi\mathrm{d}^3_{3/2}\nu\mathrm{f}_{7/2}$.

The excitation energies of the most intense calculated levels are in excellent agreement (within 40 keV) with the positions of the resonances observed both in this work and in an independent high resolution experiment with the Cluster Cube [AGR97]. This certainly confirms that the narrow resonance found experimentally is the GT-resonance corresponding to the $\mathrm{h}_{11/2} \rightarrow \mathrm{h}_{9/2}$ transition. In order to calculate more precisely the strength to each one of the levels considered, A. Gadea performed a shell model calculation with OXBASH [BRO84] by using the same two-body interactions from Table [5.1]. In this way, the fraction of B(GT) to each individual level was obtained.

Configuration	I^π	V (keV)	Configuration	I^π	V (keV)
$\pi h_{11/2}^2$	0^+	-1607	$\pi d_{3/2}^2$	0^+	-269
	2^+	-865		2^+	200
	4^+	-115	$\pi d_{3/2} \pi s_{1/2}$	0^+	-473
	6^+	189		1^+	400
	8^+	290	$\pi d_{3/2} \nu f_{7/2}$	2^-	-774
	10^+	377		3^-	-59
$\pi h_{11/2} \pi d_{3/2}$	0^+	1159		4^-	-177
	4^-	251		5^-	-429
	5^-	428	$\pi d_{3/2} \nu h_{9/2}$	3^-	-200
	6^-	579		4^-	-100
	7^-	-5		5^-	0
$\pi h_{11/2} \pi s_{1/2}$	0^+	819		6^-	-300
	5^-	-141	$\pi s_{1/2} \pi s_{1/2}$	0^+	66
	6^-	363	$\pi s_{1/2} \nu f_{7/2}$	3^-	-326
$\pi h_{11/2} \nu f_{7/2}$	2^+	-394		4^-	-411
	3^+	-291	$\nu f_{7/2}^2$	0^+	-1642
	4^+	-197		2^+	-858
	5^+	-221		4^+	-226
	6^+	-146		6^+	169
	7^+	-244	$\nu f_{7/2} \nu h_{9/2}$	1^+	-189
	8^+	-166		2^+	-293
	9^+	-482		3^+	-169
$\pi h_{11/2} \nu h_{9/2}$	1^+	-1349		4^+	-200
	2^+	-839		5^+	-179
	3^+	-399		6^+	-256
	4^+	-419		7^+	-170
	5^+	-299		8^+	-345
	6^+	-359			
	7^+	-279			
	8^+	-315			
	9^+	-246			
	10^+	-485			

Table 5.1: Two-body matrix elements used in the shell model calculation of J. Blomqvist [BLO98].

The results of this calculation are compared to the experimental ones in Fig. [5.1], where the theoretical B(GT) values are plotted on an arbitrary scale. The contributions of the individual states of given spin and parity are explicitly marked by circles (1^- states), squares (2^- states) and triangles (3^- states). Due to the extremely restricted configuration space used in the calculation, we do not expect a meaningful interpretation of the Gamow–Teller quenching from it. The aim of the calculation is to illustrate that the shape of the distribution, in particular the narrowness of the resonance, is a consequence of the fact that most of the strength occurs to a few levels between 4.3 and 4.4 MeV. The calculation by [GAD98] reveals that 23.9% of the strength is concentrated in one of 12 1^- states, 24.4% in one of 19 2^- states and 49.0% in one of 25 3^- states. The remaining 2.7% of the B(GT) is extended to higher excitation energies. However, this weak effect is not enough to explain the tail in the experimental distribution up to the Q_{EC}, which is most probably produced by configuration mixing.

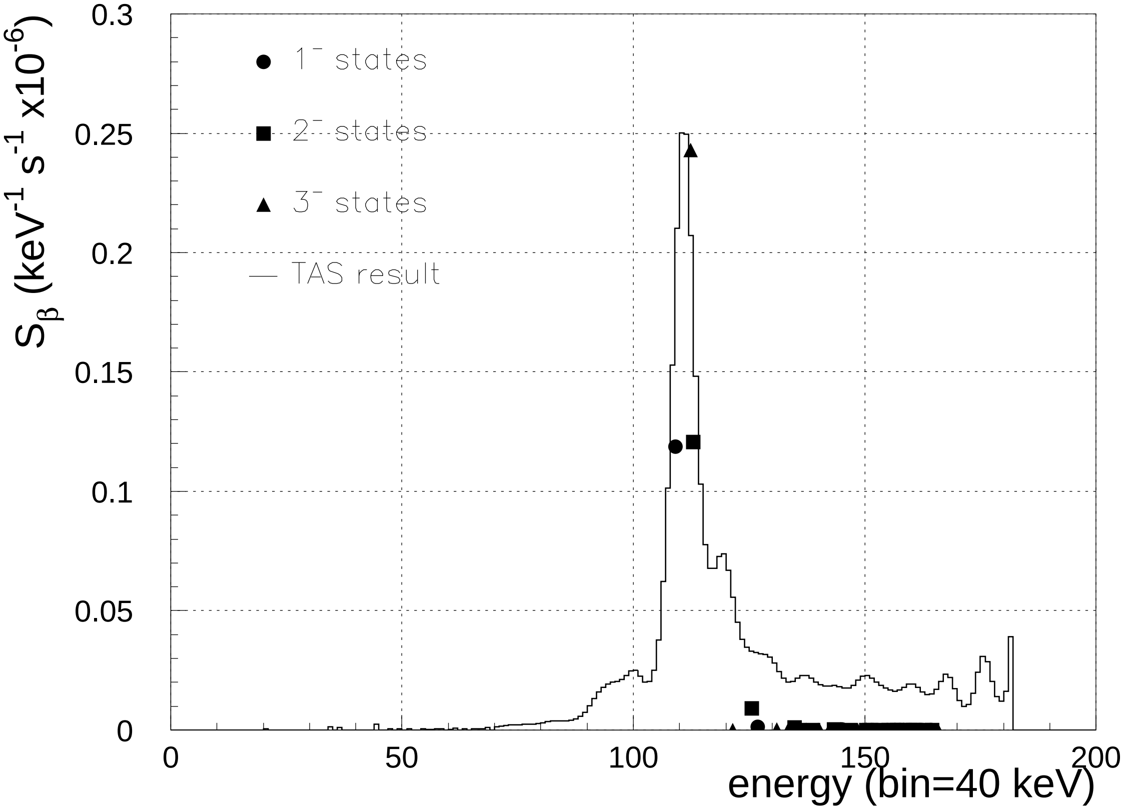

Figure 5.1: Comparison between the experimental and calculated (in arbitrary units) strength distributions for the ^{150}Ho 2^- decay.

Fig. [5.2] shows the comparison between the strength distributions of the ^{150}Ho 2^- (solid) and ^{150}Ho 9^+ (dashed) decays. The first thing we can observe is that the strength distribution for ^{150}Ho 9^+ presents a larger spreading in energy than the one for ^{150}Ho 2^-. This can be partially understood as a consequence of the larger number of accessible states in the high spin decay ($44 \times 8^+$, $36 \times 9^+$ and $28 \times 10^+$) as compared to the low spin decay ($12 \times 1^-$, $19 \times 2^-$ and $25 \times 3^-$). On the other hand, the number of other states of the same spin and parity in the region grows roughly as $(2J + 1)$, and thus, the mixing is expected to be larger for the higher spins. The resonance for the high spin isomer seems to be at lower excitation energy than for the low spin. The dominant peak in the ^{150}Ho 9^+ strength at about 4.3 MeV could be interpreted as intense transitions to few levels at such energies. Actually, feeding to such levels was observed in a previous high resolution experiment [GAD94] of much lower sensitivity.

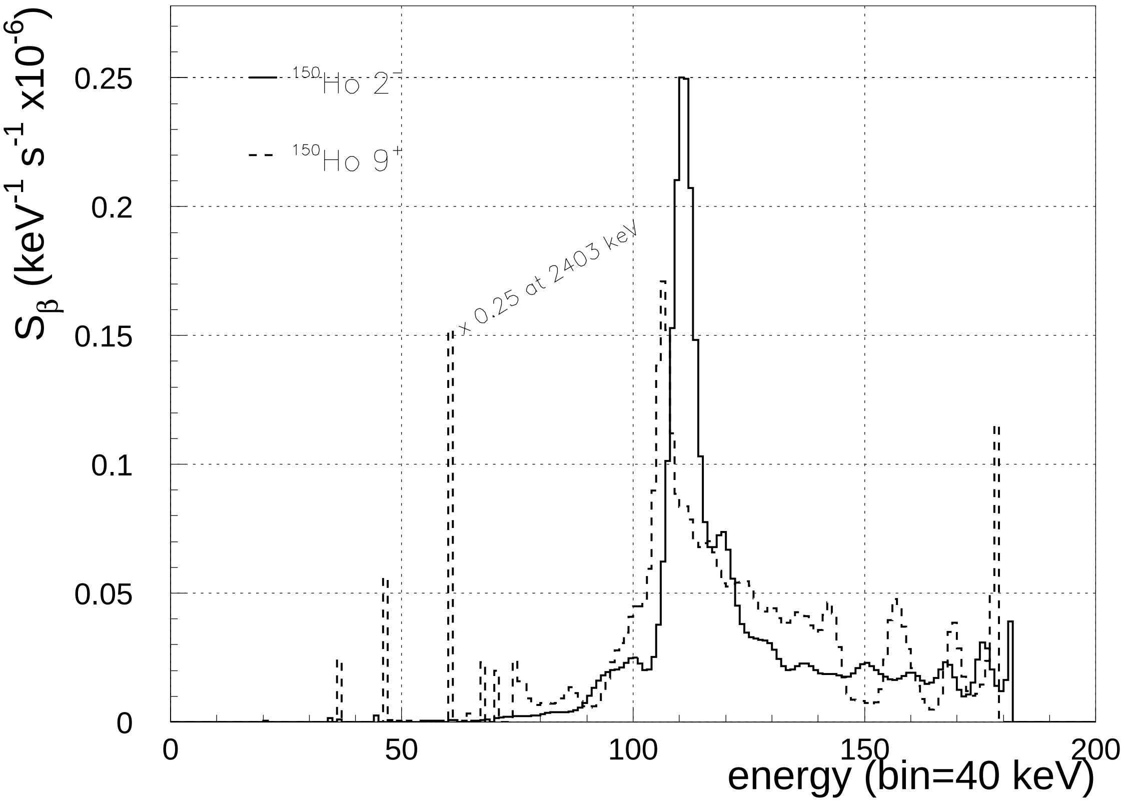

Figure 5.2: Comparison between the experimental strength distributions for the ^{150}Ho 2^- (solid) and ^{150}Ho 9^+ (dashed) decays.

In order to have a deeper understanding of these features, a comparison with a complete calculation would be necessary. The actual technology does not permit us to access the problem by a full shell model calculation in the ^{146}Gd region. The sub-shell closure forces us to consider a configuration space which is certainly too large. But there are other kind of calculation like the QRPA which can provide some information on the strength distribution, also in the ^{146}Gd region [KLE85] [SUH88]. Unfortunately, only decays of even-even nuclei can be studied by them, since the 4qp-states can not be generated within the framework defined by the QRPA (particle-hole excitations). The problem of the decay for the odd-odd case could be however treated with a 2^{nd}-order QRPA calculation. Such calculations should be feasible in practice, but the fact that they have not been done makes us think that some major difficulties must be involved. But the discussion on the total B(GT) values found can still take place. There is a set of calculations which allow us to estimate the different effects which may cause a hindrance of the total B(GT) for N=82 nuclei [TOW85]. Since the $f_{7/2}$ neutron is merely a spectator in the ^{150}Ho 2^- and ^{150}Ho 9^+ decays, we can still use our results for the comparison with the predicted values.

The retardation mechanism for the GT-transitions can be quantified [TOW85] by defining a *hindrance factor* h as

$$h = \frac{\mathrm{B}_{ESP}(\mathrm{GT})}{\mathrm{B}_{exp}(\mathrm{GT})} \tag{5.1}$$

where $\mathrm{B}_{exp}(\mathrm{GT})$ is the experimental value and $\mathrm{B}_{ESP}(\mathrm{GT})$ is the extreme single particle (ESP) shell model prediction. For nuclei of even mass, $\mathrm{B}_{ESP}(\mathrm{GT})$ adopts the form [TOW85]

$$\mathrm{B}_{ESP}(\mathrm{GT}) = n\frac{4\ell}{2\ell+1} \tag{5.2}$$

where n is the number of protons in the initial orbital ($h_{11/2}$ in our case) of angular momentum ℓ ($\ell = 5$ in our case). The remarkable point is that the typical values found in the literature are large and vary between $h = 5$ to 8.

According to [TOW85], three major effects contribute to the retardation of the GT-transitions: the pairing forces, the core polarisation and other higher order effects. This allows the decomposition of h as a product of three hindrance factors corresponding to the different effects:

$$h = h_{pair} \times h_{c.p.} \times h_{high} \tag{5.3}$$

The pairing forces smear out the sharp boundary between occupied and unoccupied orbitals of the ESP shell model. The impact this has on the hindrance factor was estimated in a standard BCS calculation [LAW80]. For $A = 146$ to 158, the pairing force strength was fixed at 0.2 MeV and the single particle orbital energies chosen so that the ^{147}Tb spectrum was reproduced. The BCS calculation was carried out separately for protons and neutrons, which permits us to adopt safely for $N = 83$ the values for $N = 82$ nuclei. Pairing correlations should be negligible for neutrons due to the $N = 82$ shell closure, and this has been confirmed by [TOW85].

The situation for our $N = 83$ cases, with one neutron in $f_{7/2}$, should not be too different. However, due to the closeness in energy of the $s_{1/2}$, $h_{11/2}$ and $d_{3/2}$ orbitals, pairing has to be properly considered on the proton side. The values of h_{pair} which were found are shown in Table [5.2].

	ℓ=5					
$n_{h_{11/2}}$	1	2	3	4	5	6
h_{pair}	0.80	1.19	1.22	1.40	1.40	1.51

Table 5.2: Values of h_{pair} calculated for even masses and for different occupation numbers $n_{h_{11/2}}$.

Of more importance than pairing is the role played by ground state correlations introduced by the proton-neutron interaction. This was treated in [TOW85] in terms of perturbation theory, by the so called 1^{st} order one-body and two-body core polarisation corrections. The correlations considered include only $h_{11/2}$ and $h_{9/2}$ orbitals. The influence of various finite range forces (zero-range and two different $\pi + \rho$ meson exchange potentials) on the hindrance factor was investigated. The results are shown in Table [5.3]

	ℓ=5					
$n_{h_{11/2}}$	1	2	3	4	5	6
$h_{c.p.}$	1.8 - 2.1	2.0 - 2.6	1.7 - 2.2	1.8 - 2.2	1.6 - 2.0	1.6 - 2.0

Table 5.3: Values of $h_{c.p.}$ calculated for various finite range forces different and different occupation numbers $n_{h_{11/2}}$.

The contribution of higher order effects was estimated by considering both the microscopic calculations available in light nuclei and the systematics of experimental data (see section 1.4 for more details). In going beyond first order in the core polarisation calculation, all the orbitals are involved and thus the perturbation series are slow to converge. At the same time one needs to consider other processes associated with isobar excitation and meson-exchange currents. All these contributions have been computed for closed-shell+1 nuclei in [TOW83]. The results could be expressed in terms of an equivalent effective GT one-body operator where a corrected $(\frac{g_A}{g_V})_{eff} \simeq 1.0$ was used instead of its free nucleon value. This is consistent with the shell model calculations in the *p*- [WIL73], *sd*- [BRO85] and *pf*- [PIN96] shells and with the strength systematics observed in (p, n) reactions when compared to the Ikeda sum rule [IKE63]. Thus, the hindrance factor from higher-order effects can be expressed as

$$h_{high} = \left|(\frac{g_A}{g_V})/(\frac{g_A}{g_V})_{eff}\right|^2 = 1.6 \tag{5.4}$$

We can find in Table [5.4] the results of multiplying all the contributions and giving the total hindrance factors h for the various occupancies n of the proton $h_{11/2}$ orbital. The possible ranges correspond to the $h_{c.p.}$ obtained for the various choices of effective interactions mentioned [TOW83].

	ℓ=5					
$n_{h_{11/2}}$	1	2	3	4	5	6
h	2.0 - 2.3	3.8 - 4.7	3.3 - 3.9	4.0 - 4.7	3.5 - 4.0	3.9 - 4.4

Table 5.4: Hindrance factors h calculated for even masses, for various choices of effective interactions and various occupancies n of the proton $h_{11/2}$ orbital.

The experimental B$_{exp}$(GT) (in $g_A^2/4\pi$ units) which have been found are:

$$^{150}\text{Ho } 2^- : \text{B}_{exp}(\text{GT}) = 0.577(43) \tag{5.5}$$

$$^{150}\text{Ho } 9^+ : \text{B}_{exp}(\text{GT}) = 0.727(90) \tag{5.6}$$

They are significantly smaller than the extreme single particle shell model (ESP) prediction B$_{ESP}$(GT)

$$^{150}\text{Ho } 2^- : \text{B}_{ESP}(\text{GT}) = 2\frac{4\cdot 5}{2\cdot 5+1} = 3.\overset{\frown}{63} \tag{5.7}$$

$$^{150}\text{Ho } 9^+ : \text{B}_{ESP}(\text{GT}) = 3\frac{4\cdot 5}{2\cdot 5+1} = 5.\overset{\frown}{45} \tag{5.8}$$

Comparing the experimental values in Eq. (5.5) and Eq. (5.6) with the respective theoretical expectations in Eq. (5.7) and Eq. (5.8), the hindrance factors are found to be

$$^{150}\text{Ho } 2^- : h = \frac{3.\overset{\frown}{63}}{0.577(43)} = 6.30(27) \tag{5.9}$$

$$^{150}\text{Ho } 9^+ : h = \frac{5.\overset{\frown}{45}}{0.727(90)} = 7.50(68) \tag{5.10}$$

The comparison of both hindrance factors evidences a slight dependence of h on the occupation number. Additionally, the values are slightly larger than the ones found by TAGS in the ^{100}Sn region [JAN98]. As an example, for the case of ^{97}Ag the comparison between the experimental B(GT) coming from a total absorption experiment [ZHU99] and the ESP prediction leads to a hindrance factor of $h = 4.15\pm0.55$.

A major difference with respect to the ESP shell model is that only $(12 \pm 3)\%$ instead of 1/3 of the total B(GT) goes to the yrast 8^+ 2qp-state. The ratio of the experimental B(GT)s for both isomers is however similar to the ESP prediction within the uncertainties.

$$\frac{\mathrm{B}_{ESP}^{^{150}\mathrm{Ho}\ 9^+}(\mathrm{GT})}{\mathrm{B}_{ESP}^{^{150}\mathrm{Ho}\ 2^-}(GT)} = \frac{3}{2} = 1.5 \simeq 1.26(17) = \frac{0.727(90)}{0.577(43)} = \frac{\mathrm{B}_{exp}^{^{150}\mathrm{Ho}\ 9^+}(\mathrm{GT})}{\mathrm{B}_{exp}^{^{150}\mathrm{Ho}\ 2^-}(\mathrm{GT})} \tag{5.11}$$

Fig. [5.3] shows a detailed comparison between the theoretical B(GT)=$h\times$ B_{ESP}(GT) from [TOW85] and several experimental results in the ^{146}Gd region, all coming from both high resolution [AGR97] [COL97] [KLE85] [MEC92] [MEN94] [MEN91] [NOL82] and total absorption experiments (this work). The theoretical values for different effective interactions as a function of the number of protons in $h_{11/2}$ lie inside the intervals marked by the vertical lines. A kind of *staggering* can be observed with the increasing $n_{h_{11/2}}$ number. This staggering is a consequence of the behaviour of the hindrance factors in Table [5.4]. For the even occupation number, the expected hindrance is larger than for the next odd one: by adding one more proton the hindrance decreases. From our results we see the opposite tendency.

The triangles in Fig. [5.3] correspond to the experimental B(GT) from several high resolution experiments. These values are clearly below the predicted ones and suffer from the low sensitivity of the Ge detectors. This has been confirmed by the total absorption values from this work, represented by squares in Fig. [5.3]. They are clearly above the previous results coming from high resolution spectroscopy, which certainly means that part of the intensity was missed in the earlier measurements. However, the B(GT)s obtained by TAGS are still below the theoretical estimations: 35% of the ^{150}Ho 2^- and 48% ^{150}Ho 9^+ B(GT) are missing respectively. An equivalent situation happens for the ^{100}Sn region, where the experimental B(GT) for ^{97}Ag is found to be 32% smaller than the calculations by [TOW85].

A QRPA calculation made for the decay of ^{148}Dy into ^{148}Tb [KLE85] overestimated the observed strength by a factor of ~6.7. Other QRPA calculations made for ^{148}Dy, ^{150}Er and ^{152}Yb [SUH88] indicate also an overestimation in the B(GT) by a factor of 4.3-5.7 after having considered the effect of pairing (BCS) and an effective axial-vector coupling constant $g_A^{eff}/g_V = 1.0$. However, the authors [SUH88] are able to reproduce the experimental B(GT) values by including a particle-particle (proton-neutron) interaction term. The same conclusion is addressed by [ENG88]. In fact, the study of the decays of ^{148}Dy, ^{150}Er and ^{152}Yb with $N = 82$ and ^{94}Ru and ^{96}Pd with N=50, ends up in calculated B(GT)s which are 2-3 times larger than the experimental values. And this happens after having applied all the corrections pointed out by [TOW85], namely pairing, core polarisation and the use of $(g_A/g_V) \simeq 1.0$ accounting for higher order effects. The authors [ENG88] have to introduce also a particle-particle (proton-neutron) interaction term in order to reproduce the experimental results. Thus, the question remains open and should be

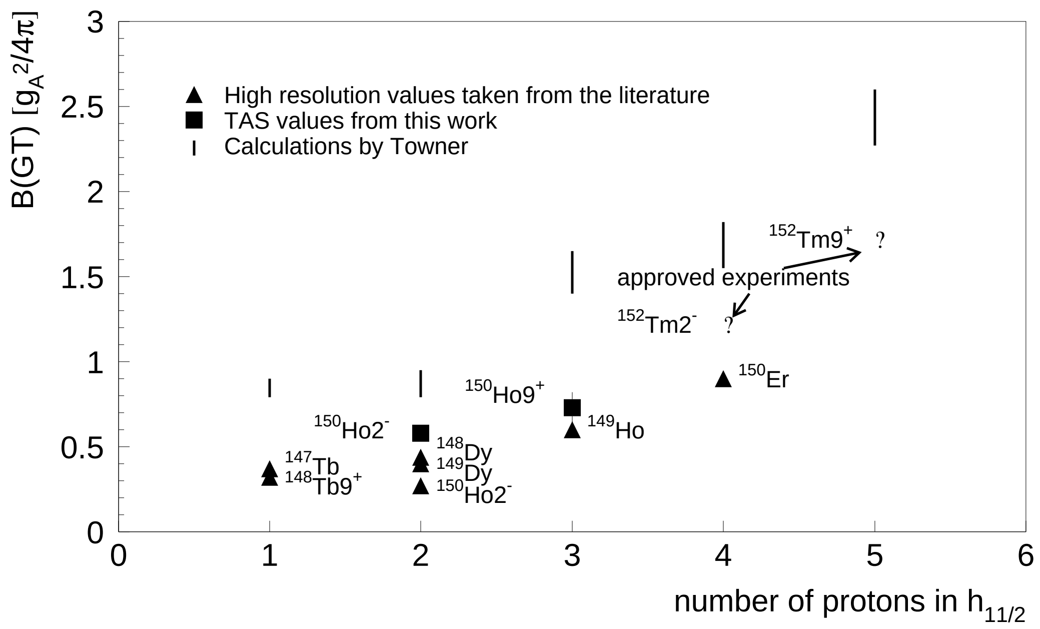

Figure 5.3: Comparison of B(GT) as a function of the number of protons in the $h_{11/2}$ orbital: theoretical values including hindrance factors (solid lines) taken from [TOW85], TAS results of this work (squares) and values coming from various high resolution experiments (triangles) [AGR97] [COL97] [KLE85] [MEC92] [MEN94] [MEN91] [NOL82].

subject of further theoretical investigation.

The results of two approved but still pending experiments could allow some further discussion. Pointed by arrows and signed by *question marks* are the next two isomers to be measured: ^{152}Tm2^- and ^{152}Tm9^+. Their configurations are analogous to the ^{150}Ho 2^- and ^{150}Ho 9^+ ones by placing one proton pair more in the $h_{11/2}$ orbital. The $B_{ESP}(GT)$ for the two cases are

$$^{152}\mathrm{Tm}\ 2^- : \mathrm{B}_{ESP}(\mathrm{GT}) = 4\frac{4\cdot 5}{2\cdot 5+1} = 7.\overset{\frown}{27} \tag{5.12}$$

$$^{152}\mathrm{Tm}\ 9^+ : \mathrm{B}_{ESP}(\mathrm{GT}) = 5\frac{4\cdot 5}{2\cdot 5+1} = 9.\overset{\frown}{09} \tag{5.13}$$

These two measurements are extremely important to explain the trend of the B(GT) with $n_{h_{11/2}}$. They will also allow a systematic study of the distribution of the strength, the β-intensity balance between 2qp and 4qp-states and the effect of pairing.

Chapter 6

Summary and Conclusions

6.1 Introduction

After reading this work it can be concluded that there are two major contributions in it. The first consists of the development of reliable analysis methods which have illustrated that Total Absorption Gamma-ray Spectroscopy is a powerful technique for measuring the β-strength. The second consists of the particular results obtained by TAGS for the decays of ^{150}Ho 2^- and ^{150}Ho 9^+.

We have dedicated much of our efforts to the first topic, since our belief was (and our conviction now is) that the TAGS technique is extremely powerful. Unfortunately, as has been mentioned several times, the complexity of the analysis has prevented TAGS from becoming popular. Thus, we decided to start our work with the progressive development of the tools related to our problem, which fortunately ended in solid and unambiguous analysis methods. The first task in the program was to obtain the response of our NaI(Tl) TAS by Monte Carlo simulation. The procedure, which is described in section 3.2, turned out to be more difficult than expected. It took us time to re-discover that the scintillation light production mechanism had to be included in the simulation in order to get the right result. All the details of this topic can be found in [CAN99a]. At the same time, we were also worried about the influence of the electronic pulse pileup on the data. This has been mentioned only briefly in this work, and presented for the correction of the experimental TAS spectra in section 4.3 and 4.4. But the algorithm behind the correction permits a high quality reproduction of the effect by use of the true pulse shape of the amplification system. All the details can be found in [CAN99b]. These first two pieces were presented in 1998 as a Diploma work within the PhD program at the University of Valencia.

The next step was to look for the correct methods which permit us to solve the inverse problem as presented in Eq. (3.3). The implementation of the three algorithms described in section 3.3, its understanding, debugging and upgrading ended up in the final FORTRAN programs which have been used in this work. In the following sections we will go through the details of the major goals achieved in this work, separating the discussion of the instrumental considerations from the physical results.

6.2 The analysis

Most of the criticism against TAGS can be summarised in two questions: How do we construct the response of the apparatus? How do we extract the feeding distribution from the spectra measured? We will not spend more time discussing the Monte Carlo simulation, since the details can be found in section 3.2 and in [CAN99a]. The main point is that in order to construct the response matrix **R** the branching ratios of all γ-transitions occurring in the decay are demanded. The usual situation is that only a part of the level scheme of the daughter nucleus at low excitation energies is known, and thus, the rest of the transitions have to be invented. This situation is certainly unpleasant, but we can get rid of it by two features: the high efficiency of our spectrometer and the comparison between the results obtained for the different assumptions made. In the ideal TAS limit, the dependency on the branching ratios disappears, and thus we may expect that for a high efficiency spectrometer like the GSI TAS, the dependency is rather weak. This does not mean there is no dependency. It means that as soon as we make use of a response for a given de-excitation path which contains the right properties like multiplicity and total energy, this response will be very similar to the real unknown de-excitation. In any case, it is possible to evaluate the systematic uncertainties in the results by comparison of several analysis made with different responses. The comparison for the cases studied in this work can be seen in Fig. [4.19] and Fig. [4.24].

This brings us to the second question, namely how the results are obtained. We have seen in chapter 2 that the procedures to extract the feeding distributions are far from being trivial. We could have approached the problem by looking at which feeding distributions are able to reproduce the data by a direct comparison with a Monte Carlo calculation. However, this technique has two problems. The ill-conditioned nature of the problem allows completely unphysical feeding distributions to be used to reproduce the same set of data. As was mentioned in section 3.1, this is the typical result when a direct inversion of Eq. (3.3) without any kind of regularisation is attempted. Additionally, the direct comparison does not permit a satisfactory determination of the uncertainties in the results coming from the uncertainties in the data. In order to be able to estimate the uncertainties, a real inversion of the problem is demanded, and this is what is achieved through the methods described in subsections 3.3.1, 3.3.2 and 3.3.3. The features of the three methods can be summarised as follows:

LR Linear Regularisation: minimisation of the least squares estimator under the condition that the solutions have to be smooth. The degree of smoothness is given by the regularisation functional and its weight is defined by a regularisation parameter. The solutions and its uncertainties are found by solving a set of linear equations and depend on the regularisation parameter. The solutions can be negative.

ME Maximum Entropy: maximises the information theoretic entropy consistent to the least squares estimator. It can be considered as a regularisation method with a non-linear regularisation functional. The minimisation cannot be done analytically and in our formulation the solutions are found in an iterative way. The solutions are always positive. As in the case of LR, they and their associated uncertainties depend on the regularisation parameter.

EM Expectation-Maximisation: It is an iterative application of Bayes formula. The solutions are always positive and its uncertainties do not depend on any arbitrary parameter.

After the application of the three methods, we have observed that the solutions found for our specific cases shown in Fig. [4.20] and Fig. [4.28] are very similar. The differences between them determine the systematic uncertainties coming from the analysis technique applied. We consider that the EM method is best adapted to our problem: it is easy to implement and the solutions found are always positive because the method intrinsically deals with probabilities. They do not depend on the arbitrary election of a parameter and the convergence of the method is very fast. There is still the problem of where to stop the iterations, but in practice this can be done as soon as the solutions start to reproduce the statistical oscillations of the data.

The strengths derived from total absorption measurements have to be interpreted as average distributions, which is implicit however in the definition of strength function. The detailed structure of the decay is not reachable by means of a low resolution detector like a TAS, and thus, we will always have to refer to high resolution spectroscopy data if particular details are needed. The correctness of the shape has been proven by inter-comparison of the results of different analysis, although large systematic uncertainties of 40% were found for particular energy bins. This is a consequence of the strong correlations present in contiguous bins in the feeding distributions, which can introduce significant variations bin to bin when converted into strength. However, the integral properties are much better preserved, and the accuracy in the integrated B(GT) achieved was of 5% for ^{150}Ho 2^- and 9% in the case of ^{150}Ho 9^+. This is a consequence of the ~100% detection efficiency of the TAS.

After this discussion we may conclude that we have been able to solve the inverse problem of the TAGS analysis, and that for the first time the uncertainties in the strength could be given in a consistent way. In fact, it turned out that the most critical part concerning the technique is the purity of the measured spectra. The X-ray tagging is seen to be a more than desirable feature even if its efficiency is small. The EC spectra obtained in this way are almost free of contamination. The major difficulties found during the analysis mostly come from the β^+ component analysis, and its origin was mainly due to contaminations in the β^+ spectra. This does not mean that the technique is not well suited for measuring the strength from pure β^+ decays, but only that much care has to be taken in order to measure clean spectra.

6.3 The results for ^{150}Ho 2^- and ^{150}Ho 9^+

The result of the total absorption measurements exposed in this work provided the β-strength functions of Fig. [6.1] for the ^{150}Ho 2^- (solid) and ^{150}Ho 9^+ (dashed) decays.

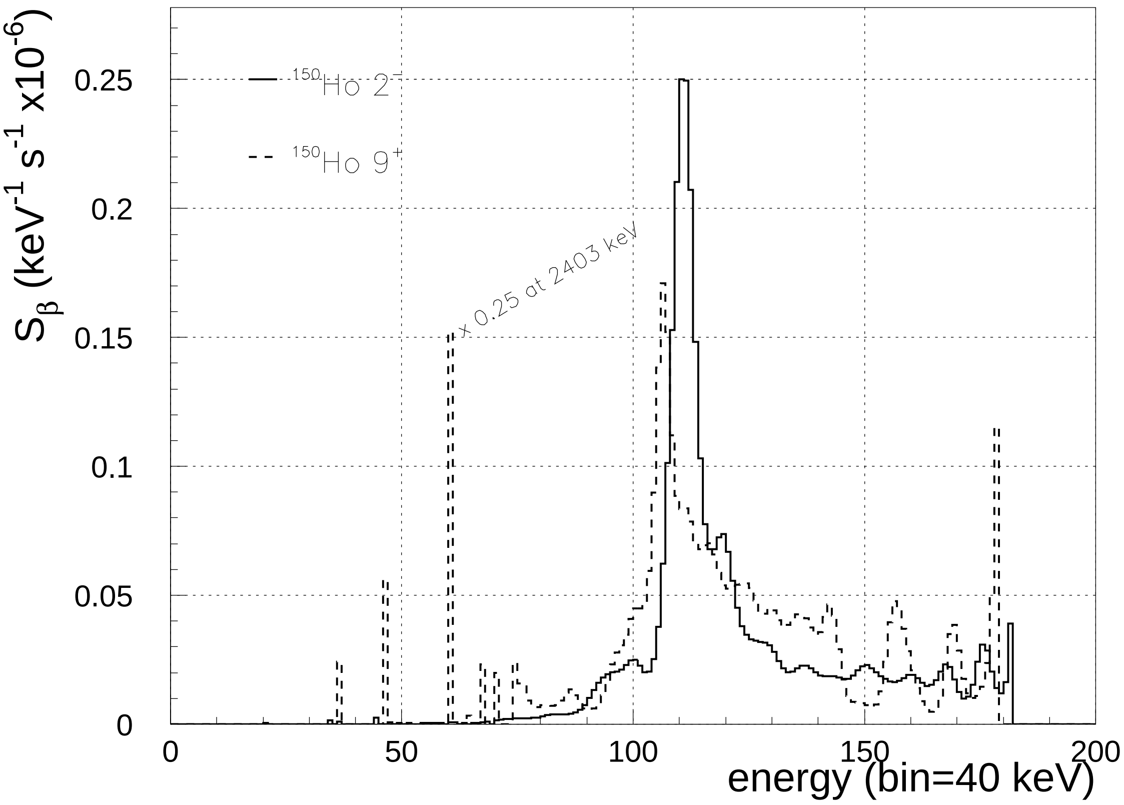

Figure 6.1: Comparison between the experimental strength distribution for the ^{150}Ho 2^- (solid) and ^{150}Ho 9^+ (dashed) decays.

Both Gamow-Teller resonances were found to be inside the Q_{EC} window. The resonance for the ^{150}Ho 2^- occurs at an excitation energy of 4.5 MeV and is extremely narrow ($\sim$ 240 keV fwhm). A shell model calculation by J. Blomqvist has shown that within the $(\pi h_{11/2})^2_{0^+}$ $(\pi d_{3/2}\ \nu f_{7/2})_{2^-}$ configuration, the strength proceeds into a very few 1^-, 2^- and 3^- states at ~4.5 MeV. Thus, the observation of a sharp resonance suggests a very similar situation to that predicted by the ESP. The larger number of accessible levels in the ^{150}Ho 9^+ decay causes the strength to be more spread out in the case of the high spin isomer. However, a strong component was found at an excitation energy of ~4.3 MeV, which probably corresponds to a few strongly fed levels observed in a previous high resolution experiment of lower sensitivity [GAD94].

The ratio of the experimental B(GT) values for both isomers given in Eq. [6.1] are very similar to the ESP predicted ones.

$$\frac{\mathrm{B}_{ESP}^{^{150}\mathrm{Ho}\ 9^+}(\mathrm{GT})}{\mathrm{B}_{ESP}^{^{150}\mathrm{Ho}\ 2^-}(GT)} = \frac{3}{2} = 1.5 \simeq 1.26(17) = \frac{0.727(90)}{0.577(43)} = \frac{\mathrm{B}_{exp}^{^{150}\mathrm{Ho}\ 9^+}(\mathrm{GT})}{\mathrm{B}_{exp}^{^{150}\mathrm{Ho}\ 2^-}(\mathrm{GT})} \tag{6.1}$$

This can be understood if the causes of the quenching act in a smooth way. On the other hand, it has been observed that the distribution of the strength between the 2qp and 4qp-states predicted by the ESP picture of the high spin isomer is not right. Only $(12 \pm 3)\%$ instead of 1/3 of the total B(GT) goes to the yrast 8^+ 2qp-state.

Isotope	$T_{1/2}$ (s)	Q_{EC} (keV)	B_{exp}(GT)	B_{ESP}(GT)	h	$h^{(1)}_{calc}$
^{150}Ho 2^-	72(4)	7372(27)	0.577(43)	$3.\overset{\frown}{63}$	6.30(27)	3.8 - 4.7
^{150}Ho 9^+	23.3(3)	7390(60)	0.727(90)	$5.\overset{\frown}{45}$	7.50(68)	3.3 - 3.9

(1) hindrance factors calculated by [TOW85]

Table 6.1: Experimental and ESP B(GT) for the isotopes studied. The experimental and calculated hindrance factors are also given together with the decay energies (Q_{EC}) and half-lives ($T_{1/2}$).

Table [6.1] also presents the comparison between the experimental hindrance factors and the corresponding calculated ones [TOW85]. The discrepancies reveal that the suppression of about 40% of the B(GT) is still not explained by theory, and this problem has also been found in the results of several TAGS experiments in the ^{100}Sn region.

6.4 Concluding remarks

Our desire is that this work will set a new standard concerning the analysis of total absorption spectroscopy experiments, which we consider as the best way to determine the β-strength from β-decay. These wishes have been already partially fulfilled by the approval of a new series of experiments on the ^{152}Tm isomers at GSI (Darmstadt-St.Petersburg-Valencia-Warsaw collaboration) and on lighter $N = Z \simeq 35$ nuclei at ISOLDE (Madrid-Strasbourg-Surrey-Valencia collaboration).

Chapter 7

Resumen del trabajo

7.1 Introducción

El trabajo expuesto en la presente memoria surge del interés por el estudio de las desintegraciones β Gamow-Teller (GT), en particular, sobre cómo medir de una manera fiable la intensidad con la que son poblados los estados nucleares tras una desintegración GT. Una forma habitual de representar esta cantidad es mediante la B(GT), que hace referencia explícita a la intensidad de las transiciones entre niveles concretos. Desde el punto de vista experimental, puede ser preferible definir la intensidad GT mediante la magnitud $S_\beta(E_x)$, denominada función de intensidad β. Dicha magnitud es el promedio de la intensidad B(GT) a todos los niveles dentro un intervalo (canal) de energía a una energía con excitación central E_x (ver sección 1.3 para su definición y más detalles).

El conocimiento de la S_β aporta una información muy valiosa sobre las funciones de onda nucleares, y por tanto, sobre la interacción nuclear residual. Así mismo, permite también comprender otros fenómenos dentro del ámbito de la física nuclear. Un ejemplo puede ser la relación existente entre la forma de la distribución S_β y la deformación de los núcleos $N = Z$, como mencionan [HAM95] y [SAR98]. Otro ejemplo viene dado por la necesidad de calibrar la interacción de los cálculos QRPA realizados para entender los posibles mecanismos de supresión del proceso de doble desintegración β [ENG88]. En la compilación de artículos realizada por Klapdor [KLA83], puede encontrarse una gran variedad de problemas para los cuales es necesario conocer fiablemente la distribución S_β. La vigencia de los argumentos expuestos en [KLA83] puede ilustrarse mediante dos ejemplos recientes. El primero viene dado por el detector de argon líquido ICARUS, que está siendo construido para estudiar el problema de los neutrinos solares [ZUB98]. Con ICARUS se prentende registrar la cantidad de neutrinos que llegan del sol y sus posibles oscilaciones. Para poder calibrar dicho detector, es perentorio conocer la sección eficaz de la reacción $^{40}\mathrm{Ar}(\nu_e, e)^{40}\mathrm{K}$. Esto ha sido posible gracias al estudio del proceso especular, mediante medida de la la probabilidad de desintegración β del ^{40}Ti en los estados excitados del ^{40}Sc. El segundo ejemplo está relacionado con los reactores nucleares. Existe una diferencia notable entre las medidas del *decay heat* (energía liberada en forma de radiación γ por los productos de fisión tras el apagado del reactor) y los cálculos integrales que combinan librerías experimentales y modelos teóricos. Según un estudio reciente [YOS99], tal discrepancia tiene su origen en medidas poco fiables de la S_β para algunos pocos isótopos. Dilucidar este problema tendría sin duda impacto, tanto en cuestiones de seguridad como de diseño de los reactores.

La cuestión de cómo medir fiablemente la S_β cobra especial importancia si tenemos en cuenta que los cálculos teóricos no son capaces de reproducir los valores experimentales. La comparación de las medidas de S_β con el modelo de capas de monopartícula extremo revela discrepancias de hasta varios órdenes de magnitud. La situación mejora con el uso de una descripción más detallada del núcleo, pero sigue siendo necesario renormalizar los observables Gamow-Teller mediante un factor de supresión $q < 1$. También suele emplearse la magnitud inversa denominada factor de retardo $h > 1$.

La comparación entre las medidas de desintegración β para núcleos ligeros con cálculos de modelo de capas sugiere el uso de factores de supresión $q = 0.897 \pm 0.035$ para los cálculos en la capa p [WIL73], $q = 0.76 \pm 0.03$ para la capa sd [BRO85] y $q = 0.744 \pm 0.015$ para la capa pf [PIN96]. Los experimentos de intercambio de carga (p, n) [GOO80] [GOO82] [GAA80] y (n, p) [VET82] [VET89] [MAD87a] [MAD87b] permiten medir la intensidad GT en un rango de energías que va más allá del valor Q de la desintegración β. También ponen de manifiesto que la intensidad observada es menor que la esperada, lo que implica según la regla de la suma de Ikeda [IKE63] que la intensidad GT debe estar localizada a energías de excitación aún mayores.

Una posible explicación al *problema de la intensidad Gamow-Teller perdida* es que, debido a efectos subnucleónicos, la constante axial-vector g_A adopte un valor menor en materia nuclear del que se le atribuye en el vacío. Otra explicación puede ser que las correlaciones nucleares hagan necesario renormalizar el operador Gamow-Teller. En cualquiera de los casos, es fundamental poder garantizar que los valores experimentales son correctos y no sufren una patología de origen sistemático. Es bien sabido que las funciones de intensidad β medidas en experimentos de intercambio de carga sufren de problemas de sustracción de fondo [OST82] y de incertidumbres en el cálculo de la sección eficaz de la reacción [TAD87]. Los medidas de desintegración β mediante espectroscopía de alta resolución con detectores de Ge hiperpuros ofrecen una alternativa más selectiva. Usualmente, la S_β se determina en dos pasos. Primeramente se construye el esquema de desexcitación del núcleo hijo mediante la técnica de coincidencias $\gamma - \gamma$. Después se obtiene la distribución poblaciones por el balance de intensidades de las transiciones γ que pueblan y desexcitan cada nivel. La S_β se calcula fianlmente a partir de la Eq. (1.34) siempre que se conozcan el semiperiodo $T_{1/2}$ y el valor Q de la desintegración. Sin embargo, se ha comprobado [HAR77] que la limitada eficiencia de los detectores de Ge hace que la intensidad β determinada de esta manera, tienda a estar desplazada hacia las energías de excitación más bajas. La técnica requiere implícitamente la detección de *todas* las cascadas γ involucradas en la desintegración. Desgraciadamente esto no es posible en la mayoría de los casos, especialmente cuando la intensidad β recae en niveles a altas energías de excitación. La fragmentación de la intensidad β, el gran número de vías de desexcitación que tiene un nivel y la baja probabilidad de detectar rayos γ de alta energía provocan que la determinación de las probabilidades de transición sea errónea.

Una solución al problema viene dada por la Espectroscopía Gamma de Absorción Total (EGAT), empleada por primera vez en ISOLDE [DUK70]. Si dispusieramos un detector ideal con 100% de eficiencia y resolución infinita, denominado Espectrómetro de Absorción Total (EAT), podríamos medir directamente la distribución de poblaciones, y por tanto, la S_β. Para cada desintegración, el EAT registraría una cuenta a la energía del nivel poblado, como resultado de sumar todas las energías de los γ involucrados en la desexcitación del nivel. El espectro final sería direcamente la distribución desto poblaciones, y la obtención de S_β por tanto inmediata. Un EAT real tiene, por el contrario, una eficiencia y resolución limitadas, lo que hace que el espectro medido deje de ser la distribución de poblaciones y deba ser procesado. La complejidad que implica este análisis es tal, que ha evitado que la EGAT, a pesar de sus ventajas, se convierta en una técnica popular. En efecto, para obtener las poblaciones $\mathbf{f}$ a partir de los datos $\mathbf{d}$, es necesario invertir una ecuación del tipo $\mathbf{d} = \mathbf{R} \cdot \mathbf{f}$. La primera dificultad que se encuentra es cómo construir la matriz de respuesta $\mathbf{R}$ del espectrómetro (ver sección 3.2 y [CAN99a]), que depende del esquema de desexcitación del núcleo. En [CAN99a] se demuestra que esto puede ser conseguido con alto grado detalle mediante la simulación Monte Carlo. La segunda dificultad es que el problema inverso planteado está muy mal condicionado, es decir, el número de soluciones distintas y compatibles con los datos experimentales es infinito. Afortunadamente, este trabajo demuestra que el problema puede ser resuelto de una forma consistente y rigurosa mediante el uso de información *a priori* y los algoritmos descritos en la sección 3.3.

Las medidas mostradas en el capítulo 4 se han realizado con el EAT de NaI(Tl) ubicado en el separador de masas del GSI de Darmstadt [KAR97] (ver capítulo 2 para más detalles). Dicho espectrómetro fue diseñado y construido por Michael Nitschke en el Lawrence Berkely Laboratory para estudiar desintegraciones EC/β^+. Como dato decir que posee una eficiencia ~3.5 veces mayor que la del de ISOLDE. El EAT permite medir independientemente las componentes EC y β^+ mediante el uso de coincidencias con rayos X y con partículas β. Desde su traslado e instalación en el GSI, ha sido empleado en sendas campañas de medidas de intensidad GT en las regiones del ^{100}Sn y el ^{146}Gd. Para dichos núcleos, un protón en un orbital de alto J decae a su homólogo espín-órbita con J-1. Este orbital suele estar en general menos ligado que el orbital de neutrón J, y por tanto vacío. Las transiciones GT que se han estudiado son las $\pi g_{9/2} \rightarrow \nu g_{7/2}$ para los núcleos bajo el ^{100}Sn y $\pi h_{11/2} \rightarrow \nu h_{9/2}$ para los núcleos por encima del ^{146}Gd. En ambos casos se espera que la resonancia GT esté dentro de la ventana de energías permitida (limitada por el valor Q).

El trabajo expuesto en la memoria puede dividirse en dos contribuciones. La primera consiste en el desarrollo de métodos de análisis fiables que han demostrado que la Espectroscopía Gamma de Absorción Total es una técnica tremendamente poderosa a la hora de medir la S_β. La segunda contribución son las medidas y resultados obtenidos mediante EGAT para los isótopos ^{150}Ho 2^- y ^{150}Ho 9^+.

7.2 Las técnicas de análisis

La mayoría de las críticas contra la EGAT están relacionadas con la construcción de la matriz de respuesta **R** y la resolución del problema inverso.

Para construir **R** es necesario conocer el esquema de desexcitación completo del núcleo hijo. Usualmente, éste solo se conoce parcialmente, por lo que la información debe ser completada con hipótesis lo más realistas posibles. Esta situación es sin duda poco satisfactoria, pero puede ser tratada gracias a la alta eficiencia del EAT del GSI (dependencia del esquema de desexcitación pequeña) y a una intercomparación de los resultados obtenidos para distintas **R**. Más aún, las diferencias halladas permiten estimar el error sistemático proveniente de las hipótesis realizadas.

La obtención de la distribución de poblaciones es un problema aún más complejo. Uno podría tratar de resolverlo mirando de forma directa qué distribución de poblaciones es capaz de reproducir los datos. El primer inconveniente que aparece es que uno no puede estar seguro del resultado, ya que muchas distribuciones de poblaciones distintas (algunas de ellas completamente inverosímiles) son capaces de reproducir los datos. El segundo problema es que de esta manera, no es posible decidir satisfactoriamente cuáles son las incertidumbres de la poblaciones. La única manera de resolver ambas cuestiones es resolver el problema inverso de verdad, y para ello se han desarrollado tres métodos distintos:

LR Método de Regularización Lineal. Minimización del estimador de mínimos cuadrados bajo la condición de que las soluciones deben ser suaves (comportamiento polinómico). El tipo de comportamiento viene impuesto por un funcional regularizador (multiplicador de Lagrange) y su peso está dado por un parámetro que debe ser escogido arbitrariamente. Las soluciones y sus incertidumbres se obtienen tras resolver un sistema de ecuaciones y dependen del parámetro de regularización. Las soluciones son siempre positivas.

ME Método de Máxima Entropía. Maximiza la entropía del sistema de manera consistente con el estimador de mínimos cuadrados. Se puede considerar también como un método de regularización con un funcional regularizador no lineal. La minimización no puede resolverse de manera analítica y la solución se obtiene de manera iterativa. Como para el método LR, las soluciones y sus incertidumbres dependen del parámetro de regularización. Una diferencia importante es que las soluciones no pueden ser negativas.

EM Maximización de la Expectación: es una aplicación iterativa de la fórmula de Bayes. Las soluciones y e incertidumbres son siempre positivas y no dependen de la elección de ningún parámetro.

Tras aplicar los tres métodos, se ha encontrado que las soluciones son muy parecidas entre sí en todos los casos (ver Fig. [4.20] y Fig. [4.28]). Las diferencias entre ellas dan cuenta del error sistemático proveniente de los algoritmos de análisis. No obstante, razones varias permiten concluir que el método EM es el que se adapta mejor al problema inverso en EGAT. Es fácil de programar y las soluciones son siempre positivas porque usa intrínsecamente distribuciones de probabilidad. Además, los resultados no dependen de la elección de un parámetro arbitrario.

Las S_β resultantes de los experimentos de absorción total deben ser interpretadas como distribuciones promedio, cosa que viene implíctamente dada en la definición de S_β. La estructura detallada sobre cómo procede la desintegración no puede ser medida mediante un detector de baja resolución como el EAT de NaI(Tl). Para ello es necesario acudir a los experimentos de alta resolución con detectores de Ge. La validez de la forma de la distribución se puede garantizar mediante la intercomparación de los resultados de análisis distintos, si bien es cierto que los errores sistemáticos pueden ser grandes (40%) para algunos canales de energía concretos. Ésto se debe a las fuertes correlaciones existentes entre canales contiguos. Sin embargo, la alta eficiencia de detección hace que el valor integrado de la intensidad sea mucho menos sensible. Las incertidumbres en la S_β integrada ascienden a un 5% para el ^{150}Ho 2^- y 9% para el ^{150}Ho 9^+.

Para concluir, es pertinente recalcar que se ha conseguido resolver el problema inverso del anĺisis en EGAT, lo que ha permitido obtener la intensidad GT y sus incertidumbres de una manera consistente. Conseguido ésto, la parte más delicada de la técnica es la pureza de las medidas. Las contaminaciones afectan de manera muy especial al análisis de la componente β^+ de la desintegración, ya que la coincidencia con partículas β no es isotópicamente selectiva.

7.3 Resultados para los isótopos ^{150}Ho 2^- y ^{150}Ho 9^+

Las ditribuciones de intensidad GT obtenidas en este trabajo pueden verse en la Fig. [7.1] para los casos del ^{150}Ho 2^- (continuo) y del ^{150}Ho 9^+ (dicontinuo).

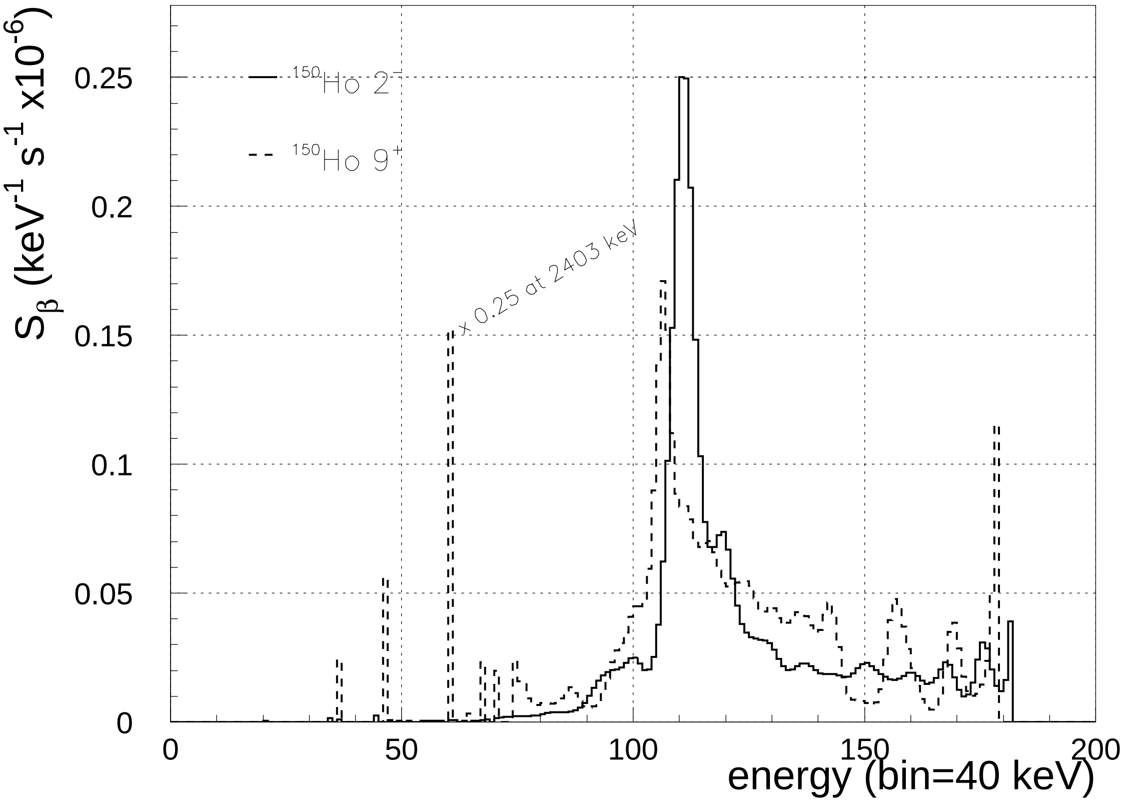

Figure 7.1: Comparación entre las distribuciones de intensidad GT para las desintegraciones del ^{150}Ho 2^- (continuo) y del ^{150}Ho 9^+ (discontinuo).

Se ha encontrado que ambas resonancias Gamow-Teller se encuentran dentro de la ventana definida por el Q_{EC}. La resonancia del ^{150}Ho 2^- es extremadamente estrecha ($\sim$ 240 keV de anchura a media altura) y está situada a 4.5 MeV de energía de excitación. Los cálculos de modelo de capas con interacciones fenomenológicas realizados por J. Blomqvist han mostrado que para la configuración $(\pi h_{11/2})^2_{0^+}$ $(\pi d_{3/2}\ \nu f_{7/2})_{2^-}$, la intensidad GT está repartida en muy pocos estados 1^-, 2^- y 3^- a unas energías de excitación de $\approx$4.5 MeV. La estrechez de la resonancia observada sugiere que la interpretación del modelo de capas de monopartícula extremo no se aleja mucho de la realidad. El mayor número de niveles accesibles en la desintegración del ^{150}Ho 9^+ hace que la intensidad esté más repartida para el caso de alto espín. Sin embargo, se ha observado una componente intensa a $\sim$4.3 MeV, que probablemete se corresponde con el reducido grupo de niveles detectado en un experimento anterior de alta resolución [GAD94].

En la Eq. [7.1] se puede comprobar que la razón entre las B(GT) experimentales de ambos isómeros es muy similar a la predicha por el modelo de capas de monopartícula extremo.

$$\frac{\mathrm{B}_{ESP}^{^{150}\mathrm{Ho}\ 9^+}(\mathrm{GT})}{\mathrm{B}_{ESP}^{^{150}\mathrm{Ho}\ 2^-}(GT)} = \frac{3}{2} = 1.5 \simeq 1.26(17) = \frac{0.727(90)}{0.577(43)} = \frac{\mathrm{B}_{exp}^{^{150}\mathrm{Ho}\ 9^+}(\mathrm{GT})}{\mathrm{B}_{exp}^{^{150}\mathrm{Ho}\ 2^-}(\mathrm{GT})} \tag{7.1}$$

Este hecho se puede interpretar como que las causas que originan la supresión de la B(GT) actúan de una manera similar (suave) en ambos casos. También se ha podido comprobar que la relación de intensidades entre los estados de 2 quasipartículas (qp) y 4qp predicha por el modelo de capas de monopartícula extremo no es correcta. En vez de 1/3 de la B(GT) total, solamente el $(12 \pm 3)\%$ va al estado yrast 8^+ de 2qp.

Isótopo	$\mathrm{T}_{1/2}$ (s)	Q_{EC} (keV)	B_{exp}(GT)	B_{ESP}(GT)	h	$h_{calc}^{(1)}$
^{150}Ho 2^-	72(4)	7372(27)	0.577(43)	$3.\overset{\frown}{63}$	6.30(27)	3.8 - 4.7
^{150}Ho 9^+	23.3(3)	7390(60)	0.727(90)	$5.\overset{\frown}{45}$	7.50(68)	3.3 - 3.9

$^{(1)}$ factores de retardo calculados por Towner [TOW85]

Table 7.1: Parámetros relevantes de las desintegraciones estudiadas.

La comparación entre los factores de retardo experimentales y los calculados por Towner [TOW85] se hallan en la Tabla [7.1]. Las discrepancias existentes revelan que sigue sin poder explicarse la supresión de un 40% de la B(GT) total. Las medidas realizadas en la región del ^{100}Sn indican el mismo problema.

7.4 Conclusiones finales

Nuestro deseo es que este trabajo establezca un nuevo estándar en lo referente al análisis de experimentos de EGAT. Consideramos que esta técnica proporciona los resultados más fiables sobre la distribución de intensidad Gamow-Teller extraída de las medidas de desintegración β. Parte de estos deseos ya se han visto cumplidos por la aceptación de dos nuevos experimentos en el GSI para estudiar los isómeros del ^{152}Tm (colaboración Darmstadt-San Petersburgo-Valencia-Varsovia), así como de otro para estudiar núcleos ligeros $N \simeq Z$ en ISOLDE (colaboración Madrid-Estrasburgo-Surrey-Valencia).

Appendix A

Calculation of the Strength and $\log ft$

The analysis methods provide the EC and β^+-feeding distributions and its uncertainties. They can be used independently or together in order to obtain the β-strength.

Considering the discrete nature of the data, the β-strength distribution for a given energy bin i can be obtained from Eq. A.1

$$S_{\beta_i} = \frac{1}{\Delta E} \frac{I_{\beta_i}}{f(\mathrm{Q_{EC}} - E_i)\, T_{1/2}} \tag{A.1}$$

where ΔE is the energy bin width (40 keV in this work), f represents the Fermi integral, E_i the energy of th i-th bin and $T_{1/2}$ stands for the half life of the decay. I_{β_i} is obtained from the EC and β^+ feeding distributions (EC_i and β_i^+) with the help of Eq. (A.2), where a and b are its respective weights :

$$I_{\beta_i} = \frac{aEC_i + b\beta_i^+}{\sum_{bins} aEC_i + b\beta_i^+} \tag{A.2}$$

The use of the Gauss error propagation formula in Eq. (A.3) allows us to calculate the uncertainty in the strength in terms of the uncertainties in the variables involved in Eq. (A.1):

$$\sigma^2_{S_{\beta_i}} = \left(\frac{\partial S_{\beta_i}}{\partial I_{\beta_i}}\right)^2 \sigma^2_{I_{\beta_i}} + \left(\frac{\partial S_{\beta_i}}{\partial T_{1/2}}\right)^2 \sigma^2_{T_{1/2}} + \left(\frac{\partial S_{\beta_i}}{\partial f_i}\right)^2 \sigma^2_{f_i} \tag{A.3}$$

which leads to Eq. (A.4) when the partial derivatives are evaluated

$$\sigma^2_{S_{\beta_i}} = \frac{1}{(\Delta E f_i T_{1/2})^2}\, \sigma^2_{I_{\beta_i}} + \left(\frac{I_{\beta_i}}{\Delta E f_i T_{1/2}^2}\right)^2 \sigma^2_{T_{1/2}} + \left(\frac{I_{\beta_i}}{\Delta E f_i^2 T_{1/2}}\right)^2 \sigma^2_{f_i} \tag{A.4}$$

The uncertainty $\sigma_{T_{1/2}}$ in the half life $T_{1/2}$ is a direct experimental input. The uncertainty in the Fermi function f_i at a given bin i comes from the interpolation of the tabulated values in [GOV71]. f_i is calculated at a given every energy by linear interpolation of the tabulated values as indicated by Eq. (A.5)

$$f_i = 10^{m_i(\mathrm{Q_{EC}}-E)+b_i} \tag{A.5}$$

The parameters m_i and b_i are the coefficients of the linear regression at a given energy E_i. Thus, the uncertainty in the interpolation becomes:

$$\sigma_{f_i} = \ln(10) m_i f_i \sigma_{\mathrm{Q_{EC}}} \tag{A.6}$$

We can see that the uncertainty in the Fermi integral is related to the uncertainty $\sigma_{\mathrm{Q_{EC}}}$ in the Q-value, which have to be determined experimentally.

The uncertainties in the feedings $\sigma_{I_{\beta_i}}$ adopt a more complex form as visible in Eq. (A.7), since the correlations between the feedings to different energy bins have to be considered.

$$\begin{aligned}\sigma^2_{I_{\beta_i}} = &\left(\frac{\partial I_{\beta_i}}{\partial a}\right)^2 \sigma_a^2 + \left(\frac{\partial I_{\beta_i}}{\partial b}\right)^2 \sigma_b^2 + 2\left(\frac{\partial I_{\beta_i}}{\partial a}\right)\left(\frac{\partial I_{\beta_i}}{\partial b}\right)\sigma_{ab} + \\ &\sum_j \sum_k \left[\left(\frac{\partial I_{\beta_i}}{\partial EC_j}\right)\left(\frac{\partial I_{\beta_i}}{\partial EC_k}\right)\sigma_{EC_{jk}} + \left(\frac{\partial I_{\beta_i}}{\partial \beta^+_j}\right)\left(\frac{\partial I_{\beta_i}}{\partial \beta^+_k}\right)\sigma_{\beta^+_{jk}}\right]\end{aligned} \tag{A.7}$$

The covariance matrices $\sigma_{EC_{jk}}$ and $\sigma_{\beta^+_{jk}}$ in Eq. (A.7), which correspond to the EC and β^+ feeding distributions respectively, have to be obtained as a result of the analysis method. The calculation of the covariance matrices for the three different methods was explained in section 3.3. In order to evaluate the value of $\sigma_{I_{\beta_i}}$, the expressions of the partial derivatives involved are given in Eqs. (A.8...A.11)

$$\left(\frac{\partial I_{\beta_i}}{\partial a}\right) = \frac{b(EC_i \sum_k \beta^+_k - \beta^+_i \sum_k EC_k)}{\left[\sum_k (aEC_k + b\beta^+_k)\right]^2} \tag{A.8}$$

$$\left(\frac{\partial I_{\beta_i}}{\partial b}\right) = \frac{a(\beta^+_i \sum_k EC_k - EC_i \sum_k \beta^+_k)}{\left[\sum_k (aEC_k + b\beta^+_k)\right]^2} \tag{A.9}$$

$$\left(\frac{\partial I_{\beta_i}}{\partial EC_j}\right) = \frac{a\delta_{ij} \sum_k (aEC_k + b\beta^+_k) - a(aEC_i + b\beta^+_i)}{\left[\sum_k (aEC_k + b\beta^+_k)\right]^2} \tag{A.10}$$

$$\left(\frac{\partial I_{\beta_i}}{\partial \beta^+_j}\right) = \frac{b\delta_{ij} \sum_k (aEC_k + b\beta^+_k) - b(aEC_i + b\beta^+_i)}{\left[\sum_k (aEC_k + b\beta^+_k)\right]^2} \tag{A.11}$$

where δ_{ij} is the delta of Kronecker.

We have shown so far how the β-strength and associated uncertainties have to be calculated. However, the integral value of S_β is also an important magnitude, since it is one of the results which can be compared with simple theoretical calculations.

A very common way to express the experimental value of the integrated β-strength is through the total $\log ft$, which is related to S_β as shown in Eq. (A.12)

$$\begin{aligned} \log ft &= \log_{10}\left(\frac{1}{\sum_i S_{\beta_i}\Delta E}\right) \\ &= \log_{10}\left(\frac{1}{\sum_i \frac{I_{\beta_i}}{f_i T_{1/2}}}\right) \end{aligned} \tag{A.12}$$

and ft can be calculated from Eq. (A.13)

$$ft = \left(\frac{1}{\sum_i \frac{I_{\beta_i}}{f_i T_{1/2}}}\right) \tag{A.13}$$

The use of the Gauss error propagation formula in Eq. (A.12) we can obtain the uncertainty in the $\log ft$ as indicated by Eq. (A.14)

$$\sigma^2_{\log ft} = \frac{1}{(\ln 10\; ft)^2}\sigma^2_{ft} \tag{A.14}$$

where σ^2_{ft} is defined in Eq.(A.15)

$$\begin{aligned} \sigma^2_{ft} = \left(\frac{\partial ft}{\partial T_{1/2}}\right)^2 \sigma^2_{T_{1/2}} + \sum_i \sum_j \left(\frac{\partial ft}{\partial I_{\beta_i}}\right)\left(\frac{\partial ft}{\partial I_{\beta_j}}\right)\sigma_{I_{\beta_{ij}}} \\ + \sum_i \sum_j \left(\frac{\partial ft}{\partial f_i}\right)\left(\frac{\partial ft}{\partial f_j}\right)\sigma_{f_i f_j} \end{aligned} \tag{A.15}$$

In order to evaluate Eq. (A.15), we need to rewrite some of the factors in terms of the experimental and analysed variables. The covariance matrices of the total feeding $\sigma_{I_{\beta_{ij}}}$ distribution in Eq. (A.15) can be expressed in terms of the EC and β^+ ones as shown in Eq.(A.16)

$$\begin{aligned} \sigma_{I_{\beta_{ij}}} &= \left(\frac{\partial I_{\beta_i}}{\partial a}\right)\left(\frac{\partial I_{\beta_j}}{\partial a}\right)\sigma^2_a + \left(\frac{\partial I_{\beta_i}}{\partial b}\right)\left(\frac{\partial I_{\beta_j}}{\partial b}\right)\sigma^2_b \\ &+ \left[\left(\frac{\partial I_{\beta_i}}{\partial a}\right)\left(\frac{\partial I_{\beta_j}}{\partial b}\right) + \left(\frac{\partial I_{\beta_i}}{\partial b}\right)\left(\frac{\partial I_{\beta_j}}{\partial a}\right)\right]\sigma_{ab} \\ &+ \sum_k \sum_l \left[\left(\frac{\partial I_{\beta_i}}{\partial EC_k}\right)\left(\frac{\partial I_{\beta_i}}{\partial EC_l}\right)\sigma_{EC_{kl}} + \left(\frac{\partial I_{\beta_i}}{\partial \beta^+_k}\right)\left(\frac{\partial I_{\beta_i}}{\partial \beta^+_l}\right)\sigma_{\beta^+_{kl}}\right] \end{aligned} \tag{A.16}$$

The covariance matrices related to the interpolation of the tabulated Fermi function values are calculated by the use of Eq. (A.17)

$$\sigma_{f_i f_j} = \ln 10^2 m_i m_j f_i f_j \sigma^2_{\mathrm{Q_{EC}}} \tag{A.17}$$

where m_i are the first order coefficients in Eq. (A.5).

The partial derivatives in Eq. (A.15) adopt the expression of Eq. (A.18), Eq. (A.19) and Eq. (A.20).

$$\left(\frac{\partial ft}{\partial T_{1/2}}\right) = \frac{ft}{T_{1/2}} \tag{A.18}$$

$$\left(\frac{\partial ft}{\partial I_{\beta_i}}\right) = -\frac{ft^2}{f_i T_{1/2}} \tag{A.19}$$

$$\left(\frac{\partial ft}{\partial f_i}\right) = \frac{I_{\beta_i}\, ft^2}{f_i^2 T_{1/2}} \tag{A.20}$$

By using all this formulae we can calculate the β-strength, the $\log ft$ and associated uncertainties starting from the EC and β^+ feeding distributions and associated covariance matrices, its weights a and b, the half-life $\mathrm{T}_{1/2}$, the Q_{EC} of the decay and the Fermi function f. However, both feeding distributions are not always available. A lack of statistics or contamination in one of the experimental spectra may lead to a situation in which only one of both feeding distributions can be used in the calculation of the β-strength and the $\log ft$. In this case, one can still arrive at the result by the use of the $r = EC/\beta^+$ relation tabulated in [GOV71]. The total intensity I_β can be expressed in terms of the EC intensity I_{EC} or the β^+ intensity I_{β^+} as indicated by Eq. (A.21) and Eq.(A.22) respectively.

$$I_{\beta_i} = \begin{cases} \left(1+\frac{1}{r_i}\right) I_{EC\,i} = \left(1+\frac{1}{r_i}\right) \frac{EC_i}{\sum_k^{\mathrm{Q_{EC}}} EC_k} & i\Delta E < \mathrm{Q_{EC}} - 1022 \\ I_{EC\,i} = \frac{EC_i}{\sum_k^{\mathrm{Q_{EC}}} EC_k} & i\Delta E > \mathrm{Q_{EC}} - 1022 \end{cases} \tag{A.21}$$

$$I_{\beta_i} = \begin{cases} (1+r_i) I_{\beta^+} = (1+r_i) \frac{\beta_i^+}{\sum_k^{\mathrm{Q_{EC}}-1022} \beta_k^+} & i\Delta E < \mathrm{Q_{EC}} - 1022 \\ 0 & i\Delta E > \mathrm{Q_{EC}} - 1022 \end{cases} \tag{A.22}$$

Here r_i represents the interpolated value of the average EC/β^+ ratio for the i-th bin calculated in Eq. (A.23)

$$r_i = 10^{\widetilde{m}_i(\mathrm{Q_{EC}} - E) + \widetilde{b}_i} \tag{A.23}$$

where $\widetilde{m}_i$ and $\widetilde{b}_i$ are the coefficients from the linear regression at a given energy E. It is worth remembering that the EC feeding distribution contains information over the whole $\mathrm{Q_{EC}}$-range, while the β^+ feeding distribution does not exist above the energy $\mathrm{Q_{EC}} - 2m_e c^2$. No information about the β-strength can be reached in the last 1022 keV of the $\mathrm{Q_{EC}}$-window if only the β^+ feeding distribution is available. The β-strength is calculated in the two cases with the help of the Eq. (A.24) and

Eq. (A.25)

$$S_{\beta_i} = \begin{cases} \frac{1}{\Delta E}\left(1+\frac{1}{r_i}\right)\frac{I_{EC\,i}}{f_i T_{1/2}} & i\Delta E < \mathrm{Q_{EC}} - 1022 \\ \frac{1}{\Delta E}\frac{I_{EC\,i}}{f_i T_{1/2}} & i\Delta E > \mathrm{Q_{EC}} - 1022 \end{cases} \tag{A.24}$$

$$S_{\beta_i} = \begin{cases} \frac{1}{\Delta E}(1+r_i)\frac{I_{\beta^+\,i}}{f_i T_{1/2}} & i\Delta E < \mathrm{Q_{EC}} - 1022 \\ 0 & i\Delta E > \mathrm{Q_{EC}} - 1022 \end{cases} \tag{A.25}$$

The use of the Gauss error formula leads to Eq. (A.26), which is analogous to Eq. (A.3) plus one additional term coming from the interpolation of the tabulated EC/β^+ values.

$$\sigma^2_{S_{\beta_i}} = \left(\frac{\partial S_{\beta_i}}{\partial I_{\beta_i}}\right)^2 \sigma^2_{I_{\beta_i}} + \left(\frac{\partial S_{\beta_i}}{\partial T_{1/2}}\right)^2 \sigma^2_{T_{1/2}} + \left(\frac{\partial S_{\beta_i}}{\partial f_i}\right)^2 \sigma^2_{f_i} + \left(\frac{\partial S_{\beta_i}}{\partial r_i}\right)^2 \sigma^2_{r_i} \tag{A.26}$$

The first three partial derivatives in Eq. (A.26) adopt the same expressions as the three in Eq. (A.4), and only the proper definitions of I_β given by Eq. (A.22) have to be applied. The evaluation of the new term in Eq. (A.26), the partial derivative on r_i, leads to Eq. (A.27) or Eq. (A.28), which correspond to the cases when the EC or β^+ feeding distributions are used.

For the EC case:

$$\left(\frac{\partial S_{\beta_i}}{\partial r_i}\right) = \begin{cases} -\frac{1}{\Delta E}\frac{1}{r_i^2}\frac{I_{\mathrm{EC}}}{f_i T_{1/2}} & i\Delta E < \mathrm{Q_{EC}} - 1022 \\ 0 & i\Delta E > \mathrm{Q_{EC}} - 1022 \end{cases} \tag{A.27}$$

For the β^+ case:

$$\left(\frac{\partial S_{\beta_i}}{\partial r_i}\right) = \begin{cases} \frac{1}{\Delta E}\frac{I_{\beta^+}}{f_i T_{1/2}} & i\Delta E < \mathrm{Q_{EC}} - 1022 \\ 0 & i\Delta E > \mathrm{Q_{EC}} - 1022 \end{cases} \tag{A.28}$$

For both EC and β^+ expressions, the value of σ_{r_i} is the indicated by Eq. (A.29), which is analogous to the expression of Eq.(A.6)

$$\sigma_{r_i} = \ln 10 \widetilde{m}_i r_i \sigma_{\mathrm{Q_{EC}}} \tag{A.29}$$

The influence of the experimental uncertainty in the half-life $\sigma_{T_{1/2}}$ has been already mentioned. Thus, the last factor to be considered in Eq.(A.26) is $\sigma_{I_{\beta_i}}$ as defined in Eq.(A.30) and Eq.(A.32).

For the EC case:

$$\sigma_{S_{\beta_i}} = \sum_j \sum_k \left(\frac{\partial I_{\beta_i}}{\partial EC_j}\right)\left(\frac{\partial I_{\beta_i}}{\partial EC_k}\right)\sigma_{EC_{jk}} \tag{A.30}$$

where

$$\left(\frac{\partial I_{\beta_i}}{\partial EC_j}\right) = \begin{cases} \left(1+\frac{1}{r_j}\right)\frac{\delta_{ij}\sum_k^{\mathrm{Q_{EC}}} EC_k - EC_j}{\left(\sum_k^{\mathrm{Q_{EC}}} EC_k\right)^2} & i\Delta E < \mathrm{Q_{EC}} - 1022 \\ \frac{\delta_{ij}\sum_k^{\mathrm{Q_{EC}}} EC_k - EC_j}{\left(\sum_k^{\mathrm{Q_{EC}}} EC_k\right)^2} & i\Delta E > \mathrm{Q_{EC}} - 1022 \end{cases} \tag{A.31}$$

For the β^+ case:

$$\sigma_{S_{\beta_i}} = \sum_j \sum_k \left(\frac{\partial I_{\beta_i}}{\partial \beta_j^+}\right)\left(\frac{\partial I_{\beta_i}}{\partial \beta_k^+}\right)\sigma_{\beta_{jk}^+} \tag{A.32}$$

where

$$\left(\frac{\partial I_{\beta_i}}{\partial \beta_j^+}\right) = \begin{cases} (1+r_j)\frac{\delta_{ij}\sum_k^{\mathrm{Q_{EC}}-1022}\beta_k^+ - \beta_j^+}{\left(\sum_k^{\mathrm{Q_{EC}}-1022}\beta_k^+\right)^2} & i\Delta E < \mathrm{Q_{EC}} - 1022 \\ 0 & i\Delta E > \mathrm{Q_{EC}} - 1022 \end{cases} \tag{A.33}$$

The $\log ft$ and ft can be calculated with the use of Eq. (A.12) and Eq. (A.13), by replacing the proper expressions of I_{β_i} into them. The calculation of σ_{ft} requires to evaluate additionally the term associated to the uncertainty in r_i. This is shown in Eq. (A.34)

$$\begin{aligned} \sigma_{ft}^2 = \left(\frac{\partial ft}{\partial T_{1/2}}\right)^2 \sigma_{T_{1/2}}^2 + \sum_i \sum_j \left(\frac{\partial ft}{\partial I_{\beta_i}}\right)\left(\frac{\partial ft}{\partial I_{\beta_j}}\right)\sigma_{I_{\beta_{ij}}} \\ + \sum_i \sum_j \left(\frac{\partial ft}{\partial f_i}\right)\left(\frac{\partial ft}{\partial f_j}\right)\sigma_{f_i f_j} + \sum_i \sum_j \left(\frac{\partial ft}{\partial r_i}\right)\left(\frac{\partial ft}{\partial r_j}\right)\sigma_{r_i r_j} \end{aligned} \tag{A.34}$$

Similarly to Eq. (A.17), $\sigma_{r_i r_j}$ is defined by Eq. (A.35) as follows:

$$\sigma_{r_i r_j} = \ln 10^2 \widetilde{m}_i \widetilde{m}_j r_i r_j \sigma_{\mathrm{Q_{EC}}}^2 \tag{A.35}$$

The evaluation of $\sigma_{I_{\beta_{ij}}}$ in the EC case is:

$$\sigma_{I_{\beta_{ij}}} = \sum_k \sum_l \left(\frac{\partial I_{\beta_i}}{\partial EC_k}\right)\left(\frac{\partial I_{\beta_j}}{\partial EC_l}\right)\sigma_{EC_{kl}} \tag{A.36}$$

where $\left(\frac{\partial I_{\beta_i}}{\partial EC_k}\right)$ has the same form as in Eq. (A.31). The partial derivative $\left(\frac{\partial ft}{\partial r_i}\right)$ is evaluated in Eq. (A.37)

$$\left(\frac{\partial ft}{\partial r_i}\right) = \begin{cases} \frac{1}{r_i^2}\frac{I_{\beta_i}\, ft^2}{f_i^2 T_{1/2}} & i\Delta E < \mathrm{Q_{EC}} - 1022 \\ 0 & i\Delta E > \mathrm{Q_{EC}} - 1022 \end{cases} \tag{A.37}$$

$$\tag{A.38}$$

The expression of $\sigma_{I_{\beta_{ij}}}$ for the β^+ case is:

$$\sigma_{I_{\beta_{ij}}} = \sum_k \sum_l \left(\frac{\partial I_{\beta_i}}{\partial \beta_k^+} \right) \left(\frac{\partial I_{\beta_j}}{\partial \beta_l^+} \right) \sigma_{\beta_{kl}^+} \tag{A.39}$$

where $\left(\frac{\partial I_{\beta_i}}{\partial \beta_k^+} \right)$ has the same form as in Eq. (A.33). The partial derivative $\left(\frac{\partial ft}{\partial r_i} \right)$ is evaluated in Eq. (A.40)

$$\left(\frac{\partial ft}{\partial r_i} \right) = \begin{cases} -\frac{I_{\beta_i} ft^2}{f_i^2 T_{1/2}} & i\Delta E < \mathrm{Q_{EC}} - 1022 \\ 0 & i\Delta E > \mathrm{Q_{EC}} - 1022 \end{cases} \tag{A.40}$$

All the rest of the terms in Eq. (A.34) are equivalent to the ones defined in Eq. (A.15) after the insertion of the proper definition of I_{β_i}.

Appendix B

De-excitation schemes used in the construction of the response matrices

B.1 Introduction

As it has been seen in section 3.2, the response matrices have to be constructed by considering the γ de-excitation paths involved in the decay. The complete electromagnetic de-excitation schemes were defined through the branching ratio matrix b_{ij}, where i and j are the initial and final bin numbers connected by the γ-transition of energy $E_\gamma = (i - j) \times 40$ keV. The electromagnetic de-excitation schemes used for the analysis presented in section 4.6 and section 4.7 are:

> ^{150}Ho 2^-: Branching ratio matrix for electromagnetic de-excitation scheme 1 in Fig. [B.1].
>
> ^{150}Ho 2^-: Branching ratio matrix for electromagnetic de-excitation scheme 2 in Fig. [B.2].
>
> ^{150}Ho 2^-: Branching ratio matrix for electromagnetic de-excitation scheme 3 in Fig. [B.3].
>
> ^{150}Ho 9^+:Branching ratio matrix for electromagnetic de-excitation scheme 1 in Fig. [B.4].
>
> ^{150}Ho 9^+: Branching ratio matrix for electromagnetic de-excitation scheme 2 in Fig. [B.5].

In the next section we discuss the statistical model for the electromagnetic de-excitation of the nucleus used in the calculation of the schemes 3 for ^{150}Ho 2^- and 2 for ^{150}Ho 9^+.

B.2 Statistical model for the electromagnetic de-excitation of the nucleus

The branching ratios for the discrete levels of the de-excitation schemes were taken from [RUB97] for ^{150}Ho 2^- (up to 2.7 MeV) and from [GAD94] for ^{150}Ho 9^+ (up to 2.4 MeV). They were obtained in both cases from high resolution γ-γ coincidence experiments. For levels above the energies mentioned (in the statistical energy region), the branching ratios were derived from a statistical model of the electromagnetic de-excitation of the nucleus. In the calculation of the average branching ratios it was assumed that within each bin, only levels populated in β-decay were decaying by γ-ray emission. The spin-parities we are refering are $J^\pi = 1^-, 2^-, 3^-$ for the ^{150}Ho 2^- decay and $J^\pi = 8^+, 9^+, 10^+$ for the the ^{150}Ho 9^+ decay. The model provides the level excitation energies, spin and parities from a level density functional $\rho(J,\pi,E_x)$. This functional describes the dependence of the average density of levels with given spin-parity on the excitation energy. We have chosen a parametrisation of the back-shifted Fermi gas model formula which is commonly employed [DIL73]:

$$\begin{aligned}
\rho(J,\pi,E_x) &= \rho(J,\pi)\rho(E_x) \qquad \text{(B.1)}\\
\rho(J,\pi) &= \frac{2J+1}{4\sigma^2}\mathrm{e}^{-\frac{J(J+1)}{2\sigma^2}}\\
\rho(E_x) &= \frac{1}{12\sqrt{2}}\frac{\mathrm{e}^{2\sqrt{a(E_x-\Delta)}}}{\sigma a^{\frac{1}{4}}(E_x-\Delta-t)^{\frac{5}{4}}}\\
\sigma^2 &= 0.0150A^{\frac{5}{3}}t\\
t &= \frac{1+\sqrt{1+4a(E_x-\Delta)}}{2a}
\end{aligned}$$

We have assumed an even distribution for both parities. The nucleus-dependent parameters a and Δ are sensitive to shell effects and are thus adjusted in order to reproduce measured level densities. We have taken the fitted values for ^{144}Nd [KOP90] $a = 15.0$ MeV^{-1} and $\Delta = 0.7$ MeV, which is the closest $N = 84$ nucleus for which there is experimental information available.

The branching ratios for the levels above the established discreteness limit are obtained from γ-strength functions related to the nuclear giant resonance excitation modes by the Axel-Brink hypothesis [BAR73]. The average radiation width from levels of spin-parity J^π at excitation energy E_x into levels within a certain energy interval $(E, E+\Delta E)$ can be expressed [KOP90]:

$$\langle\Gamma_\gamma\rangle = \frac{1}{\rho(J,\pi,E_x)}\sum_{XL}\sum_{J_f^{\pi f}}\int_E^{E+\Delta E} E_\gamma^{2L+1}f_{XL}(E_\gamma)\rho(J_f,\pi_f,E_x-E_\gamma)dE_\gamma \qquad \text{(B.2)}$$

where X represents the character of the transition ($X = E$ for electric, $X = M$ for magnetic) L is the multipolarity, and the range of final spin-parities $J_f^{\pi f}$ is given by the XL selection rules. We have considered only transitions of $E1$, $M1$ or $E2$ type. The strength functions f_{XL} have a Lorentzian shape except for $E1$ where a generalized Lorentzian shape seems to be in better agreement with experiment:

$$
\begin{aligned}
f_{E1}(E_\gamma) &= 8.68 \times 10^{-8} \sigma_0 \Gamma_0 \left[\frac{E_\gamma \Gamma(E_\gamma)}{(E_\gamma^2 - E_0^2)^2 + E_\gamma^2 \Gamma(E_\gamma)^2} + \frac{2.8\pi^2 T^2 \Gamma_0}{E_0^5} \right] \qquad \text{(B.3)} \\
\Gamma(E_\gamma) &= \Gamma_0 \frac{E_\gamma^2 + 4\pi^2 T^2}{E_0^2} \\
T &= \sqrt{\frac{B_n - E_\gamma}{a}} \\
f_{M1}(E_\gamma) &= 8.68 \times 10^{-8} \frac{\sigma_0 E_\gamma \Gamma_0^2}{(E_\gamma^2 - E_0^2)^2 + E_\gamma^2 \Gamma_0^2} \qquad \text{(B.4)} \\
f_{E2}(E_\gamma) &= 5.22 \times 10^{-8} \frac{\sigma_0 E_\gamma^{-1} \Gamma_0^2}{(E_\gamma^2 - E_0^2)^2 + E_\gamma^2 \Gamma_0^2} \qquad \text{(B.5)}
\end{aligned}
$$

Here a is the level density parameter introduced before, B_n (MeV) is the neutron binding energy, and the giant resonance parameters E_0 (MeV), Γ_0 (MeV) and σ_0 (mb) are taken from the systematics.

$$
\begin{array}{rcl}
E1 \text{ (Ref. [HAR82]): } E_0 & = & 31.2A^{-\frac{1}{3}} + 20.6A^{-\frac{1}{6}} \\
\Gamma_0 & = & 88\frac{A}{NZ} \\
\sigma_0 & = & \frac{46}{88}\frac{N^2Z^2}{A^2} \\
M1 \text{ (Ref. [KOP90]): } E_0 & = & 41A^{-\frac{1}{3}} \\
\Gamma_0 & = & 4 \\
\sigma_0 & = & 2 \\
E2 \text{ (Ref. [PRE84]): } E_0 & = & 65A^{-\frac{1}{3}} \\
\Gamma_0 & = & 6.11 - 0.012A \\
\sigma_0 & = & 0.634\frac{Z^2}{6.11A - 0.012A^2}
\end{array}
$$

where A and Z are the mass and atomic numbers of the daughter nucleus, respectively. The unit for the strength function f_{XL} is MeV^{2L+1}.

The average branching ratios are obtained from expression Eq. (B.2) by assuming that within the used bin size ΔE (40 keV), the various functions involved can be substituted by their values at the middle of the bin. Thus, the integration reduces to the introduction of a constant multiplicative factor.

B.3 Branching ratio matrices

Hereafter we present a set of figures which show the different branching ratio matrices which have been used in the analysis.

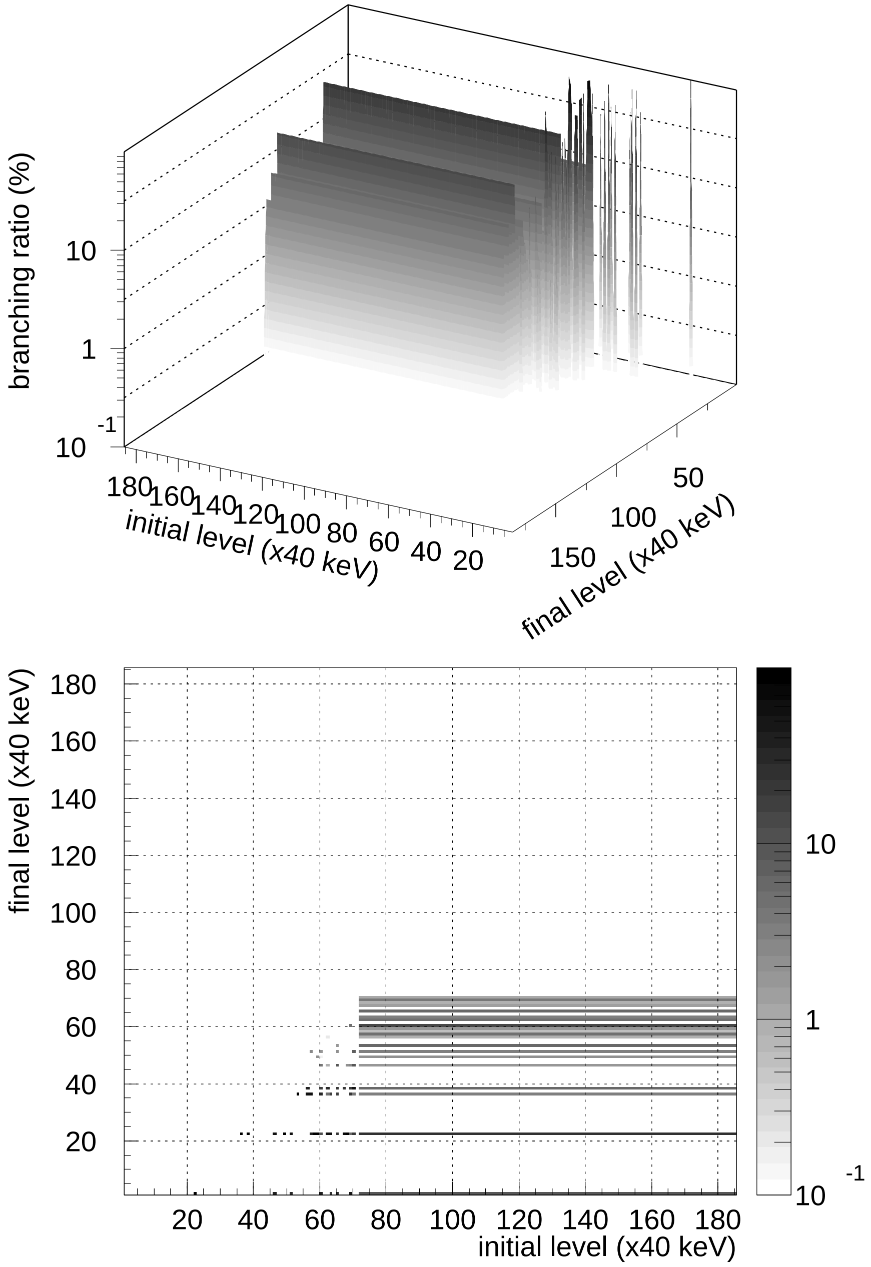

Figure B.1: Branching ratio matrix for the electromagnetic de-excitation scheme 1 for ^{150}Ho 2^{-}.

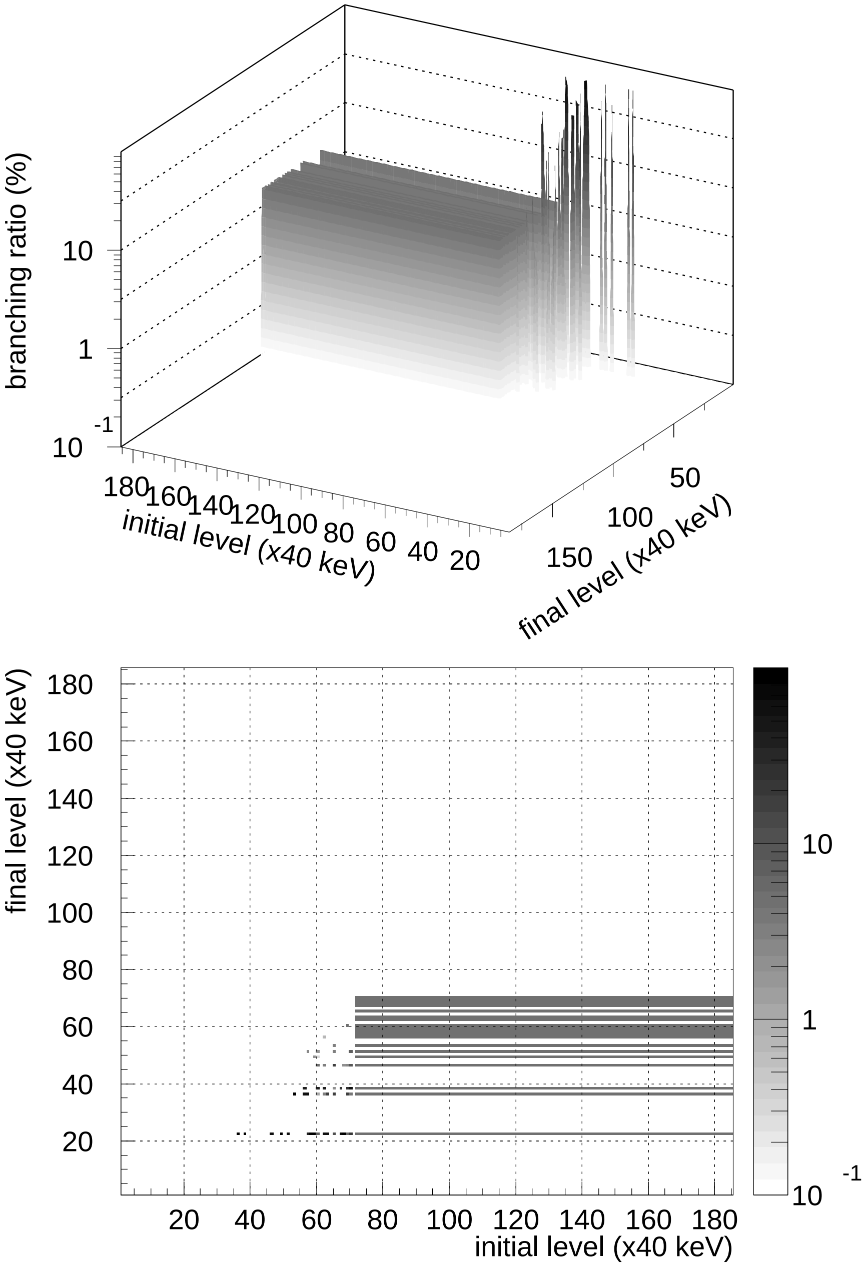

Figure B.2: Branching ratio matrix for the electromagnetic de-excitation scheme 2 for ^{150}Ho 2^{-}.

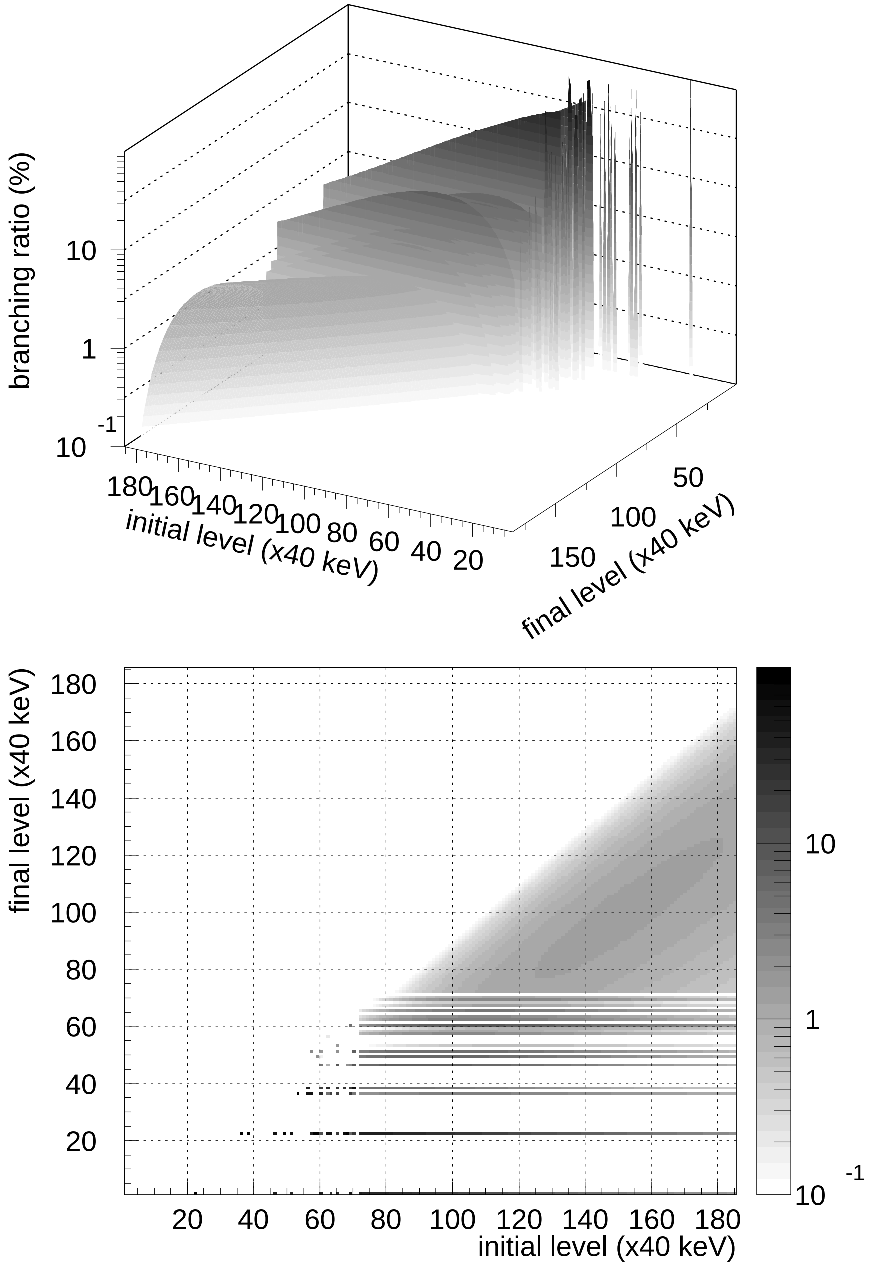

Figure B.3: Branching ratio matrix for the electromagnetic de-excitation scheme 3 for ^{150}Ho 2^{-}.

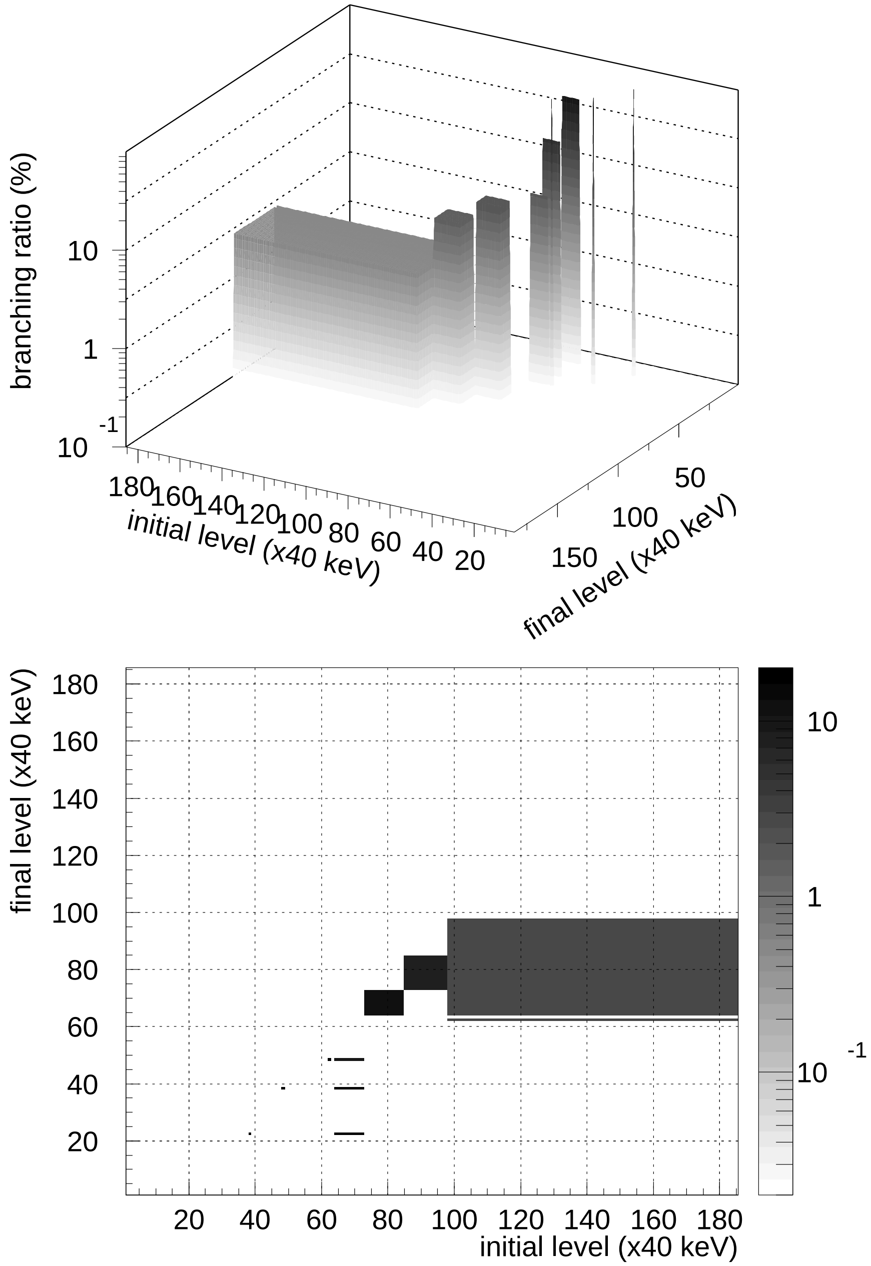

Figure B.4: Branching ratio matrix for the electromagnetic de-excitation scheme 1 for ^{150}Ho 9^+.

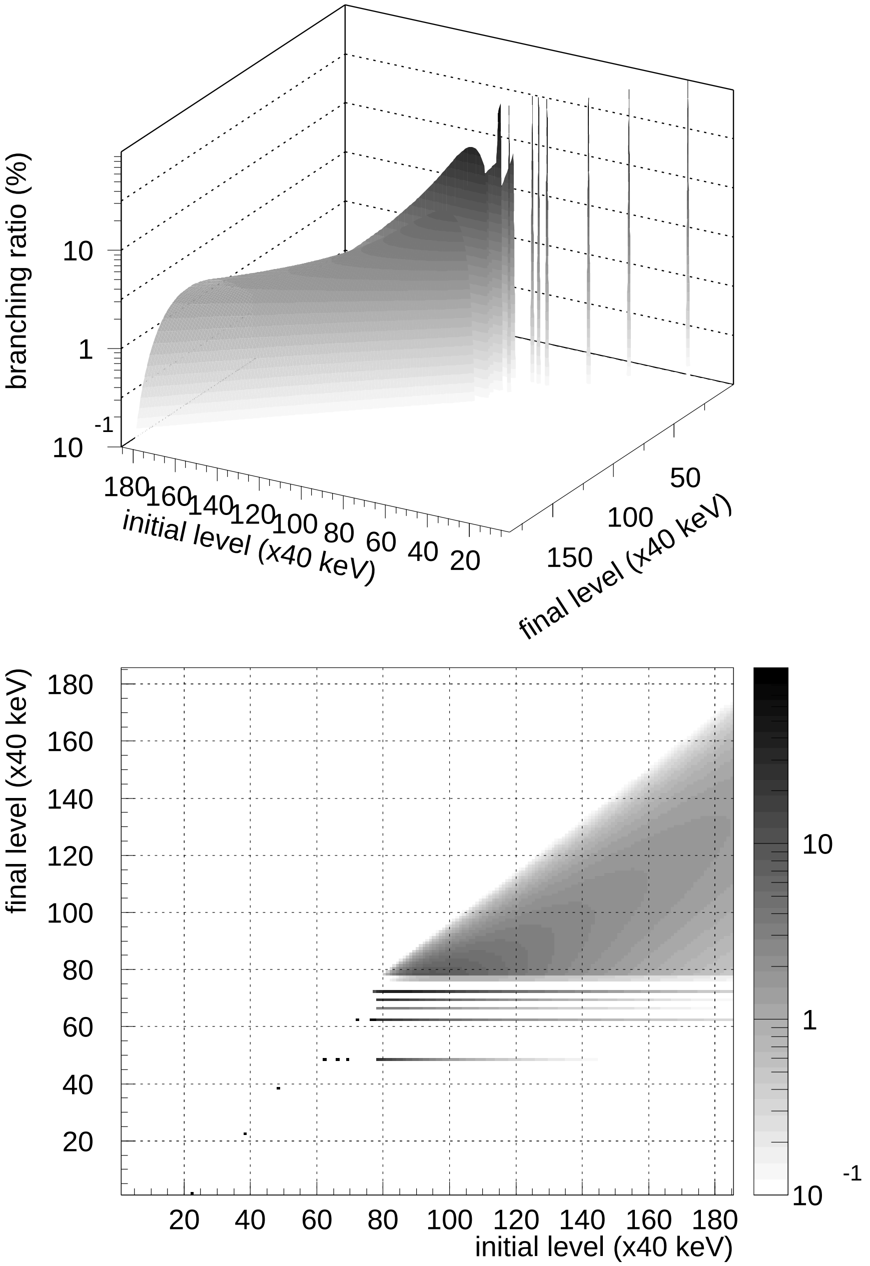

Figure B.5: Branching ratio matrix for the electromagnetic de-excitation scheme 2 for ^{150}Ho 9^{+}.

Appendix C

Tabulated β-strenghts

C.1 Tabulated ^{150}Ho2$^-$ β-strength

E_{bin}	S_β	$\sigma_{\mathrm{S}_\beta}$	E_{bin}	S_β	$\sigma_{\mathrm{S}_\beta}$
(keV)	(keV^{-1} s^{-1} $\times10^6$)		(keV)	(keV^{-1} s^{-1} $\times10^6$)	
20.	0.00E+00	.0E+00	60.	0.00E+00	.0E+00
100.	0.00E+00	.0E+00	140.	0.00E+00	.0E+00
180.	0.00E+00	.0E+00	220.	0.00E+00	.0E+00
260.	0.00E+00	.0E+00	300.	0.00E+00	.0E+00
340.	0.00E+00	.0E+00	380.	0.00E+00	.0E+00
420.	0.00E+00	.0E+00	460.	0.00E+00	.0E+00
500.	0.00E+00	.0E+00	540.	0.00E+00	.0E+00
580.	0.00E+00	.0E+00	620.	0.00E+00	.0E+00
660.	0.00E+00	.0E+00	700.	0.00E+00	.0E+00
740.	0.00E+00	.0E+00	780.	0.00E+00	.0E+00
820.	0.12E-02	.7E-04	860.	0.00E+00	.0E+00
900.	0.00E+00	.0E+00	940.	0.00E+00	.0E+00
980.	0.00E+00	.0E+00	1020.	0.00E+00	.0E+00
1060.	0.00E+00	.0E+00	1100.	0.00E+00	.0E+00
1140.	0.00E+00	.0E+00	1180.	0.00E+00	.0E+00
1220.	0.00E+00	.0E+00	1260.	0.00E+00	.0E+00
1300.	0.00E+00	.0E+00	1340.	0.00E+00	.0E+00
1380.	0.17E-02	.1E-03	1420.	0.00E+00	.0E+00
1460.	0.14E-02	.9E-04	1500.	0.00E+00	.0E+00
1540.	0.00E+00	.0E+00	1580.	0.00E+00	.0E+00

Table C.1: ^{150}Ho 2$^-$ β-strength calculated for decay scheme 3.

E_{bin}	S_β	σ_{S_β}	E_{bin}	S_β	σ_{S_β}
(keV)	(keV^{-1} s^{-1} $\times 10^6$)		(keV)	(keV^{-1} s^{-1} $\times 10^6$)	
1620.	0.00E+00	.0E+00	1660.	0.00E+00	.0E+00
1700.	0.00E+00	.0E+00	1740.	0.00E+00	.0E+00
1780.	0.21E-02	.1E-03	1820.	0.00E+00	.0E+00
1860.	0.00E+00	.0E+00	1900.	0.59E-03	.3E-04
1940.	0.00E+00	.0E+00	1980.	0.49E-03	.3E-04
2020.	0.00E+00	.0E+00	2060.	0.97E-03	.6E-04
2100.	0.00E+00	.0E+00	2140.	0.00E+00	.0E+00
2180.	0.54E-03	.3E-04	2220.	0.49E-03	.3E-04
2260.	0.51E-03	.3E-04	2300.	0.63E-03	.4E-04
2340.	0.63E-03	.4E-04	2380.	0.00E+00	.0E+00
2420.	0.99E-03	.6E-04	2460.	0.11E-02	.7E-04
2500.	0.00E+00	.0E+00	2540.	0.81E-03	.5E-04
2580.	0.00E+00	.0E+00	2620.	0.61E-03	.4E-04
2660.	0.64E-03	.4E-04	2700.	0.73E-03	.5E-04
2740.	0.12E-02	.8E-04	2780.	0.00E+00	.0E+00
2820.	0.34E-02	.2E-03	2860.	0.00E+00	.0E+00
2900.	0.00E+00	.0E+00	2940.	0.00E+00	.0E+00
2980.	0.00E+00	.0E+00	3020.	0.49E-02	.3E-03
3060.	0.27E-02	.2E-03	3100.	0.00E+00	.0E+00
3140.	0.34E-02	.2E-03	3180.	0.26E-02	.2E-03
3220.	0.28E-02	.2E-03	3260.	0.31E-02	.2E-03
3300.	0.35E-02	.2E-03	3340.	0.00E+00	.0E+00
3380.	0.35E-02	.2E-03	3420.	0.34E-02	.2E-03
3460.	0.30E-02	.2E-03	3500.	0.32E-02	.2E-03
3540.	0.36E-02	.2E-03	3580.	0.41E-02	.3E-03
3620.	0.57E-02	.3E-03	3660.	0.89E-02	.5E-03
3700.	0.15E-01	.9E-03	3740.	0.17E-01	.1E-02
3780.	0.12E-01	.8E-03	3820.	0.12E-01	.7E-03
3860.	0.17E-01	.1E-02	3900.	0.27E-01	.2E-02
3940.	0.16E-01	.1E-02	3980.	0.20E-01	.1E-02
4020.	0.25E-01	.2E-02	4060.	0.20E-01	.1E-02

Table C.2: ^{150}Ho 2^- β-strength calculated for decay scheme 3.

E_{bin} (keV)	S$_{\beta}$ (keV^{-1} s^{-1}	$\sigma_{S_{\beta}}$ $\times10^{6}$)	E_{bin} (keV)	S$_{\beta}$ (keV^{-1} s^{-1}	$\sigma_{S_{\beta}}$ $\times10^{6}$)
4100.	0.16E-01	.1E-02	4140.	0.18E-01	.1E-02
4180.	0.21E-01	.1E-02	4220.	0.31E-01	.2E-02
4260.	0.52E-01	.3E-02	4300.	0.95E-01	.6E-02
4340.	0.16E+00	.1E-01	4380.	0.25E+00	.2E-01
4420.	0.29E+00	.2E-01	4460.	0.24E+00	.2E-01
4500.	0.19E+00	.1E-01	4540.	0.17E+00	.1E-01
4580.	0.10E+00	.7E-02	4620.	0.72E-01	.5E-02
4660.	0.74E-01	.5E-02	4700.	0.72E-01	.5E-02
4740.	0.78E-01	.5E-02	4780.	0.75E-01	.5E-02
4820.	0.66E-01	.4E-02	4860.	0.59E-01	.4E-02
4900.	0.48E-01	.3E-02	4940.	0.40E-01	.3E-02
4980.	0.36E-01	.2E-02	5020.	0.35E-01	.2E-02
5060.	0.35E-01	.2E-02	5100.	0.34E-01	.2E-02
5140.	0.32E-01	.2E-02	5180.	0.32E-01	.2E-02
5220.	0.30E-01	.2E-02	5260.	0.26E-01	.2E-02
5300.	0.23E-01	.1E-02	5340.	0.22E-01	.1E-02
5380.	0.23E-01	.1E-02	5420.	0.25E-01	.2E-02
5460.	0.26E-01	.2E-02	5500.	0.24E-01	.2E-02
5540.	0.24E-01	.2E-02	5580.	0.22E-01	.1E-02
5620.	0.22E-01	.1E-02	5660.	0.21E-01	.1E-02
5700.	0.21E-01	.1E-02	5740.	0.22E-01	.1E-02
5780.	0.21E-01	.1E-02	5820.	0.20E-01	.1E-02
5860.	0.21E-01	.1E-02	5900.	0.23E-01	.2E-02
5940.	0.26E-01	.2E-02	5980.	0.28E-01	.2E-02
6020.	0.27E-01	.2E-02	6060.	0.25E-01	.2E-02
6100.	0.24E-01	.2E-02	6140.	0.23E-01	.2E-02
6180.	0.21E-01	.2E-02	6220.	0.21E-01	.2E-02
6260.	0.20E-01	.2E-02	6300.	0.22E-01	.2E-02
6340.	0.24E-01	.2E-02	6380.	0.24E-01	.2E-02
6420.	0.24E-01	.2E-02	6460.	0.22E-01	.2E-02

Table C.3: ^{150}Ho 2^{-} β-strength calculated for decay scheme 3.

E_{bin}	S$_\beta$	$\sigma_{\mathrm{S}_\beta}$	E_{bin}	S$_\beta$	$\sigma_{\mathrm{S}_\beta}$
(keV)	(keV^{-1} s^{-1} $\times 10^6$)		(keV)	(keV^{-1} s^{-1} $\times 10^6$)	
6500.	0.20E-01	.2E-02	6540.	0.20E-01	.2E-02
6580.	0.21E-01	.2E-02	6620.	0.24E-01	.3E-02
6660.	0.28E-01	.3E-02	6700.	0.30E-01	.3E-02
6740.	0.25E-01	.3E-02	6780.	0.18E-01	.2E-02
6820.	0.13E-01	.2E-02	6860.	0.13E-01	.2E-02
6900.	0.18E-01	.2E-02	6940.	0.28E-01	.4E-02
6980.	0.37E-01	.7E-02	7020.	0.33E-01	.5E-02
7060.	0.22E-01	.6E-02	7100.	0.14E-01	.4E-02
7140.	0.11E-01	.4E-02	7180.	0.13E-01	.5E-02
7220.	0.28E-01	.1E-01	7260.	0.97E-01	.7E-01

Table C.4: ^{150}Ho 2^- β-strength calculated for decay scheme 3.

C.2 Tabulated ^{150}Ho 9^+ β-strength

E_{bin}	S$_\beta$	$\sigma_{\mathrm{S}_\beta}$	E_{bin}	S$_\beta$	$\sigma_{\mathrm{S}_\beta}$
(keV)	(keV^{-1} s^{-1} $\times 10^6$)		(keV)	(keV^{-1} s^{-1} $\times 10^6$)	
20.	0.00E+00	.0E+00	60.	0.00E+00	.0E+00
100.	0.00E+00	.0E+00	140.	0.00E+00	.0E+00
180.	0.00E+00	.0E+00	220.	0.00E+00	.0E+00
260.	0.00E+00	.0E+00	300.	0.00E+00	.0E+00
340.	0.00E+00	.0E+00	380.	0.00E+00	.0E+00
420.	0.00E+00	.0E+00	460.	0.00E+00	.0E+00
500.	0.00E+00	.0E+00	540.	0.00E+00	.0E+00
580.	0.00E+00	.0E+00	620.	0.00E+00	.0E+00
660.	0.00E+00	.0E+00	700.	0.00E+00	.0E+00

Table C.5: ^{150}Ho 9^+ β-strength calculated for decay scheme 2.

E_{bin} (keV)	S_β (keV^{-1} s^{-1}	σ_{S_β} $\times10^6$)	E_{bin} (keV)	S_β (keV^{-1} s^{-1}	σ_{S_β} $\times10^6$)
740.	0.00E+00	.0E+00	780.	0.00E+00	.0E+00
820.	0.13E-08	.5E-08	860.	0.00E+00	.0E+00
900.	0.00E+00	.0E+00	940.	0.00E+00	.0E+00
980.	0.00E+00	.0E+00	1020.	0.00E+00	.0E+00
1060.	0.00E+00	.0E+00	1100.	0.00E+00	.0E+00
1140.	0.00E+00	.0E+00	1180.	0.00E+00	.0E+00
1220.	0.00E+00	.0E+00	1260.	0.00E+00	.0E+00
1300.	0.00E+00	.0E+00	1340.	0.00E+00	.0E+00
1380.	0.00E+00	.0E+00	1420.	0.00E+00	.0E+00
1460.	0.24E-01	.1E-01	1500.	0.00E+00	.0E+00
1540.	0.00E+00	.0E+00	1580.	0.00E+00	.0E+00
1620.	0.00E+00	.0E+00	1660.	0.00E+00	.0E+00
1700.	0.00E+00	.0E+00	1740.	0.00E+00	.0E+00
1780.	0.00E+00	.0E+00	1820.	0.00E+00	.0E+00
1860.	0.56E-01	.9E-02	1900.	0.00E+00	.0E+00
1940.	0.00E+00	.0E+00	1980.	0.00E+00	.0E+00
2020.	0.00E+00	.0E+00	2060.	0.00E+00	.0E+00
2100.	0.00E+00	.0E+00	2140.	0.00E+00	.0E+00
2180.	0.00E+00	.0E+00	2220.	0.00E+00	.0E+00
2260.	0.00E+00	.0E+00	2300.	0.00E+00	.0E+00
2340.	0.00E+00	.0E+00	2380.	0.00E+00	.0E+00
2420.	0.61E+00	.7E-01	2460.	0.00E+00	.0E+00
2500.	0.00E+00	.0E+00	2540.	0.00E+00	.0E+00
2580.	0.34E-02	.5E-03	2620.	0.00E+00	.0E+00
2660.	0.00E+00	.0E+00	2700.	0.23E-01	.3E-02
2740.	0.00E+00	.0E+00	2780.	0.00E+00	.0E+00
2820.	0.20E-01	.2E-02	2860.	0.00E+00	.0E+00
2900.	0.00E+00	.0E+00	2940.	0.00E+00	.0E+00
2980.	0.24E-01	.3E-02	3020.	0.16E-01	.2E-02
3060.	0.15E-01	.2E-02	3100.	0.90E-02	.9E-03
3140.	0.67E-02	.7E-03	3180.	0.66E-02	.6E-03
3220.	0.73E-02	.7E-03	3260.	0.74E-02	.7E-03

Table C.6: ^{150}Ho 9^+ β-strength calculated for decay scheme 2.

E_{bin}	S_β	σ_{S_β}	E_{bin}	S_β	σ_{S_β}
(keV)	(keV^{-1} s^{-1} $\times 10^6$)		(keV)	(keV^{-1} s^{-1} $\times 10^6$)	
3300.	0.70E-02	.8E-03	3340.	0.73E-02	.8E-03
3380.	0.92E-02	.9E-03	3420.	0.12E-01	.1E-02
3460.	0.13E-01	.1E-02	3500.	0.11E-01	.1E-02
3540.	0.80E-02	.8E-03	3580.	0.61E-02	.5E-03
3620.	0.55E-02	.4E-03	3660.	0.60E-02	.5E-03
3700.	0.78E-02	.7E-03	3740.	0.11E-01	.1E-02
3780.	0.17E-01	.1E-02	3820.	0.23E-01	.2E-02
3860.	0.28E-01	.2E-02	3900.	0.31E-01	.3E-02
3940.	0.35E-01	.3E-02	3980.	0.41E-01	.3E-02
4020.	0.45E-01	.4E-02	4060.	0.45E-01	.4E-02
4100.	0.47E-01	.3E-02	4140.	0.59E-01	.4E-02
4180.	0.90E-01	.7E-02	4220.	0.14E+00	.1E-01
4260.	0.17E+00	.1E-01	4300.	0.15E+00	.1E-01
4340.	0.11E+00	.7E-02	4380.	0.88E-01	.6E-02
4420.	0.83E-01	.7E-02	4460.	0.84E-01	.7E-02
4500.	0.79E-01	.5E-02	4540.	0.71E-01	.5E-02
4580.	0.68E-01	.4E-02	4620.	0.69E-01	.5E-02
4660.	0.70E-01	.5E-02	4700.	0.66E-01	.5E-02
4740.	0.59E-01	.4E-02	4780.	0.54E-01	.4E-02
4820.	0.53E-01	.3E-02	4860.	0.53E-01	.3E-02
4900.	0.54E-01	.4E-02	4940.	0.54E-01	.4E-02
4980.	0.55E-01	.4E-02	5020.	0.53E-01	.3E-02
5060.	0.48E-01	.3E-02	5100.	0.43E-01	.3E-02
5140.	0.43E-01	.3E-02	5180.	0.45E-01	.3E-02
5220.	0.44E-01	.3E-02	5260.	0.40E-01	.3E-02
5300.	0.38E-01	.3E-02	5340.	0.39E-01	.3E-02
5380.	0.41E-01	.3E-02	5420.	0.43E-01	.3E-02
5460.	0.43E-01	.3E-02	5500.	0.41E-01	.3E-02
5540.	0.38E-01	.3E-02	5580.	0.35E-01	.3E-02
5620.	0.36E-01	.3E-02	5660.	0.41E-01	.3E-02
5700.	0.47E-01	.4E-02	5740.	0.42E-01	.4E-02

Table C.7: ^{150}Ho 9^+ β-strength calculated for decay scheme 2.

E_{bin} (keV)	S_β (keV^{-1} s^{-1} $\times 10^6$)	σ_{S_β}	E_{bin} (keV)	S_β (keV^{-1} s^{-1} $\times 10^6$)	σ_{S_β}
5780.	0.29E-01	.3E-02	5820.	0.17E-01	.2E-02
5860.	0.11E-01	.1E-02	5900.	0.87E-02	.1E-02
5940.	0.84E-02	.1E-02	5980.	0.83E-02	.1E-02
6020.	0.73E-02	.9E-03	6060.	0.66E-02	.8E-03
6100.	0.77E-02	.1E-02	6140.	0.13E-01	.2E-02
6180.	0.24E-01	.3E-02	6220.	0.39E-01	.6E-02
6260.	0.48E-01	.7E-02	6300.	0.45E-01	.7E-02
6340.	0.37E-01	.6E-02	6380.	0.28E-01	.4E-02
6420.	0.21E-01	.4E-02	6460.	0.14E-01	.3E-02
6500.	0.88E-02	.2E-02	6540.	0.57E-02	.1E-02
6580.	0.48E-02	.1E-02	6620.	0.58E-02	.1E-02
6660.	0.10E-01	.2E-02	6700.	0.21E-01	.6E-02
6740.	0.35E-01	.1E-01	6780.	0.39E-01	.1E-01
6820.	0.28E-01	.1E-01	6860.	0.18E-01	.6E-02
6900.	0.12E-01	.4E-02	6940.	0.10E-01	.4E-02
6980.	0.11E-01	.4E-02	7020.	0.15E-01	.7E-02
7060.	0.24E-01	.1E-01	7100.	0.50E-01	.3E-01
7140.	0.12E+00	.7E-01	7180.	0.00E+00	.0E+00
7220.	0.00E+00	.0E+00	7260.	0.00E+00	.0E+00

Table C.8: ^{150}Ho 9^+ β-strength calculated for decay scheme 2.

Bibliography

[AUD97] G. Audi, O. Bersillon, J. Blachot and A.H. Wapstra, Nucl. Phys. A 624 (1997) 1

[AGR97] J. Agramunt, A. Algora, D. Cano-Ott, A. Gadea, B.Rubio, J.L. Taín, M. Gierlik, M. Karny, Z. Janas, A. Plochocki, K. Rykaczewski, J. Szerypo, R. Collatz, J. Gerl, M. Górska, H. Grawe, M. Hellström, Z. Hu, R. Kirchner, M. Rejmund, E. Roeckl, M. Shibata L. Batist, F. Moroz, V. Wittmann and P. Kleinheinz, in: Proceedings of the International Symposium on New Facet of Spin Giant Resonances in Nuclei, Tokyo 1997 H. Sakai, H. Okamura and T. Wakasa, eds., (World Scientific, Singapore, 1998) 150

[ARI80] A. Arima and K. Shimizu, Nucl. Phys. A 336 (1980) 363

[BAR73] G.A. Bartholomew, E.D. Earle, A.J. Ferguson, J.W. Knowles and M.A. Lone, Adv. Nucl. Phys. 7 (1973) 229

[BEC97] D.Beck *et al.*, Nucl. Phys. A 626 (1997) 343c

[BER88] M.J. Berger and R. Wang, in: Monte Carlo Transport of Electrons and Photons, T.M. Jenkins, W.R. Nelson and A. Rindi, eds., (Plenum Press, N.Y., 1988) 21

[BLO98] J. Blomqvist, private communication (1998)

[BNL99] http://www.nndc.bnl.gov

[BRO84] B.A. Brown, A. Etchegoyen, W.D.M. Rae and N.S. Godwin, computer code OXBASH (1984) unpublished

[BRO85] B.A. Brown and B.H. Wildenthal, At. Data Nucl. Data Tables 33 (1985) 347

[BRU81] C. Bruske, K.H. Burkard, W. Hüller, R. Kirchner, O. Klepper and E. Roeckl, Nucl. Instr. Meth. 186 (1981) 61

[BOH98] A. Bohr and B.R. Mottelson, *Nuclear Structure* I (1998) 411

[BYK80] A.A. Bykov, V.D. Witman, F.V. Moroz and Yu.V. Naumov, Izv. Akad. Nauk. SSSR, Ser. Fiz. 44 (1980) 918

[CAN98] D. Cano-Ott, *Obtención de la función de respuesta de un espectrómetro de absorción total de NaI(Tl) mediante simulación Monte Carlo y corrección de la distorsión producida por el apilamiento electrónico de pulsos*, Trabajo de Investigación, Universidad de Valencia (1998)

[CAN99a] D. Cano-Ott, J.L. Taín, A. Gadea, B. Rubio, L. Batist, M. Karny and E. Roeckl, Nucl. Instr. Meth. A 430 (1999) 333

[CAN99b] D. Cano-Ott, J.L. Taín, A. Gadea, B. Rubio, L. Batist, M. Karny and E. Roeckl, Nucl. Instr. Meth. A 430 (1999) 488

[CAU95] E. Caurier, A. Poves and P. Zuker, Phys. Rev. Lett. 74 9 (1995) 1517

[CHO93] W.T. Chou, E.K. Warburton and B.A. Brown, Phys. Rev. C 47 (1993) 163

[COL82] D.M. Collins, Nature 298 (1982) 49

[COL97] R. Collatz, P. Kleinheinz, B. Rubio, J.L. Taín, M. Piiparinen, H. Keller, R. Kirchner, O. Klepper, E. Roeckl and D. Schardt, Z. Phys. A 358 (1997) 241

[DAG95] G. D'Agostini, Nucl. Instr. and Meth. A 362 (1995) 487

[DES95] L. Desbat and D. Girard, SIAM J. Sci. Comput. 16 (1995) 1387

[DEM77] A.P. Dempster, N.M. Laird and D.B. Rubin, J. R. Statist. Soc. B 39 (1977) 1

[DIL73] W. Dilg, W. Schantl and H. Vonach, Nucl. Phys. A 217 (1973) 269

[DOU95] L. Dou, R.J.W. Hodgson and D.G. Rancourt, Nucl. Instr. and Meth. B 100 (1995) 511

[DUK70] C.L. Duke, P.G. Hansen, O.B. Nielsen, G. Rudstam and the ISOLDE Collaboration, Nucl. Phys. A 151 (1970) 609

[EAD71] W.T. Eadie, D. Drijard, F.E. James, M. Roos and B. Sadoulet, *Statistical Methods in Experimental Physics* (North-Holland, Amsterdam, 1971)

[ENG56] D. Engelkemeir, Rev. Sci. Instr. 27 (1956) 589

[ENG88] J. Engel and P. Vogel, Phys. Rev. C 37 2 (1988) 731

[ERO91] B.G. Erozolimskii, I.A. Kuznetsov, I.V. Stepanenko, I.A. Kuida and Yu.A. Mostovoi, Phys. Lett. B 263 (1991) 33

[FRE90] S.J. Freedman, Comments Nucl. Part. Phys. 19 (1990) 209

[FRO79] A.G. Frodesen, O. Skjeggestad and H. Tøfte, *Probability and Statistics in Particle Physics* (Universitetsforlaget, Bergen, 1979)

[GAA80] C. Gaarde *et al.*, Nucl. Phys. A 334 (1980) 248

[GAD94] A. Gadea, Estudio de las desintegraciones β en la región de los lantánidos mediante técnicas de espectroscopía de alta resolución y de absorción total, PhD Thesis, Universidad de Valencia (1994)

[GAD98] A. Gadea, private communication (1998)

[GEA94] GEANT: Detector description and simulation tool, CERN Program Library W5013, Geneva, 1994

[GOV71] N.B Gove and M.J. Martin, At. Data Nucl. Data Tables 10 (1971) 205

[GOO80] C.D. Goodman *et al.*, Phys. Rev. Lett 44 (1980) 1755

[GOO82] C.D. Goodman, Nucl. Phys. A 374 (1982) 241

[GRE92] R.C. Greenwood, R.G. Helmer, M.A. Lee, M.H. Putnam, M.A. Oates, D.A. Struttmann and K.D. Watts, Nucl. Instr. and Meth. A 314 (1992) 514

[GRE93] W. Greiner and B. Müller, *Theoretical Physics 5: Gauge Theory of Weak Interactions*, Springer Verlag (1993)

[GUH98] T. Guhr, A. Müller-Groeling, H.A. Weidenmüller, Phys. Rep. 299 (1998) 189

[HAM94] I. Hamamoto, Nucl. Phys. A (1994) 19c

[HAM95] I. Hamamoto and X.Z. Zhang, Z. Phys. A 353 (1995) 145

[HAN93] P.C. Hansen and D.P. O'Leary, SIAM J. Sci. Comput. 14 (1993) 1487

[HAR77] J.C. Hardy, L.C. Carraz, B. Jonson and P.G. Hansen, Phys. Lett. B 71 (1977) 307

[HAR82] J.C. Hardy, Phys. Lett 109 B (1982) 242

[HAR90] J.C. Hardy, I.S. Towner, V.T. Koslowsky, E. Hagberg and H. Schmeing, Nucl. Phys. A509 (1990) 429

[ICA93] *http://www.aquila.infn.it:80/icarus/main.html*

[IKE63] K. Ikeda, S. Fujii and J.J. Fujita, Phys. Lett. 3 (1963) 271

[JAN98] Z. Janas, J. Agramunt, A. Algora, L. Batist, B.A. Brown, D. Cano-Ott, R. Collatz, A. Gadea, M. Gierlik, M. Górska, H. Grawe, A. Guglielmetti, M. Hellström, Z. Hu, M. Karny, R. Kirchner, F. Moroz, A. Piechaczek, A. Plochocki, M. Rejmund, E. Roeckl, B. Rubio, K. Rykaczewski, M. Shibata, J. Szerypo, J.L. Taín, V. Wittmann and A. Wöhr, Proceedings of the conference on exotic nuclei and atomic masses ENAM98, Bellaire, Michigan USA June (1998) AIP Conference Proceedings 455

[JAY57] E.T. Jaynes, Phys. Rev. 106 (1957) 620

[KAR97] M. Karny, J.M. Nitschke, L.F. Archambault, K. Burkard, D. Cano-Ott, M. Hellström, W. Hüller, R. Kirchner, S. Lewandowski, E. Roeckl and A. Sulik, Nucl. Instr. and Meth. B 126 (1997) 411

[KAR98] M. Karny, L. Batist, B.A. Brown, D. Cano-Ott, R. Collatz, A. Gadea, R. Grzywacz, A. Guglielmetti, M. Hellström, Z. Hu, Z. Janas, R. Kirchner, F. Moroz, A. Piechaczek, A. Plochocki, E. Roeckl, B. Rubio, K. Rykaczewski, M. Shibata, J. Szerypo, J.L Taín, V. Wittmann and A. Wöhr, Nucl. Phys. A 640 (1998) 3

[KIR81] R. Kirchner, K. Burkard, W. Hüller and O. Klepper, Nucl. Instr. Meth. 186 (1981) 295

[KIR90] R. Kirchner, K. Burkard, W. Hüller and O. Klepper, Nucl. Instr. Meth. A 292 (1990) 203

[KLA83] H.V Klapdor, Prog. Part. Nucl. Phys. 10 (1983) 131; *ibid* 17 (1986) 419

[KLE85] P. Kleinheinz, K. Zuber, C. Conci, C. Protop, J. Zuber, C.F. Liang, P. Paris and J. Blomqvist, Phys. Rev. Lett. 55 24 (1985) 2664

[KLE88] E. Klempt, P. Bobb, L. Hornig, J. Last, S.J. Freedman, D. Dubbers and O. Schärpf, Z. Phys. C37 (1988) 179

[KON65] E.J. Konopinski and M.E. Rose, in: Alpha-, Beta and Gamma-ray Spectroscopy, K. Siegbahn, ed., (North Holland, Amsterdam, 1965) 1327

[KOP90] J. Kopecky and M. Uhl, Phys. Rev. C 41 (1990) 1941

[KRA83] K.S. Krane, *Introductory Nuclear Physics 2nd Edition*, John Wiley & Sons (1983)

[LAC91] M. Lach, P. Kleinheinz, M. Piiparinen, M. Ogawa, S. Lunardi, M.C. Bosca, J. Styczen and J. Blomqvist, Z. Phys. A 341 (1991) 25

[LAN84] K. Lange and R. Carson, J. Comput. Assist. Tomogr. 8 (1984) 306

[LAW80] R.D. Lawson, *Theory of the nuclear shell model*, Clarendon Oxford (1980)

[LIP62] H.J. Lipkin, *Beta Decay For Pedestrians*, North-Holland Publishing Company Amsterdam (1962) G. Musiol, J. Ranft, R. Reif and D. Seeliger, *Kern- und Elementarteilchenphysik 2 Auflage*, Verlag Harri Deutsch (1995)

[LIU98] W. Liu *et al.*, Phys. Rev. C 58 (1998) 2677

[MAD87a] R. Madey *et al.*, Phys. Rev. C 35 (1987) 2011

[MAD87b] R. Madey *et al.*, Phys. Rev. C 36 (1987) 1647

[MEC92] W. Meczynski, K. Zuber, R. Broda, R. Menegazzo, P. Kleinheinz, M.C. Bosca, P. Paris, C.F. Liang and J. Blomqvist, Proceedings on the 6^{th} international conference on nuclei far from stability and 9^{th} international conference on atomic masses and fundamental constants, Bernkastel-Kues (1992) 695

[MEN91] R. Menegazzo, PhD Thesis Universität zu Köln (1991)

[MEN94] R. Menegazzo, P. Kleinheinz, R. Collatz, H. Güven, J. Styczen, D. Schardt, H. Keller, O. Klepper, G. Walter, A. Huck, G. Maurguier, J. Blomqvist and the ISOLDE collaboration, Z. Phys. A 349 (1994) 13

[MUR61] R.B. Murray and A. Meyer, Phys. Rev. 122 (1961) 815

[MUS95] G. Musiol, J. Ranft, R. Reif and D. Seeliger, *Kern- und Elementarteilchenphysik 2 Auflage*, Verlag Harri Deutsch (1995)

[NOL82] E. Nolte, G. Korschinek and Ch. Setzensack, Z. Phys. A 309 (1982) 33

[OSE79] E. Oset, Phys. Rev. Lett. 42 1 (1979) 47

[OST82] F. Osterfeld, Phys. Rev. C 26 (1982) 762

[PAG72] L. Pages, E. Bertel, H. Joffre and L. Sklavenitis, Nuclear Data Tables A 4 (1972) 1

[PIN96] G. Martínez-Pinedo, A. Poves, E. Caurier and P. Zuker, Phys. Rev. C 53 6 (1996) 2602

[PRE84] W.V. Preswitch, M.A. Islam and T.J. Kennett, Z. Phys. A 315 (1984) 103

[PRE92] W.H. Press, S.A. Teukolsky, W.T. Vetterling and P. Flannery, *Numerical Recipes* (Cambridge University Press, Cambridge, 1992)

[PUL77] F. Pullhofer, Nucl. Phys. A 280 (1977) 267

[REI84] W. Reisdorf, GSI Darmstadt, private communication (1984)

[ROO96] B.D. Rooney and J.D. Valentine, IEEE Trans. Nucl. Sci. NS-43 (1996) 1271

[RUB97] B. Rubio and A. Algora, private communication (1997)

[SAR98] P. Sarriguren, E. Moya de Guerra, A. Escuderos and A.C. Carrizo, Nucl. Phys. A 635 (1998) 55

[SHA48] C.E. Shannon, Bell. Sys. Tech. J. 27 (1948) 379

[SHE82] L.A. Shepp and Y. Vardi, IEEE Trans. Med. Imaging 1 (1982) 113

[SHO80] J.E. Shore and R.W. Johnson, IEEE Trans. Inform. Theory 26 (1980) 26

[SKI84] J. Skilling and R.K. Bryan, Mon. Not. R. Astr. Soc. 211 (1984) 111

[STY87] J. Styczen, P. Kleinheinz, W. Starzecki, B. Rubio, G. de Angelis, H.J. Hähn, C.F. Liang, P. Paris, R. Reinhardt, P. von Brentano and J. Blomqvist, Proceedings of the 5^{th} conference on nuclei far from stability NFFS, Ontario (1987) 489

[SUH88] J. Suhonen, A. Faessler, T. Taigel and T. Tomoda, Phys. Lett. B 202 2 (1988) 174

[TAD87] T.N. Taddeucci, C.A. Goulding, T.A. Carey, R.C. Byrd, C.D. Goodman, C. Gaarde, J. Larsen, D. Horen, J. Rapaport and E. Sugarbaker, Nucl. Phys. A 469 (1987) 125

[TAI89] J.L. Taín, B. Rubio, P. Kleinheinz, D. Shardt, R. Barden and J. Blomqvist, Z. Phys. A 333 (1989) 29

[TAI99] J.L. Taín, D. Cano-Ott, A. Gadea and B. Rubio, in preparation.

[TIK84] Y. Tikochinsky, N.Z. Tishby and R.D. Levine, Phys. Rev. Lett. 52 (1984) 1357

[TIT85] D.M. Titterington, Astron. Astrophys. 144 (1985) 381

[TOW83] I.S. Towner and F.C. Khanana, Nucl. Phys. A 399 (1983) 334

[TOW85] I.S. Towner, Nucl. Phys. A 444 (1985) 402

[VET82] M.C. Vetterly *et al.*, Phys. Rev. Lett. 59 (1987) 439

[VET89] M.C. Vetterly *et al.*, Phys. Rev. C 40 (1989) 559 ORNL-2309 (1957) 59

[WIL73] D.H. Wilkinson, Nucl. Phys. A 209 (1973) 470

[WIL83] B.H. Wildenthal, M.S. Curtin and B.A. Brown, Phys. Rev. C 28 (1983) 1343

[WIL93] D.H. Wilkinson, Nucl. Instr. Meth. A 335 (1993) 172

[YOS99] Yoshida T. *et al.*, J. Nucl. Sci. Technol. 36 (1999) 135

[ZER61] C.D. Zerby, A. Meyer and R.B. Murray, Nucl. Instr. and Meth. 12 (1961) 115

[ZHA93] C. Zhang, PhD Thesis/Report Jülich-2857 (1993)

[ZHU99] Z. Hu, L. Batist, J. Agramunt, A. Algora, B.A. Brown, D. Cano-Ott, R. Collatz, A. Gadea, M. Gierlik, M. Górska, H. Grawe, M. Hellström, Z. Janas, M. Karny, R. Kirchner, F. Moroz, A. Plochocki, M. Rejmund, E. Roeckl, B. Rubio, M. Shibata, J. Szerypo, J.L. Taín, V. Wittmann, Phys. Rev. C 60 (1999) 024315

[ZUB98] K. Zuber, Phys. Rep. 305 (1998) 295

Agradecimientos

Mis primeras palabras de agradecimiento son para José Luis Taín y Berta Rubio. Al primero por algo más que dirigir este trabajo, y a los dos por haberme ofrecido su amistad y haber hecho de mí un "experimental". Ahora ya lo soy.

I would like to thank Bill Gelletly for the revision of the text. Any improper use of the English language should be attributed to the author. Even though, I hope it is now readable and understandable also for a true Scotsman.

Gracias también a mis amigos del grupo γ del IFIC, porque con ellos el trabajo se pudo compaginar con unas buenas dosis de humor y café. A Alejo Algora, mi hermano y compay del Caribe, con quien sigo teniendo pendiente una cita en Varadero (cada vez estamos más cerca de lograrlo). A su lado siempre lo he pasado en grande, y que siga así por mucho tiempo. A Pepito Bea, porque está cuando le necesitas y siempre tiene un chiste a mano. Gracias, Pepe. A Enrico Farnea "Male", el godellano adoptivo. A Andrés Gadea e Isabel (que es de la familia), porque su amistad siempre suele ir acompañada de una deliciosa tortilla de patatas y un buen caldo. A Lluis García "Rafilón", un verdadero matemático nuclear converso. To Peter Kleinheinz, who was and is always ready for a nice discussion. Y finalmente, pero no el último, a Trino. Nuestros veranos e inviernos de hamsters, con algunas salidas del cesto, siempre nos han mantenido unidos.

I would like to express my gratitude to all my friends from the mass separator group. I shared with them much more than beam-times. Good times is the proper way to say it! To Charly Burkhard, Rüdiger Collatz, Magda Górska "remember we still have to dance sevillanas", Maggie Hellström, Zhiqiang Hu, Wilfried Hüller, Weiping Liu, Reinhard Kirchner, Siggi Raiss and Ernst Roeckl. It has been really a pleasure to work with you and I hope it will continue like that.

I would like to thank also all the collaborators from the PNPI-San Petersburg for their knowledge, experience and kindness: Leonid Batist, Fedor Moroz and Vladimir Wittmann.

I can not forget the ^{100}Sn freaks from the Experimental Physics Institute at the University of Warsaw: Zenon Janas, Marek Karny, A. Plochocki, Krzysztof

Rykaczewski and Jurek Szerypo. I enjoyed with them my stay in TASmania.

Agradecer por su recibimiento a mis nuevos compañeros de trabajo del grupo FACET del CIEMAT: David, Jesús, Miguel y Raúl. A Enrique González le doy especialmente gracias por haberme dejado el tiempo que necesitaba (y un poquito más) para acabar esta tesis. A Antonio Perez, nuestra más reciente adquisición, le deseo mucho ánimo, suerte, éxito y “decisión”.

A mis amigos en Darmstadt, Anita, Axel, Axelle, Caterina, Celine, Chilo, Fred “Bubu”, Fred “Too”, Hector, Ingo, John, Karsten “y su maravilloso Vindaloo”, Lola, el infatigable Matthias Kaspar, Pepe “macho grande” y Victor Ninov, con quienes he pasado algunos de los mejores ratos en estos últimos años.

También quiero recordar a mis compañeros del IFIC y del departamento de FAMN, Amparo, Ana, Asun, Eduardo Cortina “LaTeX”, Enrique, Paqui, Pepe Salt, Rosa, Rosario, Sanchezj y Tere, porque ha sido un verdadero placer estar con ellos.

A mis amigos en Valencia: Alfredo “instigador del lethal team y destructor de estómagos”, Alicia “con su mente siempre abierta”, Ana, Carmen “Ay Carmela”, Carolina “que no para”, Estrella y José Luís “young forever”, Jordi “el Cimmerio”, Javi “con su gente de Cuenca y Ciudad Real”, Jesús “abierto hasta el amanecer” y Tamar “la bailaora”, Juan Luís “Jpulpitus, altius fortius et non pluribus”, Iñaki “That’s life”, María “que nunca me hace caso”, Mariela y Daniel “esteee, viste, ché”, Nuria “y su Karaoke”, Pas “y sus toques sobre el lenguaje correcto”, Roberto “Sandman” y Robert “Gigatron”, Silvia y Jose Luís, Susana “la científica imparable”, Talo “el indómito postre-man” y la “recientemente descubierta” Titi. Sois estupendos... No Glo, no me he olvidado... Los maullidos siempre al final.

Gracias también a mis amigos de Madrid: Al Cappa “con trombón nuevo” y Ada, Ariel, Beatriz “que se rió como nadie y ahora se me casa”, Belén “y sus enredos”, Carmela “con sus cambios de peinado” y Rafa “y el salmón de Bergen rebozado con lava”, Carola y David “como te iba diciendo... bla bla bla... pero que rica está la cerveza”, David Barrado “Giulio mon amour”, David Elizondo “Pichurri el camerunés”, Eva Verdugo “te sigo esperando para la crisis de los 40”, Fernando “Miles”, “Tito y papá” Fer y Mapi “con su alienigena Paula”, Fernando “Canarinho”, Gloria “la mejor empanada de hogar”, Inma “y los pingos con mingas”, Inma “la poetisa del UNIX”, Javi “del Atleti” y Mariajo, Jesús “y las noches por Huertas”, José Ramón “mi eterno vecino”, Juan “el economista”, Julio “mi poeta muerto, más vivo que nunca”, Laura y Angel, Nurita “y Mondoñedo”, Paco “Padrazo y sus salvajes órdagos”, Rafael “Tafo”, Ru Ben Kenobi “mi fuerza, mi serenidad, mi hombre de principios sin fines”, Santi “el profesor imperturbable”, Susana y Javi “Bolli”.

Por último, mi cariño para mis padres y mi familia, porque son una gente fantástica (casi siempre...) y se lo debo todo a ellos...

Madrid, Diciembre de 1999.